The Paragenesis and Chemical Variation of Alteration Minerals Associated with Basement Rocks of the P2 Fault and the McArthur River Uranium Deposit, Athabasca Basin, Northern Saskatchewan, Canada.

Erin Elizabeth Adlakha

A thesis submitted to the
Faculty of Graduate and Postdoctoral Studies
in partial fulfillment of the requirements for the
PhD degree in Earth Sciences

Ottawa-Carleton Geoscience Centre
Faculty of Science
University of Ottawa

Abstract

The P2 reverse fault in the metasedimentary basement rocks of the eastern Athabasca Basin is the main structural control of the world-class McArthur River uranium deposit. The earliest preserved assemblage along the fault is oxy-dravite, rutile, quartz, pyrite and graphite. This assemblage formed at temperatures of up to 890 °C, during regional metamorphism or a thermal event at ~1.75 Ga. The exhumation and surface exposure of the rocks was accompanied by paleo-weathering, and the deposition of the Athabasca sandstones. Diagenetic fluids of the sandstones altered the basement rocks to form Sr-Ca-SO_4^{2-} rich aluminum phosphate sulfate (APS) minerals + hematite ± kaolin. The onset of hydrothermal activity along the basement and the P2 fault is recorded by local anatase at 1569 ± 31 Ma. Uraniferous fluid formed an assemblage of sudoite illite, magnesio-foitite and LREE+P rich APS minerals (rims earlier diagenetic-type APS minerals) along the entire P2 fault. Magnesio-foitite exhibits a high X-site vacancy (0.70 – 0.85 apfu) and contains high Al in its Y-site (0.70 – 1.12 apfu), suggesting that magnesio-foitite likely replaced kaolin. The REE pattern of magnesio-foitite is similar to that of uraninite ($Ce_N<Y_N$), likely due to their co-crystallization with LREE-rich APS minerals. APS minerals show variably high S/P ratios (0.05 - 0.21) in proximity to the deposit and low ratios (0.11 - 0.13) far from the deposit along the P2 fault, indicating reducing conditions in the ore zone. Low values of δD (-41 to -98 ‰) and high values of $\delta^{11}B$ (+13.1 to +23.2 ‰) for magnesio-foitite suggest that groundwater interacted with carbonates or evaporites and was progressively enriched in ^{11}B through interaction with illite and kaolin minerals.

This work demonstrates that i) the P2 fault was a site of extensive fluid-rock interaction, ii) mineralizing fluids travelled along the entire P2 fault in the basement, iii) the deposition of the McArthur River deposit was controlled by the availability of a reducing fluid through the P2 fault,

and iv) mineral chemistry (tourmaline and APS minerals) may help identify fertile faults in exploration for uranium deposits.

Acknowledgements

First and foremost, I would like to acknowledge my PhD supervisor Professor Keiko Hattori. Her enthusiasm and curiosity paired with her wealth of knowledge in the field of geology was instrumental in the success in this thesis. Thank you for having the confidence in me as a researcher and for convincing me to fast-track to a PhD since us "Canadians take too long to do anything." Your feedback of my work has been fundamental in the development of my writing, critical thinking and research skills.

I would like to extend thanks to the examining committee of this thesis: Prof. George Beaudoin of Laval University, and Profs. Ingrid Kjarsgaard, Ian Honsberger and Mark Hannington of the OCGC. Their input helped improve this thesis. I would like to also thank the reviewers of the manuscripts in this thesis (see individual chapter acknowledgements).

I would like to thank Cameco for providing logistics for field work and the geologists from Cameco, in particular Gerald Zaluski, Tom Kotzer and Brian McGill, whose feedback during the early years of the project was very much appreciated. Additionally, I would like to thank Aaron Brown and Remi Labelle for their help on-site.

Thank you to Eric Potter of the GSC for heading the uranium division of the TGI4 program which funded this project. I also thank you for your encouragement and feedback on written works. I would also like to thank SEG and the OGS programs for scholarship opportunities.

Many thanks extend to all of those who aided in analytical work: Jiri Mrazek for thin and thick section preparation, Zhaoping Zhang of the GSC for LAICPMS work, Bill Davis and Tom Pestja of the GSC for SHRIMP work, Paul Middlestead and Wendy Abdi of G. G. Hatch Lab, uOttawa, for stable isotope work, Nimal De Silva and Smita Mohanty of uOttawa for OES analysis, Chris McFarlane of UNB for U-Pb work, David Diekrup of uOttawa for probe work, Mitch Kerr of SMU for Raman work, and Nathan Steeves of uOttawa for Terraspec training. I would like to especially thank Glenn Poirier of uOttawa for all of his assistance with many hours of SEM and probe work, and for always finding time to squeeze me in for "emergencies." I would also like to especially thank my dear friend Brandon Boucher of UNB for many hours logged on the LACIPMS.

I would like to acknowledge the support staff at uOttawa Helene De Gouffe, Caroline Bisson, and Lisa-Robin Murphy for administration assistance.

I give special thanks to my undergraduate supervisor, Professor Jacob Hanley of SMU, for writing numerous reference letters, his words of encouragement and for keeping tabs on me during my PhD. I especially thank him for procuring me a desk at SMU so I could finish writing my thesis from my home town of Halifax.

I give so many thanks to all of my wonderful friends, office-mates and colleagues at uOttawa. Special thanks are extended to Stacey Wetmore, Jeremy Powell, Shamus Duff, Mary Devine, David Diekrup, Octavia Bath, Dave Lowe, Lindsay Coffin, and Mike Power for rarely saying no to after work (sometimes afternoon) beverages.

Lastly I would like to thank my fiancé Mitchell Kerr for his continuous support.

Table of Contents

CHAPTER 1.

Global Introduction

1.0 Preamble

Unconformity-type U deposits account for more than 33% of the global U resources (Jefferson et al. 2007) and the high grade deposits, e.g., the McArthur River deposit, are found in the Athabasca Basin of northern Saskatchewan, Canada. In the Athabasca Basin, these hydrothermal deposits occur along the unconformity between overlying Paleoproterozoic Athabasca Group sandstones and underlying Archean to Paleoproterozoic metamorphic, crystalline basement rocks (Fig. 1 and 2). It is generally accepted that uranium deposition occurred through the reduction of U^{6+} to U^{4+}, from oxidizing, uraniferous fluids by a reducing, basement-sourced fluid, or the basement rocks themselves, during or following diagenesis of the Athabasca Basin (e.g., Jefferson et al. 2007). However, the source of the fluids, U, and the reductant are still debated (e.g., Fayek and Kyser 1997, Cuney and Hecht 2000, Yeo & Potter 2010, Richard et al. 2011, Ng et al. 2013). Exploration for unconformity-type U deposits typically targets (i) the alteration haloes comprised of illite, chlorite, tourmaline and aluminum phosphate sulfate (APS) minerals and (ii) reactivated graphitic basement faults, which structurally control the deposits (e.g., Hoeve and Sibbald 1978). The alteration minerals associated with unconformity-type U deposits have been the topic of many studies (e.g., Hoeve and Sibbald 1978, Hoeve and Quirt 1984, Miller and LeCheminant 1985, Kotzer and Kyser 1995, Kyser et al. 2000, Kister et al. 2006, Alexandre et al. 2005, 2009, 2012, Cloutier et al 2010, Laverret et al. 2006, 2010, Ng et al. 2013). However, despite field evidence, which suggests that alteration can occur deep in the basement along ore-bearing structures, it is unclear how far the alteration extends and whether it deviates along strike of the deposit-hosting faults.

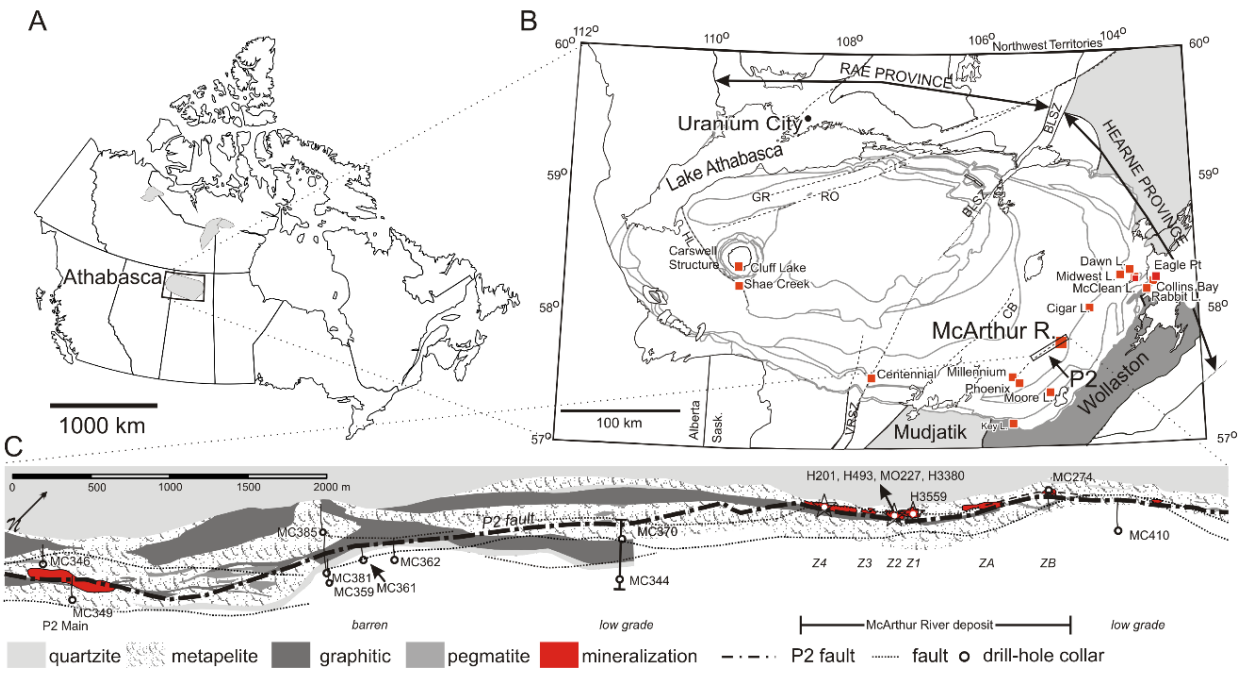

Figure 1.1 A) A map of Canada shows the locations of the Athabasca Basin relative to other two Mesoproterozoic sedimentary basins: Hornby and Thelon basins. B) A geologic map showing major uranium deposits (squares), including McArthur River deposit, and basement structures (dashed lines), including the P2 fault, in the Athabasca Basin (modified from Jefferson et al., 2007). The Wollaston and Mudjatik Domains of the western Churchill Province underlie the south-eastern margin of the Athabasca Basin. Major shear zones: BB = Black Bay, BLSZ= Black Lake Shear Zone, CB = Cable Bay, GR = Grease River Shear Zone, RO = Robbilard, VRSZ = Virgin River Shear Zone. C) A plan view map of the P2 fault showing sampled drill-core (circles) and the location of the McArthur River deposit (to the north-east). The McArthur River deposit comprises six ore bodies Zones 1-4 (Z1-Z4) and Zones A and B (ZA and ZB). See Appendix 1 for the detailed sample list and drill-hole UTM locations. Figure modified from Adlakha and Hattori 2016.

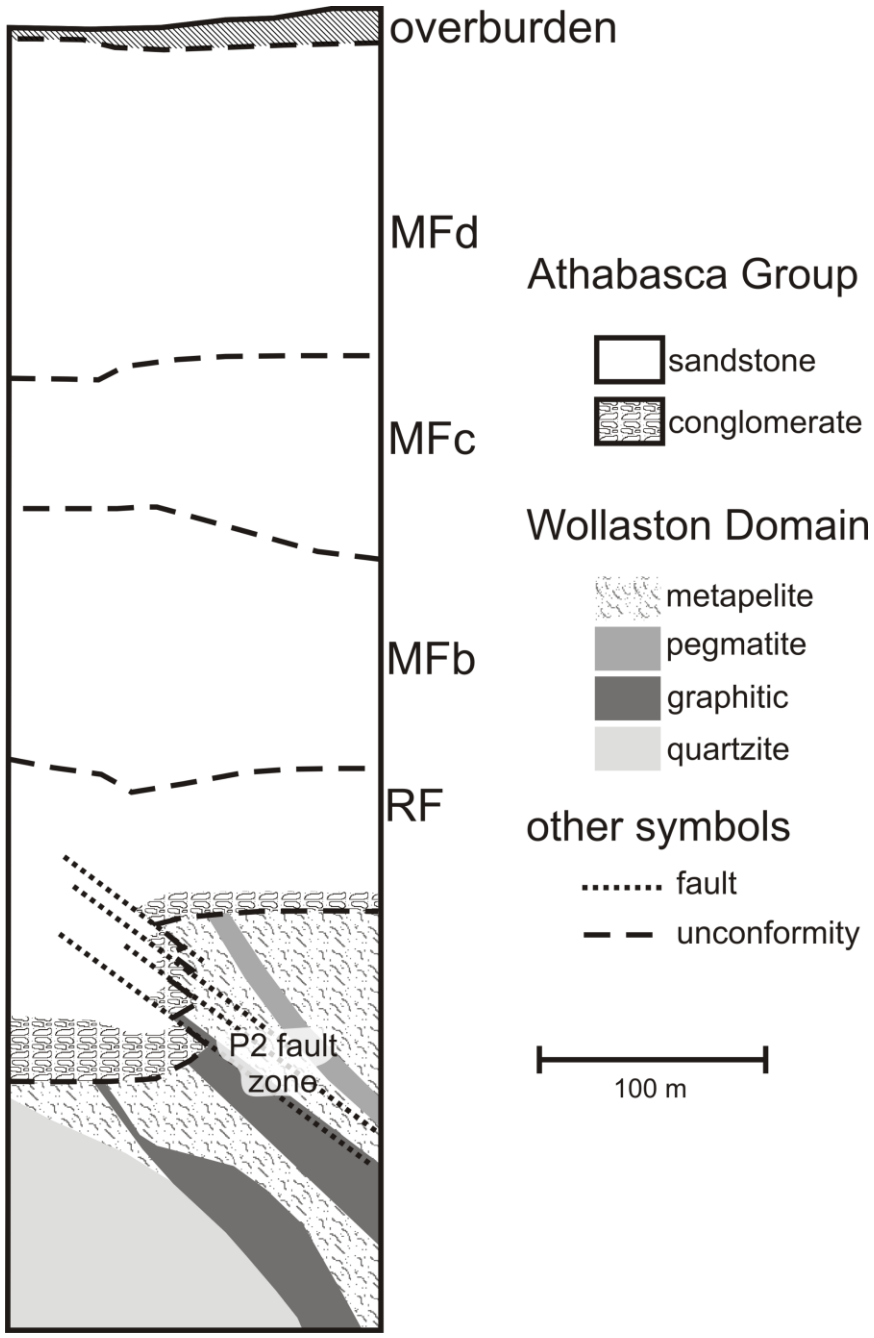

Figure 1.2 A simplified cross-section, looking north-east, showing the stratigraphic units of the Athabasca Group, the P2 fault zone, and the basement rocks. Cross-section modified from that provided by Cameco Corporation. MFb, MFc and MFd = Bird, Collins and Dunlops members of the Manitou Falls Formation, RF = Read Formation.

Mineral assemblages and the chemistry of certain minerals (e.g., tourmaline, APS minerals) in hydrothermal ore deposits provide information related to the conditions under which they form (e.g., Kister et al. 2006, Gaboreau et al. 2005, 2007, Slack and Trumbull 2011). Therefore, mineralogical studies that resolve the timing of mineral assemblages associated with hydrothermal ore deposits, and which investigate alteration mineral chemistry, allow for a better understanding of the events before, during and after mineralization and may contribute to effective exploration programs. A mineralogical study of alteration along an ore-hosting structure may further enhance understanding of the ore-forming processes related to unconformity-type U deposits and indicate the role of basement faults during mineralization. e.g., are the faults acting simply as fluid pathways, or are they also sites for extensive fluid modification and/or fluid mixing? Exploration vectors toward these deposit types may also become evident by identifying variation in alteration minerals and/or mineral chemistry as alteration extends away from the main sites of mineralization.

This thesis project focuses on the alteration of basement rocks along the P2 fault, a 13 km long reverse fault that hosts the world-class McArthur River U deposit. The P2 fault has been drilled extensively in search for other U deposits. While a few low-grade deposits, such as the P2 Main deposit, and minor U mineralization have been found sporadically along the P2 fault, the 1.7 km striking McArthur River deposit is the only economic deposit discovered to date. The Zone 2 ore body (previously known as the P2 North deposit) of the McArthur River deposit is almost entirely hosted in the basement rocks immediately below the unconformity with the overlying Athabasca sandstones. The rocks adjacent to the P2 fault and proximal to the Zone 2 ore body show field evidence of extensive fluid-rock interaction as they are strongly brecciated and altered. For these reasons, the Zone 2 ore body and the P2 fault provide an excellent study site to investigate

how alteration minerals associated with unconformity-type U deposits change along strike of an ore-bearing fault.

1.2 Thesis Objectives

This project serves to understand the role of the P2 fault and basement rocks of the Athabasca Basin during the U mineralization at McArthur River and identify exploration targets for unconformity-type U deposits. The study takes a novel approach by systematically studying the basement alteration that occurs along strike of a major deposit-hosting fault, in areas of mineralization and areas apparently barren of mineralization. The objectives of this project are:

i. Establish a paragenetic sequence for the alteration of the basement rocks at McArthur River and the P2 fault.
ii. Discriminate fertile alteration and/or mineralogical fingerprints to aid exploration for high-grade unconformity-type U deposits.
iii. Identify different fluids along the fault (e.g. uraniferous fluids and/or reducing fluids).
iv. Determine whether the P2 fault served as a fluid pathway and/or site of fluid modification for during mineralization.
v. Evaluate the role of the basement rocks (i.e., a reductant and/or a structurally viable environment) below the Athabasca sandstones in the main mineralizing event.
vi. Constrain the composition and source of the mineralizing fluid.

1.3 Past Work

1.3.1 Regional and district-scale alteration of the Athabasca Basin basement rocks

The crystalline basement rocks immediately below the regional unconformity comprise biotite ± garnet ± cordierite metapelite and granitite pegmatite and exhibit an alteration profile,

where Fe^{3+} content increases with proximity to the unconformity and alkalis (Mg, Ca, Na) decrease (Macdonald 1985). Macdonald (1985) identified four zones of alteration planar to the unconformity: the three lower zones are considered to be analogues for deep lateritic profiles that developed under sub-tropical climate and the fourth, upper zone formed by the reaction of the regolith with diagenetic fluids from the overlying basin. The zones are as follows (listed in order of closest proximity to the unconformity):

i) a Bleached Zone along the unconformity is characterized by white, buff, pale yellow and green clay (predominately kaolinite) that replaces all minerals except quartz,

ii) a Hematite Zone (akin to a laterite zone) that varies from 2 – 12 m thick where hematite replaces all mafic minerals (predominately biotite),

iii) a discontinuous White Zone (pallid zone) that only forms in felsic units and where white clay replaces feldspar and dark green-black mafic minerals,

iv) and a Green/Red Zone (saprolite zone) where feldspar is replaced by light green, yellow or pink/red clay (partially illitized), and mafic minerals were altered to green to dark-green/black Mg-Al chlorite + illite.

Macdonald (1985) attributed the Mg-Al chlorite in the Red/Green Zone to be a product of burial metamorphism beneath the Athabasca sandstones from a former smectite + illite assemblage, as chlorite does not typically form under weathering conditions. It was also speculated that the Bleached Zone formed from a later reducing diagenetic fluid because the Bleached Zone replaces the hematite alteration (oxidization) along the underlying Hematite Zone. The author also demonstrated that the trace element enrichment patterns in the Bleached Zone were similar to those, which accompany U mineralization (V, Mo, Pb, Ag, Ni, Co, and As), and speculated that

mineralization and related alteration were the products of a diagenetic fluid under reducing conditions.

Multiple generations and varieties of chlorite and illite have been identified in the basement rocks (e.g., Quirt and Wasyliuk 1997, Laverret et al. 2002). The earliest chlorite is characterized as "Fe-Mg chlorite" and is of intermediate composition between clinochlore and chamosite end-members. It is regionally occurring and replaced metamorphic biotite, likely during retrogression or the waning stages of metamorphism. Later, hydrothermal chlorite is of the sudoite variety (high Al-Mg content) and replaced the earlier formed Fe-Mg chlorite. Sudoite is commonly reported in the vicinity of U deposits but is also common regionally in the basement. Local occurrences of clinochlore and chamosite have been reported within ore bodies.

Different generations of illite show similar chemical compositions and early, pseudomorphic replacement of feldspars related to retrograde metamorphic reactions and later open-space filling related to diagenetic-related hydrothermal activity (Quirt 2012). Work by Laverret et al. (2002) has distinguished different polytypes of illite: diagenetic illite is of the *cv*-1M vs. later mineralization-related diagenetic-hydrothermal *tv*-1M illite. Distinction between diagenetic and hydrothermal illite in the Athabasca Group sandstone was possible using scanning electron microscope-back scattered electron (SEM–BSE) imaging: diagenetic illite occurs as plates or laths whereas hydrothermal illite is fine-grained, has a lath-like and "hairy" habit and replaces earlier diagenetic illite (Laverret et al. 2002). However, in the basement rocks hydrothermal illite replaces clay mineral paleo-weathering products and has a more platy habit with fewer "hairy" whisps. X-ray diffraction (XRD) can also be applied to distinguish polytypes of illite.

Many studies have attempted to create a generalized paragenesis of alteration related to unconformity-type U deposits (e.g., Kotzer and Kyser 1995, Kyser et al. 2000, Alexandre et al. 2005). Interpretations by Alexandre et al. (2005) are summarized here because the author only considered alteration in basement-hosted unconformity-type deposits (specifically the McArthur River, Rabbit Lake and Dawn Lake deposits). According to the author, the hydrothermal event progressed by:

i) a "pre-ore" stage (ca. 230 °C) that illitized plagioclase and amphibole, crystallized chlorite in voids created by illitization and chloritized biotite, and the pseudomorphic replacement of illite by chlorite proximal to mineralization,

ii) a "syn-ore" event (ca. 240 °C) that crystallized massive uraninite and coarse-grained illite in voids that were formed by pre-ore alteration, and

iii) a "post-ore" stage (135 °C) that remobilized and recrystallized uraninite, crystallized spherulitic dravite in voids and chlorite in veinlets, and formed kaolinite, minor carbonate, drusy quartz, disseminated sulfides and fine-grained hematite.

1.3.2 Regional and district-scale alteration of the Athabasca Group sandstones

The fluvial conglomeratic sandstones, which overlie the unconformity and host the unconformity-type U deposits, were originally comprised of over 99% hematite-dusted framework quartz with a clay matrix of kaolinite, montmorillonite, low-Mg-Fe illite, rare chlorite and K-feldspar (e.g., Hoeve and Quirt 1984). Heavy minerals include rutile, monazite, apatite and zircon. The diagenesis of the Athabasca Group sandstones led to multiple alteration events, the earliest of which is quartz overgrowth of detrital minerals (Jefferson et al. 2007). Later, diagenetic fluids (ca. 200 °C; Pagel 1980) altered matrix clays to dickite with minor illite and chlorite (e.g., Quirt and

Wasyliuk 1997, Wasyliuk 2002). Notably, Sr-Ca-SO_4^{2-} rich APS minerals occur with the diagenetic clay assemblage and encased in quartz overgrowths (e.g., Gaboreau et al. 2007).

A 10 – 20 km wide by 100 km long anomalous illite "corridor" trends north-east between the Key Lake and Cigar Lake U deposits and contains sub-parallel, narrower, anomalous chlorite and dravite zones (Earle and Sopuck 1989, Jefferson et al. 2007). This alteration corridor overprints the regional diagenetic dickite. Most major U deposits in the south-eastern part of the Basin, such as Key Lake and McArthur River, occur within the anomaly.

1.3.3 Genetic models for unconformity-type U deposits:

The *diagenetic-hydrothermal model* for unconformity-type U deposits, initially proposed by Hoeve & Sibbald (1979), suggests that an oxidized, diagenetic fluid was percolating throughout the basin and mobilized U as U^{6+} from detrital heavy minerals such as zircon and monazite. Due to a high geothermal gradient, this fluid reached temperatures of up to 200 °C (Pagel et al. 1980) and reacted with graphite of the basement to produce methane. Deposition of U occurred at the unconformity when U was reduced (U^{4+}) through the interaction with the methane-rich fluid. This model has been modified and bolstered by researchers of the past 35 years in order to constrain or re-examine the timing of mineralization, composition and source of the mineralizing fluid, the source of U, and the reductant.

The timing of mineralization is debated because uraninite from unconformity-type U deposits (such as McArthur River, Cigar Lake and Sue deposits) yields four different periods of crystallization based on U/Pb and Pb/Pb ages: 1600 – 1500 Ma, 1350 Ma, 1000 Ma, and 350 Ma (e.g., Cumming and Krstic 1992, McGill et al. 1993; Fayek et al. 2002; Alexander et al. 2009). It has been suggested that the sets of ages reflect either individual mineralization events, or the main

mineralization event with subsequent local remobilizations/resetting ages. Textural evidence suggests the latter (Fayek and Kyser 1997).

Numerous microthermometric studies have been conducted on quartz-hosted fluid inclusions of ore-breccias in order to constrain the composition and source of mineralizing fluids (Pagel et al. 1980, Kotzer and Kyser 1995, Derome et al. 2005, Richard et al. 2010, 2011, 2012). These studies identified two fluids within the ore zone: i) an earlier, acidic (pH = 2.5 – 4.5), oxidized (fO_2 > hematite-magnetite buffer), hot (up to 200 °C), NaCl-rich (up to 35 wt% $NaCl_{equiv.}$) brine and ii) a $CaCl_2$-rich (up to 20 wt%) brine. These previous workers suggest that i) the NaCl-rich brine is a basinal brine, ii) the $CaCl_2$-rich formed through the interaction of the basinal brine with the basement, and iii) ore deposition was triggered through the mixing of these two fluids in the ore zone. Studies also noted that these fluids were capable of mobilizing high concentrations of rare earth elements (REE) based on high REE contents of fluid inclusions (e.g., Ce = 20–700 ppm and La = 20–300 ppm; Richard et al. 2013), the presence of hydrothermal REE-rich minerals (e.g., fluorapatite, APS minerals, xenotime; Fayek and Kyser 1997), and high REE contents in uraninite (up to 12000 ppm; Fayek and Kyser 1997).

The source of mineralizing fluids is considered to be a diagenetic brine with contribution of marine components (e.g., evaporated sea water or fluids from evaporitic layers of the basin; Kotzer and Kyser 1995, Derome et al. 2005, Richard et al. 2011, Mercadier et al. 2012). Supporting evidence for these interpretations include molar Cl/Br ratios (150 – 350) of the fluid inclusions lower than that of seawater (650) indicating evaporated seawater, $\delta^{37}Cl$ values for fluid inclusions similar to seawater (-0.6 to 0 ‰) and high $\delta^{11}B$ (19.6 – 36.5 ‰; Mercadier et al. 2012) of tourmaline in ore breccias (Richard et al. 2011). However, it is important to note evaporites have not been observed in the Athabasca Basin. Raemakers (1990) alludes to the presence of salt casts

in the upper formations of the Athabasca Basin, and many suggest that evaporites may have been dissolved during diagenesis or eroded away.

The source of U is debated. Two main sources have been proposed: dissolution of detrital minerals in sandstones of the basin (e.g., Hoeve and Sibbald 1978, Kotzer & Kyser 1995, Fayek and Kyser 1997, Alexandre et al. 2005) or dissolution of monazite and other U-bearing minerals in granitic pegmatite of the basement (e.g., Hecht and Cuney 2000). The Athabasca Basin is permeable and porous, which is favourable for substantial fluid and rock interaction, and leaching of U from heavy minerals. Detrital zircon is the most abundant U-bearing mineral in the basin; however, studies indicate that zircons are relatively unaltered and contain normal U/Th ratios (Rayner et al. 2003). Fayek and Kyser (1997) proposed detrital monazite as the main U source because monazite is conspicuously lacking in the basin. It is possible that the abundant Th- and REE-rich APS minerals observed in the basin are alteration products of monazite (Gaboreau et al. 2007). Hecht and Cuney (2000) argue that monazite of the basin occurs as inclusions in detrital quartz, or is surrounded in quartz cement, and that the quartz inhibited dissolution of monazite. Alternatively, the basement contains abundant monazite and zircon, and these minerals exhibit strong alteration/dissolution textures (e.g., Hecht and Cuney 2000). However, the basement rocks have generally low permeability and fluid-rock interactions are restricted to faults and the unconformity. Therefore, fluids would not be efficient at mobilizing high concentrations of U required to form high-grade deposits (Jefferson et al. 2007).

Mobile U^{6+} in hydrothermal fluids must be reduced to form U deposits. The most commonly proposed reductant is a carbonic fluid (predominately methane) produced from graphite of the basement, as described above. Yeo and Potter (2010) reviewed other commonly suggested reductants: graphite (Alexandre et al. 2005), basement sulfides, and Fe^{2+} released during the

chloritization of ferromagnesian minerals of the basement (Ng et al. 2013). Oxidation of graphite should produce carbonate, but carbonate only locally occurs in proximity to mineralization. In addition, some deposits do not occur in association with graphitic pelite (e.g., Eagle Point). It has been suggested that basement sulfides supplied Fe^{2+} through oxidation of sulfide to sulfate. The Fe^{2+} would have been oxidized to $Fe^{3+}{}_2O_3$ (hematite), which is consistent with abundant hematite observed in ore zones. However, the sulfate/phosphate ratio of APS minerals decreases near mineralization (Gaboreau et al. 2007) which indicates low sulfate of the ore zones. An alternative source of Fe^{2+} is ferromagnesian minerals. Sudoite (Al-Mg rich chlorite) with hematite is abundant in the basement and near unconformity-type U deposits. The alteration of ferromagnesian minerals such as Fe^{2+}-rich chlorite, biotite, garnet and amphibole of the basement to Fe-poor sudoite allows for the liberation of Fe^{2+}, and its oxidation to form hematite (Ng et al. 2013).

1.4 Thesis Outline

This thesis comprises seven chapters, beginning with a global introduction that includes a preamble, a description of thesis objectives, relevant previous work, statement of original contribution and thesis outline. The following five chapters are manuscripts with appendices written by the author. The final chapter provides a global summary of the thesis work and final conclusions. An addendum was appended at the end of Chapters 2 and 3 following the comments by thesis examiners.

Chapter 2 is a manuscript published as Geological Survey of Canada Open File Report in 2014 and presents the mineralogy and mineral paragenesis of least altered and altered basement rocks outside of the P2 fault. This research was necessary to understand the "background" alteration of the basement, as the rocks have undergone multiple generations of alteration, from

retrograde metamorphism, to paleo-weathering of the unconformity to interaction of the unconformity with diagenetic fluids.

Chapter 3 reports the chemical variation and timing of aluminum-phosphate sulfate (APS) minerals along the P2 fault. An electron probe micro-analyzer (EPMA) and a laser ablation inductively coupled plasma mass spectrometer (LAICPMS) were used to determine the chemistry of these small (<15 μ) alteration minerals. This study recognises that the zoned APS minerals record the presence of different fluids along the P2 fault. The variation in chemistry of the APS mineral records fluid evolution along the P2 fault and suggests that the basement rocks of the ore zone was a site for fluid modification whereby oxidizing diagenetic fluids became reducing hydrothermal fluids. This manuscript was published in July 2015 in the American Mineralogist.

Chapter 4 describes the occurrence and distribution of three types of tourmaline along the P2 fault and presents a paragenesis of tourmaline containing mineral assemblages from metamorphism to uraniferous hydrothermal activity. Results of this work identify fertile alteration assemblage which may help fingerprint ore-bearing basement faults during exploration of unconformity-type U deposits. This manuscript was accepted for publication in The Canadian Mineralogist in October 2015.

Chapter 5 investigates the trace element compositions and stable isotope (B and D/H) signatures of tourmaline related to the U mineralization at the McArthur River deposit. This chapter suggests the source of mineralizing fluids in the Athabasca Basin and confirms that similar fluids occurred along the length of the P2 fault, an idea that was proposed in Chapters 4 and 5. This chapter was submitted to Chemical Geology in December, 2015, and is currently in review.

Chapter 6 is a report on the chemical variation and geochronology in rutile and anatase along the P2 fault. Rutile is of metamorphic or early hydrothermal origin. Anatase was identified using Raman Microspectrometry. The data suggests the crystallization of anatase is associated with the mineralization. The chemistry of anatase suggests water/rock ratios were very high along the fault.

Chapter 7 is the Global Summary and Conclusions which summarizes the work and implication of this thesis.

Appendices are located at the end of the thesis. They supply the data not included in manuscripts and reports, as well as abstracts and posters for conferences and meetings presented by the author during the duration of the PhD.

1.5 Statement of Original Contribution

This thesis encompasses original research conducted by Erin Elizabeth Adlakha under the supervision of Professor Keiko Hattori at the University of Ottawa. Permissions were obtained to include the manuscripts (3 published, 2 in preparation) in the thesis document from the publisher and co-authors. This section outlines the contribution of the author, collaborators and colleagues to each chapter.

Chapter 1. Global Introduction

- Includes a preamble introducing the thesis topic, the thesis objectives, previous work, a statement of original contribution, thesis outline and details of the study area.

Chapter 2. Alteration within the basement rocks associated with the P2 fault and the McArthur River U deposit, Athabasca Basin.

E.E. Adlakha, K. Hattori, G. Zaluski, T. Kotzer and E.G. Potter

Contributions:

- E.E. Adlakha wrote the chapter and produced all figures and tables.
- E.E. Adlakha conducted short-wave infrared spectrometry, scanning electron microscope (SEM) work, and petrography at the University of Ottawa.
- E. Adlakha conducted electron probe micro-analyzer (EPMA) work with the assistance of Glenn Poirier (lab manager) at the University of Ottawa. Reduction of EPMA data was conducted by Glenn Poirier.
- K. Hattori, G. Zaluski, T. Kotzer and E.G. Potter edited the manuscript and provided valuable feedback to E.E. Adlakha.
- E.E. Adlakha acted as the corresponding author during the submission and review process.

Dr. Charlie Jefferson internally reviewed this document. The article was published as an open file report by the Geological Survey of Canada in 2014:

Adlakha, E.E., Hattori, K., Zaluksi, G., Kotzer, T., and Potter, E.G., (2014) Alteration within the basement rocks associated with the P2 fault and the McArthur River U deposit, Athabasca Basin; Geological Survey of Canada, Open File 7462, 35 p. doi:10.4095/293364

Various aspects of the report were published in meeting abstracts and presented orally or by poster:

Adlakha, E., Hattori, K., and Potter, E. (2013) The paragenesis & chemistry of alteration minerals within the basement rocks associated with the P2 fault & the McArthur River U deposit, Athabasca Basin: Proceedings, 12th Biennial meeting of Society for geology Applied to Mineral Deposits (SGA) at Uppsala, Sweden (Appendix 1)

Adlakha, E.E., Hattori, K., Zaluksi, G., Kotzer, T., and Potter, E.G. (2013) Unraveling the alteration history of the basement rocks along the P2 Fault Zone and in the McArthur River U deposit. Saskatchewan Geological Open House, Canada. (Appendix 1)

Adlakha, E.E., Hattori, K., Potter, E.G., and Sopuck, V. (2013) The paragenesis and chemistry of alteration associated with the P2 fault in metamorphic rocks underlying the Athabasca Basin; Geological Survey of Canada, Open File 7365, 1 poster. doi:10.4095/292559 (Appendix 1)

Adlakha, E, Hattori, K., and Potter, E. (2013) The chemistry and paragenesis of alteration minerals within the basement rocks along the P2 fault including the McArthur River U deposit, Athabasca Basin, Saskatchewan. Advances in Earth Sciences Research Conference London, ON, Canada (Appendix 1)

Adlakha, E, Hattori, K., Potter, E., and Sopuck, V. (2012) The paragenesis of alteration associated with the P2 fault in the basement rocks of the Athabasca Basin. Saskatchewan Geological Open House, Canada

Adlakha, E., Hattori, K., Potter, E., and Sopuck, V. (2012) Alteration associated with U mineralization and P2 thrust fault, Athabasca Basin, Saskatchewan. Geological Survey of Canada Targeted Geoscience Initiative 4 U Workshop, Saskatoon, SK, Canada.

Chapter 3. Compositional variation and timing of aluminum phosphate-sulfate minerals in the basement rocks along the P2 fault and in association with the McArthur River U deposit, Athabasca Basin, Saskatchewan, Canada.

E. Adlakha and K. Hattori

Contributions:

- E. Adlakha wrote the chapter and produced all figures and tables.
- E. Adlakha conducted petrography and SEM work at the University of Ottawa.

- E. Adlakha conducted EPMA analyses with the assistance of Glenn Poirier (lab manager) at the University of Ottawa. Reduction of EPMA data was conducted by Glenn Poirier.
- E. Adlakha conducted laser ablation inductively coupled plasma mass spectrometry (LAICPMS) at the Geological Survey of Canada with the assistance of Zhaoping Yang (lab worker). E.E. Adlakha conducted data reduction.
- K. Hattori, G. Zaluski, T. Kotzer and E.G. Potter edited the manuscript and provided valuable feedback to E. Adlakha.
- E. Adlakha acted as the corresponding author during the submission and review process.

This manuscript was peer reviewed by Dr. Julien Mercadier (Associate Editor), David Quirt and an anonymous reviewer. It was published in American Mineralogist in July 2015:

Adlakha, E. E., & Hattori, K. (2015) Compositional variation and timing of aluminum phosphate-sulfate minerals in the basement rocks along the P2 fault and in association with the McArthur River U deposit, Athabasca Basin, Saskatchewan, Canada. American Mineralogist, 100(7), 1386-1399.

Various aspects of the report were published in meeting abstracts and presented orally or by poster:

Adlakha, E.E., Hattori, K., Zaluski, G., Kotzer, T.G., Davis, W.J., and Potter, E.G., (2015) Mineralogy of a fertile fluid conduit related to unconformity-type U deposits in the Athabasca Basin, Saskatchewan, in Targeted Geoscience Initiative 4: unconformity-related U systems, (ed.) E.G. Potter and D.M. Wright; Geological Survey of Canada, Open File 7791, p. 74–82. doi:10.4095/295776 (Appendix 1)

Adlakha, E E; Hattori, K; Zaluski, G; Kotzer, T G; Potter, E G (2015) Mineralogy of a fertile fluid conduit related to unconformity-type uranium deposits in the Athabasca Basin, Saskatchewan. Presentations of the 2014 TGI-4 unconformity-related uranium

workshop; by Potter, E G (ed.); Geological Survey of Canada, Scientific Presentation 34, 2015; p. 41-67 (Appendix 1)

Adlakha, E.E., Hattori, K., Zaluksi, G., Kotzer, T., and Potter, E.G. (2015) Fluid Evolution Recorded in the composition of Tourmaline and Aluminum Sulfate-Phosphate Minerals along the P2 Fault and McArthur River U Deposit, Saskatchewan. AGU-GAC-MAC-CGU Joint Assembly, Montreal, QC, Canada. Abstract Volume p. 593, Abstract ID: 34340 (Appendix 1)

Adlakha, E.E., Hattori, K., Zaluksi, G., Kotzer, T., and Potter, E.G. (2014) Ore fluids recorded in the compositions of magnesiofoitite and alumino-phosphate-sulfate (APS) minerals in the basement along the P2 structure and the McArthur River deposit, Athabasca Basin. GAC-MAC Joint Annual Meeting, Fredericton, NB, Canada. Abstract Volume 37. p. 82 (Appendix 1)

Adlakha, E.E., Hattori, K., Zaluksi, G., Kotzer, T., and Potter, E.G. (2014) Evidence for an uraniferous fluid in alumino-phosphate-sulfate (APS) minerals and magnesiofoitite along the P2 structure and the McArthur River deposit, Athabasca Basin. PDAC-SEG 2014 Student Minerals Colloquium, Toronto, ON, Canada. (Appendix 1)

Chapter 4. Paragenesis and composition of tourmaline types along the P2 fault and McArthur River U deposit, Athabasca Basin, Canada.

E. Adlakha and K. Hattori

Contributions:

- E. Adlakha wrote the chapter and produced all figures and tables.
- E. Adlakha conducted petrography and SEM work at the University of Ottawa.

- E. Adlakha conducted EPMA analyses with the assistance of Glenn Poirier at the University of Ottawa. Reduction of EPMA data was conducted by Glenn Poirier.
- K. Hattori edited the manuscript and provided valuable feedback to E. Adlakha.
- E. Adlakha acted as the corresponding author during the submission and review process.

This manuscript was peer reviewed by Drs. Jan Cempírek (Associate Editor), Radek Škoda, and Peter Bačík. It was accepted for publication on October 14th, 2015, and is currently in press in The Canadian Mineralogist:

E. Adlakha and K. Hattori (2016) Paragenesis and composition of tourmaline types along the P2 fault and McArthur River U deposit, Athabasca Basin, Canada. Canadian Mineralogist, in press.

Various aspects of the report were published in meeting abstracts and presented orally or by poster:

Adlakha, E.E., Hattori, K., Zaluski, G., Kotzer, T.G., Davis, W.J., and Potter, E.G., (2015) Mineralogy of a fertile fluid conduit related to unconformity-type U deposits in the Athabasca Basin, Saskatchewan, in Targeted Geoscience Initiative 4: unconformity-related U systems, (ed.) E.G. Potter and D.M. Wright; Geological Survey of Canada, Open File 7791, p. 74–82. doi:10.4095/295776 (Appendix 1)

Adlakha, E E; Hattori, K; Zaluski, G; Kotzer, T G; Potter, E G (2015) Mineralogy of a fertile fluid conduit related to unconformity-type uranium deposits in the Athabasca Basin, Saskatchewan. Presentations of the 2014 TGI-4 unconformity-related uranium workshop; by Potter, E G (ed.); Geological Survey of Canada, Scientific Presentation 34, 2015; p. 41-67 (Appendix 1)

Adlakha, E.E., Hattori, K., Zaluksi, G., Kotzer, T., and Potter, E.G. (2015) Fluid Evolution Recorded in the composition of Tourmaline and Aluminum Sulfate-Phosphate Minerals along the P2 Fault and McArthur River U Deposit, Saskatchewan. AGU-GAC-MAC-CGU Joint Assembly, Montreal, QC, Canada. Abstract Volume p. 593, Abstract ID: 34340 (Appendix 1)

Adlakha, E.E., and Hattori, K. (2014) Tourmaline in the metasedimentary country rocks of the McArthur River U deposit, Saskatchewan. GAC-MAC Joint Annual Meeting, Fredericton, NB, Canada. Abstract Volume 37. p. 4 (Appendix 1)

Adlakha, E.E., Hattori, K., Zaluksi, G., Kotzer, T., and Potter, E.G. (2014) Ore fluids recorded in the compositions of magnesiofoitite and alumino-phosphate-sulfate (APS) minerals in the basement along the P2 structure and the McArthur River deposit, Athabasca Basin. GAC-MAC Joint Annual Meeting, Fredericton, NB, Canada. Abstract Volume 37. p. 82 (Appendix 1)

Adlakha, E.E., Hattori, K., Zaluksi, G., Kotzer, T., and Potter, E.G. (2014) Evidence for an uraniferous fluid in alumino-phosphate-sulfate (APS) minerals and magnesiofoitite along the P2 structure and the McArthur River deposit, Athabasca Basin. PDAC-SEG 2014 Student Minerals Colloquium, Toronto, ON, Canada.

Adlakha, E., Hattori, K., and Potter, E. (2013) Fluid Evolution Recorded by Alteration Minerals along the P2 Reverse Fault and Associated with the McArthur River U-Deposit. Mineralogical Magazine, 77(5) 558. (Appendix 1)

Chapter 5. Characterizing fluids associated with the McArthur River U deposit based on tourmaline trace element and stable (B, H) isotope compositions

E. Adlakha, K. Hattori, W. Davis, and B. Boucher

- E. Adlakha wrote the chapter and produced all figures and tables.
- E. Adlakha was assisted by T. Pestaj and P. Hunt of the Geological Survey of Canada during sample preparation for boron isotope analysis.
- E. Adlakha and W. Davis (lab manager) conducted analysis of boron isotopes at the Geological Survey of Canada. Data reduction was completed by W. Davis.
- E. Adlakha conducted LAICPMS at the Geological Survey of Canada with the assistance of Zhaoping Yang (lab worker). E.E. Adlakha conducted data reduction.
- E. Adlakha and B. Boucher (lab technician) conducted LAICPMS work at the University of New Brunswick. E. Adlakha and B. Boucher reduced the data.
- E. Adlakha conducted sample preparation for hydrogen isotope analysis.
- P. Middlestead ran samples for hydrogen isotope analysis at the University of Ottawa and completed data reduction.
- K. Hattori, W. Davis, and B. Boucher edited the manuscript and provided valuable feedback to E. Adlakha.
- E. Adlakha is acting as the corresponding author during the submission and review process.

This manuscript was submitted to Chemical Geology on Dec 3rd 2015.

Various aspects of the report were published in meeting abstracts and presented orally or by poster:

Adlakha, E.E., Hattori, K., Zaluski, G., Kotzer, T.G., Davis, W.J., and Potter, E.G., (2015) Mineralogy of a fertile fluid conduit related to unconformity-type U deposits in the Athabasca Basin, Saskatchewan, in Targeted Geoscience Initiative 4: unconformity-related U systems, (ed.) E.G. Potter and D.M. Wright; Geological Survey of Canada, Open File 7791, p. 74–82. doi:10.4095/295776 (Appendix 1)

Adlakha, E E; Hattori, K; Zaluski, G; Kotzer, T G; Potter, E G (2015) Mineralogy of a fertile fluid conduit related to unconformity-type uranium deposits in the Athabasca Basin, Saskatchewan. Presentations of the 2014 TGI-4 unconformity-related uranium

workshop; by Potter, E G (ed.); Geological Survey of Canada, Scientific Presentation 34, 2015; p. 41-67 (Appendix 1)

Adlakha, E., Hattori, K., and Potter, E. (2013) Fluid Evolution Recorded by Alteration Minerals along the P2 Reverse Fault and Associated with the McArthur River U-Deposit. Mineralogical Magazine, 77(5) 558. (Appendix 1)

Chapter 6. Geochemistry and U-Pb Geochronology of TiO_2 polymorphs along the P2 fault, McArthur River U Deposit, Athabasca Basin, SK.

- E. Adlakha wrote the chapter and produced all figures and tables.
- E. Adlakha conducted SEM work at Saint Mary's University.
- E. Adlakha conducted EPMA analyses with the assistance of Glenn Poirier and David Diekrup (lab assistant) at the University of Ottawa. Reduction of EPMA data was conducted by Glenn Poirier and David Diekrup.
- E. Adlakha conducted trace element LAICPMS work at the University of New Brunswick with the help of B. Boucher (lab technician). E. Adlakha and B. Boucher reduced the data.
- E. Adlakha conducted U-Pb geochronology LAICPMS work at the University of New Brunswick which was assisted by B. Boucher. Data Reduction was completed by Chris McFarlane.
- E. Adlakha conducted Raman Microspectrometry at Saint Mary's University with the assistance of Mitchell Kerr (lab technician).
- K. Hattori, edited the data report and provided valuable feedback to E. Adlakha.

Chapter 7. Global summary

- Summarizes the major conclusions of the thesis

References

Alexandre, P., Kyser, K., Polito, P., & Thomas, D. (2005). Alteration mineralogy and stable isotope geochemistry of Paleoproterozoic basement-hosted unconformity-type uranium deposits in the Athabasca Basin, Canada. Economic Geology, 100(8), 1547-1563.

Alexandre, P., Kyser, K., Thomas, D., Polito, P., & Marlat, J. (2009). Geochronology of unconformity-related uranium deposits in the Athabasca Basin, Saskatchewan, Canada and their integration in the evolution of the basin. Mineralium Deposita, 44(1), 41-59.

Alexandre, P., Kyser, K., Jiricka, D., & Witt, G. (2012). Formation and evolution of the centennial unconformity-related uranium deposit in the South-Central Athabasca Basin, Canada. Economic Geology, 107(3), 385-400.

Cloutier, J., Kyser, K., Olivo, G. R., & Alexandre, P. (2010). Contrasting patterns of alteration at the Wheeler River area, Athabasca Basin, Saskatchewan, Canada: insights into the apparently uranium-barren zone K alteration system. Economic Geology, 105(2), 303-324.

Cumming, G. L., & Krstic, D. (1992). The age of unconformity-related uranium mineralization in the Athabasca Basin, northern Saskatchewan. Canadian Journal of Earth Sciences, 29(8), 1623-1639.

Derome, D., Cathelineau, M., Cuney, M., Fabre, C., Lhomme, T., & Banks, D. A. (2005). Mixing of sodic and calcic brines and uranium deposition at McArthur River, Saskatchewan, Canada: a Raman and laser-induced breakdown spectroscopic study of fluid inclusions. Economic Geology, 100(8), 1529-1545.

Earle, S. A. M., & Sopuck, V. J. (1989). Regional lithogeochemistry of the eastern part of the Athabasca Basin uranium province, Saskatchewan, Canada.

Fayek, M., & Kyser, T.K. (1997). Multiple fluid events and rare earth elements associated with unconformity-type U mineralization from the Athabasca Basin, Saskatchewan, Canada. The Canadian Mineralogist, 35, 327 – 658.

Fayek, M., Kyser, T. K., & Riciputi, L. R. (2002). U and Pb isotope analysis of uranium minerals by ion microprobe and the geochronology of the McArthur River and Sue Zone uranium deposits, Saskatchewan, Canada. The Canadian Mineralogist, 40(6), 1553-1570.

Gaboreau, S., Vieillard, P., Beaufort, D., Patrier, P., & Bruneton, P. (2005). Aluminium Phosphate Sulfate minerals (APS): Some markers of paleoconditions in unconformity related uranium deposits.

Gaboreau, S., Cuney, M., Quirt, D., Patrier, P., & Mathieu, R. (2007). Significance of aluminum phosphate-sulfate minerals associated with U unconformity-type deposits: The Athabasca basin, Canada. American Mineralogist, 92(2-3), 267-280.

Hecht, L., & Cuney, M. (2000). Hydrothermal alteration of monazite in the Precambrian crystalline basement of the Athabasca Basin (Saskatchewan, Canada): implications for the formation of unconformity-related uranium deposits. Mineralium Deposita, 35(8), 791-795.

Hoeve, J., & Sibbald, T. I. I. (1978). Uranium metallogenesis and its significance to exploration in the Athabasca Basin

Jefferson, C.W., Thomas, D.J., Gandhi, S.S., Ramaekers, P., Delaney, G., Brisbin, D., Cutts, C., Quirt, D., Portella, P., and Olson, R.A., (2007). Unconformity associated U deposits of the Athabasca Basin, Saskatchewan and Alberta, In: Goodfellow, W.D. (ed.) Mineral Deposits of Canada: A Synthesis of Major Deposit-Types, District Metallogeny, the Evolution of

Geological Provinces, and Exploration Methods: Geological Association of Canada, Mineral Deposits Division, Special Publication No. 5, 273-305.

Kister, P., Vieillard, P., Cuney, M., Quirt, D., & Laverret, E. (2005). Thermodynamic constraints on the mineralogical and fluid composition evolution in a clastic sedimentary basin the Athabasca Basin (Saskatchewan, Canada). European Journal of Mineralogy, 17(2), 325-342.

Kotzer, T. G., & Kyser, T. K. (1995). Petrogenesis of the Proterozoic Athabasca Basin, northern Saskatchewan, Canada, and its relation to diagenesis, hydrothermal uranium mineralization and paleohydrogeology. Chemical Geology, 120(1), 45-89.

Kyser, K., Hiatt, E., Renac, C., Durocher, K., Holk, G., & Deckart, K. (2000). Diagenetic fluids in Paleo-and Meso-Proterozoic sedimentary basins and their implications for long protracted fluid histories. Fluids and Basin Evolution, 28, 225-262.

Laverret, E., Clauer, N., Fallick, A., Mercadier, J., Patrier, P., Beaufort, D., & Bruneton, P. (2010). K–Ar dating and δ 18 O–δD tracing of illitization within and outside the Shea Creek uranium prospect, Athabasca Basin, Canada. Applied Geochemistry, 25(6), 856-871.

Laverret, E., Mas, P. P., Beaufort, D., Kister, P., Quirt, D., Bruneton, P., & Clauer, N. (2006). Mineralogy and geochemistry of the host-rock alterations associated with the Shea Creek unconformity-type uranium deposits (Athabasca Basin, Saskatchewan, Canada). Part 1. Spatial variation of illite properties. Clays and Clay Minerals, 54(3), 275-294.

Lewry, J. F., & Sibbald, T. I. (1980). Thermotectonic evolution of the Churchill Province in northern Saskatchewan. Tectonophysics, 68(1), 45-82.

Macdonald, C. (1985). Mineralogy and geochemistry of the sub-Athabasca regolith near Wollaston Lake. Geology of Uranium Deposits: Canadian Institute of Mining and Metallurgy Special, 32, 155-158.

McGill, B. D., Marlatt, J. L., Matthews, R. B., Sopuck, V. J., Homeniuk, L. A., & Hubregtse, J. J. (1993). The P2 North U deposit, Saskatchewan, Canada. Exploration and Mining Geology, 2(4), 321-331.

Mercadier, J., Richard, A., & Cathelineau, M. (2012). Boron-and magnesium-rich marine brines at the origin of giant unconformity-related uranium deposits: δ11B evidence from Mg-tourmalines. Geology, 40(3), 231-234

Miller, A. R., and LeCheminant, A. N., (1985). Geology and uranium metallogeny of Proterozoic supracrustal successions, central District of Keewatin, N.W.T., with comparisons to northern Saskatchewan. Canadian Institute Mining Metallurgy Special Vol. 32, 167-185.

Ng, R., Alexandre, P., & Kyser, K. (2013). Mineralogical and geochemical evolution of the unconformity-related McArthur River Zone 4 Orebody in the Athabasca Basin, Canada: implications of a silicified zone. Economic Geology, 108(7), 1657-1689.

Pagel, M., Poty, B., & Sheppard, S. M. F. (1980). Contribution to some Saskatchewan uranium deposits mainly from fluid inclusion and isotopic data. In Uranium in the Pine Creek Geosyncline.

Quirt, D.H., and Wasyliuk, K., (1997). Kaolinite, dickite, and other clay mineral in the Athabasca Group, Canada and the Kombolgie Formation, Australia: International Clay Conference, 11th, Ottawa, Ontario, June 1997, Proccedings, A61.

Ramaekers, P. (1990). Geology of the Athabasca Group (Helikian) in Northern Saskatchewan. Saskatchewan Energy and Mines, Saskatchewan Geological Survey, Report 195, 48 p.

Rayner, N. M., Stern, R. A., & Rainbird, R. H. (2003). SHRIMP U-Pb detrital zircon geochronology of Athabasca Group sandstones, northern Saskatchewan and Alberta. Current Research, 2, 22.

Richard, A., Pettke, T., Cathelineau, M., Boiron, M. C., Mercadier, J., Cuney, M., & Derome, D. (2010). Brine–rock interaction in the Athabasca basement (McArthur River U deposit, Canada): consequences for fluid chemistry and uranium uptake. Terra Nova, 22(4), 303-308.

Richard, A., Banks, D. A., Mercadier, J., Boiron, M. C., Cuney, M., & Cathelineau, M. (2011). An evaporated seawater origin for the ore-forming brines in unconformity-related uranium deposits (Athabasca Basin, Canada): Cl/Br and δ 37 Cl analysis of fluid inclusions. Geochimica et Cosmochimica Acta, 75(10), 2792-2810.

Richard, A., Rozsypal, C., Mercadier, J., Banks, D. A., Cuney, M., Boiron, M. C., & Cathelineau, M. (2012). Giant uranium deposits formed from exceptionally uranium-rich acidic brines. Nature Geoscience, 5(2), 142-146

Slack, J. F., & Trumbull, R. B. (2011). Tourmaline as a recorder of ore-forming processes. Elements, 7(5), 321-326.

Wasyliuk, K. (2002). Petrogenesis of the kaolinite-group minerals in the eastern Athabasca Basin of northern Saskatchewan: Applications to uranium mineralization. Unpublished M. Sc. Thesis, Saskatoon, Canada: University of Saskatchewan, 140.

Yeo, G. M., & Potter, E. G. (2010). Review of reducing mechanisms potentially involved in the formation of unconformity-type uranium deposits and their relevance to exploration. Summary of Investigations, 2, 2010-4.

CHAPTER 2.

Alteration within the basement rocks associated with the P2 fault and the McArthur River uranium deposit, Athabasca Basin

E.E. Adlakha, K. Hattori, G. Zaluski, T. Kotzer and E.G. Potter

Geological Survey of Canada Open File 7462

Abstract

The P2 reverse fault in the Athabasca Basin was a conduit for basinal fluids to enter the basement rocks below the regional unconformity and modify the rocks through fluid-rock interactions. Along the P2 fault, the basement rocks consist predominately of graphitic metapelite with quartzite and pegmatite. Immediately below the unconformity is an alteration profile consisting of a lower Green Zone with chlorite and illite, middle Red Zone dominated by hematite and kaolinite, and a discontinuous Bleached Zone of kaolin-group minerals and illite right at the unconformity. Preliminary data suggest that the alteration profile cannot be attributed solely to paleo-weathering but rather must include multiple fluid events from paleo-weathering through diagenetic to late hydrothermal fluids.

2.0 Introduction

The P2 reverse fault is a relatively minor regional structure in the southeastern Athabasca Basin yet is spatially associated with the McArthur River deposit, the largest high-grade uranium deposit discovered to date (Fig. 2.1). Whereas a few low-grade deposits, such as the P2 Main and minor uranium occurrences have been found along the P2, the McArthur River deposit is the only economic deposit associated with the fault. The Zone 2 ore body of the McArthur River deposit is almost entirely hosted in basement rocks below Athabasca Basin; therefore, it is classified as a basement-hosted unconformity-type uranium deposit. The rocks adjacent to the P2 fault and below the Zone 2 ore body show evidence of extensive fluid-rock interaction as they are highly brecciated and altered. Therefore, the P2 fault may have served as a fluid pathway for uraniferous fluids to permeate the basement rocks and precipitate the ore.

This study began in the fall of 2012 and serves to explore the role of the P2 fault in the sub-Athabasca Basin during the uranium mineralization event at McArthur River in order to constrain

the composition and source of the mineralizing fluids and identify fertile alteration. The outcomes of this study may be useful in discriminating fertile structures from the multiple generations of minor faults in the area and in targeting favourable areas for mineralization along the P2 and similar structures in the Athabasca Basin. The project is taking a systematic approach to studying the alteration of the basement rocks below the basin by describing and comparing the chemistry and paragenetic sequences of alteration minerals in the basement rocks below the basin in general, along the P2 reverse fault in the basement, and along the P2 fault proximal to uranium mineralized vs. non-mineralized rocks. This paper describes the preliminary findings from the first year of study and includes detailed petrography and major element chemistry of alteration minerals.

2.1 Geological setting

2.1.1 Regional Geology

The basement rocks below the eastern Athabasca Basin are comprised in part of the Wollaston Supergroup and host the Zone 2 ore body of the McArthur River deposit (Fig. 2.1). The Wollaston Group here consists of pelite, semipelite, arkose, calc-silicate and quartzite that were metamorphosed during the Trans-Hudson Orogeny (ca. 1800 - 1900 Ma; Lewry and Sibbald 1980) under upper amphibolite facies conditions. Granitic pegmatite lenses intrude the metasediments and likely formed from local partial melting during peak metamorphism (Annesley et al., 2005). Substantial erosion during the exhumation of the basement rocks beginning at ca. 1.73 Ga resulted in weathering of the basement before the deposition of the Athabasca Group conglomerate and sandstone sequences (Kyser et al. 2000).

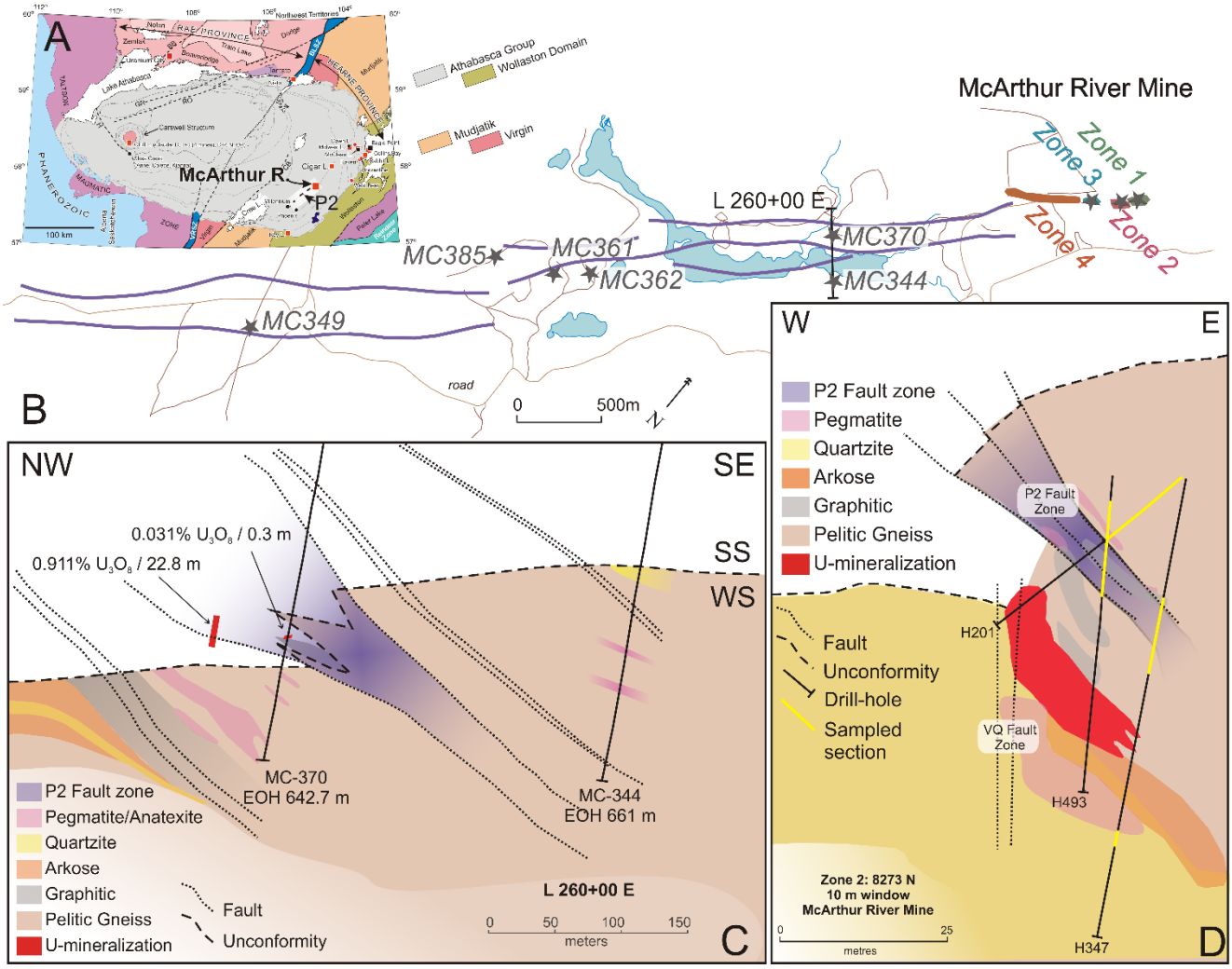

Figure 2.1. A) Map of the Athabasca Basin showing the locations of high-grade uranium deposits and major structural features, including the P2 reverse fault (highlighted in purple) (adapted from Jefferson et al., 2007). B) Plan-view map showing the surface expression of the P2 fault in purple, access roads in brown, collars of diamond drill holes sampled for this study, and the McArthur River mine site. C) Cross-section of exploration line 260+00 E shows sampled drill holes MC-370 and MC-344 in geological context. D) An underground cross-section (8273N; 10 m window) of the Zone 2 from McArthur River Mine showing sampled drill-holes H201, H347 and H493 (sampled areas highlighted in yellow). The Zone 2 cross-section was interpreted by this author based on drill-core logs and cross-sections provided by Cameco. Plan-view map and cross-sections are adapted from Bronkhorst et al. (2012). SS= sandstone; WS = Wollaston Supergroup.

The Athabasca Group comprises four major sequences of dominantly fluvial to marine, quartz pebble conglomerate and quartz-dominated sandstone (99% quartz framework grains with minor K-feldspar + clay matrix), currently preserved at a maximum thickness of 1500 m in the centre of the basin (Ramaekers et al. 2007).

2.1.2 Geological Setting of the McArthur River deposit and structure of the P2 fault

Above the McArthur River deposit, the thickness of the conglomerate-sandstone succession is approximately 500 m. Some conglomerate and sandstone units have been intensely silicified (Hiatt and Kyser, 2007; Matthews et al., 1997). During and after deposition of the Athabasca Group, diagenetic fluids extensively altered much of the stratigraphic section (except for the intensely silicified units), as well as the basement rocks close to the unconformity. Subsequent hydrothermal activity further altered and brecciated these rocks, particularly along intersecting faults that provided the fluid pathways. Breccias host ore pods along the ~050° P2 fault, the Vertical Quartzite (VQ) fault, and ~140° trending cross faults (Fig. 2.1).

The main ore body at McArthur River is termed Zone 2, hosted by the P2 reverse fault and bounded by the vertical quartzite (VQ) fault in the basement rocks. The deposit is classified as unconformity-type because it is located at the basal unconformity (~500 m depth) between the Athabasca Group and underlying metamorphic basement rocks (Fig. 2.1D). The primary mineralization event for the Zone 2 ore body was dated at 1521 ± 8 Ma with subsequent remobilization at 1348 ± 16 Ma (U-Pb on uraninite, McGill et al., 1993). The P2 fault zone preserves a record of multiple reactivations with a subtle to 80 m net reverse offset of the basal unconformity that placed the basement rocks above the basal conglomerate and sandstone units (McGill et al. 1993). In the basement the P2 fault is hosted within graphite-bearing metapelite and can be traced seismically as a listric structure down at least 2 km and laterally some 1.5 km (Hajnal

et al., 2007). In the sandstone the P2 splays into multiple faults that flatten toward sub-parallelism with bedding (McGill et al., 1993). Hydrothermal alteration has been documented to be structurally controlled along the P2 fault zone, as alteration occurs along the shear zone, splay faults, and fractures (Jefferson et al. 2007). The VQ fault is a steeply dipping structure located between the footwall quartzite and cordierite-bearing pelite.

2.2 Previous research

2.2.1 Regional and district-scale alteration

Macdonald (1980; 1985) examined the alteration of the basement rocks and identified four zones in the regolith. He considered the lower three zones to be analogues for deep lateritic profiles that developed under sub-tropical climate and the upper zone created by the reaction of the regolith with diagenetic fluids from the overlying basin. The four zones are as follows (listed in order of closest proximity to the unconformity):

i) Bleached zone along the unconformity characterized by white, buff, pale yellow and green clay (predominately kaolinite) that replaced all primary minerals except quartz, and was generated by a reducing diagenetic fluid,

ii) Hematite zone (akin to a laterite zone) that varies from 2 – 12 m thick where hematite replaced all mafic minerals (predominately biotite),

iii) Discontinuous White zone (pallid zone) that only forms in felsic units and where white clay replaced feldspar and dark green-black mafic minerals,

iv) Green/Red Zone (saprolite zone) where feldspar was replaced by light green, yellow or pink/red clay (partially illitized), and mafic minerals were altered to green to dark-green/black Mg-Al chlorite with illite.

Macdonald (1980; 1985) also investigated the bulk rock geochemistry of the different zones and noted that Fe (III) concentrations increase with proximity to the unconformity, whereas alkalis and Mg decrease. He attributed the Mg-Al chlorite in the Red/Green zone to be a product of burial metamorphism beneath the Athabasca Group from a former smectite + illite assemblage, as chlorite does not form under weathering conditions. He also speculated that the Bleached zone formed from a later reducing diagenetic fluid because the Bleached zone replaces the hematite alteration (oxidization) along the upper Hematite zone. Finally, as the trace element enrichment pattern in the Bleached zone is similar to that which accompany uranium mineralization (V, Mo, Pb, Ag, Ni, Co, and As), Macdonald (1980; 1985) speculated that mineralization and related alteration were generated by a diagenetic fluid under reducing conditions.

According to Alexandre et al. (2005), for the McArthur River, Rabbit Lake and Dawn Lake deposits, alteration around these basement-hosted unconformity-type deposits progressed in three stages:

i) a “pre-ore” stage illitized plagioclase, crystallized chlorite in voids created by illitization and chloritized biotite, and pseudomorphic replacement of illite by chlorite proximal to mineralization,

ii) a “syn-ore” event crystallized massive uraninite and coarse-grained illite in voids that were formed by pre-ore alteration, and

iii) a “post-ore” stage remobilized and recrystallized uraninitite, crystallized spherulitic dravite in voids and chlorite in veinlets, and formed kaolinite, minor carbonate, drusy quartz, disseminated sulfides and fine-grained hematite.

Quirt (2012) compared basement clay alteration mineralogy below the Athabasca and Thelon Basins and provided important insights in recognizing retrograde (Fe-Mg) vs. prograde hydrothermal (Al-Mg) chlorite, and diagenetic (1Mc) illite vs. later mineralization-related diagenetic-hydrothermal (1Mt) illite. He interpreted retrograde chlorite from the waning stage of metamorphism as characterized by Fe-Mg rich chlorite (compositions intermediate between clinochlore and chamosite), whereas prograde hydrothermal chlorite is of the sudoite variety and replaced earlier formed Fe-Mg chlorite. Different illite generations, such as pseudomorphic replacements and open-space filling grains, are chemically similar and cannot be distinguished by composition alone. Distinction between diagenetic vs. hydrothermal illite in the Athabasca Group sandstone is possible using scanning electron microscope-back scattered electron (SEM–BSE) imaging: diagenetic illite occurs as fine-grained plates whereas hydrothermal illite has a lath-like "hairy" habit and replaces earlier diagenetic illite. However, in the basement rocks hydrothermal illite (1Mt) replaces paleo-weathering clay minerals and has a more platy habit with fewer "hairy" whisps. Finally, the author noted that X-ray diffraction (XRD) can distinguish polytypes of illite.

District-scale alteration haloes that overprint the background dickite alteration in the Athabasca Group and that surround Athabasca U-deposits are summarized by Jefferson et al. (2007). A 10 – 20 km wide by 100 km long anomalous illite "corridor" trends north-east between Key Lake and Cigar Lake (Earle and Sopuck, 1989) and contains sub-parallel, narrower, anomalous chlorite and dravite zones. All the uranium deposits in the south-eastern part of the Basin, such as Key Lake and McArthur River, are located within this corridor. The timings of main mineralization events are uncertain because dates obtained on uraninite from a number of deposits range from 1600 to 1500 Ma (Cumming and Krstic 1992; Fayek et al. 2002; Alexander et al. 2003) and 1460 to 1350 Ma (McGill et al. 1993; Fayek et al. 2002; McArthur River, Cigar Lake, and

Sue deposits). For example, Carl et al. (1992) found the oldest mineralization to be 1421 ± 49 Ma (U/Pb) with subsequent remobilization at 1215 Ma (Sm/Nd). Höhndorf (1985) documented three ages for Key Lake ore: 1250, 900 and 300 Ma (U-Pb & Pb-Pb discordia).

The Athabasca Group sandstones were locally silicified during a pre-ore quartz overgrowth event (Hiatt and Kyser, 2007). Diagenetic fluids (ca. 200 °C; Pagel, 1975) altered the kaolinite, montmorillonite, chlorite and low-Mg-Fe illite sandstone matrix to dominantly dickite (background alteration), with minor illite and chlorite (Quirt and Wasyliuk 1997; Earle et al. 1999; Quirt 2001; Wasyliuk, 2002; Jefferson et al. 2007). Dissolution of detrital feldspar and mica may have provided K to form illite from kaolinite (Hoeve and Quirt 1984).

2.3 Sampling for this study

This project commenced in August 2012, with examination and sampling of drill-core from along the P2 structure (exploration holes beginning with MC) and within the McArthur River underground mine (underground collared drill-holes are denoted H or MO) (Fig. 2.1). Most samples collected are basement metapelite and pegmatite. However, seven samples of sandstone close to the unconformity were also collected. Two barren drill-holes that did not intersect the P2 fault (MC344 and MC385), two barren holes that did intersect the P2 fault (MC361 and MC362), and two weakly mineralized holes that intersect the P2 fault outside of the mine area (MC370 and MC349) were sampled. Drill-holes MC344 and MC385 intersected the hanging-wall and footwall of the P2 fault, respectively. Drill-hole MC370 intersected the P2 fault where it comprises two structural slices of the unconformity between the Athabasca Group and basement (Fig. 2.1C). MC349, MC361 and MC362 transected the P2 fault zone strictly in the basement. Drill-hole MC349 (EOH 665 m) intersected the basement in both the P2 fault zone and footwall. Drill-hole MC361 (EOH 654.5 m) intersected the P2 fault zone at the unconformity (at a depth of ~500 m

downhole) from the basement hanging-wall and into the footwall. Low-grade disseminated uraninite is perched in the Athabasca sandstone within the P2 fault zone proximal to MC349 and MC370.

Nine drill-holes from the McArthur River mine were also sampled: two from Zone 1 (H3559 and H3576), six from Zone 2 (MO227, H201, H203, H231, H347, and H493), and one from Zone 3 (H729). The sampled Zone 2 drill-holes were from three sections (10 m window width): H231 and MO227 were from section 8180 W, H203 was from 8240 W, and H201, H347 and H493 were from section 8273 W (Fig. 2.1D). Drill-holes H201, H347 and H493 from the Zone 2 underground mine intersected the basement rocks where the P2 fault zone is in contact with the basement hanging-wall and middle wedge. Drill-hole H729 was collared in the underground mine of Zone 3 where it first intersected the basement hanging-wall, then the P2 fault zone, middle block and quartzite footwall. The total of 159 drill-core samples collectively represent characteristic features such as the least altered rocks, Green Zone, Red Zone, Bleached Zone, and Zone 2 breccia.

2.4 Methodology

After careful examination of drill-core samples, representative samples were selected for polished thin-sections (89 in total). Minerals were identified using short-wave infrared spectroscopy (SWIR) on clean drill-core samples, using a TerraSpec 4 Hi-Res Mineral Spectrometer with collection time of at least 5 seconds to ensure the reproducibility of spectra. The software SpecMIN and SpecWin were used to resolve spectra, and identify alteration minerals. Mineral spectra were also compared to Athabasca standard clays (Percival, pers. comm.) and the spectra for Athabasca clay minerals presented by Zhang et al. (2001) and Percival et al. (in press).

Petrography was described first for hand-specimens, then for selected thin-sections using plane-polarized (PPL) and cross-polarized (XPL) transmitted microscopy. Detailed textures were

analyzed by a JEOL 6610LV scanning electron microscope (SEM; University of Ottawa) on carbon-coated polished thin-sections. Energy-dispersive spectroscopy (EDS) was used to semi-quantitatively analyze mineral compositions using a spectrum acquisition time of 40 seconds, a working distance of 10 mm and an accelerating voltage of 20 kV.

Quantitative analyses of biotite, garnet, illite, chlorite, kaolinite and tourmaline for major and minor constituents (SiO_2, TiO_2, Al_2O_3, FeO, MnO, ZnO, MgO, CaO, Na_2O, K_2O, Cl, BaO, F and SrO) were obtained at the University of Ottawa using a JEOL 8230 electron-probe microanalyzer (EMPA) at an accelerating voltage of 15 kV, a beam current of 20 nA and a focused beam (10s on peak and 10s off peak counting times). The focused beam size was 5-10 μm depending on grain size to ensure a representative average composition. The standards used are as follows: sanidine (Si), rutile (Ti), sanidine (Al), hematite (Fe), tephroite (Mn), sphalerite (Zn), diopside (Mg and Ca), albite (Na), sanidine (K), tugtupite (Cl), barite (Ba), fluorite (F) and celestine (Sr). Each grain was analyzed 5-7 times (different spot locations) to ensure precision.

2.5 Results

2.5.1 Least-altered rocks

The least-altered samples were collected at least 100 m below the unconformity at the base of background drill-hole MC344. The metapelite (Fig. 2.2E1) and pegmatite are mineralogically similar, both being dominated by quartz and biotite, with illitized feldspar, chloritized cordierite, garnet and minor graphite (Fig. 2.2E). Cordierite and graphite were found only in metapelite samples. The highest concentrations of graphite were found in samples from within the P2 fault zone. Metapelite shows weak to very strong foliation that is defined by the orientation of elongated quartz, biotite, garnet and cordierite (Fig. 2.2E). Biotite laths are 0.5 – 1mm long, some are partially chloritized by Fe-Mg chlorite and many also occur as ubiquitous, oval 50-100 μm

inclusions in quartz. Quartz forms coarse (> 1 mm), anhedral grains and smaller (50-100 μm) inclusions within coarse subhedral garnet grains (1 - 3 mm). K-feldspar grains vary in length from 0.5 – 2 mm in metapelite to > 1 cm in pegmatite, and are illitized along twinning planes and fractures. Illite occurs as fine-grained (< 2 μm) radiating needles. Cordierite is pseudomorphically replaced by randomly oriented, fine-grained (<2 μm) sudoite needles. The sudoite that replaced cordierite is partly illitized along fractures and grain boundaries (see BSE images, Fig. 2.2-D3).

2.5.2 Alteration petrography and textural relationships

SWIR:

Representative spectra of samples and Athabasca clay standards (Percival, written comm.; Percival et al. in press) are shown in Figure 2.3. Reflective spectroscopy of most drill-core samples produced spectra characteristic of sudoite and illite (Fig. 2.3; spectra C & D), where the sudoite spectrum has diagnostic absorption peaks at 1400, 2190, 2250 and 2340 nm, and that of illite has sharp peaks at 1400 and 2200 nm. Absorption peaks ranging from 2100 to 2500 nm were obtained from brecciated metapelite (560.2 m) and sandstone (543 m, Fig. 2.3A) from drill-hole MC370 where the P2 fault offsets the unconformity. These peaks are considered to be characteristic of magnesiofoitite (Zhang et al., 2001, Percival, written Comm.; Percival et al. in press). Double peaks at ca. 1400 and 2200 μm were observed from basal quartzite (499.4 m; Fig. 2.3B) immediately below the unconformity in drill-hole MC344 and hematitized metapelite (686 m) in the footwall to the P2 from drill-hole MC385, and are interpreted to be of dickite.

Hangingwall & footwall alteration in metapelite and pegmatite:

The basement rocks from background drill-holes exhibit a colour profile consistent with the studies of MacDonald (1980; 1985): a Green Zone at deeper levels, a middle Red Zone, and a discontinuous Bleached Zone that extends along the unconformity. All three zones were observed

in drill-hole MC344 (Fig. 2.1B) that intersects the P2 hanging-wall. However, only the Red Zone and Bleached Zone were recognized in drill-hole MC385 (P2 footwall), as the drill-hole terminated before entering the Green Zone in the footwall. Below the Green Zone in dill-hole MC344, the rocks are relatively unaltered metapelite and pegmatite.

The least altered rocks gradationally transition into the overlying Green Zone (Fig. 2.2C). Chlorite and illite replace mafic minerals (garnet and biotite) and feldspar (Fig. 2.2-C2) and chlorite also forms fine-grained radial aggregates (ca. 200 μm; Fig. 2.2-C3). In drill-core, the metamorphic foliation is preserved (Fig. 2.2-C1), although dark green chlorite replaces garnet, and lighter yellow-green and white clay replaces all other material except quartz. In a thin-section of moderately chloritized metapelite, light green Fe-Mg chlorite is distinguished by blue-purple birefringence. It forms pseudomorphs of biotite, veinlets that fragmented garnet and radial aggregates along grain boundaries (Fig. 2.2D). Fe-Mg chlorite that replaces biotite is partially replaced by illite, as indicated in thin section by a higher birefringence in cross-polarized light (Fig. 2.2-D1). In strongly chloritized metapelite from the Green Zone, sudoite is ubiquitous and completely replaced garnet and pyrite fills veinlets. Fine-grained aggregates and veinlets of illite, and grains of quartz are within the sudoite pseudomorphs of garnet (Fig. 2.2-C2). Biotite inclusions in quartz remain unaltered (Fig. 2.2-C2) yet Fe-Mg chlorite pseudomorphs of biotite are absent and there are no relict grains of cordierite.

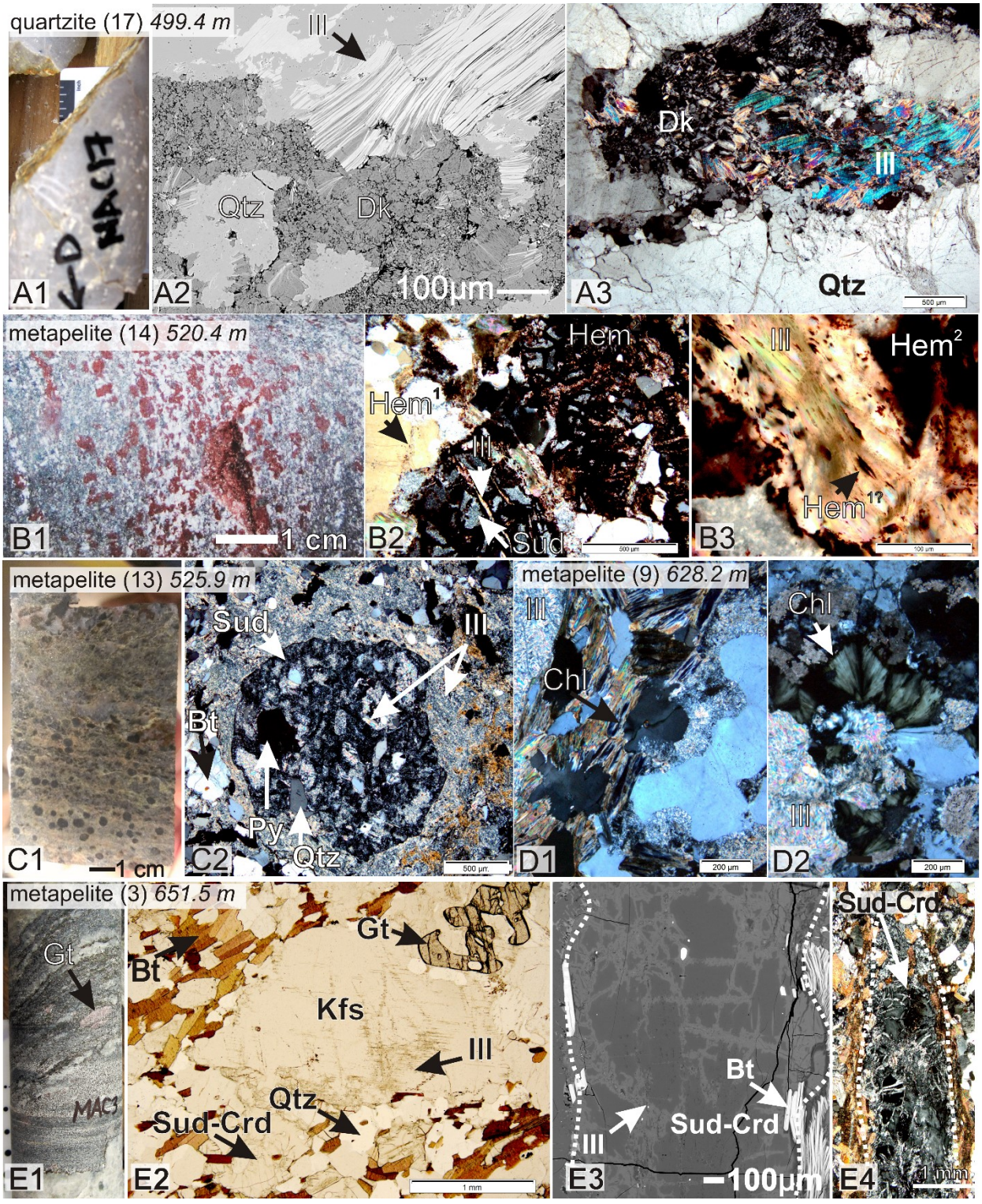

Figure 2.2. Drill-core photos, photomicrographs and BSE-images of samples from background drill-hole MC344 that intersected the basement rocks within the hanging-wall to the P2 fault. Samples are shown in order of proximity to the unconformity (~498 m) with

"A" being the closest. **A1)** Drill-core sample of bleached quartzite from immediately below the unconformity. **A2)** BSE-image of fine-grained dickite "books" (Dk; dark grey) that are replaced by fine- and coarse-grained illite (Ill; light grey). **A3)** Photomicrographs (XPL) of coarse-grained illite and dickite within bleached quartzite. **B1)** Drill-core sample of hematized metapelite from the Red Zone. **B2)** Photomicrographs of the two generations of hematite: Hem^1 is early and trapped between annealed quartz grains and within recrystallized illite cleavages and Hem^2 is later and overprints sudoite-altered garnet (Sud). The grain boundary of the relict garnet is distinguishable and the hematized garnet in the lower left corner of the image is cross-cut by a veinlet of illite. **B3)** Photomicrograph (400X; XPL) of hematite ($Hem^{1?}$) that was possibly trapped in cleavages of coarse-grained illite (pseudomorphic replacement of Fe-Mg chlorite). **C1)** Drill-core sample showing chloritized metapelite from the upper Green Zone. **C2)** Photomicrograph (XPL) showing garnet replaced by sudoite and that contains fine-grained illite aggregates, pyrite (Py), and inclusions of quartz (Qtz). Fine-grained illite has partially replaced sudoite and quartz. **D)** Photomicrograph (XPL) of moderately chloritized metapelite from Green Zone that shows anomalous blue chloritized biotite that is altered to high-birefrengent illite **D2)** Photomicrograph (XPL) of green radial aggregate of Fe-Mg chlorite in metapelite. **E1)** Drill-core sample of relatively unaltered and weakly foliated metapelite. **E2)** Photomicrograph (PPL) of metapelite composed of garnet (Gt), biotite (Bt), slightly illitized K-feldspar (Kfs), cordierite altered by sudoite (Sud-Crd) and quartz. **E3/E4)** BSE-image (E3) and photomicrograph (E4; XPL) of sudoite altered cordierite. The BSE-image shows that the sudoite is illitized along fractures.

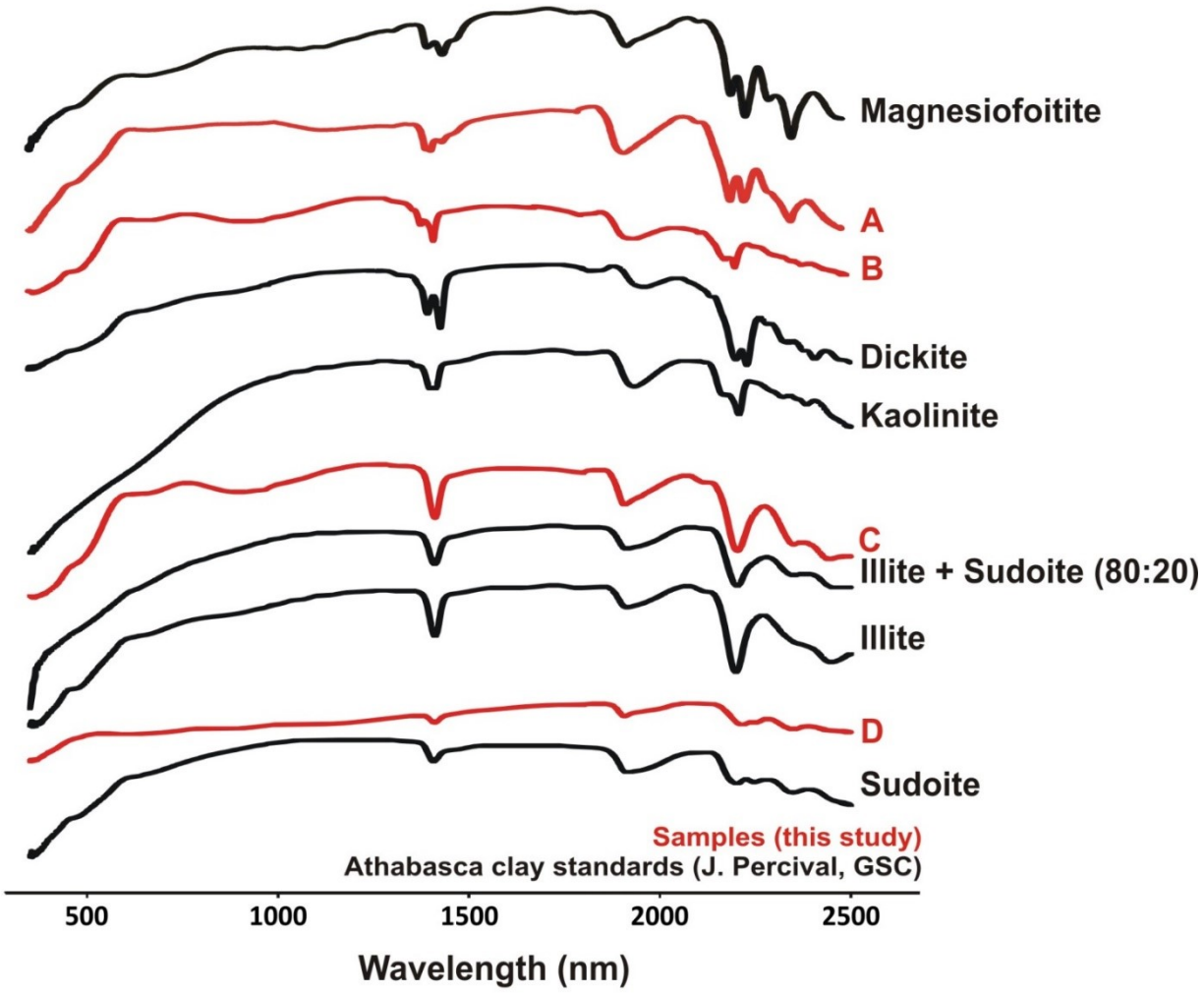

Figure 2.3. Representative infrared spectra of samples analysed in this study (red) and Athabasca clay standards (black). Spectrum A is interpreted to be magnesiofoitite and was produced from blue clay altered sandstone, immediately above the unconformity within the P2 fault (MC370, 543 m). Spectrum B (MC344, 499.4 m) is interpreted to be a mixture of dickite and kaolinite (based on double peaks at 1400 and 200 nm) and is produced by samples from the Bleached Zone and Red Zone. Spectra C and D are most typical for samples of alteration of the basement and represent sudoite and illite mixtures.

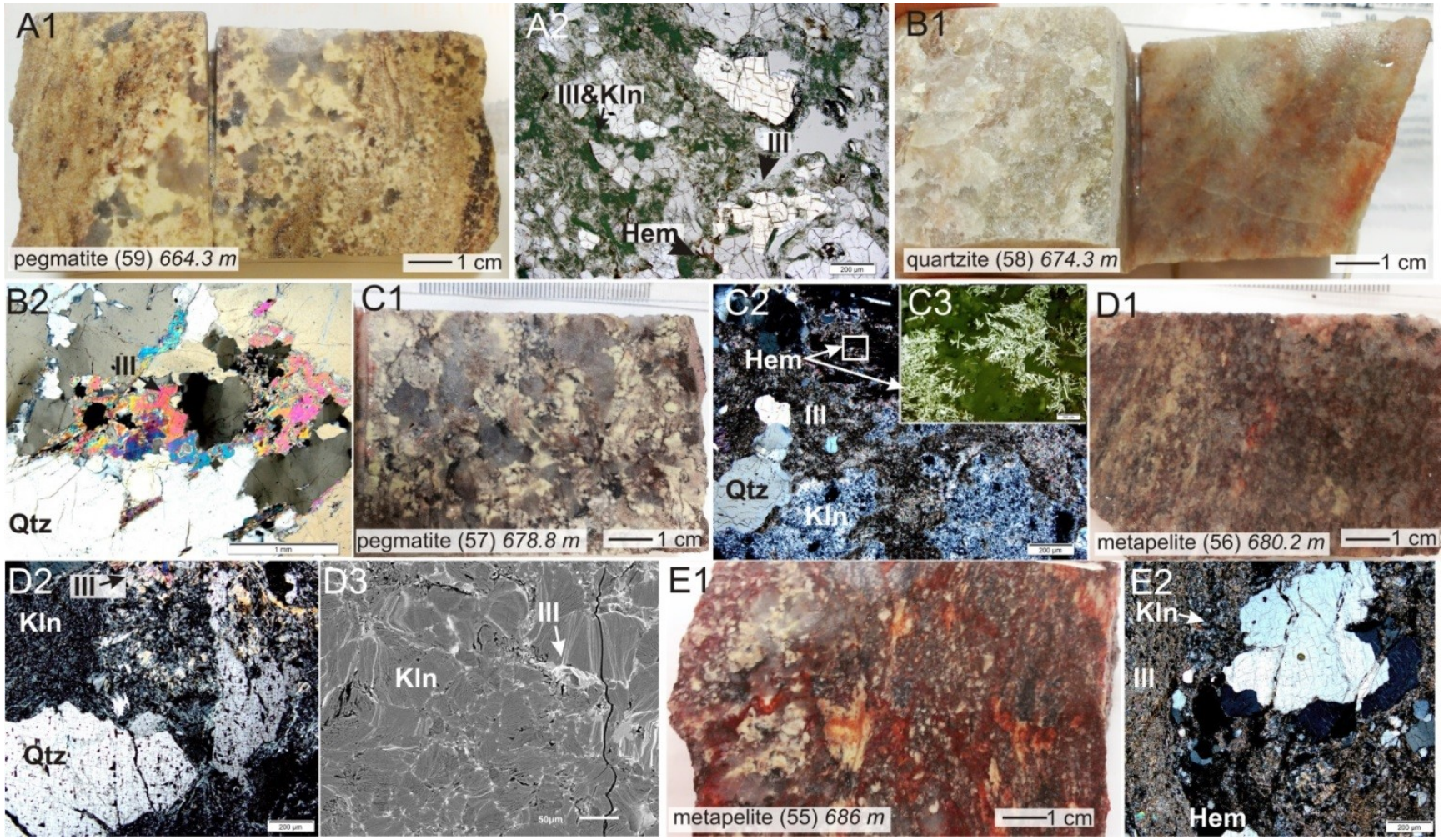

Figure 2.4. Drill-core photos, photomicrographs and BSE-images of samples that represent the Red and Bleached Zone intersected by drill-hole MC385 in the footwall to the P2 fault. Samples are shown in order of proximity to the unconformity (~498 m) with "A" being the closest. **A1)** Drill-core sample of bleached pegmatite from immediately below the unconformity. The pegmatite is

altered by buff coloured clay with remnant hematite and quartz. **A2)** Photomicrograph (PPL) of relict hematite (Hem) coated quartz (Qtz) that is surrounded by a mixture of green, fine-grained illite (Ill) and a kaolin-group mineral (Kln). Recrystallized colourless coarser-grain illite is abundant and replaces finer-grained clays. **B1)** Drill-core sample of quartzite with remnant hematite staining. **B2)** Photomicrograph (XPL) of recrystallized coarse-grained illite that crystallized in a fracture in quartzite. **C1)** Drill-core sample of bleached pegmatite showing white clay that overprints hematite. **C2)** Photomicrograph of fine-grained kaolinite, fine-grained illite and brick-red hematite. Illite has a red tint. **C3)** Photomicrograph (400X; RL) of hematite blades. **D1)** Drill-core sample of hematized metapelite from the Red Zone. **D2)** Photomicrograph of abundant kaolinite with coarse-grained illite. Hematite occurs in fractures in quartz. **D3)** BSE-image of illite (light grey) partially replacing aggregates of kaolinite (dark grey) along grain boundaries. **E1)** Drill-core sample of hematized metapelite from the Red Zone. **E2)** Photomicrograph (XPL) of hematite, kaolinite and reddish illite.

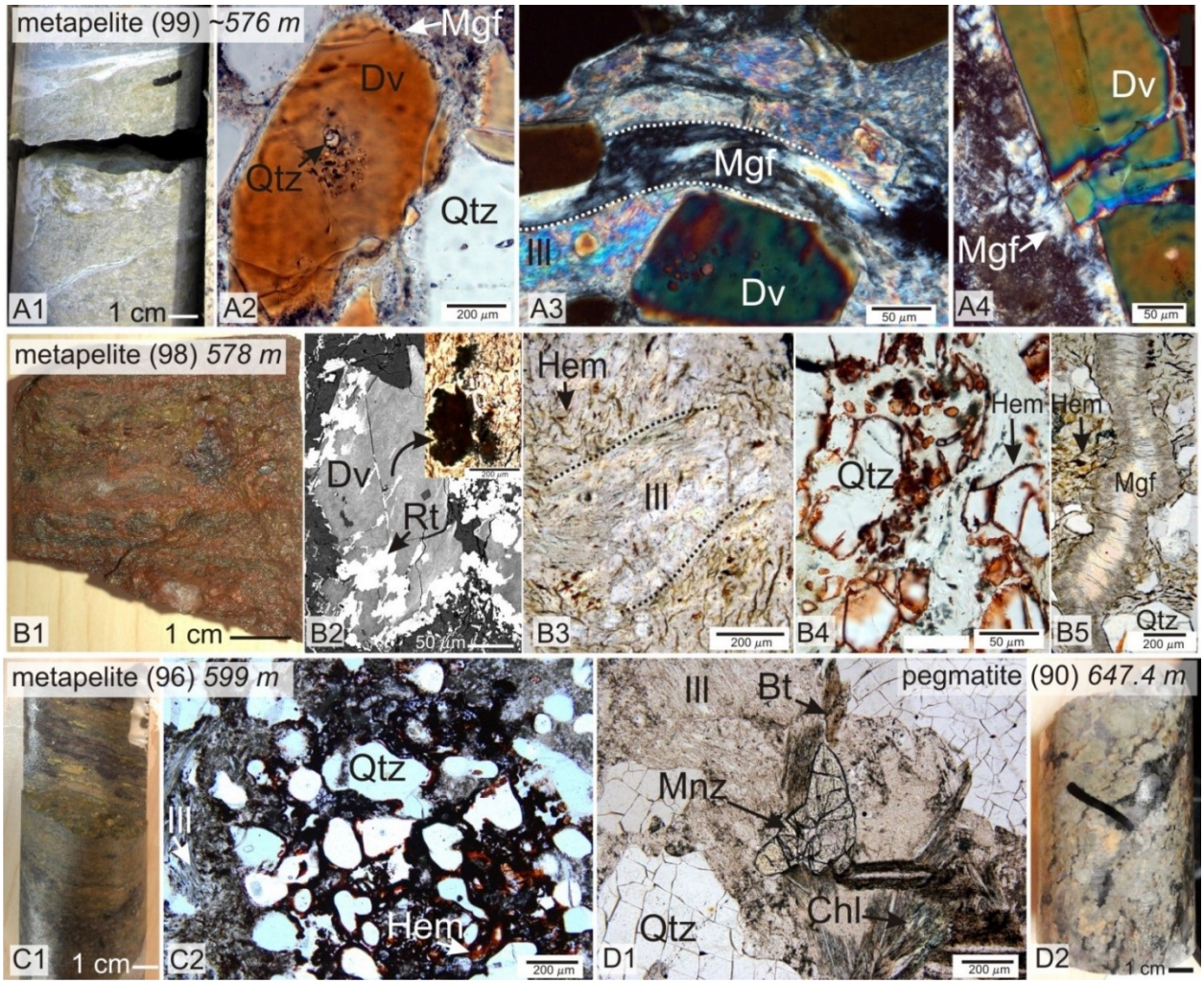

Figure 2.5. Samples from drill-hole MC349 (EOH 667) that cross-cut the P2 fault. Samples are shown in order of proximity of the unconformity (~575 m), with "A" being the closest. **A1)** Drill-core sample of tourmaline-bearing metapelite from the P2 fault. **A2)** Photomicrograph (PPL) of an euhedral grain of dravite (Dv) containing hexagonal, inclusions of quartz (Qtz) and overgrowth of fine-grained magnesiofoitite (Mgf). **A3)** Photomicrograph (XPL) of euhedral dravite bordered by fine-grained, high-birefringent, platy illite (Ill) and a veinlet of fine-grained magnesiofoitite. **A4)** Photomicrograph (XPL) of magnesiofoitite along the boundary of a dravite grain. **B1)** Fractured drill-core surface of metapelite showing brick-red to yellow-orange hematite alteration. **B2)** BSE-image and photomicrograph (top right corner; PPL) of rutile overprinting dravite and reddish-orange hematite in micro-fractures in a fine-grained illite and sudoite mixture. **B3)** Photomicrograph (PPL) showing recrystallized coarse-grained illite that cross-cuts hematite alteration. **B4)**

Photomicrograph of bright red hematite coating quartz grains but not recrystallized illite. **B5)** A microphotograph showing a veinlet of magnesiofoitite that cross-cuts hematite alteration. **C1)** A drill-core sample of hematized metapelite (599 m) from the P2 fault. **C2)** Photomicrograph (PPL) showing red hematite coating quartz and fine-grained mixed chlorite-illite, and recrystallized coarse-grain illite overprinting hematite alteration. **D1)** Photomicrograph (PPL) of pegmatite that shows Ce-monazite (Mnz), surrounded by fine-grained illite, reddish-brown biotite (Bt) and chloritized biotite (Chl). **D2)** Drill-core sample showing green chlorite alteration, yellow clay and orange hematite in pegmatite.

The Green Zone is overlain by the Red Zone (Fig. 2.2B, 2.4D & 2.4E), separated by a transition zone of alternating green and red alteration. The Red Zone is best preserved in drill-hole MC385 (at depths 686 m-678.8 m) where it comprises at least two generations of hematite. Early hematite (Hem^1) is trapped between annealed quartz grains and along cleavages in coarse-grained illite. Later hematite (Hem^2) is pervasive and overprints sudoite-altered garnet and earlier minerals (Figs. 2.2-B2 & B3). Red Zone samples also contain relict fractured quartz (Qtz^1), secondary re-crystallized quartz (Qtz^2), massive reddish fine-grained (<2 μm) illite, fine-grained (<2 μm) radial aggregate "books" of kaolin-group minerals (Fig. 2.4-D3), and coarser-grained illite laths (20-300 μm; Fig. 2.4-D2). Coarse-grained illite in the Red Zone is a pseudomorph of earlier Fe-Mg chlorite (Fig. 2.2B) or a product of recrystallization (Fig. 2.4-D2). Hematite (Hem^2) is also cross-cut by veinlets of fine-grained illite (Fig. 2.2-B2, 2.4-A2) and kaolinite is replaced by re-crystallized illite (Fig. 2.4-C2, -D2 & E2). Red Zone samples taken closer to the unconformity contain a higher abundance of kaolin-group minerals and illite with less hematite (Fig. 2.4).

Along the unconformity, the Red Zone is overprinted by buff-coloured clay in the Bleached Zone (MC385: ~678.8 – 662 m). Figure 2.4 shows the transition of hematite dominated alteration of the Red Zone to the white-yellow clay dominated Bleached Zone as observed in drill-core MC385. Basal quartzite from the Bleached Zone that was intersected by MC344 is dominated by

red-stained quartz grains (Fig. 2.4-B1), and contains trace amounts of fine-grained kaolin-group minerals plus coarse-grained illite laths (Figs. 2.4A & 2.4-B2). Pegmatite from the Bleached Zone (Fig. 2.4A & 2.4C) that was intersected by MC385 is dominated by yellow-white clay that overprints relict hematite and quartz. In thin-section, the pegmatite is dominated by fine-grained green illite and kaolinite (Fig. 2.4-A2). Hematite in the Bleached Zone is preserved in the rims of quartz grains (Fig. 2.4A).

Alteration of the P2 fault rocks:

The basement rocks from the P2 fault zone intersected by drill-hole MC349 contain dravite, quartz, magnesiofoitite, hematite, illite and sudoite (Fig. 2.5). The dravite is coarse-grained (0.2 – 1 mm), euhedral-subhedral, brown and pleochroic in thin sections and occurs in metapelite (Figs. 2.5A & B) proximal to the unconformity (~2 m). Dravite is altered to magnesiofoitite at its rim (Figs. 2.5-A2 & 2.5-A4) or is overprinted by rutile along grain boundaries and fractures (Fig. 2.5-B2). Magnesiofoitite forms fine-grained, spherical to radial aggregates along grain boundaries and veinlets (Figs. 2.5-A3 & 5-B5). Hematite coats quartz grains (Figs. 2.5-B4 & C2) and invaded fine-grained sudoite and illite along microfractures (Fig. 2.5-B3). Hematite alteration is cross-cut by magnesiofoitite veinlets (Fig. 2.5-B5) and illite (Fig. 2.5-B3). A single grain of monazite was noted in illite-rich pegmatite from the contact between the P2 fault zone and the footwall rocks (Fig. 2.5-D).

The P2 fault intersected by drill-hole MC361 (EOH 654.5 m) has an overall bleached appearance due to white and light-green clay replacements of metamorphic and secondary minerals such as hematite (Fig. 2.6-B1). Thin-section petrography shows biotite is pseudomorphed by Fe-Mg chlorite whereas illite replaced K-feldspar (Figs. 2.6D & 6E). Hematite is in contact with illite (Figs. 2.6-B2 & C). Sudoite is ubiquitous in most samples; it partially replaced fine-

grained illite (Fig. 2.6-B2), dravite (Fig. 2.6-J1), and metamorphic garnet (Fig. 2.6-J2). Apatite is in fine-grained sudoite immediately below the unconformity. Magnesiofoitite forms veinlets in sandstone immediately above the unconformity. Illite commonly overprints hematite (Fig. 2.6B2) and alters sudoite (Fig. 2.6F & 6-J3) and biotite (Fig. 2.6-J1). Pyrite is a common phase in late fractures. Where pyrite forms coarser (20-40 µm) veinlets and cubic grains, graphite is present as fine (5-10 µm) elongated laths.

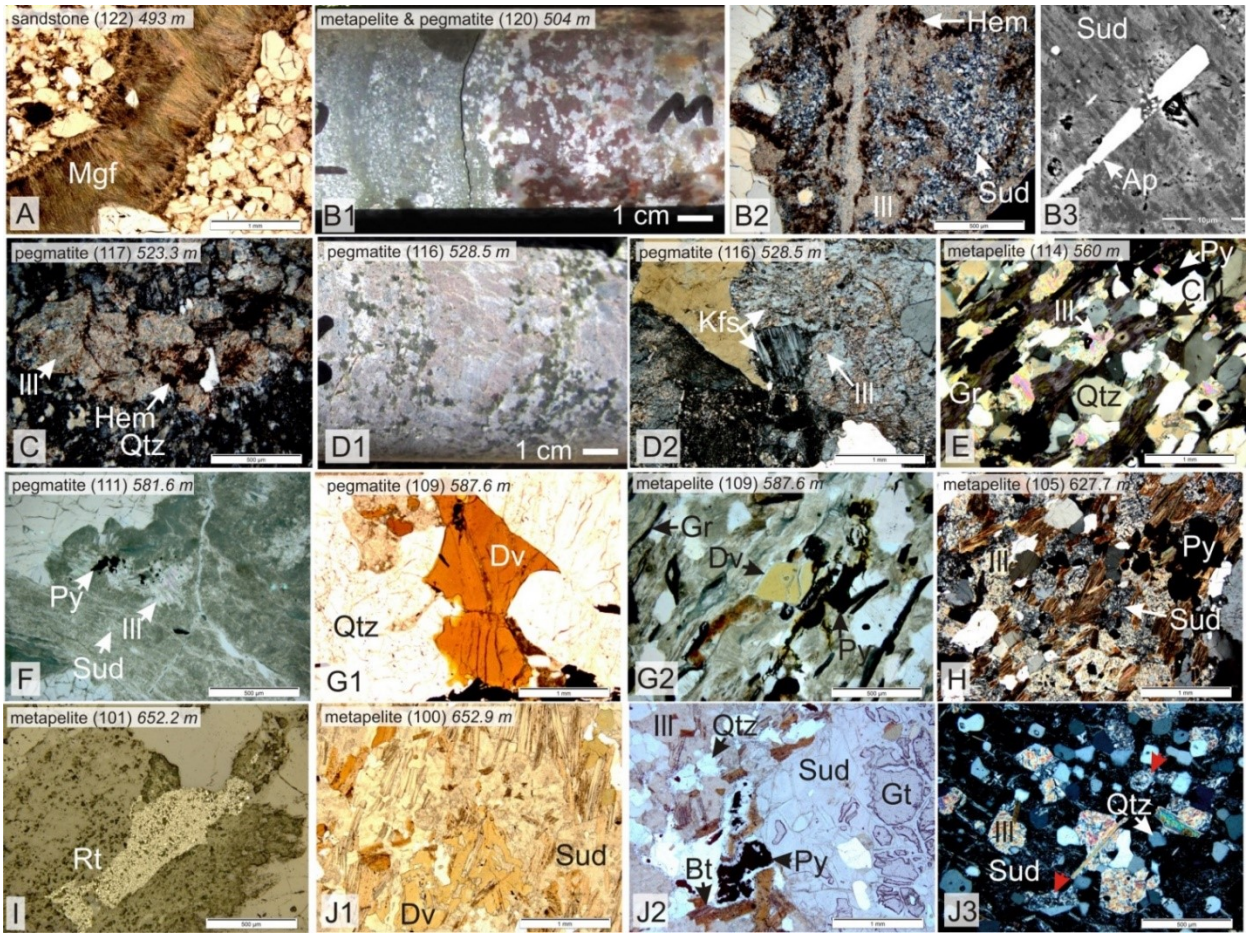

Figure 2.6. Photographs, photomicrographs and BSE-images of samples from drill-hole MC361 that intersected the P2 fault in the basement from the hanging-wall to the footwall. Sample numbers are listed in brackets beside lithology name followed by the sample depth (italicized). **A)** Veinlet of radial magnesiofoitite (Mgf) that cross-cuts sandstone. **B1)** Drill-core sample showing Green Zone alteration in contact with brick-red hematite. **B2)**

Photomicrograph from B1 showing sudoite that partially replaced fine-grained illite (Ill) that was overprinted by hematite (Hem). A veinlet of recrystallized illite occurs down the middle of the image. **B3)** BSE-image of apatite (Ap) grains surrounded by fine-grained sudoite (Sud). **C)** Photomicrograph of fine-grained illite that partially replaced hematite and quartz (Qtz), surrounded by fine-grained sudoite and quartz. **D1)** Drill-core sample showing partially illitized K-feldspar in pegmatite. **D2)** Photomicrograph of partially illitized K-feldspar (Kfs). **E)** Photomicrograph of metapelite showing illite, Fe-Mg chlorite (Chl) included by rutile, graphite, quartz and pyrite cubes. **F)** Photomicrograph of pegmatite that contains coarse-grained illite, embayed quartz and pyrite surrounded by sudoite. **G1)** Photomicrograph (PPL) of quartz in contact with dravite. **G2)** Photomicrograph showing dravite, pyrite, quartz, fine-grained illite and graphite. **H)** Photomicrograph (XPL) of metapelite showing slightly chloritized biotite, quartz, pyrite and the replacement of sudoite by illite. **I)** Photomicrograph (RL) of illite overprinted by rutile. **J1)** Photomicrograph of metapelite with dravite replaced by sudoite and biotite replaced by illite in pegmatite. **J2)** Photomicrograph showing sudoite that replaced garnet (Gt). **J3)** Photomicrograph (XPL) showing sudoite, quartz and illite that replaced garnet. Illite has partially replaced sudoite and quartz (red arrows).


metapelite (33) 533.2 m
MAC33
7D
A
1 cm
sandstone (32) 543 m
MAC32
Mgf
B1
1 cm
Mgf
B2
metapelite (30) 552.5 m
MAC30
C
1 cm
brecciated metapelite (29) 560.2 m
MAC29
D
basal conglomerate (26) 569 m
MAC26
E1
1 cm
Ill
Hem
Qtz
E2
pegmatite (22) 578.45 m
MAC22
F
1 cm
metapelite (25) 590 m
MAC
G1
1 cm
Hem
Qtz
Ill
G2
pegmatite (23) 593.5 m
MAC23
H1
1 cm
Ill1
Hem
Ill2
Qtz
H2
Hem
Ill
Qtz
H3
H4
metapelite (21) 606.9 m
MAC21
I1
1 cm
Qtz
Py
Py
Ill
I2
metapelite & pegmatite (18) 630.8 m
MAC18
Gt
J1
1 cm
Bt
Kfs
Gt
Qtz
J2

Figure 2.7. Samples from drill-hole MC370 that intersected the P2 fault at the sandstone-basement interface (570.4 m). **A)** Metapelite from the P2 fault that was placed over the Athabasca Group, showing hematite alteration overprinted by pervasive illite alteration. **B1)** Drill-core sample of sandstone from between two wedges of basement rocks within the P2 fault brecciated by magnesiofoitite (Mgf) veinlets. **B2)** Photomicrograph (XPL) of a magnesiofoitite veinlet in sandstone. **C)** Drill-core sample of chloritized and illitized metapelite from the basement wedge overlying sandstone within the P2 fault. **D)** Illitized and magnesiofoitite altered metapelite from the basement wedge overlying sandstone within the P2 fault. **E1)** Drill-core sample of pervasively hematized basal quartz conglomerate. **E2)** Photomicrograph (PPL) of fine-grained green illite replaced and cross-cut by hematite blocks and veins **F)** Drill-core sample of hematized pegmatite with relict green alteration. **G1)** Drill-core sample of orange-red hematized metapelite. **G2)** Photomicrograph (XPL) of coarse-grained illite overprinted by dark red-brown hematite along cleavage planes. **H1)** Drill-core sample that shows hematized pegmatite with relict green alteration. **H2)** Photomicrograph (PPL) of illite (Ill_1) overprinted by brick-red-brown hematite and veinlets of green illite (Ill_2) cross-cut by orange brown hematite. **H3)** Photomicrograph (XPL) of illite rimmed by hematite along grain boundaries and cleavage planes. **H4**) Photomicrograph (400X; PPL) of illite overprinted by hematite. **I1)** A drill-core sample of green metapelite**. I2)** Photomicrograph that shows relict light orange-red hematite coated grains of illitized and chloritized feldspar, biotite, and cordierite. Pyrite occurs as fine-grained veinlets that infilled fractures (RL image upper left had corner). **J1)** Drill-core sample of relatively unaltered metapelite and pegmatite. **J2)** Photomicrograph of relatively unaltered metapelite that shows the typical metamorphic mineral assemblage of the basement metapelite.

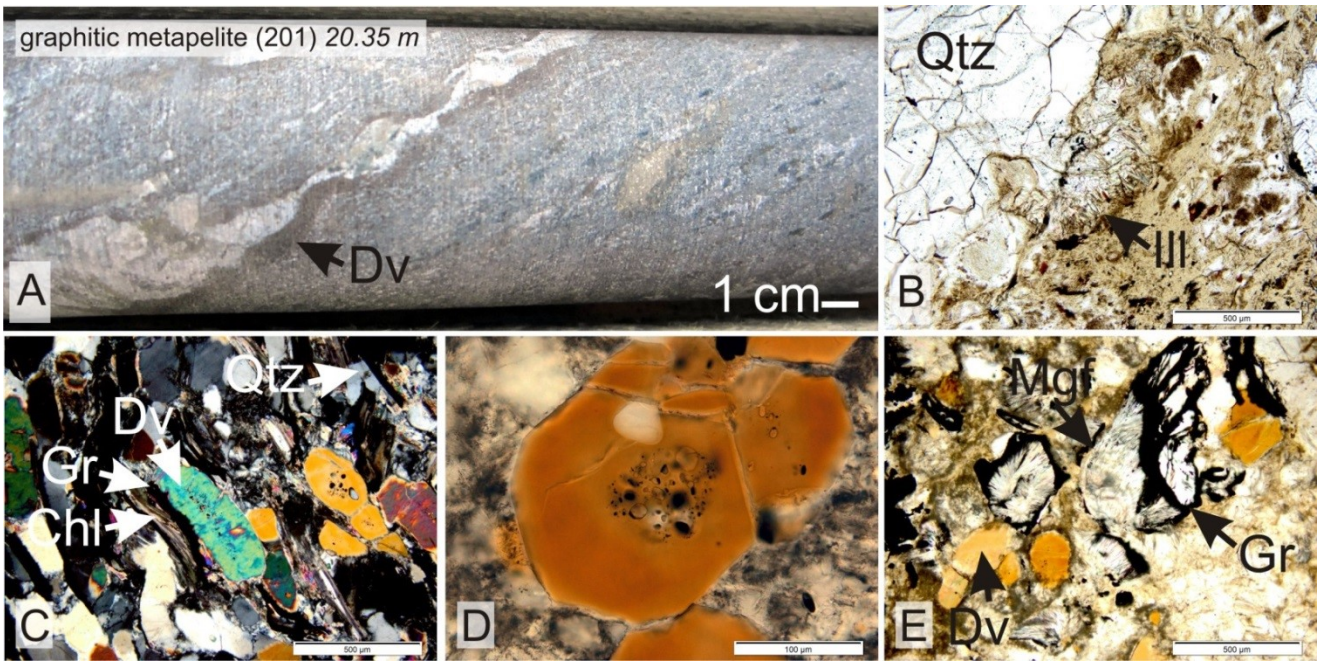

Figure 2.8. Graphitic metapelite intersected by drill-hole H3559 in the middle block within the P2 fault from Zone 1 of the underground McArthur River Mine. **A)** Drill-core photo of dravite veins within metapelite. **B)** Photomicrograph (PPL) of embayed quartz rimmed by coarse-grained illite in metapelite. **C)** Photomicrograph (XPL) of the dravite vein in A showing oriented dravite, illitized Fe-Mg chlorite and graphite. **D)** Photomicrograph (PPL) of a grain of dravite that contains many relict quartz inclusions and is bounded by fine-grained magnesiofoitite. **E)** Photomicrograph (PPL) of magnesiofoitite pseudomorphs of dravite, rimmed by early graphite.

Toward the base of drill-hole MC370 (642.7 - ~607 m; Fig 2.1C), metapelite and pegmatite (Fig. 2.6-J1) are characterized by unaltered-to-weakly chloritized biotite, and quartz, with subordinate illitized feldspar, chloritized cordierite, garnet and minor graphite (Fig. 2.7-J2). In pegmatite, unaltered feldspar is white; illitized feldspar is green. Chlorite and illite are pervasive in altered metapelite at 606.9 m (Fig. 2.7-I1) and metapelite and pegmatite are overprinted by hematite for ~35 m below the unconformity (Fig. 2.7F-H). Fine grained hematite forms light orange-red coatings on fine-grained illite and chlorite (Fig. 2.7-I2) and deep red-brown micro-veinlets (Fig. 2.6-H4). Rocks within the hematitized zone also include abundant hematite-coated, coarse-grained illite (Fig. 2.7-G2) and fine-grained illite (Fig. 2.7-H2 & 2.7-H3). The basal quartz-pebble conglomerate immediately overlying the unconformity (569 m; Fig. 2.7-E1) is also hematitized pervasively. A wedge of basement metapelite structurally overlying the basal conglomerate (Fig. 2.1C) is altered by chlorite and illite (Fig. 2.7-C) and the sandstone above the basement wedge (543 m) is cross-cut by veinlets of light blue magnesiofoitite (Fig. 2.7B). A second wedge of metapelite overlying the sandstone is pervasively altered to illite and hematite (Fig. 2.7A).

Two samples of graphitic metapelite from the middle block (a structural repetition of the unconformity sequence between the footwall and hanging-wall) of the P2 fault zone were obtained from drill-hole H3559. Dravite fills veinlets along the foliation (Fig. 2.8A & 2.8C) and contains numerous quartz inclusions (Fig. 2.8D). Coarse-grained illite coats the boundaries of embayed quartz grains (Fig. 2.8B), and altered Fe-Mg chlorite laths (biotite pseudomorphs). Magnesiofoitite forms spherical or radiating fine-grained aggregates or pseudomorphs of dravite and are rimmed by graphite (Fig. 2.8E).

The metapelite and pegmatite from drill-holes H201, H347 and H493 (Zone 2 underground mine; Fig. 2.1D) are extensively altered to greenish-yellow clay (Fig. 2.9-G1), and brecciated by green and white-blue veinlets (Fig. 2.9-F1). Coarse tourmaline grains are schörl at their core and dravite at their rim (Fig. 2.9-G2) and are replaced by sudoite along grain boundaries. Fe-Mg chlorite and sudoite co-exist (Fig. 2.9A): sudoite as fine-grained needles with platy fine-grained quartz (Figs. 2.9-A1, -A2 & -E3), and Fe- Mg chlorite as coarse-grained aggregates that are replaced by sudoite (Figs. 2.9-A1 & A2) or as veinlets that cross-cut fine-grained sudoite (Fig. 2.9-F3). Magnesiofoitite replaces quartz (Figs. 2.9-B, -D, and -E3) and an unidentified brown glassy mineral that has the composition of chlorite (Fig. 2.9-F1). Pyrite forms isolated grains or veinlets along grain boundaries of magnesiofoitite (Fig. 2.9-G1) and is replaced by sudoite (Fig. 2.9-C).

Drill core samples from drill-hole H203 have a pervasively bleached appearance due to abundant yellow-white clay (Fig. 2.10-C1). Thin-section petrography illustrates that illite replaced dravite (Fig. 2.10-B2), Fe-Mg chlorite (Figs. 2.10-A & -B3), and sudoite (Fig. 2.10A).

Magnesiofoitite replaced illite (Fig. 2.10-C3) and quartz (Fig. 2.10-C4), and contains graphite along cleavage planes (Fig. 2.10-C5). Late pyrite fills fractures in illite (Fig. 2.10A, -B1, & -B3).

Microphotographs of samples intersected by drill-hole H729 are in Figure 2.11. Metamorphic biotite (foliation evident) is replaced by Fe-Mg chlorite and fine-grained illite (Fig. 2.11-A). Fe-Mg chlorite fills pore-spaces and was illitized (Fig. 2.11A). Quartz is replaced by dravite (Fig. 2.10-B2) and magnesiofoitite (Fig. 2.11D). Pyrite is a late phase, and forms cubic grains and fine-grained veinlets that filled fractures in illite and fine-grained sudoite. Pyrite has a reddish tint in transmitted light, likely a result of late limonite (Figs. 2.11-B1, B2- & -C1). Kaolinite is in pegmatite close to the VQ fault, between the middle block and footwall quartzite.

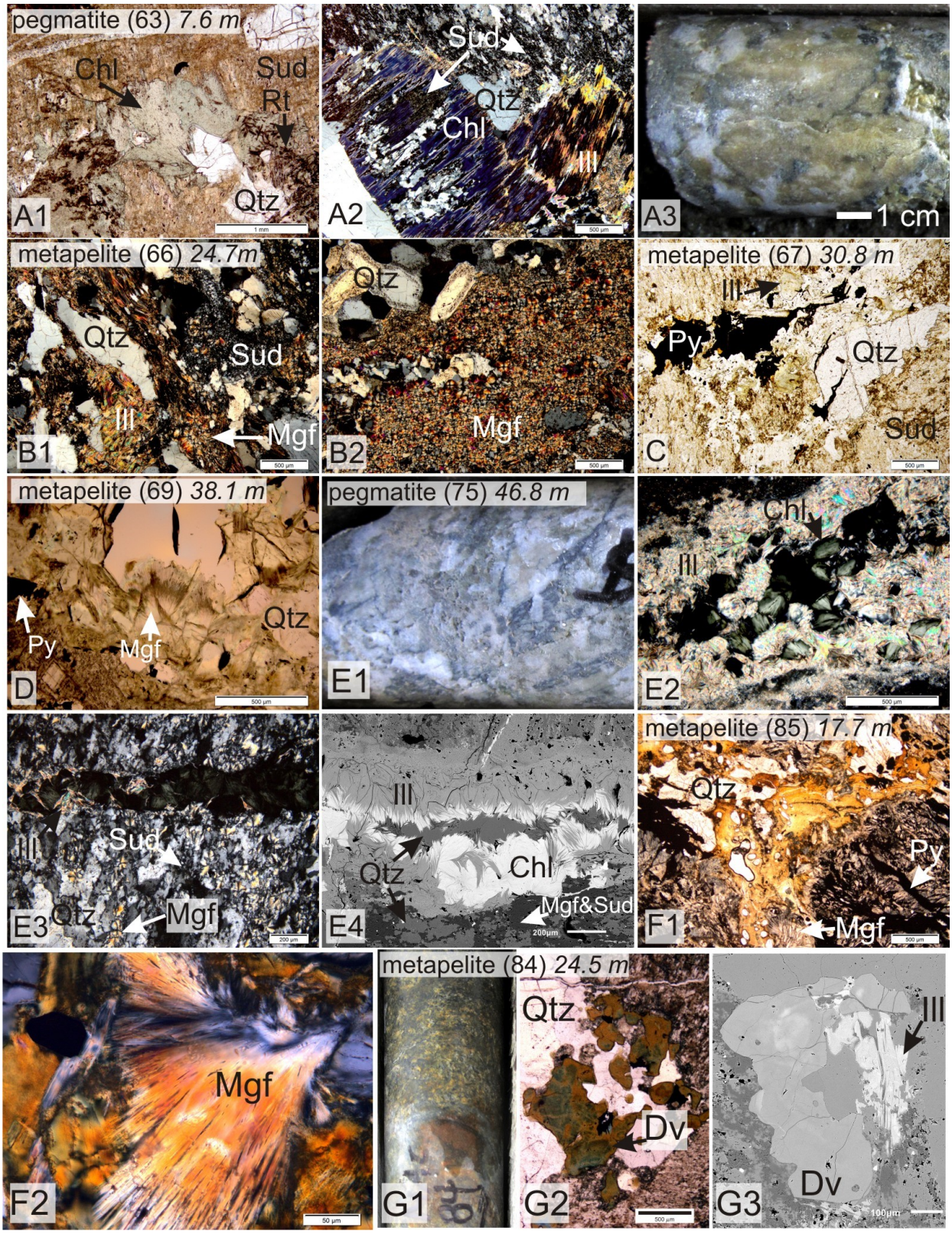
pegmatite (63) 7.6 m
Chl
Sud
Rt
Qtz
A1
Sud
Qtz
Chl
Ill
A2
A3
1 cm
metapelite (66) 24.7m
Qtz
Sud
Ill
Mgf
B1
Qtz
Mgf
B2
metapelite (67) 30.8 m
Ill
Py
Qtz
Sud
C
metapelite (69) 38.1 m
Py
Mgf
Qtz
D
pegmatite (75) 46.8 m
E1
Chl
Ill
E2
Ill
Sud
Qtz
Mgf
E3
Ill
Qtz
Chl
Mgf&Sud
E4
metapelite (85) 17.7 m
Qtz
Py
Mgf
F1
Mgf
F2
metapelite (84) 24.5 m
G1
Qtz
Dv
G2
Ill
Dv
G3

Figure 2.9. Photographs of drill-core and photomicrographs of samples from basement rocks along the P2 fault proximal to the Zone 2 ore body. A-D are metapelites intersected by H201 over ~ 30 m, E1-4 are from metapelite intersected by H347, and F-G are from pegmatite and metapelite intersected by H493. **A1)** Photomicrograph (PPL) of Fe-Mg chlorite (Chl) included by rutile (Rt) needles and partially replaced by fine-grained sudoite (Sud). Sudoite occurs as fine-grained blue-grey clay with platy quartz. **A2)** Photomicrograph of Fe-Mg chlorite partially replaced by high–birefringent illite (Ill) and fine-grained low birefringent sudoite. Quartz (Qtz) was also partially replaced by sudoite. **A3)** Photograph of pegmatite in drill-core showing yellow-green pervasive alteration. **B1)** Photomicrograph of coarse-grained illite, fine-grained magnesiofoitite, and fine-grained sudoite in metapelite. **B2)** Photomicrograph showing pervasive magnesiofoitite alteration. The rims of the larger quartz grains in the upper left hand corner of the photo shows disequilibrium textures. **C)** Photomicrograph showing coarse-grained illite and fine-grained sudoite that partially replaced quartz. Pyrite was late and infilled a fracture. **D)** Photomicrograph showing magnesiofoitite that partially replaced quartz. **E1)** Metapelite in drill-core brecciated by chlorite and illite veinlets. **E2-4)** Veinlet of Fe-Mg chlorite that cross-cut fine-grained sudoite and replaced quartz (fine-grained plates) and magnesiofoitite. Fe-Mg chlorite is partially replaced by coarse-grained illite. **F1)** Photomicrograph of metapelite containing brown chlorite replaced by magnesiofoitite. Pyrite was late and infilled cleavage planes in magnesiofoitite. **F2)** Photomicrograph (400X; PL) showing magnesiofoitite replacement of chlorite. **G1)** Metapelite and pegmatite in drill-core altered by yellow-white clay. **G2-3)** Photomicrograph and BSE-image showing dravite (Dv) that partially replaced quartz and altered an earlier green tourmaline in pegmatite. SEM-EDS analysis shows that the altered green tourmaline has a greater wt% FeO than the brown dravite and was probably schörl.

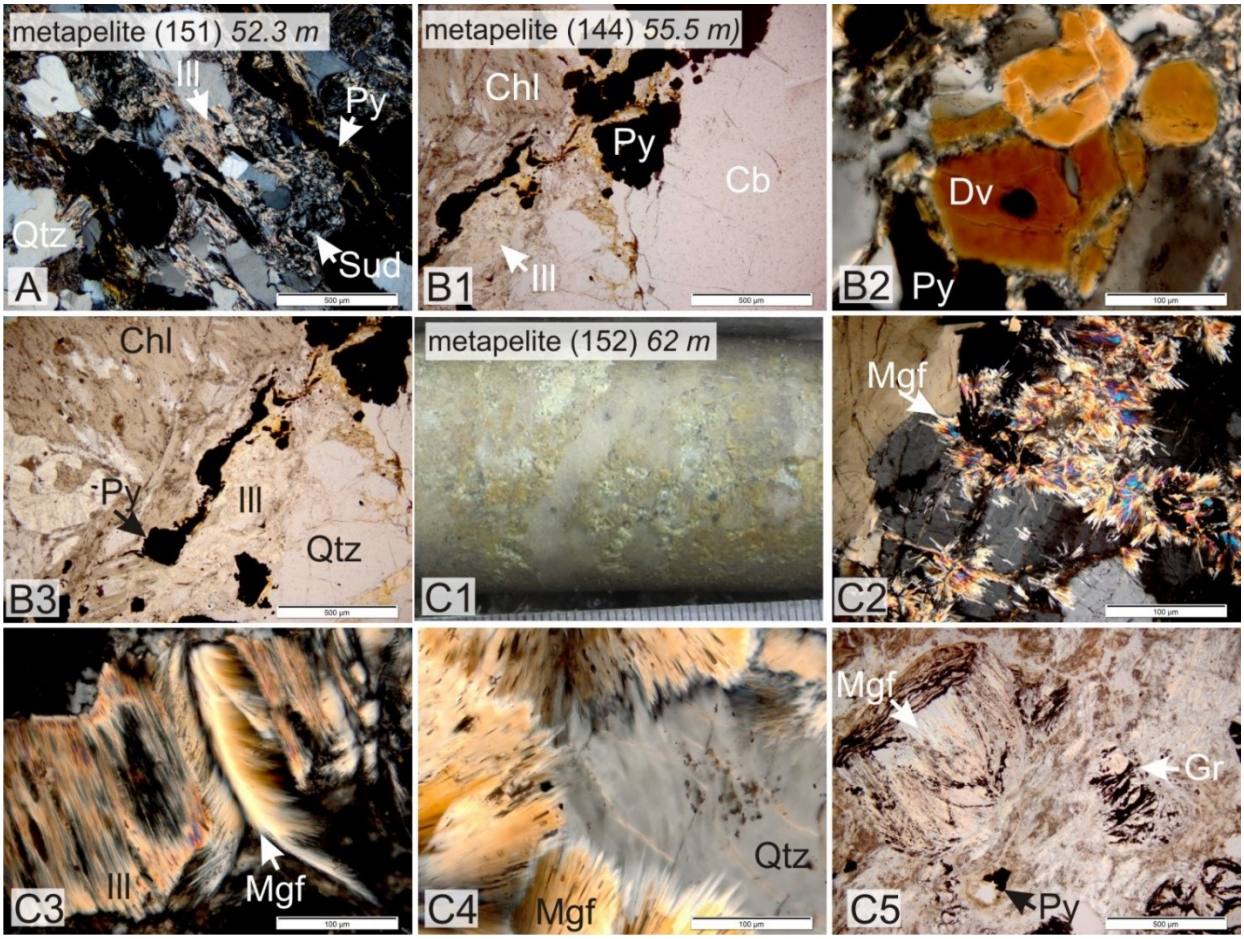

Figure 2.10. Drill-core and thin-section photos of samples from drill-hole H203 (Zone 2 underground). **A)** Photomicrograph of metapelite showing illite that replaced sudoite and Fe-Mg chlorite, and pyrite veinlets. **B1)** Photomicrograph of metapelite showing a large carbonate grain, pyrite cubes that infilled a fracture, and illite replacement of Fe-Mg chlorite. **B2)** Photomicrograph of dravite that is partially replaced by illite and pyrite. **B3)** Photomicrograph showing pyrite cubes that infilled a fracture and the replacement of chlorite by illite. **C1)** Drill-core sample of metapelite showing yellow-white pervasive clay alteration. **C2)** Photomicrograph (XPL) showing magnesiofoitite replacement of quartz. **C3)** Photomicrograph (400X; XPL) showing magnesiofoitite replacement of illite. **C4)** Photomicrograph (400X; PPL) showing magnesiofoitite that replaced quartz. **C5)** Photomicrograph (PPL) showing magnesiofoitite that replaced illite. Graphite occurs along cleavage planes and grain boundaries.

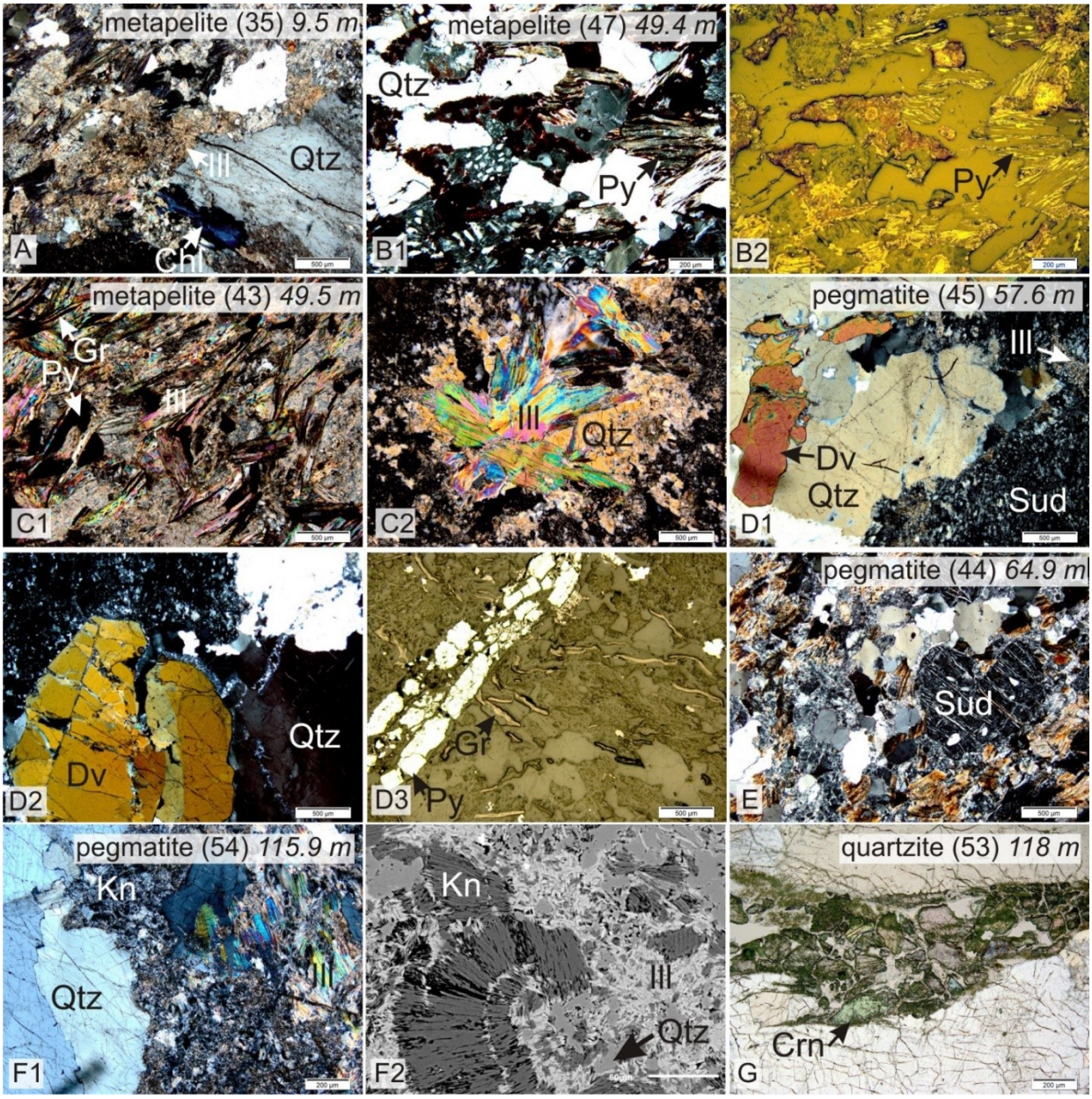

Figure 2.11. Photomicrograph of rocks intersected by drill-hole H729 (Zone 3 underground mine collared drill-hole). Samples are shown in order progressing from the hanging-wall to the P2, into middle block of the P2 fault, and in the quartzite footwall. **A)** Metapelite from the footwall to the P2 fault containing fine-grained Fe-Me chlorite aggregates (Chl) and as replacement of biotite. Fine-grained illite (Ill) partially replaced quartz (Qtz) and the Fe-Mg chlorite. **B1 & B2)** Metapelite from the middle block in the P2 fault shown in cross-polarized (B1) and reflected light (B2) showing pyrite (Py) replacement of hematite that infilled cleavages in illite and rimmed quartz grains. Remnant quartz grains that occur in fine-grained

illite are evidence for quartz dissolution. **C1)** Pyrite and graphite (Gr) infilled cleavage planes in coarse-grained illite pseudomorphs of Fe-Mg chlorite. **C2)** Coarse-grained illite partially replaced quartz in metapelite. **D1 & D2)** Quartz replaced by dravite in pegmatite from the middle block in the P2 fault. Quartz, fine-grained illite, and dravite are partially replaced by sudoite (Sud). **D3)** A late pyrite vein that cross-cut graphite laths. **E)** Sudoite replaced fine-grained illite, biotite and cordierite in pegmatite. **F1)** Photomicrograph showing coarse-grained illite replaced quartz and kaolinite (Kn) partially replaced the illite. **F2)** BSE-image showing illite (light grey) that overprinted kaolinite (dark grey). **G)** Crystalline corundum (Crn) that partially replaced kaolinite and quartz in a veinlet in quartzite.

BSE imaging (Fig. 2.11-F2) shows that illite overprints kaolinite. Corundum partly replaces fine-grained kaolinite within a fracture in the quartzite footwall (Fig. 2.11-G), here interpreted as evidence for desilicification.

Mineral chemistry:

Complete data tables are located in Appendix 2. Representative analyses of metamorphic biotite and garnet from metapelite in drill-hole MC344 are presented in Table 2.1. Biotite is intermediate composition (X_{Fe}= ~0.50 where [X_{Fe} = Fe/(Fe+Mg)]) between annite and phlogopite end-members. Garnet is Fe-rich almandine (X_{Fe} = 0.83) and contains low MnO (2.09 wt %) and CaO (0.96 wt%). K-feldspar composition, which was semi-quantitatively determined using SEM-EDS, is almost pure orthoclase (K_2O = ~15 wt%; Na_2O = ~1 wt%).

EMPA and SEM-EDS data for chlorite are in Table 2.2. Iron is assumed to be Fe(II) in all minerals. Sudoite and Fe-Mg chlorite were identified based on Al, Fe and Mg at the octahedral site (Fig. 2.12). Sudoite has three main compositions, those replacing cordierite and garnet, and that which forms a fine-grained matrix in altered metapelite. Sudoite that replaces cordierite has an average chemical formula of $(Mg_{1.14}Fe_{0.61}Al_{2.86})(Si_{3.6}Al_{0.4})O_{10}((OH_{7.78})F_{0.22})$, whereas sudoite

that replaces garnet is more Mg-rich with an average chemical formula of $(Mg_{1.67}Fe_{0.19}Al_{2.9})(Si_{3.45}Al_{0.55})O_{10}(OH_8)$.

Table 2.1. EMPA chemical analyses of biotite and garnet in the least altered rocks from the base of drill-core MC344.

	Sample (depth)	3 (651.5 m)						9 (628.2 m)	
	lithology	*least altered metapelite*						*chloritized metapelite*	
	mineral	biotite		biotite		biotite		garnet	
		x̄	σ	x̄	σ	x̄	σ	x̄	σ
wt%	SiO_2	35.85	0.67	36.27	0.53	35.89	0.14	37.02	0.17	36.74	0.12
	TiO_2	3.66	0.65	1.30	0.80	3.90	0.16	0.01	0.01	0.00	0.00
	Al_2O_3	20.41	2.24	19.51	0.51	18.99	0.18	21.45	0.09	21.26	0.07
	FeO	18.44	2.02	16.59	1.75	19.38	0.22	33.78	0.20	34.31	0.11
	MnO	0.04	0.01	0.04	0.01	0.04	0.02	1.32	0.04	2.86	0.07
	ZnO	0.04	0.03	0.07	0.04	0.05	0.02	nd		nd	
	MgO	8.58	0.76	12.82	1.76	9.08	0.05	5.05	0.10	3.97	0.10
	CaO	bdl		bdl		bdl		0.98	0.02	0.93	0.01
	Na_2O	0.10	0.02	0.24	0.12	0.09	0.01	0.02	0.01	0.02	0.01
	K_2O	8.87	1.32	9.10	0.48	9.77	0.21	0.00	0.00	0.00	0.01
	P_2O_5	nd		nd		nd		0.05	0.02	0.10	0.04
	Cl	0.06	0.01	0.04	0.02	0.07	0.00	nd		nd	
	BaO	0.03	0.02	0.06	0.03	0.06	0.03	nd		nd	
	F	0.33	0.06	0.54	0.07	0.40	0.02	nd		nd	
	Total	96.27	1.94	96.36	0.47	97.54	0.37	99.68	0.43	100.20	0.22
	Fe/Fe+Mg	0.55		0.42		0.54		0.79		0.83	
apfu											
	Si	5.35		5.39		5.36		2.96		2.95	
	Ti	0.41		0.15		0.44					
	Al	3.59		3.42		3.34		2.02		2.01	
	Fe	2.30		2.06		2.42		2.26		2.31	
	Mn	0.00		0.00		0.00		0.09		0.19	
	Mg	1.91		2.84		2.02		0.60		0.48	
	Ca	0.00		0.00		0.00		0.08		0.08	
	Na	0.03		0.07		0.03					
	K	1.69		1.73		1.86					
	∑	15.29		15.64		15.46		8.02		8.02	
	F	0.15		0.23		0.19					
	O*	21.93		21.89		21.82		12.00		12.00	

*atom proportions normalized to O = 21 for biotite ($O_{20}(OH)_4$) and O = 12 for garnet.;
SrO below detection limits (bdl); na = no data

Table 2.2. EMPA & SEM† analyses of chlorite in the basement rocks below the Athabasca Basin. Atoms per formula unit are normalized to O = 14 ($O_{10}(OH)_8$).

		MC344 (background hole)											H347 (Zone 2)		H201 (Zone2)	
		3 (651.5 m)				9 (628.2 m)					13 (525.9 m)		75 (u/g)		67 (u/g)	
		relatively unaltered metapelite				*moderately chloritized metapelite*					*chloritized metapelite*		*altered metapelite*		*altered metapelite*	
	occurrence	sud-cordierite	sud-cordierite	sud-cordierite	sud-cordierite	chloritized bt	chloritized bt	chloritized bt	chlorite aggregate	chlorite aggregate	sud-gt	sud-gt	chlorite aggregate		fine-grained matrix	
		x̄ σ	x̄ σ	x̄ σ	x̄ σ	x̄ σ	x̄ σ	x̄ σ	x̄ σ	x̄ σ	x̄ σ	x̄ σ	x̄ σ		x̄	x̄
wt%	SiO_2	37.33 0.50	38.19 0.44	37.44 0.71	37.85 0.36	27.57 0.61	27.92 0.33	28.62 1.60	26.44 0.55	34.43 6.95	37.70 0.84	37.98 0.68	26.47	0.10	44.74†	45.39†
	TiO_2	bdl 0.01	bdl 0.01	bdl 0.01	bdl 0.01	0.18 0.14	0.11 0.04	0.17 0.11	bdl	0.06 0.10	bdl	bdl	bdl		bdl	bdl
	Al_2O_3	28.39 0.25	30.14 0.17	28.46 0.44	28.90 0.22	21.41 0.12	20.98 0.17	21.19 0.54	21.71 0.33	25.01 3.68	32.06 0.56	32.27 0.26	22.83	0.12	38.92	36.39
	FeO (T)	8.25 0.09	5.33 0.20	9.26 0.53	7.94 0.44	24.84 0.74	24.91 0.23	23.82 1.57	22.17 0.65	21.80 10.79	2.73 0.42	2.35 0.08	20.16	0.19	bdl	0.70
	MnO	0.05 0.01	0.05 0.00	0.07 0.01	0.05 0.01	0.11 0.01	0.12 0.01	0.12 0.03	0.09 0.01	0.49 0.55	bdl	bdl	0.48	0.03	bdl	bdl
	ZnO	nd	nd	nd	nd	bdl	0.03 0.03	0.05 0.03	bdl 0.03	0.01 0.01	bdl	bdl	bdl		bdl	bdl
	MgO	7.37 0.28	6.76 0.25	8.77 0.63	9.28 0.20	13.91 0.42	14.64 0.31	14.25 0.97	16.71 0.56	7.80 2.67	12.31 0.73	12.29 0.85	16.60	0.19	15.87	16.89
	CaO	0.32 0.09	0.34 0.02	0.42 0.07	0.46 0.00	bdl	bdl	bdl	bdl	0.11 0.18	0.09 0.13	bdl	bdl		bdl	bdl
	Na_2O	0.07 0.02	0.07 0.01	0.03 0.02	0.03 0.01	bdl	bdl	bdl	bdl	0.04 0.04	bdl	bdl	bdl		bdl	bdl
	K_2O*	2.62 0.39	2.11 0.12	1.51 0.59	0.82 0.12	0.30 0.29	0.19 0.14	0.63 0.71	bdl	2.93 2.95	0.89 0.20	0.89 0.24	0.02	0.01	0.46	0.63
	Cl	nd	nd	nd	nd	bdl	bdl	bdl	0.03 0.01	0.04 0.03	0.03 0.01	0.03 0.01	bdl		bdl	bdl
	F	nd	nd	nd	nd	0.13 0.02	0.17 0.06	0.21 0.04	0.09 0.04	0.10 0.09	0.07 0.02	0.03 0.02	0.06	0.04	bdl	bdl
	Total	84.41 0.48	82.98 0.32	85.99 0.39	85.35 0.24	88.44 0.24	89.04 0.15	89.00 0.34	87.27 0.40	92.78 2.31	85.88 0.41	85.88 0.31	86.64	0.23	100.00	100.00
	Fe/Fe+Mg	0.39	0.31	0.37	0.32	0.62	0.49	0.48	0.43	0.50	0.11	0.10	0.41			
apfu																
	Si	3.61	3.66	3.55	3.57	3.28	2.87	2.93	2.74	2.86	3.44	3.45	2.74		3.43	3.50
	Al	3.23	3.41	3.18	3.21	2.83	2.54	2.56	2.66	2.62	3.45	3.46	2.78		3.53	3.30
	Fe	0.67	0.43	0.73	0.63	1.83	2.14	2.04	1.93	2.15	0.21	0.18	1.74		0.00	0.04
	Mn	0.00	0.00	0.00	0.00	0.04	0.00	0.00	0.00	0.00	0.00	0.00	0.04		0.00	0.00
	Mg	1.06	0.97	1.24	1.31	1.14	2.25	2.18	2.59	2.15	1.67	1.67	2.56		1.82	1.95
	K	0.03	0.03	0.04	0.05	0.34	0.03	0.08	0.00	0.04	0.10	0.10	0.00		0.07	0.10
	F	0.32	0.26	0.18	0.10	0.03	0.05	0.07	0.03	0.04	0.00	0.00	0.00		0.00	0.00
	O	13.84	13.87	13.91	13.95	13.99	13.97	13.97	13.99	13.98	14.00	14.00	14.00		14.00	14.00

†semi-quantified using SEM-EDS (normalized to 100% total); *K_2O is contamination of illite; nd= no data; bdl = below detection limits; BaO & SrO below detection limits; u/g = underground collared hole; FeO (T) = total Fe as FeO

In altered metapelite Fe-Mg chlorite replaces biotite, forms fine grained aggregates and has an average chemical formula of $(Mg_{2.14}Fe_{1.97}Al_{0.56})(Si_{2.90}Al_{2.10})O_{10}((OH)_{7.96}F_{0.04})$.

Chemical data from EMPA analysis of kaolinite, fine-grained and coarse-grained illite from background hole MC344 are in Table 2.3. Kaolinite has an average mineral formula of $Al_{1.91}Si_{2.03}O_5(OH)_4$. Fine-grained illite from metapelite sampled in drill-hole MC344 has a mineral formula of $K_{1.63}(Mg_{0.34}Fe_{0.21}Al_{3.59})(Al_{1.54}Si_{6.46})O_{20}(OH)_4$. Coarse-grained illite contains slightly less MgO on average, with an average mineral formula of $K_{1.81}(Mg_{0.11}Fe_{0.10}Al_{3.82})(Al_{1.81}Si_{6.19})O_{20}(OH)_4$. EMPA data for coarse-grained illite from sandstone, metapelite and pegmatite along the P2 fault are in Table 2.4. Illite from pegmatite and metapelite typically contain greater MgO contents (0.40 to 9.03 wt.% MgO) whereas sandstone illite is richer in Fe (2.95 wt.% Fe_2O_3).

EMPA data for dravite and magnesiofoitite are presented in Tables 2.5 and 2.6, respectively. Dravite calculated assuming stoichiometric boron and based on 24.5 oxygens is: $(\square_{0.4}Na_{0.6})(\square_{0.2}Mg_{1.9}Fe_{0.5}Ca_{0.2}Ti_{0.2})(Al_{5.9}Fe_{0.1})(Si_{5.7}Al_{0.3}O_{18})(BO_3)_3(OH_{3.8}F_{0.2})$, where □ represents vacancy. The mineral formula of magnesiofoitite is: $(\square_{0.75}K_{0.08}Na_{0.17})(\square_{0.23}Ca_{0.02}Fe_{0.04}Mg_{2.10}Al_{0.61})Al_6\ (Al_{0.22}Si_{5.78}O_{18})(BO_3)_3(OH_{3.98}F_{0.02})$. Schörl (partially replaced by dravite) was identified in one sample from Zone 2 and its chemistry, semi-quantitatively determined using SEM-EDS, is 39.1 – 40.9 wt% SiO_2, 0 – 1.4 wt% TiO_2, 11 – 14 wt% FeO, 4.6 – 6.0 wt% MgO, 0.8 – 1.1 wt% CaO, and 1.9 – 2.1 wt% Na_2O.

Table 2.3. EMPA analyses of illite and kaolinite from background drill-hole MC344. Atoms per formula unit normalized to O = 22 for illite ($O_{20}(OH)_4$)and O = 7 for kaolinite ($O_5(OH)_4$).

sample (depth)		9 (628.2 m)		13 (525.9 m)				17 (499.4 m)							
lithology		*moderately chloritized metapelite*		*chloritized metapelite*				*basal quartzite*							
mineral		coarse-grained illite	fine-grained illite	fine-grained illite	fine-grained illitized chlorite			coarse-grained illite				kaolinite lamella in illite		fine-grained kaolinite	
		x̄ σ	x̄ σ	x̄ σ	x̄ σ	x̄ σ	x̄ σ	x̄ σ	x̄ σ	x̄ σ	x̄ σ	x̄ σ	x̄ σ	x̄ σ	x̄ σ
wt%	SiO_2	48.61 0.41	46.52 0.86	48.58 0.71	49.73 0.24	47.89 1.06	48.80 1.10	45.85 0.38	45.93 0.37	45.92 0.31	46.42 0.22	46.26 0.20	45.75 0.02	46.13 0.27	46.80 0.42
	TiO_2	bdl	bdl	bdl 0.01	bdl	bdl	bdl	0.24 0.19	0.28 0.20	bdl	0.06 0.07	bdl	0.16 0.16	bdl	bdl
	Al_2O_3	31.50 0.22	31.75 0.31	32.54 0.30	32.22 0.34	33.57 0.40	32.64 0.57	35.68 0.78	36.11 0.85	37.66 0.38	37.16 0.60	37.01 0.49	35.57 1.16	37.09 1.45	37.46 0.41
	FeO (T)	2.63 0.24	2.28 0.64	2.04 0.40	1.49 0.11	1.94 0.64	1.81 0.31	0.78 0.17	0.75 0.20	0.11 0.04	0.50 0.35	0.18 0.03	0.41 0.23	0.15 0.08	0.12 0.05
	MgO	1.97 0.18	2.39 0.39	1.79 0.43	1.15 0.11	1.42 0.55	1.66 0.31	0.49 0.22	0.43 0.24	0.07 0.04	0.05 0.06	0.08 0.03	0.25 0.18	0.05 0.05	0.03 0.02
	Na_2O	0.11 0.02	0.15 0.01	0.03 0.01	0.03 0.01	0.02 0.01	0.03 0.02	0.41 0.10	0.42 0.12	0.29 0.01	0.24 0.02	0.06 0.01	0.08 0.04	0.03 0.01	bdl
	K_2O	10.05 0.24	9.16 0.24	9.80 0.63	9.77 0.10	9.69 0.73	9.26 0.63	10.96 0.23	10.95 0.14	10.98 0.07	10.50 0.91	1.93 0.20	3.98 1.25	1.02 0.69	0.82 0.24
	BaO	0.21 0.01	0.35 0.13	bdl	bdl	bdl	bdl	0.03 0.02	0.04 0.03	bdl	0.06 0.04	bdl	bdl	bdl	bdl
	F	0.22 0.06	0.17 0.05	0.08 0.04	0.15 0.04	0.06 0.07	0.12 0.05	0.08 0.04	0.07 0.04	0.04 0.04	0.06 0.04	0.08 0.10	0.04 0.04	0.11 0.06	0.08 0.07
	Total	95.29 0.34	92.76 0.22	94.89 0.55	94.55 0.36	94.61 0.95	94.34 0.45	94.54 0.26	94.99 0.20	95.13 0.38	95.05 0.86	85.61 0.40	86.28 0.62	84.58 0.66	85.34 0.42
apfu															
	Si	6.49	6.36	6.46	6.60	6.38	6.49	6.15	6.05	6.09	6.15	2.03	2.03	2.03	2.04
	Al	4.96	5.12	5.10	5.04	5.27	5.12	5.64	5.85	5.88	5.80	1.92	1.86	1.93	1.93
	Fe	0.29	0.26	0.23	0.17	0.22	0.20	0.09	0.06	0.01	0.06		0.02		
	Mg	0.39	0.49	0.35	0.23	0.28	0.33	0.10	0.04	0.01	0.00		0.02		
	Na	0.00	0.00	0.00	0.00	0.00	0.00	0.11	0.16	0.07	0.06				
	K	1.71	1.60	1.66	1.65	1.65	1.57	1.88	1.84	1.86	1.77	0.09	0.23	0.06	0.05
	F	0.09	0.07	0.04	0.06	0.02	0.05	0.03	0.02	0.02	0.02			0.01	0.01
	O*	22	22	22	22	22	22	22	22	22	22	7	7	7	7

MnO, CaO, ZnO, Cl & SrO below detection limits (bdl); FeO (T) = total Fe as FeO; *O determined stoichiometrically

Table 2.4. EMPA analyses of coarse-grained illite from along the P2 fault. Atomic proportions are normalized to O = 22 ($O_{20}(OH)_4$).

		MC370 (sub-ec P2)				MC349 (sub-ec P2)	MC361 (barren P2)		H201 (Zone 2)	MO227 (Zone 2)			H3559 (Zone 1)	H347 (Zone 2)
		32 (543 m)		29 (560.2 m)		89 (645.5 m)	111 (581.6 m)		69 (u/g)	146 (u/g)			201 (u/g)	75 (u/g)
		sandstone above unconformity		*brecciated metapelite thrusted over sandstone*		*pegmatite*	*pegmatite*		*metapelite*	*metapelite*			*graphitic metapelite*	*brecciated pegmatite*
		x̄ σ	x̄ σ	x̄ σ	x̄ σ	x̄ σ	x̄ σ	x̄ σ	x̄ σ	x̄ σ	x̄ σ	x̄ σ	x̄ σ	x̄ σ
wt%	SiO_2	44.81 0.36	46.07 0.15	45.79 0.45	45.27 0.53	46.67 2.70	46.82 1.19	45.99 0.17	41.89 3.98	43.86 0.33	44.67 0.60	45.13 0.63	46.33 0.92	47.53 0.45
	TiO_2	0.98 0.04	0.99 0.02	0.08 0.01	0.10 0.03	0.22 0.20	0.04 0.03	0.02 0.01	0.05 0.03	0.27 0.10	0.03 0.01	0.03 0.01	0.01 0.01	0.01 0.01
	Al_2O_3	33.61 0.13	33.56 0.10	34.81 0.43	34.84 1.02	30.46 0.93	32.61 0.83	33.50 0.64	31.74 0.94	33.68 0.29	35.07 0.78	34.71 1.00	32.49 0.76	34.80 0.75
	FeO (T)	2.95 0.09	1.22 0.02	1.02 0.11	1.51 0.50	1.05 1.20	1.62 0.71	2.48 0.23	0.41 0.08	0.79 0.03	0.64 0.05	0.65 0.10	0.90 0.01	1.17 0.40
	MgO	0.56 0.07	1.07 0.02	0.86 0.18	1.29 0.47	5.89 2.56	2.01 0.50	1.08 0.31	9.03 3.36	0.40 0.10	0.59 0.29	0.46 0.26	1.15 0.35	0.20 0.11
	Na_2O	0.47 0.05	0.40 0.01	0.34 0.05	0.33 0.04	0.03 0.01	0.17 0.03	0.21 0.02	0.04 0.01	0.39 0.04	0.32 0.07	0.33 0.12	0.08 0.00	0.20 0.09
	K_2O	10.59 0.08	10.96 0.04	10.71 0.24	10.27 0.43	7.37 1.17	10.11 0.66	10.43 0.20	4.23 2.68	9.54 0.05	9.70 0.31	9.84 0.24	10.84 0.07	10.95 0.14
	Cl	bdl	bdl	bdl	0.10 0.09	bdl	0.10 0.07	0.13 0.02	0.07 0.01	bdl	bdl	bdl	bdl	bdl
	BaO	0.45 0.18	0.03 0.03	0.12 0.04	0.12 0.04	0.01 0.01	0.15 0.09	0.17 0.06	0.01 0.02	0.01 0.01	0.01 0.01	0.01 0.02	0.09 0.03	0.06 0.04
	F	0.11 0.03	0.47 0.04	0.08 0.06	0.13 0.06	0.19 0.08	0.20 0.09	0.12 0.01	0.17 0.06	0.02 0.03	0.09 0.03	0.05 0.06	0.16 0.08	0.07 0.02
	Total	94.52 0.32	94.60 0.20	93.81 0.33	93.90 0.67	91.88 0.68	93.75 0.91	94.08 0.50	87.56 2.32	88.96 0.32	91.09 0.31	91.25 0.32	92.02 0.53	94.98 0.26
apfu:														
	Si	6.10	6.16	6.19	6.11	6.31	6.27	6.25	5.86	6.21	6.17	6.22	6.38	6.33
	Al	5.39	5.29	5.54	5.54	4.86	5.29	5.37	5.24	5.62	5.71	5.64	5.28	5.47
	Ti	0.10	0.10	0.00	0.00	0.00	0.00	0.00	0.00	0.00	0.00	0.00	0.00	0.00
	Fe	0.34	0.14	0.12	0.17	0.12	0.22	0.28	0.05	0.09	0.07	0.08	0.10	0.13
	Mg	0.11	0.21	0.17	0.26	1.19	0.35	0.22	1.88	0.08	0.12	0.10	0.24	0.04
	Na	0.12	0.10	0.09	0.09	0.01	0.05	0.06	0.00	0.11	0.09	0.09	0.02	0.05
	K	1.84	1.87	1.85	1.77	1.27	1.81	1.81	0.76	1.72	1.71	1.73	1.91	1.86
	F	0.05	0.20	0.00	0.00	0.08	0.09	0.00	0.07	0.00	0.00	0.00	0.07	0.00
	O*	22	22	22	22	22	22	22	22	22	22	22	22	22

MnO, CaO, ZnO, & SrO below detection limits (bdl); FeO (T) = total Fe as FeO; *O determined stoichiometrically

Table 2.6. Chemical composition of dravite determined by EMPA and SEM† analysis. Atom proportions are O = 24.5 ($(BO_3)_3O_{15}(OH)_4$)

	drill-hole	H3559 (Zone 1)								MC361 (barren)					MC349 (sub-economic)				H493 (Zone 2)			
	sample (depth)	201 (u/g)								109 (587.6 m)			111 (581.6 m)		99 (~578 m)				85 (u/g)			
	host rock	*graphitic pelite*								*pegmatite*			*pegmatite*		*brecciated metapelite*				*altered metapelite*			
		x̄	σ	x̄	σ	x̄	σ	x̄	σ	x̄	σ	x̄	σ	x̄	σ	x̄	σ	x̄	σ	x̄	σ	x̄	σ
wt%	SiO_2	35.35	0.31	34.94	0.07	35.36	0.35	34.96	0.08	35.23	0.05	35.09	0.17	35.10	0.24	35.20	0.07	35.50	0.13	35.34	0.09	35.16	0.16	34.83	0.09	34.67	0.09	35.52	0.26	35.63	0.32	35.68	0.47	35.45	0.17	41.78†	0.55	40.39†	0.6
	TiO_2	1.06	0.15	1.23	0.07	1.08	0.10	1.21	0.07	1.28	0.03	1.24	0.08	1.14	0.01	1.23	0.06	1.34	0.04	1.36	0.08	1.36	0.19	1.14	0.07	1.25	0.05	1.29	0.08	1.23	0.09	1.27	0.17	1.28	0.13	0.96	0.19	1.12	0.3
	Al_2O_3	32.06	0.15	32.20	0.23	31.76	0.22	31.75	0.16	31.88	0.24	32.05	0.19	32.54	0.13	31.98	0.09	31.65	0.23	31.75	0.15	32.02	0.14	32.30	0.06	32.21	0.16	31.83	0.19	31.80	0.13	31.68	0.27	31.94	0.23	38.32	0.92	39.05	0.7
	FeO (T)	3.56	0.02	3.63	0.15	3.57	0.10	3.50	0.11	3.40	0.19	3.58	0.14	3.67	0.11	3.69	0.08	4.78	0.04	4.77	0.02	5.32	0.12	5.14	0.01	5.26	0.04	4.68	0.18	4.90	0.02	4.78	0.16	4.87	0.00	7.79	0.57	12.18	0.9
	MnO	0.01	0.01	0.02	0.01	bdl		0.01	0.01	0.02	0.01	0.01	0.01	0.01	0.01	bdl		0.03	0.00	0.03	0.01	0.03	0.01	0.01	0.01	0.02	0.00	0.02	0.02	0.02	0.02	0.01	0.01	0.01	0.01	bdl		bdl	
	ZnO	0.01	0.01	0.01	0.01	0.01	0.02	0.01	0.01	0.01	0.01	0.01	0.02	0.01	0.01	0.01	0.01	0.01	0.02	0.00	0.01	0.01	0.01	0.03	0.03	0.02	0.02	0.01	0.02	0.02	0.01	0.01	0.02	0.01	0.01	bdl		bdl	
	MgO	8.34	0.06	8.34	0.06	8.32	0.04	8.40	0.07	8.34	0.08	8.31	0.03	8.16	0.08	8.26	0.06	7.74	0.07	7.63	0.04	7.15	0.19	7.10	0.03	7.05	0.06	7.68	0.06	7.73	0.04	7.62	0.09	7.51	0.04	7.86	0.48	5.09	0.5
	CaO	1.27	0.25	1.51	0.07	1.27	0.22	1.51	0.14	1.61	0.01	1.60	0.08	1.51	0.02	1.58	0.08	1.20	0.08	1.01	0.05	0.92	0.07	1.27	0.04	1.36	0.05	1.36	0.12	1.28	0.12	1.31	0.27	1.38	0.15	1.03	0.03	0.92	0.2
	Na_2O	1.71	0.11	1.68	0.05	1.77	0.08	1.65	0.09	1.61	0.05	1.62	0.04	1.66	0.02	1.64	0.02	1.95	0.04	2.05	0.04	1.98	0.09	1.72	0.02	1.67	0.03	1.73	0.07	1.78	0.07	1.74	0.15	1.71	0.03	2.25	0.06	2.00	0.1
	K_2O	0.07	0.01	0.07	0.01	0.06	0.01	0.07	0.00	0.08	0.01	0.08	0.00	0.08	0.01	0.07	0.00	0.07	0.00	0.07	0.01	0.06	0.01	0.08	0.01	0.08	0.01	0.07	0.01	0.06	0.02	0.07	0.02	0.07	0.01	bdl		bdl	
	BaO	0.01	0.01	0.03	0.04	0.03	0.01	0.00	0.00	0.02	0.02	0.01	0.01	0.02	0.01	0.01	0.01	0.02	0.03	0.02	0.02	0.02	0.02	0.01	0.01	0.02	0.01	0.01	0.01	0.03	0.02	0.01	0.01	0.00	0.00	bdl		bdl	
	F	0.42	0.03	0.45	0.06	0.41	0.04	0.41	0.01	0.44	0.07	0.54	0.05	0.47	0.02	0.50	0.03	0.25	0.06	0.22	0.08	0.25	0.05	0.39	0.08	0.45	0.07	0.57	0.08	0.44	0.06	0.53	0.07	0.54	0.07	bdl		bdl	
	SrO	bdl		bdl		bdl		bdl		bdl		0.02	0.02	bdl		bdl		0.01	0.02	0.01	0.01	bdl		0.01	0.01	0.01	0.01	0.02	0.02	bdl		0.03	0.04	0.03	0.04	bdl		bdl	
	Total	83.70	0.22	83.93	0.18	83.47	0.07	83.31	0.14	83.75	0.31	83.93	0.16	84.19	0.18	83.98	0.07	84.45	0.21	84.15	0.13	84.18	0.26	83.86	0.06	83.88	0.21	84.56	0.13	84.76	0.23	84.52	0.18	84.58	0.06	100.00		100.00	
	F/Cl	134		1513		443		497		332		266		1444		bdl		173		246		98		278		245		557		564		1496		10876					
apfu																																				brown rim^		green core^	
T:	Si	5.75		5.69		5.77		5.72		5.74		5.71		5.69		5.73		5.77		5.76		5.74		5.71		5.69		5.77		5.77		5.79		5.76					
	Al	0.25		0.31		0.23		0.28		0.26		0.29		0.31		0.27		0.23		0.24		0.26		0.29		0.31		0.23		0.23		0.21		0.24					
Z:	Al	5.90		5.86		5.88		5.85		5.85		5.86		5.91		5.86		5.82		5.85		5.90		5.95		5.92		5.86		5.84		5.86		5.87					
	Fe	0.10		0.14		0.12		0.15		0.15		0.14		0.09		0.14		0.18		0.15		0.10		0.05		0.08		0.14		0.16		0.14		0.13					
Y:	Fe	0.39		0.36		0.37		0.33		0.32		0.35		0.41		0.36		0.47		0.50		0.62		0.65		0.64		0.49		0.51		0.51		0.53					
	Ti	0.13		0.15		0.13		0.15		0.16		0.15		0.14		0.15		0.16		0.17		0.17		0.14		0.15		0.16		0.15		0.15		0.16					
	Mg	2.02		2.02		2.02		2.05		2.02		2.02		1.97		2.00		1.87		1.85		1.74		1.73		1.72		1.86		1.87		1.84		1.82					
	Ca	0.22		0.26		0.22		0.26		0.28		0.28		0.26		0.28		0.21		0.18		0.16		0.22		0.24		0.24		0.22		0.23		0.24					
	□	0.24		0.20		0.25		0.21		0.22		0.21		0.21		0.21		0.28		0.31		0.31		0.25		0.24		0.26		0.25		0.27		0.25					
X:	Na	0.54		0.53		0.56		0.52		0.51		0.51		0.52		0.52		0.62		0.65		0.63		0.55		0.53		0.55		0.56		0.55		0.54					
	K	0.01		0.02		0.01		0.01		0.02		0.02		0.02		0.02		0.02		0.01		0.01		0.02		0.02		0.02		0.01		0.02		0.01					
	□	0.44		0.45		0.43		0.46		0.48		0.47		0.46		0.47		0.37		0.34		0.36		0.44		0.45		0.44		0.43		0.44		0.45					
B:	B*	3.00																																					
O:	O*	24.5		24.5		24.5		24.5		24.5		24.5		24.5		24.5		24.5		24.5		24.5		24.5		24.5		24.5		24.5		24.5		24.5					
	OH*	3.79		3.77		3.79		3.79		3.78		3.73		3.76		3.75		3.87		3.89		3.87		3.80		3.77		3.71		3.77		3.73		3.73					
	F	0.21		0.23		0.21		0.21		0.22		0.27		0.24		0.25		0.13		0.11		0.13		0.20		0.23		0.29		0.23		0.27		0.27					

□ = vacancy; * determined by stoichiometry; FeO (T) = total Fe, †SEM analysis of green altered dravite (normalized to 100% total) see Fig. 7-F2

Table 2.6. EMPA analyses of magnesiofoitite from basement rocks and sandstone along the P2 Fault. Atom proportions are normalized to O = 24.5 ($(BO_3)_3O_{18}(OH)_4$).

	drill-hole	MC349 (sub-ec)				MC362 (barren)	MC370 (sub-ec)			H201 (Zone 2)							H3559 (Zone 1)				MO227 (Zone 2)
	sample (depth)	89 (645.5 m)			99 (~578 m)	122 (637.9 m)	29 (560.2 m)	32 (543 m)		69 (u/g)				70 (u/g)			201 (Zone 1 underground)				146 (u/g)
	host rock	*quartz-rich altered pegmatite*			*brecciated metapelite*	*bleached SS above u/c*	*brecciated metapelite*	*bleached SS above u/c*		*altered metapelite*				*altered metapelite*			*graphitic graphitic pelite*				*metapelite*
	EMPA data	x̄ σ	x̄ σ	x̄ σ	x̄ σ	x̄ σ	x̄ σ	x̄ σ	x̄ σ	x̄ σ	x̄ σ	x̄ σ	x̄ σ	x̄ σ	x̄ σ	x̄ σ	x̄ σ	x̄ σ	x̄ σ	x̄ σ	x̄ σ
wt%	SiO_2	37.39 0.21	37.65 0.29	37.51 0.59	33.89 2.32	34.37 0.29	35.94 0.35	32.97 0.28	34.07 0.93	37.23 0.14	36.62 0.58	36.11 0.23	36.12 0.29	36.52 0.72	36.83 0.75	36.81 0.60	35.68 3.31	37.12 0.54	36.13 1.09	36.68 0.54	35.03 1.22
	Al_2O_3	35.47 0.14	35.31 0.17	35.45 0.66	30.69 2.54	33.29 0.91	36.85 0.63	38.21 0.22	37.67 0.32	35.36 0.22	35.90 0.44	35.49 0.23	35.02 0.24	35.35 0.21	36.15 0.42	35.88 0.54	34.06 1.25	34.47 0.66	32.79 0.44	33.30 0.56	34.85 0.88
	FeO	0.14 0.03	0.14 0.01	0.10 0.04	1.39 0.14	2.10 0.20	1.21 0.07	0.69 0.04	0.86 0.11	0.12 0.02	0.13 0.04	0.13 0.02	0.16 0.02	0.11 0.03	0.09 0.02	0.10 0.03	0.20 0.02	0.20 0.03	0.26 0.05	0.23 0.05	1.45 0.33
	MgO	8.52 0.10	8.56 0.12	8.64 0.21	6.67 0.53	6.96 0.04	7.88 0.12	7.43 0.14	7.39 0.11	8.74 0.05	8.50 0.07	8.62 0.05	8.77 0.16	8.39 0.08	8.40 0.10	8.47 0.13	8.11 0.80	8.35 0.17	8.37 0.34	8.42 0.32	7.26 0.20
	CaO	0.11 0.01	0.11 0.01	0.03 0.02	0.07 0.01	0.05 0.01	0.09 0.01	0.25 0.03	0.22 0.04	0.10 0.02	0.13 0.03	0.10 0.01	0.09 0.02	0.11 0.01	0.12 0.02	0.11 0.02	0.02 0.01	0.02 0.01	0.02 0.00	0.02 0.02	0.11 0.04
	Na_2O	0.79 0.07	0.79 0.05	0.57 0.14	0.74 0.08	0.83 0.07	0.55 0.08	0.44 0.02	0.55 0.05	0.68 0.03	0.64 0.07	0.62 0.05	0.60 0.02	0.64 0.07	0.59 0.09	0.61 0.06	0.59 0.04	0.59 0.07	0.67 0.06	0.61 0.08	0.73 0.21
	K_2O	0.02 0.02	0.02 0.01	0.01 0.01	0.02 0.02	bdl	0.01 0.01	0.00 0.00	0.01 0.01	0.04 0.02	0.02 0.01	0.03 0.01	0.04 0.02	0.02 0.01	0.06 0.08	0.03 0.01	bdl	0.02 0.01	bdl	bdl	0.02 0.02
	Cl	0.01 0.00	0.02 0.00	bdl	bdl	bdl	0.01 0.00	0.01 0.00	0.01 0.00	0.03 0.01	0.02 0.01	0.02 0.01	0.03 0.01	0.01 0.00	0.01 0.00	0.02 0.00	bdl	bdl	bdl	bdl	bdl
	F	0.05 0.03	0.05 0.05	0.02 0.02	0.31 0.13	0.18 0.09	0.05 0.03	0.04 0.05	0.08 0.04	0.12 0.03	0.08 0.04	0.08 0.03	0.05 0.03	0.06 0.04	0.06 0.06	0.06 0.03	0.14 0.22	0.03 0.05	0.04 0.04	0.05 0.02	0.04 0.02
	SrO	bdl	bdl	0.01 0.02	bdl	0.03 0.04	0.03 0.04	bdl	0.02 0.02	0.01 0.01	bdl	bdl	0.02 0.02	0.02 0.02	bdl	0.02 0.02	bdl	bdl	0.02 0.03	bdl	bdl
	Total	82.52 0.29	82.66 0.28	82.35 0.63	73.69 5.25	77.77 0.93	82.64 0.43	80.03 0.39	80.86 0.84	82.38 0.26	82.03 0.36	81.20 0.26	80.91 0.31	81.23 0.75	82.32 0.57	82.12 0.31	78.79 5.22	80.82 1.40	78.33 1.82	79.34 0.78	79.51 1.51
	F/Cl	5	3			24	17	6	8	4	3	8	3	8	11	6					12
apfu:	*T:* Si	5.93	5.96	5.95	6.07	5.87	5.73	5.42	5.54	5.90	5.84	5.83	5.85	5.88	5.86	5.87	5.92	6.00	6.04	6.04	5.81
	Al	0.07	0.04	0.05		0.13	0.27	0.58	0.46	0.10	0.16	0.17	0.15	0.12	0.14	0.13	0.08				0.19
	Z Al	6	6	6	6	6	6	6	6	6	6	6	6	6	6	6	6	6	6	6	6
	Y: Al	0.55	0.54	0.58	0.48	0.56	0.66	0.82	0.77	0.52	0.58	0.58	0.54	0.60	0.63	0.61	0.60	0.57	0.46	0.47	0.64
	Mg	2.01	2.02	2.04	1.78	1.77	1.87	1.82	1.79	2.07	2.02	2.08	2.12	2.01	1.99	2.01	2.00	2.01	2.08	2.07	1.80
	Fe	0.02	0.02	0.01	0.21	0.30	0.16	0.10	0.12	0.02	0.02	0.02	0.02	0.01	0.01	0.01	0.03	0.03	0.04	0.03	0.20
	Ca	0.02	0.02	0.01	0.01	0.01	0.02	0.04	0.04	0.02	0.02	0.02	0.02	0.02	0.02	0.02					0.02
	□	0.39	0.40	0.36	0.52	0.36	0.29	0.22	0.29	0.39	0.36	0.31	0.30	0.35	0.35	0.34	0.36	0.39	0.42	0.43	
	X: Na	0.24	0.24	0.18	0.26	0.26	0.17	0.14	0.17	0.21	0.20	0.19	0.19	0.20	0.18	0.19	0.19	0.18	0.22	0.19	0.23
	K									0.01					0.01	0.01					
	□	0.76	0.76	0.82	0.74	0.74	0.83	0.86	0.83	0.78	0.80	0.81	0.81	0.80	0.81	0.80	0.81	0.82	0.78	0.81	0.77
	B: B*	3.00	3.00	3.00	3.00	3	3.00	3.00	3.00	3.00	3.00	3.00	3.00	3.00	3.00	3.00	3.00	3.00	3.00	3.00	3.00
	O: O*	24.5	24.5	24.5	24.5	24.5	24.5	24.5	24.5	24.5	24.5	24.5	24.5	24.5	24.5	24.5	24.5	24.5	24.5	24.5	24.5
	OH*	3.97	3.97	3.99	3.82	3.90	3.97	3.98	3.95	3.93	3.95	3.96	3.97	3.97	3.97	3.97	3.92	3.98	3.98	3.97	3.99
	F	0.03	0.03	0.01	0.18	0.10	0.03	0.02	0.04	0.06	0.04	0.04	0.03	0.03	0.03	0.03	0.08	0.02	0.02	0.03	0.1

□ = vacancy; u/c = unconformity; u/g = unground collared hole; * determined by stoichiometry; FeO (T) = total Fe; *OH & B calculated by stoichiometry; Ba, Ti, Mn, Zn are below detection limits of 0.01%

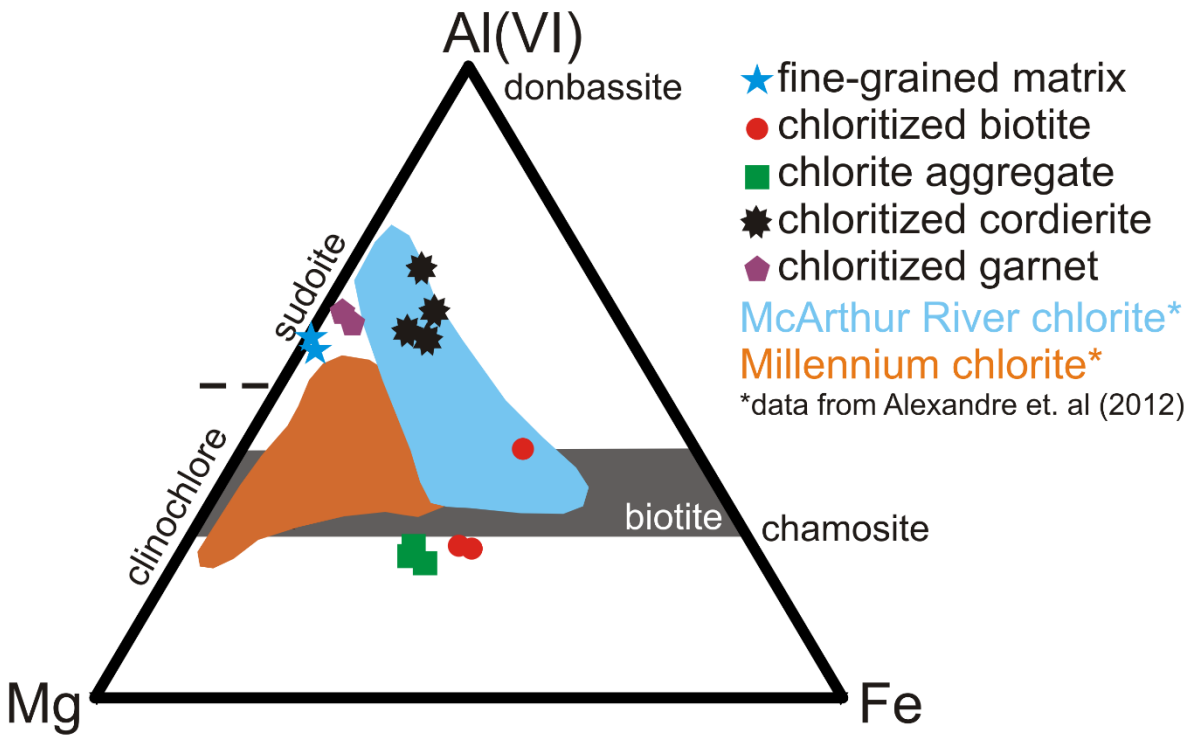

Figure 2.12. AFM diagram (Al^{VI} = octahedral site Al) to classify chlorite species analyzed by EMPA and SEM. Two species of chlorite are identified: sudoite and Fe-Mg chlorite. The blue and orange fields outline chlorite data from Alexandre et al. (2012).

2.6 Discussion

2.6.1 Preliminary paragenesis of alteration in the basement and in the P2 fault zone

At least two compositionally distinct generations of chlorite occur in the Green Zone (Fig. 2.12): Fe-Mg chlorite, which replaced metamorphic biotite and garnet, and forms radial aggregates, and sudoite, which replaced garnet and cordierite. Notably, chloritized biotite is partially illitized in the Green Zone and is completely pseudomorphed by illite in the Red Zone. In drill-hole H201, Fe-Mg chlorite is altered to fine-grained sudoite + quartz, and is also illitized. Therefore, the alteration of Fe-Mg chlorite to coarse-grained illite is complete in the Red Zone, but not in the

Green Zone, and the formation of sudoite post-dated formation of Fe-Mg chlorite. Locally, Fe-Mg chlorite also forms fine veinlets with illite that brecciate pegmatite and metapelite and may be a second, late, generation. Sudoite replaced garnet and cordierite before the latest hematization event (Hem^2) because hematite overprints the sudoite of the Green Zone. This sudoite formed after the formation of Fe-Mg chlorite because sudoite is present but Fe-Mg chlorite is absent in the most extensively altered Green Zone rocks.

Kaolinite and hematite (Hem^2) appear to be coeval in the Red Zone as one does not replace the other and both minerals are partially replaced by late illite. An early hematite event (Hem^1) is characterized by fine veinlets present between annealed quartz grains and along cleavages in coarse-grained illite (Fe-Mg chlorite pseudomorph). Dickite is present in some Red Zone and Bleached Zone samples based on double peaks from SWIR spectra; however, the optical properties, morphologies, and textures of kaolinite and dickite are similar microscopically and it is difficult to differentiate them.

Illite is ubiquitous throughout all alteration zones in the basement. At least two generations of illite are recognized in the basement rocks: i) early illitization of feldspar, and ii) later illite that formed by recrystallization of early illite. Later illite also replaced Fe-Mg chlorite and sudoite in the Green Zone and in the least altered rocks. The second generation of illite also altered kaolin-group minerals and cross-cuts hematite (Hem^2) in the Red and Bleached Zones. The illite described in this Open File is compositionally variable and plots in the muscovite field of the Velde diagram (Fig. 2.13). The average compositions align with illite described by previous authors (Zhang et al. 2001; Laverett et al. 2006; Alexandre et al. 2009).

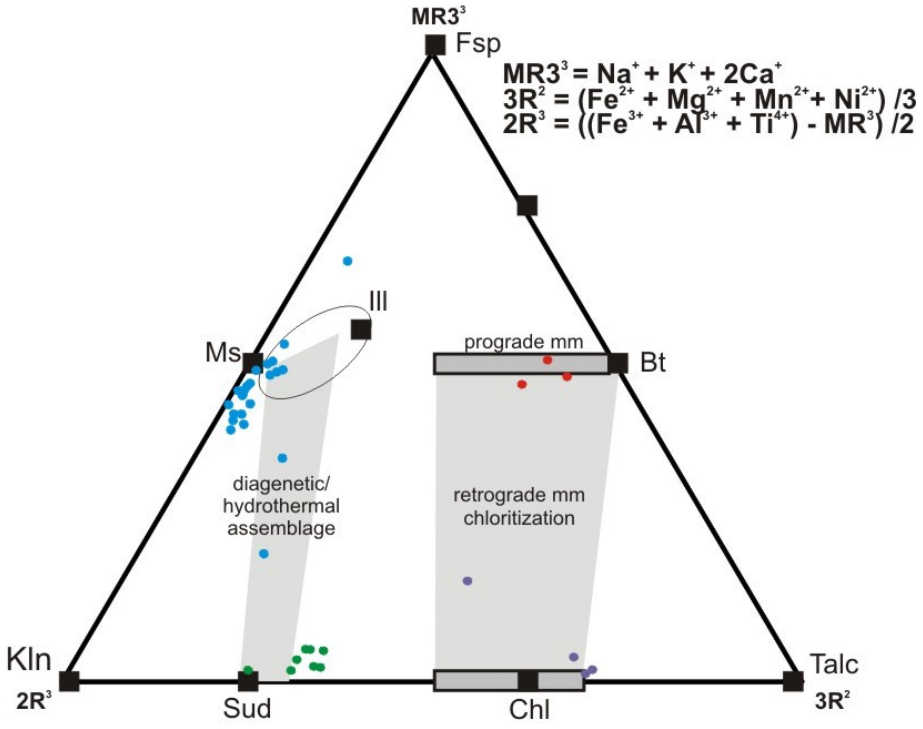

Figure 2.13. A Velde diagram (Velde, 1985) adopted from Quirt (2012) showing plotted atomic compositions of analyzed biotite (red), Fe-Mg chlorite (purple), sudoite (green) and illite (blue) from the basement rocks at McArthur River. mm = metamorphism/metamorphic

Most alteration phases described in rocks from the P2 fault follow the paragenetic sequence described above. The only minerals that occur along the P2 fault but are apparently absent from samples outside of the fault zone are dravite and magnesiofoitite. All rocks in this study fall within a regional dravite corridor (Jefferson et al. 2007 after Earle and Sopuck 1989) that is narrower and differs in position from the regional illite corridor. However, much of the "dravite" described by the previous researchers is reinterpreted here as magnesiofoitite (alkali deficient dravite; Rosenberg and Foit, 2006). The recognition of magnesiofoitite as a main alteration that was previously interpreted in the field as dravite opens the door to new opportunities for regional mapping. Evidence for an earlier green Fe-tourmaline (schörl) was observed in the P2 fault zone in that the cores of tourmaline grains are Fe-rich and the rims are dravite in composition. The dravite is

commonly replaced by illite and magnesiofoitite. Interestingly, inclusions of quartz in dravite have the same crystallographic orientation and similar degrees of fluorescence in CL-SEM (Fig. 2.14), suggesting that the quartz inclusions are relicts of larger grains that were replaced by the tourmaline. Magnesiofoitite formed after the second illitization event, possibly coeval with pyrite.

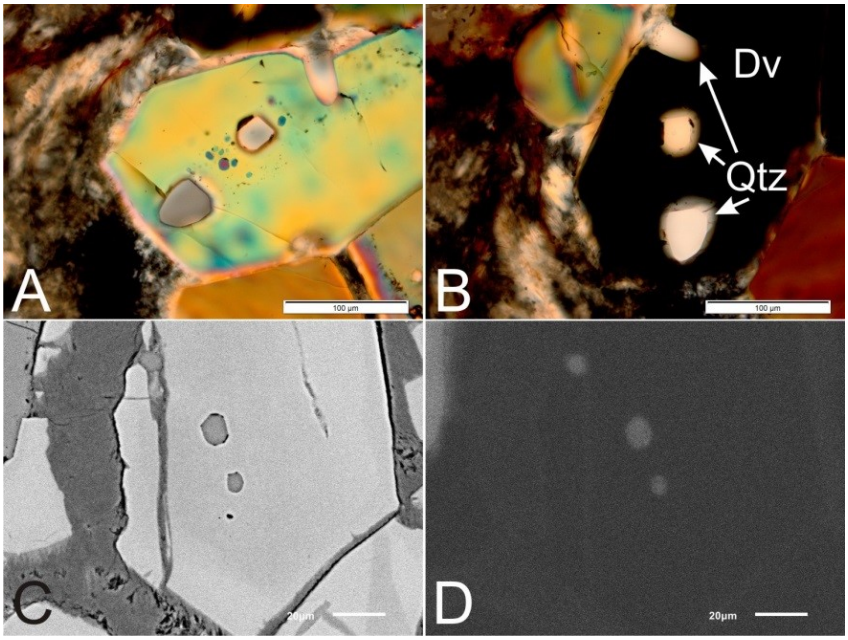

Figure 2.14. A&B) Photomicrograph (XPL) of dravite showing that quartz inclusions share the same crystallographic orientation as all inclusions are extinct (A) and transmit light (B) at the same orientation. **C&D)** Quartz inclusions in dravite (C) fluorescing while dravite did not (D).

The following paragenesis of alteration assemblages (Fig. 2.15) is listed chronologically and is based on the above petrography and geochemistry, which helps to reinterpret previous research:

i) Before the earliest alteration, the basement rocks contained quartz (Qtz^1), K-feldspar, biotite, cordierite, and garnet ± graphite ± pyrite ± schörl ± dravite;

ii) Fine-grained illite (Ill^1) replaced K-feldspar; Fe-Mg chlorite fragmented garnet, pseudomorphically replaced biotite (chlorite ± rutile) and crystallized as fine-grained acicular aggregates;

iii) Hematization (Hem^1) took place before silicification (Qtz^2) of Qtz^1;

iv) Sudoite (C^2) replaced Fe-Mg chlorite (C^1), garnet and cordierite;

v) Hematite (Hem^2) overprinted fine-grained illite; kaolinite probably formed from the destruction of fine-grained illite in the Red Zone;

vi) An illite recrystallization event (Ill^2, with minor Fe-Mg chlorite C^3) was focused along the unconformity, but illite also forms veinlets that cross-cut hematite alteration, illite overprinted kaolinite in the Red-Zone and Bleached Zones, and illite forms veinlets and aggregates that altered sudoite and pseudomorphed Fe-Mg chlorite in the Red Zone and Green Zone in the least-altered rocks.

vii) Magnesiofoitite altered dravite and illite, cross-cut Hem^1 hematite in veinlets, and possibly crystallized coeval with pyrite.

2.6.2 The source of alteration in the basement

All chemical data collected from illite, Fe-Mg chlorite, sudoite and biotite are presented in Figure 2.13 on a Velde (1984) diagram. According to Quirt (2012), Fe-Mg chlorite is a product of regional metamorphic retrogression and sudoite is an alteration product that developed during later hydrothermal activity. The textural evidence presented in this study shows that Fe-Mg chlorite was replaced by sudoite and both Fe-Mg chlorite and sudoite were illitize. It is possible that Fe-Mg chlorite originally replaced cordierite and garnet and was subsequently replaced by sudoite. However, cordierite is replaced by sudoite in samples where biotite and garnet are unaltered.

Cordierite was preferentially chloritized prior to biotite and garnet, which (in general) is very common. The coarse-grained dravite observed in the pegmatite and metapelite along the P2 is an alteration product of earlier schörl which formed during regional metamorphism and/or is the result of B-bearing pegmatitic fluids that concentrated along the P2 fault.

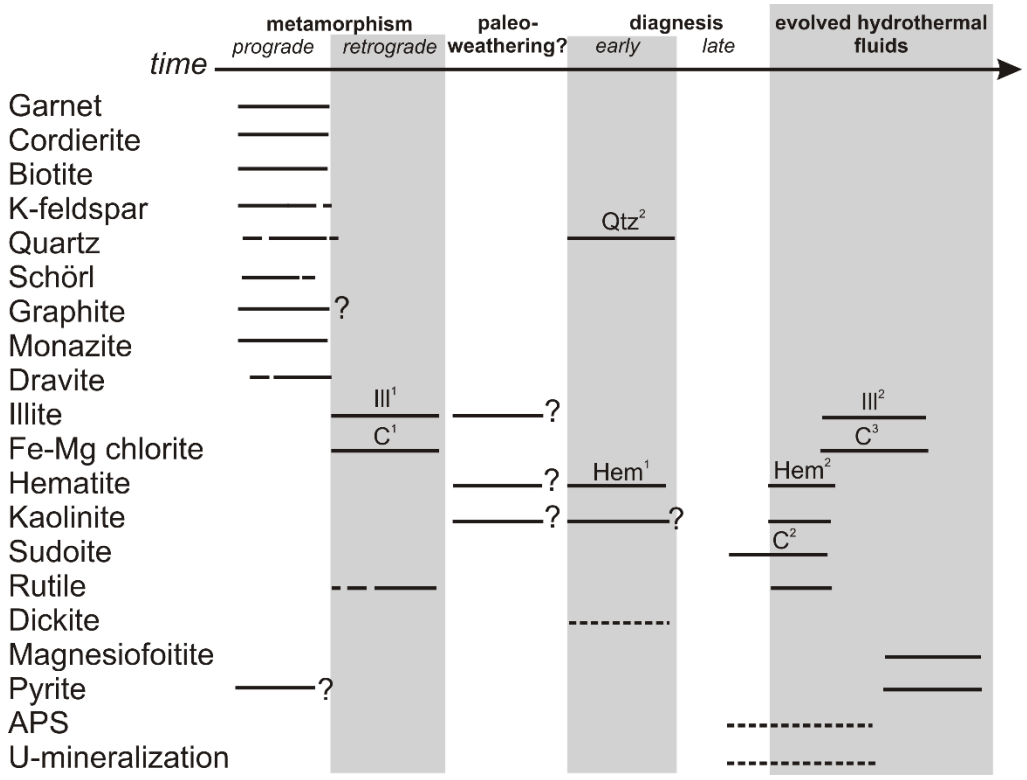

Figure 2.15. The paragenesis of alteration assemblages in the basement rocks at McArthur River. Dashed lines represent research of the Athabasca Basin rocks from Jefferson et al., (2007) and references therein.

Macdonald (1985) interpreted the Red Zone and the Green Zone as products of weathering of the basement. This is not supported by the paragenesis of the Red Zone described above. In the Red Zone, silicates (including sudoite) are overprinted by hematite or altered to form kaolinite. Therefore, sudoite formed before the pervasive hematization in the Red Zone. It is likely that the rocks underwent multiple hematization events including paleoweathering, early diagenesis and

later hydrothermal activity (post-sudoite). It was also noted in drill cores that hematitization is not restricted to the Red Zone but also extends upwards into the overlying conglomerate and sandstone units. Furthermore, in some deep drill-cores of basement rocks along the P2 (~200 m below the unconformity), wide (>10 m) zones of red hematite alteration are in contact with green alteration and bleaching that mimics the Bleached Zone, Red Zone, and Green Zone below the unconformity. Preserved hematite is also observed in basement Red Zone samples in this study. Multiple hematization events are recorded in the Athabasca Basin sandstones, with a 'primary' paleoweathering hematite, early diagenetic hematite generations preserved in overgrowths on detrital quartz grains and associated with clay development, and a late diagenetic-hydrothermal cement, Liesegang banding and discontinuous disseminations (Jefferson et al. 2007; Kyser et al. 2000; and references therein). Therefore, it is possible that the preserved hematite (Hem^1) between quartz grains is a product of paleo-weathering. But Hem^1 is more likely evidence for early diagenetic fluids that penetrated the basement rocks, because any alteration formed during the weathering of the basement rocks would have been overprinted by a diagenetic fluid from the overlying strata. It is probable that the pervasive hematization and kaolinite observed in the basement rocks of the Red Zone and in the Athabasca sandstones were formed by an oxidizing fluid during hydrothermal activity related to the diagenesis of the Athabasca Group and that this fluid may have been propagated along the P2 fault where it altered underlying basement rocks. It is also possible that the deeper basement hematite alteration along the P2 is due to an early diagenetic fluid.

The transition zone between the Green and Red Zones preserves fluid interactions where an oxidizing basinal fluid mixed with a reduced basement fluid. Many studies have suggested a reduced basement fluid as a reductant for uranium precipitation (Wilson and Kyser, 1987; Kotzer

and Kyser, 1995; Fayek and Kyser, 1997). The evolved fluid may have been enriched in Mg, permitting alteration of Fe-Mg chlorite to sudoite.

The Bleached Zone is discontinuous along the unconformity, and lenses of bleaching also occur in the Athabasca siliciclastic rocks. The bleached appearance is caused predominately by illite and kaolin-group minerals (kaolinite ± dickite). Illite is a late phase in the Bleached Zone as it cuts kaolin-group minerals. There are several possible sources of K. The Athabasca Group sandstones contain K-feldspar and mica, and the contents of K_2O exceed 5% locally (Card and Bosman, 2012). Alteration of feldspars likely released K_2O into basinal fluids. The second possible source of K is pegmatite bodies in the basement which contain coarse-grained K-feldspar (1 – 2 cm).

The Athabasca Basin evolved into a hydrothermal fluid dominated system. Magnesiofoitite is a late phase in the paragenesis of the basement rocks. The basinal fluid may have evolved to crystallize magnesiofoitite, or B was locally sourced from alteration of dravite-schörl in the basement rocks. It is interesting that magnesiofoitite has been documented throughout the Read and Manitou Falls Formations of the Athabasca Group and in the basement with high concentrations along the P2 fault (Quirt, 1991; Kotzer, 1993; Rosenburg and Foit 2006; Ng, 2012; this study).

2.7 Summary

The preliminary findings of this study suggest:

i) The alteration profile below the regional unconformity of the Athabasca Basin records the changes in fluid chemistry through fluid-rock interactions during evolution of the Athabasca basin. The Bleached Zone, Red Zone and Green Zone resulted from multiple events, including

paleoweathering, diagenesis and hydrothermal alteration. An early paleoweathering profile would have been overprinted by early diagenetic fluids and these events are evidenced by hematite rims wihtin quartz overgrowths in the Red Zone, which are very similar to diagenetic hematite-quartz overgrowths in the overlying sandstone units. The pervasive hematite in the Red Zone and along the P2 is the result of an oxidizing hydrothermal fluid that propagated along the unconformity, and along faults in the area, and overprinted late diagenetic-hydrothermal sudoite alteration in the Green Zone from a Mg-bearing basement fluid.

ii) The overlying Athabasca Basin conglomerate and sandstone units, and the granitoid basement rocks contributed K for the formation of ubiquitous illite in the basement (in agreement with Hoeve and Quirt 1984). Illite and kaolinite are most abundant along the discontinuous Bleached Zone. The Bleached Zone and other "bleached" basement rocks are interpreted to represent rock volumes subjected to sustained fluid flow and the dissolution of hematite as the Bleached Zone overprinted the Red Zone.

iii) The P2 fault in the McArthur River area was a focus for fluid flow during the evolution of a diagenetic-hydrothermal system. Most rocks along the fault are pervasively altered to fine-grained clay minerals. Previous authors have described a regional alteration "corridor" that trends 45°N and envelopes the P2 fault. The presence of this alteration corridor, the observation that alteration is strongest along the P2 fault, and the fact that the largest high-grade uranium ore deposit occurs along the P2 fault is evidence that the P2 fault allowed for multiple generations of basinal and hydrothermal fluids to enter the basement rocks below the Athabasca Basin.

References

Alexandre, P., Kyser, K., and Polito, P., 2003. Geochronology of the Paleoproterozoic basement-hosted unconformity-type uranium deposits in northern Saskatchewan, Canada; Uranium Geochemistry 2003, International Conference, Université Henri Poincaré, Nancy,France, April 13-16, 2003, Proceedings, p. 37-40.

Alexandre, P., Kyser, K., and Polito, P., and Thomas, D. 2005. Alteration mineralogy and stable isotope geochemistry of Paleoproterozoic basement-hosted unconformity-type uranium deposits in the Athabasca Basin, Canada; Economic Geology, v. 100, p.1547–1563.

Alexandre, P., Kyser, K., Jiricka, D., and Witt, G., 2012. Formation & Evolution of the Centennial Unconformity-Related Uranium Deposit in the South-Central Athabasca Basin, Canada; Economic Geology v. 107, p. 385 – 400

Annesley, I.R., Madore, C., and Portella, P., 2005: Geology and thermotectonic evolution of the western margin of the Trans-Hudson Orogen: evidence from the eastern sub-Athabasca basement, Saskatchewan; Canadian Journal of Earth Sciences, v. 42, p. 573-597.

Bronkhorst, D., Mainville, A. G., Murdock, G. M., Yesnik, L. D. 2012. McArthur River Operation Northern Saskatchewan, Canada: National Instrument 43-101 Technical Report.

Carl, C., Pechmann, E. V., Höhndorf, A., & Ruhrmann, G. 1992. Mineralogy and U/Pb, Pb/Pb, and Sm/Nd geochronology of the Key Lake uranium deposit, Athabasca Basin, Saskatchewan, Canada. Canadian Journal of Earth Sciences, v. 29 (5), p. 879-895.

Cumming, G. L., and Krstic, D., 1992. The age of unconformity-related uranium mineralization in the Athabasca Basin, northern Saskatchewan. Canadian Journal of Earth Sciences, v. 29 (8), p. 1623-1639.

Earle, S. and Sopuck, V.J., 1989. Regional lithogeochemistry of the eastern part of the Athabasca Basin uranium province, Saskatchewan, Canada; in Uranium Resources and Geology of North America, (ed.) E. Muller-Kahle; IAEA-TECDOC-500, p. 263-296.

Earle, S., Wheatley, K., and Wasyliuk, K., 1999. Application of reflectance spectroscopy to assessment of alteration mineralogy in the Key Lake area; MinExpo '96 Symposium - Advances in Saskatchewan geology and mineral exploration, Saskatoon, November 21-22, 1996, Proceedings, p. 109-123.

Fayek, and Kyser, 1997. Characterization of multiple fluid events and rare-earth-element mobility associated with formation of unconformity-type uranium deposits in the Athabasca Basin, Saskatchewan; Canadian Mineralogist v. 35, p. 627–658.

Fayek, M., Kyser, T. K., & Riciputi, L. R. 2002. U and Pb isotope analysis of uranium minerals by ion microprobe and the geochronology of the McArthur River and Sue Zone uranium deposits, Saskatchewan, Canada. The Canadian Mineralogist, 40(6), 1553-1570.

Hoeve, J., and Quirt, D. H., 1984. Mineralization and Host Rock Alteration in Relation to Clay Mineral Diagenesis and Evolution of the Middle-Proterozoic, Athabasca Basin, northern Saskatchewan, Canada; Saskatchewan Research Council, SRC Technical Report 187, 187 p.

Höhndorf, A., Lenz, H., Von Pechmann, E., Voultsidis, V., & Wendt, I. 1985. Radiometric age determinations on samples of Key Lake uranium deposits. Geology of uranium deposits. Special, v. 32, p. 48-53.

Jefferson, C.W., Thomas, D.J., Gandhi, S.S., Ramaekers, P., Delaney, G., Brisbin, D., Cutts, C., Portella, P. and Olson, R.A., 2007. Unconformity-associated uranium deposits of the Athabasca basin, Saskatchewan and Alberta; in EXTECH IV: Geology and Uranium

EXploration TECHnology of the Proterozoic Athabasca Basin, Saskatchewan and Alberta, (eds.) C.W. Jefferson and G. Delaney; Geological Survey of Canada Bulletin 588, p. 23-67.

Kotzer, T.G. 1993. Fluid history of the Prorerozoic Athabasca Basin, Ph D. thesis, University of Saskatchewan, Saskatoon, Saskatchewan.

Kotzer, T.G., and Kyser, T.K., 1995. Petrogenesis of the Proterozoic Athabasca Basin, northern Saskatchewan, Canada, and its relation to diagenesis, hydrothermal uranium mineralization and paleohydrogeology: Chemical Geology, v. 120, p. 45–89.

Kyser, K., Hiatt, E., Renac, C., Durocher, K., Holk, G., and Deckart, K., 2000. Diagenetic fluids in Paleo- and Meso-Proterozoic sedimentary basins and their implications for long protracted fluid histories; in Fluids and Basin Evolution, (ed.) K. Kyser; Mineralogical Association of Canada Short Course Series, v. 28, p. 225–262

Lewry, J.F., Sibbald, T. 1980 Thermotectonic evolution of the Churchill province in northern Saskatchewan. Tectonophysics v. 68 p.45–82

MacDonald, C., 1980. Mineralogy and geochemistry of a Precambrian regolith in the Athabasca Basin. Dissertation. University of Saskatchewan

Macdonald, C., 1985. Mineralogy and geochemistry of the sub-Athabasca regolith near Wollaston Lake. Geology of Uranium Deposits: Canadian Institute of Mining and Metallurgy Special v. 32, p. 155-158.

McGill, B., Marlatt, J., Matthews, R., Sopuck, V., Homeniuk, L., Hubregtse, J., 1993. The P2 North uranium deposit Saskatchewan, Canada. Exploration Mining Geology v. 2(4) p.321- 333

Ng, Ronald., 2012. Geochemical and mineralogical evolution of the McArthur Rive Zone 4 unconformity-related uranium ore body and application of iron oxidation state in clay alteration as indicator of uranium mineralization, M.Sc. thesis, Queen's University

Pagel, M., and Poty, B., and Sheppard, S.M.F., 1980. Contributions to some Saskatchewan uranium deposits mainly from fluid inclusions and isotopic data, in Ferguson, S. and Goleby, A., eds., Uranium in the Pine Creek geosyncline: Vienna, International Atomic Energy Agency, p. 639–654.

Percival, J.B., Bosman, S.A., Potter, E.G., Ramaekers, P., Venance, K.E., Hunt, P.A., Davis, W. and Jefferson, C.W., in press. Hydrothermal alteration in hydro-fractured Athabasca Basin sandstone: distal expression of uranium mineralization?; i*n* Uranium in Canada: Geological Environments and Exploration Developments, (eds.) E.G. Potter, D. Quirt and C.W. Jefferson; Exploration Mining and Geology v.21.

Quirt D H 2001. Kaolinite and Dickite in the Athabasca Sandstone, Northern Saskatchewan, Canada: Saskatchewan Research Council, Publication No. 10400-16D01, p. 27

Quirt D H 2012. Clay alteration mineralogy comparisons between the Athabasca and Thelon Basins- basement alteration. Presentation at the GEM-U workshop, St. John's, NF, May 30, 2012

Quirt D H, and Wasyliuk K 1997, Kaolinite, dickite, and other clay minerals in the Athabasca Group, Canada, and the Kombolgie Formation, Australia: 11th International Clay Conference, Ottawa, Ontario, June 1997, Proceedings, p. A61.

Ramaekers, P., Jefferson, C.W., Yeo, G.M., Collier, B., Long, D.G.F., Drever, G., McHardy, S., Jiricka, D., Cutts, C., Wheatley, K., Catuneau, O., Bernier, S., Kupsch, B and Post, R.T.,

2007. Revised geological map and stratigraphy of the Athabasca Group, Saskatchewan and Alberta; in EXTECH IV: Geology and Uranium EXploration TECHnology of the Proterozoic Athabasca Basin, Saskatchewan and Alberta, (eds.) C.W. Jefferson and G. Delaney; Geological Survey of Canada Bulletin 588, p. 155-192.

Rosenberg, P.E., and Foit, F.F., Jr., 2006. Magnesiofoitite from the uranium deposits of the Athabasca Basin, Saskatchewan; The Canadian Mineralogist, v.44, p. 959-965.

Velde B., 1985. Clay Minerals: a Physico Chemical Explanation of their Occurrence. Developments in Sedimentology No. 40. Elsevier, Amsterdam

Wasyliuk K., 2002. Petrogenesis of the Kaolinite-Group Minerals in the eastern Athabasca Basin of northern Saskatchewan: Applications to Uranium Mineralization: M.Sc. thesis, University of Saskatchewan, Saskatoon, Saskatchewan, 140 p.

Wilson, M.R., and Kyser, T.K., 1987. Stable isotope geochemistry of alteration associated with the Key Lake uranium deposit, Canada: Economic Geology, v. 82, p. 1540–1557.

Zhang, G., Wasyliuk, K., and Pan, Y., 2001. The characterization and quantitative analysis of clay minerals in the Athabasca Basin, Saskatchewan: application of short-wave infrared reflectance spectroscopy: Canadian Mineralogist, v. 39, p. 1347–1363.

Addendum

This chapter has been modified for grammatical errors since its publication in 2014. As suggested by an examiner of this thesis, Table 1 (below) is modified whereby biotite is normalized to 22 oxygens and cation totals are shown.

Table 1: EMPA chemical analyses of biotite and garnet in the least altered rocks from the base of drill-core MC3

	Sample (dept	3 (651.5 m)				9 (628.2 m)
	lithology	*least altered metapelite*				*chloritized metapelite*
	mineral	biotite	biotite	biotite	garnet	garnet
		x̄ σ	x̄ σ	x̄ σ	x̄ σ	x̄ σ
wt%	SiO_2	35.85 0.67	36.27 0.53	35.89 0.14	37.02 0.17	36.74 0.12
	TiO_2	3.66 0.65	1.30 0.80	3.90 0.16	0.01 0.01	0.00 0.00
	Al_2O_3	20.41 2.24	19.51 0.51	18.99 0.18	21.45 0.09	21.26 0.07
	FeO	18.44 2.02	16.59 1.75	19.38 0.22	33.78 0.20	34.31 0.11
	MnO	0.04 0.01	0.04 0.01	0.04 0.02	1.32 0.04	2.86 0.07
	ZnO	0.04 0.03	0.07 0.04	0.05 0.02	nd	nd
	MgO	8.58 0.76	12.82 1.76	9.08 0.05	5.05 0.10	3.97 0.10
	CaO	bdl	bdl	bdl	0.98 0.02	0.93 0.01
	Na_2O	0.10 0.02	0.24 0.12	0.09 0.01	0.02 0.01	0.02 0.01
	K_2O	8.87 1.32	9.10 0.48	9.77 0.21	0.00 0.00	0.00 0.01
	P_2O_5	nd	nd	nd	0.05 0.02	0.10 0.04
	Cl	0.06 0.01	0.04 0.02	0.07 0.00	nd	nd
	BaO	0.03 0.02	0.06 0.03	0.06 0.03	nd	nd
	F	0.33 0.06	0.54 0.07	0.40 0.02	nd	nd
	Total	96.27 1.94	96.36 0.47	97.54 0.37	99.68 0.43	100.20 0.22
	Fe/Fe+Mg	0.55	0.42	0.54	0.79	0.83
apfu						
	Si	5.35	5.39	5.36	2.96	2.95
	Ti	0.41	0.15	0.44		
	Al	3.59	3.42	3.34	2.02	2.01
	Fe	2.30	2.06	2.42	2.26	2.31
	Mn	0.00	0.00	0.00	0.09	0.19
	Mg	1.91	2.84	2.02	0.60	0.48
	Ca	0.00	0.00	0.00	0.08	0.08
	Na	0.03	0.07	0.03		
	K	1.69	1.73	1.86		
	∑	15.29	15.64	15.46	8.02	8.02
	F	0.15	0.23	0.19		
	O*	21.93	21.89	21.82	12.00	12.00

*atom proportions normalized to O = 21 for biotite ($O_{20}(OH)_4$) and O = 12 for garnet.;
SrO below detection limits (bdl); na = no data

CHAPTER 3.

Compositional variation and timing of aluminum phosphate-sulfate minerals in the basement rocks along the P2 fault and in association with the McArthur River uranium deposit, Athabasca Basin, Saskatchewan, Canada

Erin E. Adlakha and Keiko Hattori

American Mineralogist, v. 100(7), 1386-1399

Abstract

The Athabasca Basin hosts world class uranium deposits, such as the McArthur River deposit. This paper presents the occurrence of aluminum phosphate-sulfate (APS) minerals in the metasedimentary rocks along the P2 fault, the main ore-hosting fault of the McArthur River deposit. It compares the APS minerals along the P2 fault with those outside the fault, examined in this study, and those from other deposits of the Athabasca Basin and from other Paleo- to Mesoproterozoic basins worldwide.

APS minerals are common along the P2 fault but rare outside of the P2 fault zone in the basement and along the unconformity between the Athabasca sandstones and the basement. The APS minerals along the P2 fault occur with sudoite (± illite, magnesiofoitite) and are zoned with Sr-, Ca- and S-rich cores (solid solution between svanbergite, crandallite and goyazite) and LREE- and P-rich rims (close to florencite composition). APS minerals in the Bleached Zone (altered rocks along the unconformity consisting predominantly of kaolin and illite) are Sr-, Ca- and S-rich (high svanbergite component) and occur with kaolin. APS minerals in the Red-Green Zone (mingled red hematitic and green chloritic basement rocks below the Bleached Zone) occur with sudoite and clinochlore. They contain relict cores of LREE- and As-rich arsenoflorencite-(Ce) and rims of svanbergite-goyazite-crandallite solid solution.

The occurrence of svanbergite-crandallite-goyazite along the unconformity suggests their formation by relatively oxidizing fluids during diagenesis of the overlying sandstones. The relict cores of arsenoflorencite-(Ce) in the Red-Green Zone are interpreted to be the product of paleo-weathering before the deposition of the Athabasca sandstones. Florencitic APS minerals are found along the entire studied strike length (7 km) of the P2 fault, including the ore zone and non-mineralized areas, but are absent outside the fault zone. The florencitic APS minerals contain low

SO_4^{2-} in the ore zone, suggesting relatively reducing conditions during their crystallization. Zoned APS minerals (with svanbergitic cores and florencitic rims) proximal to ore contain elevated U (up to 16 ppm). These features suggest that diagenetic, oxidizing, and uranium-bearing fluids travelled along the P2 fault and became relatively reducing, especially within the ore zone. It also suggests florencitic APS minerals are contemporaneous with uranium mineralization. The restricted occurrence of florencitic APS mineral along the P2 fault in the basement suggests their use in identifying fertile basement structures associated with uranium mineralization.

3.0 Introduction

The Athabasca Basin hosts numerous large uranium deposits (Fig. 3.1), which are classified as unconformity-related uranium deposits. The prevalent model for mineralization was first proposed by Hoeve and Sibbald (1978) and modified later by many researchers (e.g. Alexandre et al. 2005; Derome et al. 2005; Richard et al. 2011; Mercadier et al. 2012). This model suggests that sea-water derived, uranium-bearing oxidizing brines (25-35 wt.% eq. NaCl) precipitated uranium ore at the unconformity when it reacted with a reducing fluid of currently unknown origin. Many deposits occur in the proximity of deformation zones in the basement and it is suggested that re-activated basement faults served as conduits for uranium-bearing fluids (Jefferson et al. 2007) or reducing basement fluids to reach the unconformity (McGill et al. 1993). The McArthur River deposit, the largest discovered high-grade (average grade of 16.46 %U_3O_8; Bronkhorst et al. 2012) uranium deposit on Earth, is situated along the P2 fault, a 13 km long reverse fault constrained to graphitic metapelite below the Athabasca Basin. Although geophysical and structural studies have been carried out on the P2 fault (e.g., Hajnal et al., 2010), the exact role of the fault in the mineralization remains uncertain.

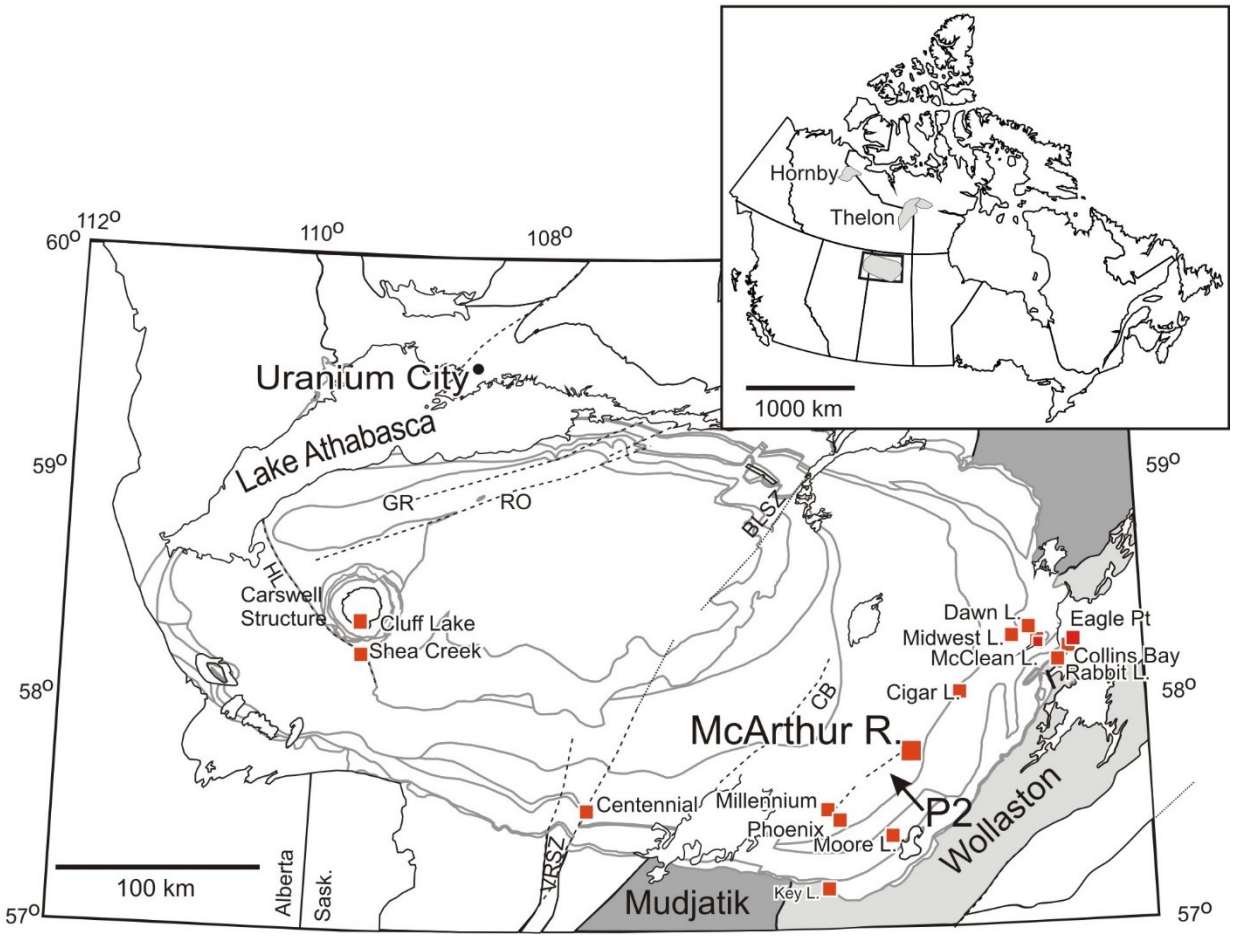

Figure 3.1. A map showing the location of the major uranium deposits (squares), including McArthur River deposit, and basement structures (dashed lines), including the P2 fault, in the Athabasca Basin (modified from Jefferson et al., 2007). The south-eastern margin of the Athabasca Basin is underlain by the basement rocks of the Wollaston and Mudjatik Domains of the western Churchill Province. An insert shows the locations of the Athabasca basin relative to other two Mesoproterozoic sedimentary basins: Hornby and Thelon basins. Major shear zones: BB = Black Bay, BLSZ= Black Lake Shear Zone, CB = Cable Bay, GR = Grease River Shear Zone, RO = Robbilard, VRSZ = Virgin River Shear Zone.

In the Athabasca and Thelon basins of Canada, aluminum phosphate-sulfate (APS) minerals (also known as alumino-phosphate sulfate) spatially associated with uranium deposits have been reported (Quirt et al. 1991, Gall and Donaldson 2006, Gaboreau et al. 2007, Riegler et al. 2014). APS minerals occur in a variety of environments (Dill, 2001) and form many solid

solution series with over 40 end-members (Jambor 1999; Stoffregen et al. 2000; Dill 2001). APS minerals have the general formula: $AB_3(XO_4)_2(OH)_6$, where A = mono-, di-, tri- or, more rarely, tetravalent cations (K^+, Na^+, Rb^+ , Ca^{2+}, Sr^{2+}, REE^{3+}, Th^{4+} etc.); B = trivalent cations (Al^{3+}, Fe^{3+}); and X = P^{5+}, S^{6+}, or As^{5+}. Since the incorporation of ions with different valences requires coupled substitution to accommodate charge balance, compositional zoning of APS minerals is commonly well preserved. This makes APS minerals excellent candidates for evaluating the chemical and physical characteristics of fluids from which they formed (Dill 2001; Beaufort et al. 2005; Gaboreau et al. 2005, 2007).

The focus of this paper is to present the occurrence and compositional variation of APS minerals in basement rocks along the P2 fault, discuss the role of the fault during mineralization, and the timing of APS mineral formation with respect to uranium mineralization. In addition, the chemistry of APS minerals is compared with those along and outside of the fault zone in the basement, from other APS minerals studied in the Athabasca Basin (within deposits or not), and from other Paleo- to Mesoproterozoic basins worldwide. The potential use of APS minerals in exploration for unconformity-related uranium deposits is also discussed.

3.1 Geological Setting

3.1.1 Regional Geology

The basement rocks in the eastern Athabasca Basin area are part of the Wollaston Supergroup and Mudjatik domain. The Wollaston Supergroup consists of metapelite, metasemipelite, meta-arkose, calc-silicate and quartzite (e.g., Annesley et al. 2005). They were metamorphosed under upper amphibolite to lower granulite conditions during the Trans-Hudson Orogeny (ca. 1.8-1.9 Ga; Lewry and Sibbald 1980, McKechnie et al. 2012). Abundant granitic

pegmatite lenses intruded the metasedimentary rocks during peak metamorphism (Annesley et al. 2005; Jefferson et al. 2007).

Alteration immediately below the unconformity is laterally extensive and consists of a deeper Green Zone with sudoite (Al-Mg chlorite) and illite ± Fe-Mg chlorite, a transitional Red-Green Zone with illite, sudoite and hematite, an upper Red Zone with hematite and kaolin ± illite, and, locally, there is Bleached Zone of kaolin and illite, immediately beneath the unconformity (Macdonald 1985; Quirt 2001; Adlakha et al. 2014). In addition to the Red-Green transitional Zone, the Red and Green Zones are mingled in places. The origin of these Zones has been in discussion. Macdonald (1985) considered them as the products of paleo-weathering before sandstone deposition, whereas Cuney (2003) proposed their formation after the deposition of sandstones. Quirt (2001) and Adlakha et al (2014) pointed out extensive overprinting of alteration minerals by subsequent hydrothermal fluids, which makes it difficult to determine the condition of their initial crystallization. Rocks of the Bleached Zone are altered to white due to loss of hematite and interpreted to be a reaction product of the Red Zone with late diagenetic fluids from the overlying basin (Macdonald 1985; Quirt 2001). The least-altered metapelite occurs > 50 m below the unconformity and away from faults.

The sedimentary rocks of the Athabasca Group are comprised of dominantly fluvial to shallow marine, quartz pebble conglomerate and quartz arenite, with a preserved maximum thickness of 1500 m in the centre of the basin (Ramaekers et al. 2007). Early diagenesis included silica cementation on hematite-dusted detrital quartz grains (Hoeve and Quirt 1984; Jefferson et al. 2007), alteration of kaolinite by dickite with minor illite and locally traces of sudoite (Quirt 2001; Laverret et al. 2006). Uranium deposits are localized near the intersection of the unconformity and basement faults or down-dip along these faults into the basement. These deposits are surrounded

by alteration haloes of sudoite, illite and magnesio-foitite (alkali-deficient dravite). Sandstone-hosted unconformity-type deposits show the inner halo of sudoite with an outer alteration halo of illite (e.g., Hoeve et al. 1981; Hoeve and Quirt 1984; Alexandre et al. 2012). Basement-hosted unconformity-type deposits are accompanied by the inner alteration halo of illite and the outer halo of sudoite. The different proportions of sudoite and illite between two types of unconformity-type deposits are considered to be related to differences in fluid circulation (i.e. Ingress vs Egress; Hoeve and Quirt 1984).

3.1.2 Structure and alteration of the McArthur River deposit and P2 fault

The McArthur River deposit is comprised of six ore bodies, Zones 1-4 and Zones A and B, which collectively have a strike length of approximately 1.7 km near the intersection of the P2 fault (~050°/45-60°) and the unconformity, ~500 m below surface (Fig. 3.2) (McGill et al. 1993; Alexandre et al. 2005; Bronkhorst et al. 2012). The total reserves of the McArthur River deposit as of August 31, 2012, were 385.5 Mlbs U_3O_8 (Bronkhorst et al. 2012). All ore bodies are hosted in the sandstone immediately above the unconformity except for the Zone 2 ore body which occurs immediately below the unconformity and is bounded by the vertical quartzite (VQ) fault and ~140° trending series of cross faults (Fig. 3.2b). Late minor remobilizations of uraninite formed veinlets and fractures with pyrite, chalcopyrite and minor nickel-cobalt sulfarsenides (McGill et al. 1993).

The P2 fault zone is a series of reverse faults with a strike length of approximately 13 km (McGill et al. 1993) and has been traced seismically at least 2 km below the unconformity (Hajnal et al. 2010). In the basement, the several fault planes of the P2 fault are mostly constrained to graphite-bearing metapelite and trend parallel to the basement foliation (McGill, 1993). Reactivation of P2 faulting formed differences in the thickness of the basal conglomerate at the unconformity and broad fracture and breccia zones in the sandstones. The reverse movement of the

P2 fault raised a wedge of basement rocks above the unconformity with vertical displacement of up to 80 m (McGill et al. 1993; Figs. 3.2a,b). The basement wedge is also referred to as the "middle block" by workers (Bronkhorst et al. 2012) as it is offset by differential movement of fault planes (Figs 3.2a,b). These offsets commonly host the uranium mineralization of McArthur River deposit and sporadic occurrences of low-grade (<1 $\%U_3O_8$) mineralization along the P2 fault (Fig. 3.2a). The P2 fault and basement rocks show minor lateral displacement by three sets of steeply dipping faults that strike 100 – 110° in the mine-site area (Fig. 3.2b). These faults and offsets likely provided pathways for mineralizing fluids, but also truncate high-grade zones, especially the Zone 2 ore body (Fig. 3.2b; McGill et al. 1993; Bronkhorst et al. 2012).

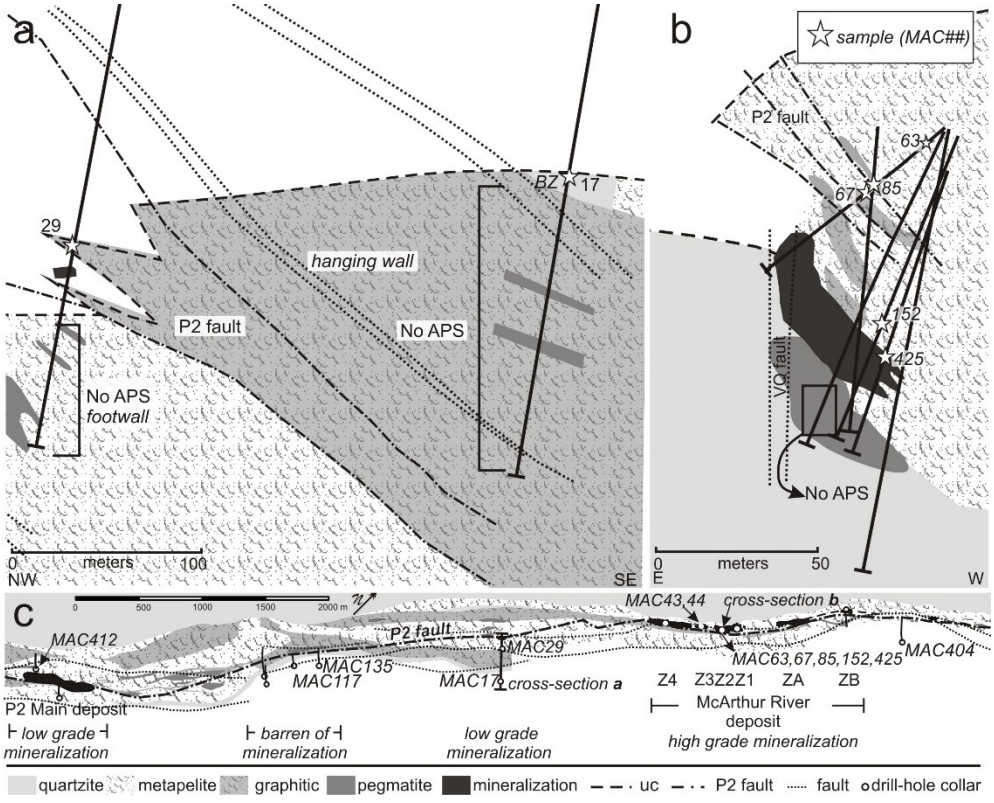

Figure 3.2. Schematic cross-sections **(a, b)** showing the distribution of APS minerals, sample locations (stars), and a geologic map **(c)** at the unconformity showing drill-hole locations. **(a)** APS minerals are found in the P2 fault proximal to low-grade mineralization (sample

MAC29) and in the Bleached Zone (BZ) in quartzite (sample MAC17); (**b)** APS minerals are found in the P2 fault proximal to the Zone 2 ore body (samples MAC63, 67, 85, 152, 425). APS minerals were not found in samples from the footwall and hanging-wall (indicated ``No APS``) nor in samples collected from the VQ fault. **(c)** An interpreted geological strip map at the unconformity showing the P2 fault, the locations of sampled drill-holes and ore bodies, sample locations, and the sites of the cross sections (a,b). The P2 fault is essentially barren in the southwestern part. Low-grade mineralization occurs along the middle and southeast (P2 Main deposit) portions of the P2 fault. APS minerals were found in one sample (sample MAC412) of the Red-Green Zone in the footwall proximal to the P2 Main mineralization. Z1 - 4 = Zone numbers of ore body at the McArthur River deposit; uc = unconformity. Cross-sections and map were modified from Cameco internal reports.

Basement rocks along the P2 fault were intensely altered to form sudoite, illite, magnesio-foitite, Fe-Mg chlorite, and sulfides (McGill et al. 1993; Adlakha et al. 2014). The hanging wall basements rocks, including the ore-hosting wedge, commonly show intense alteration forming sudoite and illite ± kaolin. Illite and/or kaolin gives the rocks a creamy white colour, and this alteration is called "bleaching". Bleaching is common, especially in close proximity to the fault, mineralization and the unconformity (McGill et al. 1993). The most intense alteration of the basement rocks is found in close proximity to the Zone 2 ore body where sudoite and magnesiofoitite are the dominate alteration minerals (Adlakha et al. 2014). In comparison, illite with minor sudoite are the dominate alteration minerals in the moderately altered basement rocks in unmineralized areas (the south-west portion of the P2 fault) and near the weakly mineralized P2 Main deposit (Fig. 3.2b), that is "perched" higher in sandstones. APS minerals only occur in highly altered rocks where primary metamorphic minerals and textures are altered.

3.2 Sampling

A total of 192 samples of metasedimentary rocks, predominately metapelites with fewer pegmatite and quartzite, were collected from 27 different drill-holes along, and within proximity

to, the P2 fault zone from the McArthur River mine site to ~7 km southwest (Fig. 3.2c). Of these, 139 samples were selected for examination of APS minerals in thin sections. Out of the 139 samples, APS minerals were found in only 17 samples. Among these 17 samples, APS minerals in 4 samples were too small for quantitative analysis with electron microprobe analyzer (EPMA). Of the remaining 13 samples (Table 3.1), nearly all were from metapelites located along the P2 fault (11 of 13) that showed intense/pervasive alteration in which clay-sized minerals replaced most metamorphic minerals and metamorphic textures were obliterated by alteration, fractures and/or veinings. In this paper, samples collected within 50 m of the centre of the fault are considered to be associated with P2 fault, as the fault is accompanied by splay structures and alteration extending outside the fault zone.

The samples associated with the P2 fault were collected from varying distances to the McArthur River uranium deposit (Fig. 3.2c; Table 3.1). MAC425 was collected within the Zone 2 ore body (Fig. 3.3A), MAC152 < 15 m from the Zone 2 ore body, MAC67 (Fig. 3.3b) and MAC85 < 20 m from the Zone 2 ore body, MAC63 < 50 m from the Zone 2 ore body, MAC43 and MAC44 <50 m from the Zone 3 ore body. MAC29 was within 1 m of low grade (< 1 wt% U_3O_8) uranium mineralization disseminated within the sandstone (Fig. 3.2a), MAC404 was approximately 50 m from low grade uranium mineralization within the sandstone. MAC117 and MAC35 are >500 m away from low grade uranium mineralization in the sandstone, >1 km from the low grade P2 Main deposit and > 2 km from the McArthur River deposit.

Although 5 samples from the Bleached Zone were examined in detail, APS minerals were found only in one sample (MAC17; Fig. 3.3c) of quartzite along the unconformity, > 250 m from low grade mineralization and > 1 km from the McArthur River deposit (Fig. 3.2a,c). Twenty-two samples of metasedimentary rocks of the Green, Red-Green and Red Zones outside the P2 fault

were examined and APS minerals were found only in one sample (MAC412) of strongly hematized and chloritized metapelite from the Red-Green Zone in the footwall near the P2 Main deposit (Figs. 3.2c, 3.3d). Here we use field terminology “Bleached Zone” and the “Red-Green Zone” to reflect the samples position within the basement rocks as these terms are commonly used by geologists in the area. The Bleached Zone occurs along the unconformity and it refers to a creamy-white colored zone where kaolin and illite predominate. The Red-Green Zone is a physical mixture of hematitic Red Zone and chloritic Green Zone.

3.3 Methods

Thin sections were examined using an optical petrographic microscope with reflected and transmitted light sources. Due to the very fine-grained nature of minerals in the samples, detailed textural analysis was also carried out on carbon-coated polished thin sections using a JEOL 6610LV scanning electron microscope (SEM) at the University of Ottawa. Minerals were identified using energy-dispersive spectroscopy with the spectrum acquisition time of 40 s and an accelerating voltage of 20 kV.

Quantitative analysis for the major and minor elemental compositions of the APS minerals was carried out using a JEOL 8230 EMPA at the University of Ottawa. APS minerals were analyzed at an accelerating voltage of 15 kV and under a beam current of 20 nA using a focused beam of 5 μm (to account for alkali migration). Counting times were 20s on-peak and 10s off-peak for all elements except for S (10s on and 5 s off), F (50s on and 25s off), Pr (20s on and 5s off) Cl (25s on 12s off), P (10s on and 5s off), Si (10s on and 5s off) and As (20s on and 20 s off). The mineral standards used were sanidine (Si, Al, K), hematite (Fe), apatite (Ca, P, F), albite (Na), tugtupite (Cl), celestine (Sr, S), synthetic $NdPO_4$ (Nd), PrPO4 (Pr), $CePO_4$ (Ce), $LaPO_4$ (La), ThO_2 (Th) and GaAs (As). The elemental concentrations were calculated after matrix interference

correction using ZAF. Elemental maps of selected APS grains were acquired at an accelerating voltage of 10 kV with a 10 nA current at a counting time of 0.5 s per pixel with a total of 10000 pixels per image.

APS minerals are small (mostly < 20 μm, rarely up to 40μm) and surrounded by quartz and fine-grained alteration minerals (Fig. 3.4; Tables 3.1 and 3.2), but it was necessary to use a broad electron beam of 5 μm to minimize the loss of alkalis from APS minerals during the EPMA analysis. This made it unavoidable for the surrounding minerals to contribute to the analytical results. To evaluate the possible contributions of surrounding minerals in the chemical composition obtained for the APS, their compositions were measured by EMPA. The contents of SiO_2 were used to monitor the contribution of surrounding minerals because APS minerals rarely contain Si. For the data showing Si, the amounts of K, Al, and Na of the surrounding phases were subtracted from the analytical results. For example, for Al_2O_3 using the equation, $Al_2O_{3APS\ corrected} = Al_2O_{3APS\ analyzed} - (SiO_{2APS\ analyzed} * Al_2O_{3matrix}/SiO_{2matrix})$. The remaining concentration values were normalized to the original analytical total. Table 3.2 shows the contents of SiO_2 before subtracting the contribution of surrounding minerals. The contribution of surrounding minerals never exceeded 5% of the total.

Trace element contents in the APS minerals were determined using polished thick (>60 μm) sections by laser ablation inductively coupled plasma mass spectrometer (LA-ICP-MS) at the Geological Survey of Canada, Ottawa, using a Photon-Machines Analyte193 ArF excimer laser (λ = 193 μm) with Helex ablation cell and Agilent 7700x quadrupole ICP-MS. Helium gas was used to transport ablated sample from the ablation cell and was mixed with Ar plasma (flow rate of 1.05 mL/min) via a T-connector before entering the ICP. The detailed operating conditions for the LA-ICP-MS instrument and the isotopes quantified are listed in Appendix Table A3.1.

Table 3.1. Sample descriptions.

zone[a]	DDH[b]	sample	depth[c]	proximity to P2 fault[d]	proximity to uc[d]	proximity to U-min[d]	degree of alteration and rock-type[d]	APS occurrence	clay[c]	mineralogy[c]
P2	MC370	MAC29	560.2	in the P2 fault zone	u/c (Fig. 2A)	<1 m from lg U-min in ss	moderately altered mp	isolated, 3-10 µm	Sud	Mgf, Xtm, Qz
	H729	MAC43	49.5	in the P2 fault zone	~15 m	<50 m from Z3 ore	green intensely altered graphitic mp	isolated, 3-10 µm	Sud/Ilt	Mgf, Gr, Py, Ap, Zrn, Xtm
	H729	MAC44	64.5	~15 m laterally from P2 in fw	~15 m	<50 m from Z3 ore	red and white intensely altered peg	zoned, clustered, 5-20 µm	Sud/Ilt	Hem, Mnz, Zrn, Qz, Gr, Py
	H201	MAC63	7.6	~30 m laterally from P2 in hw	~20 m	<50 m from Z2 ore	green intensely altered mp	zoned, clustered, fragmented, 1-20 um	Sud	Ilt, Rt, Ap, Fe-Mg Chl, Ilt, Py, Qz
	H201	MAC67	30.8	the P2 fault zone	~20 m	<20 m from Z2 ore	green intensely altered peg	zoned, clustered, 5-20 µm	Sud	Mgf, Ilt, Py, Ap, Qz
	H493	MAC85	17.7	in the P2 fault zone	~20 m	<20 m from Z2 ore	intensely altered graphitic mp w/ peg boudins	zoned, disseminated, 5-20 µm	Sud/Ilt	Drv, Py
	H203	MAC152	62	in the P2 fault zone	~50 m	<15 m from Z2 ore	green-white intensely altered mp	zoned, disseminated, 5-30 µm	Sud/Clc	Mgf, Ill, Py, Qz, Ccp
	MC410	MAC404	542.7	~50 m laterally from P2 in hw	~15 m	~50m laterally from lg in ss	red moderately altered mp w/ peg boudins	disseminated, < 1 µm	Kln	Hem, Ap
	H3380	MAC425	57.1	in the P2 fault zone	~50 m	Z2 ore	green intensely altered mp with U-ore	some cores missing, isolated, 3-10 µm	Mgf/Sud	U, Hem
	MC361	MAC117	523.3	in the P2 fault zone	~25 m	>500 m from U-min	white-green intensely altered peg	isolated, 3-10 µm	Ilt	Fe-Mg Chl, fg Qz, Qtz
	MC362	MAC135	520.2	~40 m above P2 in hw	~10 m	>500 m from U-min	red-green intensely altered peg	disseminated, < 1 µm	Ilt	Hem, Rt, fg Qz
GRZ	MC346	MAC412	669	~100 m laterally from P2	~50 m	~100 m below P2 Main	red-green intensely altered mp	large clusters up to .5 mm, 10-40 µm	Sud/Clc	Hem
BZ	MC344	MAC17	499.4	~250 m laterally from P2 in hw	<1 m	>250 m from U-min	quartzite with bleached matrix	disseminated, < 1 µm	Kln	Ilt, Zrn, Qz

Notes:

[a]P2 = P2 fault sample; RGZ = Red-Green Zone sample; BZ = Bleached Zone sample

[b]DDH= diamond dril-hole number

[c]drillhole with the prefix H are collared underground, therefore sample depths are not from the surface

[d]U-min= uranium mineralization in the McArthur River deposit; fw= footwall; hw = hangingwall; lg = low-grade (<1 wt% U_3O_8); ss = sandstone; uc = unconformity; peg = pegmatite; mp = metapelite

[e]Ap = apatite; Clc = clinochlore; Dck = dickite; Drv = dravite; Fe-Mg chl = Fe-Mg Chlorite; fg = fine-grained; Gr = graphite; Ilt = illite; Mgf = magnesiofoitite, Py = pyrite; Qz = quartz; Rt = rutile sud = sudoite, U = uraninite; xtm = xenotime; zrn = zircon

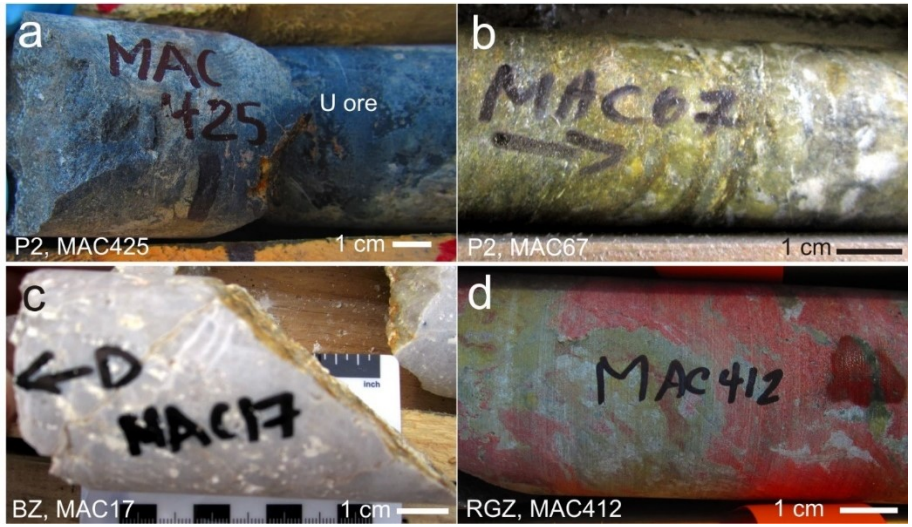

Figure 3.3. Photographs of selected drill-core samples; **(a)** uranium ore of the Zone 2 ore body and P2 fault (MAC425); **(b)** intensely sudoite-altered pegmatite from the P2 fault (MAC67); **(c)** quartzite from the Beached Zone along the unconformity (MAC17); and **(d)** hematitized and chloritized metapelite from the Red-Green Zone (MAC412). Sample locations are shown in Fig. 3.2.

During analysis, ~40 s of background signal with the laser turned off was collected and then ablation was performed by a laser focused to 10 μm for a data acquisition time of ~60 s (total time of 100 s for one analysis) for a total time of 100 s for one analytical cycle. The isotope counts were monitored during the analysis, and the acquisition time for the data of APS minerals was adjusted (Appendix Fig. A3.1). Aluminum contents are similar among grains of APS minerals and Al does not vary between the core and rim of APS minerals (Table 3.2). Therefore, the elemental concentrations were obtained based on the count ratios of elements to the average Al in the sample (determined by EMPA; Table 3.2) and the reference NIST610 (National Institute of Standards and Technology) (Longerich et al. 1996). The average Al content was used as the same grains could not be analyzed both by EPMA and LA-ICP-MS because the electron beam decomposes APS minerals (Appendix Fig. A3.2). EMPA and LA-ICP-MS data are comparable (Appendix Fig. A3.3). There is no international standard that has the composition similar to APS minerals. Therefore, the standard NIST610 was used as it contains high Al and it is the most used standard. One round of LA-ICPMS analysis consisted of seven analyses of grains, bracketed by two analyses of the NIST610 reference and one analysis of the BCR2G (Basalt, Columbia River) reference from the USGS. The analysis of NIST610 shows a counting precision of > 98 % for all elements. Accuracy, determined by BCR2G, was > 90 % for all elements except for Sc, Ti, Fe, Zn, Ce, Pr, Sm, Ho, Lu, Gd, Tb, Pb and Th which were > 85 % and Cu, Y, Zr, Cr, Tm, Yb and Hf which were > 75%.

3.4 Results

3.4.1 Mineral occurrence and distribution

APS minerals were found along the entire 7 km section of the P2 fault examined (Fig. 3.2). APS minerals were found only in one sample from the Bleached Zone (sample MAC17 in quartzite) (Figs. 3.2a, 3c, 4i; Table 3.1). APS minerals are rare in the basement rocks distal from the

unconformity and outside the P2 fault. They were found in only one sample (sample MAC 412) of the Red-Green Zone in the footwall 100 m from the P2 fault, 50 m below the unconformity and 100 m away from uranium mineralization (Figs. 3.3d and 4h; Table 3.1). APS minerals were not observed in samples along the VQ fault (Fig. 3.2b) or in samples of the least-altered basement rocks.

APS minerals along the P2 fault occur together with fine-grained sudoite and/or illite intergrown with magnesiofoitite (Adlakha et al. 2014; Figs. 3.4a-f). In the Bleached Zone sample, APS minerals occur with kaolin and illite (Fig. 3.4i). APS minerals in the transitional Red-Green Zone occur predominately with clinochlore (Fig. 3.4h).

APS minerals are small (mostly < 20 μm, rarely up to 40 μm), transparent, pseudo-cubic (rarely hexagonal) crystals, disseminated and/or clustered in fine-grained clay minerals (Fig. 3.4). There is no evidence of dissolution between APS minerals and surrounding clay minerals. The texture suggest that they are in equilibrium (Figs. 3.4a-j,l). APS minerals are commonly zoned. Zoning may be observed using plane polarized light microscopy as some cores show high relief. SEM BSE-images commonly show darker cores with lighter rims (Fig. 3.4c), although grains with lighter cores and darker rims are also observed (Fig. 3.4h). Darker parts in BSE images are due to greater amounts of Sr and Ca, and brighter parts contain higher LREE.

In all samples, APS minerals commonly occur in contact and/or are spatially associated with zircon (Figs. 3.4f,g), primary apatite (Fig. 3.4l), or sulfide minerals, such as pyrite (Fig. 3.4k) and lesser chalcopyrite (Fig. 3.4d). Zircon grains associated with APS minerals are commonly fractured and/or partially dissolved and rimmed by xenotime (cf. Quirt et al. 1991) (Fig. 3.4g). Apatite forms subhedral, rounded crystals. APS minerals also occur with small hydrothermal fluorapatite crystals. APS minerals commonly contain inclusions of sulfides or Fe-oxide (Figs. 3.4h,k,l). APS minerals in the Zone 2 ore body are in close proximity (within the same thin section) with uraninite.

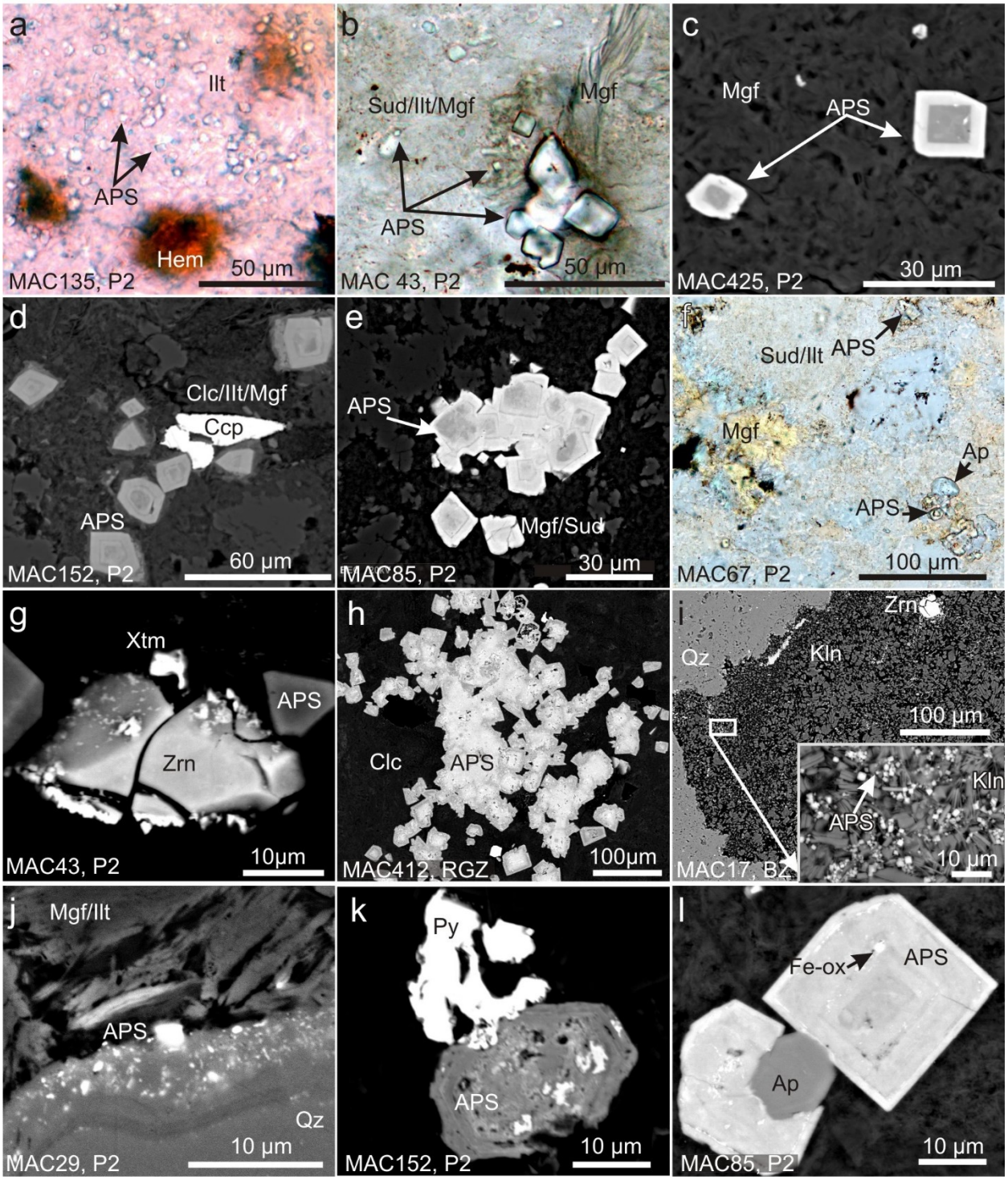

Figure 3.4. Photomicrographs **(a, b, f)** and SEM BSE **(c-e, g-l)** images of APS minerals. **(a)** Disseminated APS grains in fine-grained illite (Ilt) and with hematite (Hem); **(b)** Clustered APS grains in contact with an aggregate of feather-textured, magnesiofoitite (Mgf) and a mixture of sudoite+illite+magnesiofoitite (Sud/Ilt/Mgf); **(c)** Zoned APS grains in

magnesiofoitite; **(d)** Oscillatory zoned APS crystals disseminated in a mixture of clinochlore+illite+magnesiofoitite (Clc-Ilt-Mgf) with chalcopyrite (Ccp); **(e)** Zoned APS crystals clustered in magnesiofoitite+sudoite; **(f)** Zoned APS crystals, apatite, and magnesiofoitite in a mixture of sudoite+illite; **(g)** Partially corroded zircon (Zrn) mantled by xenotime (Xtm) and APS grains; **(h)** Aggregate of euhedral, zoned APS crystals in a clinochlore+sudoite matrix; **(i)** Disseminated, sub-hedral APS grains in fine-grained kaolin (Kln); **(j)** A mixture of APS minerals and quartz rimming coarse quartz grain; **(k)** APS grain in contact with pyrite (Py); **(l)** APS crystal with inclusions of Fe-oxide in contact with apatite (Ap). Sample number and location are indicated at the bottom left corner of each image. Qz = Quartz

---

3.4.2 APS mineral chemistry – major elements

The APS mineral formulae were calculated based on 6 cations (Table 3.2) as the ideal formula is expressed as $AB_3(XO_4)_2(OH)_6$, where A = mono-, di-, tri- or, more rarely, tetravalent cations (K^+, Na^+, Rb^+ , Ca^{2+}, Sr^{2+}, REE^{3+}, Th^{4+} etc.); B = Al^{3+}, Fe^{3+}; and X = P^{5+}, S^{6+}, and As^{5+}. Cation charges were allocated using the following:

i. the X-site was filled with P^{5+}, S^{6+}, As^{5+},
ii. the B-site was filled by Al^{3+}, then Fe^{3+} to have 3 cations,
iii. the A site was then filled by remaining cations.

High contents of trivalent cations occur in the A-site and create excess cation charges. To compensate for this, $PO_3(OH)^{2-}$ was assigned for $(PO_4)^{3-}$, as has been used by previous researchers (e.g., Gaboreau et al. 2007).

Along the P2 fault, APS minerals occur predominately with sudoite and lesser illite and magnesiofoitite, in intensely altered metapelite and pegmatite. These APS minerals contain high ΣLREE (0.35 – 0.58 apfu; LREE = La + Ce + Pr + Nd) relative to Sr (0.16 – 0.32 apfu) and Ca (0.18 – 0.28), and high PO_4^{3-} (1.70 - 1.97 apfu) relative to SO_4^{2-} (0.06 – 0.35 apfu) and AsO_4^{3-} (<0.01

apfu) (Table 3.2). Ce is high (0.15 – 0.27 apfu) relative to La (0.09 – 0.17 apfu), and Pr (<0.01 – 0.03 apfu), producing $[Ce]_N /[Ce]_N^*$ of ~0.8 – 1.6, where $[Ce]_N^* = \sqrt{([La]_N \cdot [Pr]_N)}$. Cores of zoned grains are enriched in Sr-, Ca-, and S, and rims contain high LREE and P (Fig. 3.5a; Table 3.2). Within the cores, Ca and P contents are inversely correlated with Sr and S contents (Fig. 3.5a). The narrow width of zoning and small size of grains prevented acquisition of quantitative compositions of individual zones excluding coarse grains in MAC152 (Table 3.2). Therefore, most data presented in Table 3.2 represent mixtures (referred to as mixed data) of compositional zones identified in SEM-BSE.

APS minerals in the sample of Bleached Zone quartzite (MAC17) contain high Sr (0.68 apfu) relative to Ca (0.16 apfu) and ΣLREE (0.13 apfu) and high SO_4^{2-}(0.54 apfu; Table 3.2).

APS minerals are abundant in the Red-Green Zone sample of the basement footwall (MAC412) near the P2 Main deposit. APS minerals occur with clinochlore and sudoite and contain high AsO_4^{3-}, (~ 0.63 apfu), Fe^{3+} (0.16 apfu), and Ce (~0.32 apfu) showing positive Ce anomalies ([Ce]/[Ce]*) of up to 6. APS minerals from this sample are also zoned with high-Ce cores, and a Ca- and P-rich inner rim and Sr-rich outer rim (Fig. 3.5b). APS minerals in this sample were relatively coarse-grained; therefore, individual core and rims were analyzed in two grains (Table 3.2). The data shows that the cores contain high As (0.78 apfu) and low P (0.92 apfu) relative to the rim (0.26 and 1.46 apfu, respectively; Table 3.2).

Table 3.2. EMPA major element oxide data and atomic proportion formula units for APS minerals.

	P2 fault							
Sample	**MAC67**	**MAC85**	**MAC152**			**MAC404**	**MAC117**	**MAC425**
a	Sud	Sud/Ilt		Sud/Clc		Kln	Ilt	Mgf/Sud
b	Mixed	Mixed	Mixed	Core	Rim	Mixed	Mixed	Mixed
# grains	10 1σ	11 1σ	8 1σ	3 1σ	3 1σ	10 1σ	10 1σ	9 1σ
CaO	2.72 0.30	2.70 0.36	2.86 0.44	2.92 0.24	2.37 0.31	3.40 0.18	2.68 0.36	2.79 0.67
SO_3	1.68 0.77	1.69 1.29	2.06 0.53	2.58 0.44	1.14 0.30	0.94 0.37	3.70 0.46	3.43 1.48
Al_2O_3	28.96 1.56	31.26 1.30	32.01 1.08	32.30 0.31	31.26 0.63	31.13 1.25	32.22 1.07	32.37 1.10
Fe_2O_3	0.85 0.77	0.54 0.51	0.54 0.24	0.58 0.24	0.44 0.05	0.91 0.63	0.82 0.71	0.96 0.57
Nd_2O_3	3.26 0.44	3.29 0.79	2.77 0.50	2.44 0.33	3.80 0.47	4.26 0.37	2.16 0.42	2.20 0.36
Pr_2O_3	0.94 0.16	0.87 0.23	0.76 0.21	0.75 0.08	0.97 0.08	0.96 0.06	0.60 0.12	0.70 0.15
Ce_2O_3	8.67 1.21	8.33 1.09	7.81 0.78	7.74 0.37	9.44 0.54	7.50 0.48	7.85 0.80	7.50 1.78
La_2O_3	5.40 0.82	5.55 0.31	5.18 0.47	5.11 0.29	5.33 0.42	3.58 0.19	5.58 0.87	4.50 1.22
P_2O_5	25.84 1.71	26.76 1.17	27.10 0.58	26.66 0.64	28.20 0.27	28.85 1.43	25.24 0.73	25.71 1.17
SrO	3.14 0.64	3.17 1.08	3.73 0.62	4.09 0.37	2.64 0.25	3.65 0.74	4.38 0.45	5.49 1.64
ThO_2	0.51 0.29	0.27 0.38	0.16 0.05	0.15 0.09	0.11 0.07	0.15 0.10	0.04 0.02	0.13 0.09
As_2O_5	0.02 0.01	0.02 0.02	0.01 0.01	0.01 0.01	0.01 0.01	0.06 0.05	0.04 0.01	0.01 0.02
Total	81.98 2.61	84.46 1.99	84.98 0.92	85.34 0.96	85.70 0.76	85.40 0.89	0.04 1.40	85.78 1.45
SiO_2 [c]	*1.44 1.54*	*0.63 0.30*	*0.39 0.10*	*0.41 0.12*	*0.36 0.29*	*5.85 4.21*	*1.19 0.77*	*1.88 1.44*
apfu								
Ca	0.25	0.24	0.25	0.25	0.21	0.29	0.23	0.24
Sr	0.16	0.16	0.17	0.19	0.13	0.17	0.21	0.25
Nd	0.10	0.10	0.08	0.07	0.11	0.12	0.06	0.06
Pr	0.03	0.03	0.02	0.02	0.03	0.03	0.02	0.02
Ce	0.27	0.25	0.23	0.23	0.28	0.22	0.23	0.22
La	0.17	0.17	0.16	0.15	0.16	0.11	0.17	0.13
Fe^{3+}		0.03	0.03	0.04	0.03	0.02	0.05	0.06
Al		0.05	0.06	0.07	0.02		0.07	
Th	0.01							
A	**1.00**	**1.02**	**1.00**	**1.02**	**0.97**	**0.97**	**1.04**	**0.99**
Al	2.95	3.00	3.00	3.00	3.00	2.96	3.00	3.06
Fe^{3+}	0.06					0.04	0.00	0.00
B	**3.01**	**3.00**	**3.00**	**3.00**	**3.00**	**3.00**	**3.00**	**3.06**
P	1.89	1.87	1.86	1.82	1.96	1.97	1.73	1.75
S	0.11	0.10	0.12	0.16	0.07	0.06	0.23	0.21
As								
X	**2.00**	**1.97**	**1.98**	**1.98**	**2.03**	**2.03**	**1.96**	**1.95**
ΣLREE	0.58	0.54	0.51	0.47	0.58	0.48	0.48	0.44
Ce anomaly[d]	0.83	0.81	0.85	0.85	0.89	0.87	0.92	0.90
S/P	0.06	0.05	0.06	0.09	0.04	0.03	0.13	0.12

Notes: *(Extended to Next Page)*

Due to small grain size of APS minerals and the relatively large electron beam size (5 μm) for the analysis, it was difficult to obtain precise composition of individual compositional zones in grains, as some rims are narrower than 5 μm. Most cores are also smaller than 5 μm (Figs. 4,5). Therefore, most of the compositional data presented in Table 2 reflect mixtures of different zones. Rim and core anlysis was conducted on two samples containing relatively large APS (MAC152 and MAC412).

a: adjacent minerals, Ilt=illite, Sud=sudoite, Mgf = magnesiofoitite; Clc = clinochlore

b: Area of analysis in grains, ie. rim, core or mixed. Compositional zones are narrower than the beam size of 5 μm. The mixed area refers to the data from different compositional zones defined in SEM-BSE images

c: contribution of surrounding minerals in the analytical data was evaluated using SiO_2 contents (see the Results for detailed description)

d: $[Ce]_N^* = \sqrt{([La]_N \cdot [Pr]_N)}$

Table 3.2. – *Extended*

	P2 fault					GRZ			BZ
Sample	**MAC135**	**MAC63**	**MAC29**	**MAC44**	**MAC43**	**MAC412**			**MAC17**
a	Ilt	Sud	Sud	Sud/Ilt	Sud/Ilt	Sud/Clc			Kln
b	Mixed	Mixed	Mixed	Mixed	Mixed	Mixed	Core	Rim	Mixed
# grains	3 1σ	7 1σ	4 1σ	14 1σ	2 1σ	10 1σ	2 1σ	2 1σ	3 1σ
CaO	3.14 0.11	3.34 0.31	1.95 0.26	3.18 0.19	2.98 0.45	3.49 0.36	3.46 0.42	3.87 0.44	1.76 0.19
SO_3	3.40 0.28	4.49 0.35	3.14 0.83	4.80 0.71	5.86 1.33	2.84 0.24	2.89 0.17	3.27 0.53	8.41 0.85
Al_2O_3	29.49 0.98	32.82 0.64	30.28 1.90	32.52 0.78	31.99 0.46	30.15 1.01	28.78 0.65	31.57 1.76	29.33 0.90
Fe_2O_3	1.40 0.56	0.23 0.11	1.90 0.87	0.50 0.19	0.31 0.14	3.49 1.66	5.85 2.02	3.37 2.99	0.34 0.11
Nd_2O_3	1.41 0.17	2.79 0.54	2.62 0.33	1.84 0.19	2.26 0.37	0.68 0.26	0.74 0.02	0.48 0.23	1.21 0.32
Pr_2O_3	0.50 0.12	0.71 0.16	0.76 0.09	0.58 0.12	0.46 0.17	0.12 0.09	0.25 0.08	0.19 0.07	0.31 0.25
Ce_2O_3	8.81 0.63	6.75 0.46	4.65 0.70	6.07 0.70	5.84 0.44	11.16 0.80	9.40 1.05	10.19 1.26	1.71 0.64
La_2O_3	2.83 0.27	3.78 1.01	4.08 1.33	3.95 0.47	3.28 0.25	1.32 0.39	1.56 0.52	1.26 0.74	1.01 0.36
P_2O_5	26.65 0.66	25.52 0.63	23.95 0.49	25.61 0.73	25.09 0.85	15.56 2.78	13.02 0.36	21.64 3.87	20.66 0.97
SrO	5.95 0.74	5.01 0.61	6.27 0.68	6.77 0.79	7.01 1.59	4.52 0.58	4.51 0.23	5.18 1.69	13.70 0.74
ThO_2	0.27 0.06	0.08 0.05	0.19 0.09	0.02 0.03	0.04 0.01	0.01 0.01	0.02 0.02	0.01 0.01	0.06 0.03
As_2O_5	0.13 0.05	0.02 0.02	0.05 0.03	0.01 0.01	0.05 0.03	15.72 4.32	17.85 0.79	6.04 5.16	0.24 0.06
Total	83.97 1.17	85.56 1.25	79.85 1.57	85.86 1.46	85.19 0.74	89.04 1.16	88.34 0.22	87.07 0.96	78.75 1.90
SiO_2[c]	*6.75 1.47*	*0.84 0.35*	*8.32 3.91*	*0.88 0.30*	*0.98 0.17*	*0.70 0.59*	*0.70 0.22*	*0.69 0.58*	*9.74 5.57*
apfu									
Ca	0.28	0.28	0.18	0.27	0.25	0.31	0.31	0.33	0.16
Sr	0.28	0.23	0.31	0.31	0.32	0.18	0.22	0.24	0.68
Nd	0.04	0.08	0.08	0.05	0.06	0.02	0.02	0.01	0.04
Pr	0.02	0.02	0.02	0.02	0.01				0.01
Ce	0.27	0.20	0.15	0.18	0.17	0.34	0.29	0.30	0.05
La	0.09	0.11	0.13	0.12	0.10	0.04	0.05	0.04	0.03
Fe^{3+}		0.01	0.12	0.03	0.02	0.14	0.21	0.17	
Al		0.08		0.03	0.01				
Th	0.01								
A	**0.97**	**1.01**	**0.99**	**1.00**	**0.95**	**1.03**	**1.10**	**1.09**	**0.98**
Al	2.86	3.00	3.06	3.00	3.00	2.92	2.84	2.96	2.96
Fe^{3+}	0.09	0.00	0.00	0.00	0.00	0.08	0.16	0.04	0.02
B	**2.95**	**3.00**	**3.06**	**3.00**	**3.00**	**3.08**	**3.00**	**3.00**	**2.98**
P	1.86	1.72	1.74	1.71	1.70	1.08	0.92	1.46	1.50
S	0.21	0.27	0.20	0.28	0.35	0.18	0.18	0.19	0.54
As	0.01					0.63	0.78	0.26	0.01
X	**2.07**	**1.99**	**1.94**	**2.00**	**2.05**	**1.89**	**1.88**	**1.91**	**2.05**
ΣLREE	0.41	0.41	0.38	0.36	0.35	0.40	0.36	0.35	0.13
Ce anomaly[d]	1.59	0.89	0.57	0.86	1.02	6.00	3.25	4.42	0.65
S/P	0.11	0.16	0.12	0.17	0.21	0.17	0.20	0.13	0.36

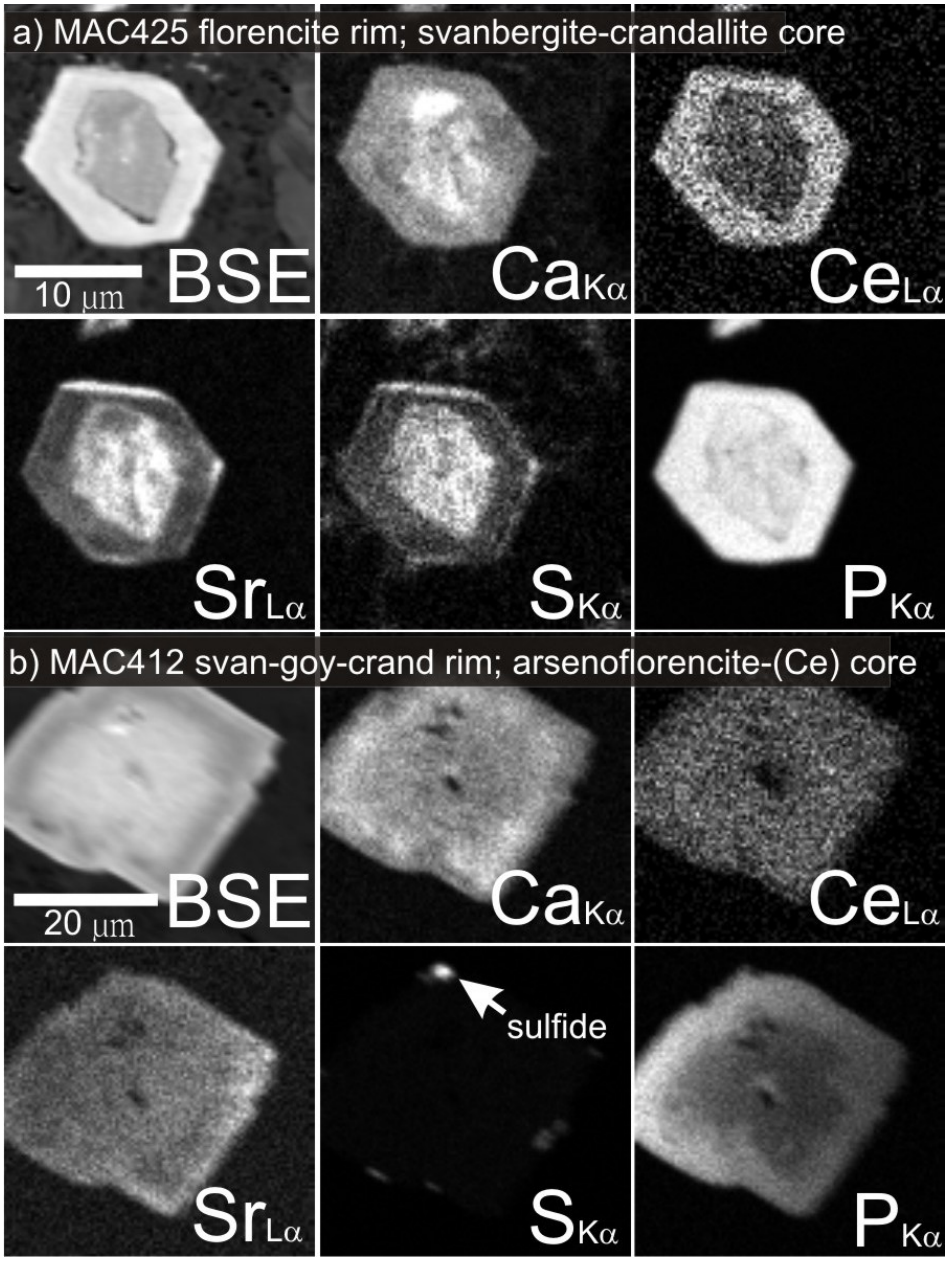

Figure 3.5. X-ray maps of APS minerals showing zoning with respect to Ca, Ce, Sr, S and P obtained by wave-length dispersive spectra of EPMA: **(a)** sample MAC425 from the P2 fault and Zone 2 ore body and **(b)** sample MAC412 from the Red-Green Zone (locations shown in Fig. 3.2; see Table 3.2 for quantitative chemical data). svan-goy-crand = svanbergite-goyazite-crandallite. Note that very dark areas in BSE images contain low mass elements and they are not holes or other mineral inclusions.

3.4.3 APS mineral chemistry – trace elements

LA ICP-MS analyses were conducted on relatively coarse-grained (>10 μm) APS minerals proximal to the Zone 3 (sample MAC44) and Zone 2 ore deposits (samples MAC63 and MAC85). Counts of all elements were monitored during the analysis to detect mineral inclusions and contributions of surrounding minerals. Mineral inclusions should give sharp increases in the counts of certain elements, but no such spikes were observed during the analysis, confirming the lack of mineral inclusions. None of the surrounding minerals contained any significant concentrations of elements, such as U, Y, Pb and Th, which were at background levels in surrounding minerals and only high when the laser beam hit APS grains. Unlike clays, APS minerals show high counts of LREE, Sr, Ca and P (Appendix Fig. A3.1). This confirms that these elements are in the APS crystal structure and were not incorporated from surrounding minerals. Furthermore, different grains from individual sections yielded comparable concentrations of minor and trace elements, suggesting that these trace elements originate from APS minerals and that the values are minima since the dilution effects by the surrounding minerals were not corrected. The dilution effects by surrounding minerals are confirmed by the detection of significant Si (48000 – 99000 ppm) during the ablation of the APS minerals.

APS minerals of the P2 fault proximal to Zone 3 (MAC44) ore deposit contain appreciable Se (130 ppm; Table 3.3), U (0.39 – 0.88 ppm), Pb (160 - 180 ppm), and Th (1100 - 1600 ppm). Similarly, APS from sample MAC63 (~50 m) from Zone 2 ore and ~ 20 m into the hanging-wall of the P2 fault) show appreciable Se (100 – 160 ppm), U (1.7 – 4.2 ppm), Pb (82 – 190 ppm), and Th (1000 – 1400 ppm). Sample MAC85, from within 20 m of Zone 2 ore and directly within the P2 fault, contains APS with relatively high U (16 ppm), Pb (260 ppm), and Th (2300 ppm). Similar to samples MAC44 and MAC63, sample MAC85 showed appreciable Se (130 ppm). Combined with

the EPMA data of major elements (La, Ce, Pr, Nd), these APS minerals from the P2 fault area contain high LREE relative to HREE ($[LREE]_N/[HREE]_N$ = 800 – 2500; Fig. 3.6) and show low S/Se weight ratios, ranging from 100 – 150.

3.5 Discussion

3.5.1 Major element compositions of APS minerals

The following elemental relationships are observed:

i. the P contents positively correlate with LREE and both inversely correlate with Sr and S (Figs. 3.5a, 3.7c,d); the LREE inversely correlate with Ca (Figs. 3.5a, 3.7e);
ii. the S contents positively correlate with Sr and inversely correlate with Ce (Figs. 3.5a, 3.7b).
iii. high Ca correlates with high P (Figs. 3.5a,b);
iv. the As contents inversely correlate with P (Fig. 3.7a);
v. high As APS minerals contain high Ce relative to other REE (Fig. 3.7a).

The above relationships and cations in A-site and X-site suggest the presence of the following end-members (Fig. 3.8):

i. high LREE and P contents correspond to high proportions of florencite $(REE)Al_3(PO_4)_2(OH)_6$ (Figs. 3.8a-c);
ii. high S and Sr contents correspond to high proportions of svanbergite $SrAl_3(PO_4)(SO_4)(OH)_6$ with a minor goyazite component $SrAl_3(PO_4)_2(OH)_6$ (Figs. 3.8a-d);
iii. high Ca contents correspond to high proportions of crandallite $CaAl_3(PO_4)_2(OH)_6$ (Figs. 3.8a,b,d);
iv. high As and high Ce contents correspond to high proportions of arsenoflorencite(-Ce) $(Ce, REE)Al_3(AsO_4)_2(OH)_6$ (Figs. 3.8a,b).

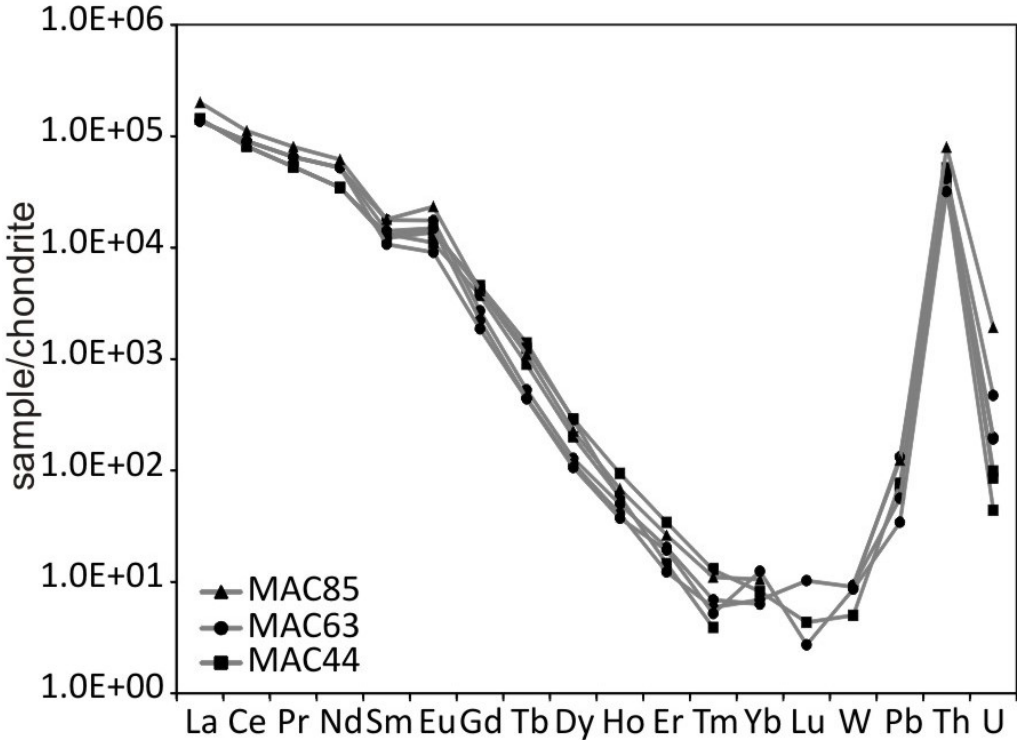

Figure 3.6. Chondrite-normalized REE, U, Th, Pb and W for APS grains from sample MAC44 (along the P2 fault proximal to the Zone 3 ore body of the McArthur River deposit) and from samples MAC63 and MAC85 (close to Zone 2 ore). The abundance of these elements was obtained using EPMA (La, Ce, Pr and Nd) and LA-ICP-MS (Sm, Eu, Gd, Tb, Dy, Ho, Er, Tm, Yb, Lu, W, Pb, Th and U). Error bars are not shown in the diagram because the uncertainty of the analysis (< 10 %) is smaller than the size of symbols. Sample locations are in Figure 3.2c and Table 3.1. Each line represents one APS grain. Chondrite values from McDonough and Sun (1995).

Table 3.3. LA-ICPMS data of APS (ppm).

Sample:	**44**	**63**	**85**	**BCR2G[a] 1σ**	**precision**	**accuracy[b]**
# grains	3 1σ	3 1σ	1		%	%
Li	150 19	190 16	150	9 0.97	1.3	0.78
Si	48000 12000	68000 12000	99000	247000 3900	1.11	2.5
Ca	15000 1000	13000 3000	18000	48000 540	1.2	6.8
Sc	8.1 1.7	4.9 0.80	<3	28 0.35	0.46	14
Ti	31 17	26 5.5	52	12000 83	1.13	13
V	20 10	20 7.5	13	400 1.43	1.08	4.7
Cr	31 12	16 3.6	<30	15 0.29	0.50	18
Mn	30 7.6	18 5.8	55	1560 2.11	0.27	2.9
Fe	7600 1600	6300 3100	3500	85000 1300	1.48	12
Co	4.0 0.42	70 96	3.7	36 0.05	0.46	2.4
Ni	21.43 1.21	49 43	<10	10 0.82	1.07	
Cu	5.4 0.53	5.7 0.79	72	16 0.12	0.67	16
Zn	4.4 0.19	9.0 4.7	<8	150 1.4	1.56	15
Se	130 2.6	120 20	130	< 3	1.85	
Rb	17 11	2.0 0.23	5.0	46 0.45	0.40	4.9
Sr	42000 7000	23000 6300	24000	310 2.7	0.79	10
Y	57 7.6	38 2.7	60	28 0.025	1.16	23
Zr	1.1 0.66	7.0 2.1	7.1	160 0.87	0.35	17
Nb	0.28 0.16	0.15 0.04	<0.3	10 0.01	0.53	
Mo	3.4 1.3	8.3 9.5	<4	240 0.86	1.06	3.1
Sn	2.3 0.86	3.3 1.2	2	2 0.03	1.08	
Ba	630 63	250 74	440	620 9.6	0.72	9.9
La	20000 3500	24000 5300	34200	23 0.25	1.36	6.3
Ce	39000 8000	45000 9400	58000	50 0.97	0.70	11
Pr	3800 500	4600 840	5900	5.8 0.035	0.75	15
Nd	14000 1400	17000 3200	20400	26.0 0.74	1.21	7.3
Sm	2000 69	2200 440	2800	5.7 0.17	0.68	14
Eu	760 87	800 200	1300	1.8 0.059	0.67	9.0
Gd	820 68	450 69	810	6.0 0.42	1.05	11
Tb	43 7.6	17 1.5	40	0.9 0.012	1.28	15
Dy	64 10	28.63 2.3	60	6 0.01	0.99	
Ho	3.8 0.94	2.3 0.29	3.7	1.2 0.0095	0.84	10
Er	2.9 1.9	2.8 0.58	4	3 0.095	1.24	
Tm	0.25 0.11	0.148 0.017	0.27	0.40 0.02	1.37	28
Yb	0.94 0.34	1.4 0.45	1.7	2.8 0.21	0.77	18
Lu	0.13 0.033	0.14 0.081		0.41 0.032	0.75	20
Hf	0.91 0.40	0.30 0.099	<0.53	4.3 0.23	1.32	11
Ta	0.17 0.10	0.077 0.08	<0.161	0.6 0.007	1.56	
W	0.79 0.36	0.9 0.029	1	0.5 0.03	0.61	
Pb	160 10	120 39	260	10.3 0.005	0.92	12
Th	1300 200	1100 140	2300	5.4 0.035	0.91	13
U	0.62 0.19	2.4 1.1	16	1.7 0.065	1.46	1.9

[a]BCR2G from US Geological Survey

[b]based on the data of BCR2G provided by USGS

data is the average of anaylzed grains (# grains) in the sample (± 1 standard deviation)

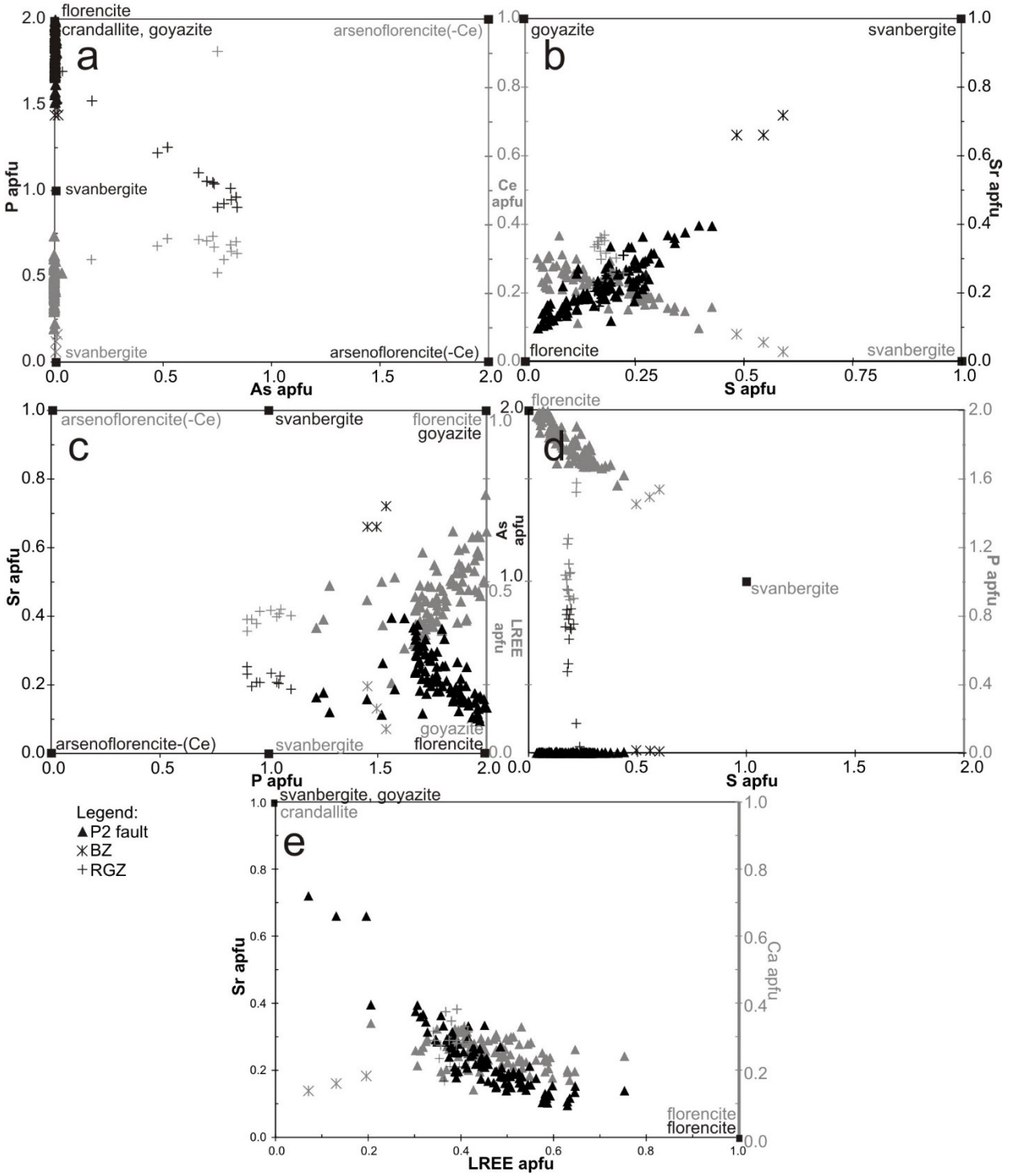

Figure 3.7. Binary plots showing substitution and elemental relationships of APS minerals based on EPMA data: **(a)** As vs P (black) and As vs. Ce (gray); **(b)** S vs. Sr (black) and S vs. Ce (gray); **(c)** P vs Sr (black) and P vs. LREE (gray); **(d)** S vs. As (black) and S vs. P (gray); and **(e)** LREE vs. Sr (black) and LREE vs. Ca (gray). Each data point represents one grain. P2

fault = P2 fault samples (triangles). BZ = Bleached Zone sample (stars), RGZ = Red-Green Zone sample (crosses).

APS minerals show wide compositional variations, but all can be expressed using the above five end members (crandallite, goyazite, svanbergite, florencite, arsenoflorencite).

3.5.2 Spatial, chemical and temporal variation of APS minerals and associated clay minerals

Along the entire studied range of the P2 fault, APS minerals occur with sudoite (± illite, magnesiofoitite) in metapelite and pegmatite. The APS minerals are florencitic, but contain significant Ca, Sr, and SO_4^{2-} reflecting a minor component of svanbergite, mainly as core (Figs. 3.5a and 3.9). Gaboreau et al. (2005, 2007) found that APS minerals proximal to uranium deposits contain high LREE and P relative to those in intermediate and distal areas (Fig. 3.9). The present study found a large compositional variation of APS minerals, even within the ore zone, compared to the narrow range presented by Gaboreau et al (2005, 2007), and the compositional variation does not correlate with distance from uranium mineralization (Fig. 3.9). For example, the (LREE+P)/(Ca+Sr+S) ratios of APS minerals near (<1 m) the uranium ore range from 1.6 to 5.6, whereas those from barren samples far (>500 m) from mineralization vary from 2.8 - 4 (Fig. 3.9). We suggest that our data reflect the evolution of fluids in the ore zone where the earlier fluids contained high Ca, Sr and SO_4^{2-}, and evolved to have high LREE and P. This proposed interpretation is supported by compositional zoning of APS minerals with Ca-, Sr- and S-rich cores and LREE- and P-rich rims (Fig. 3.5a).

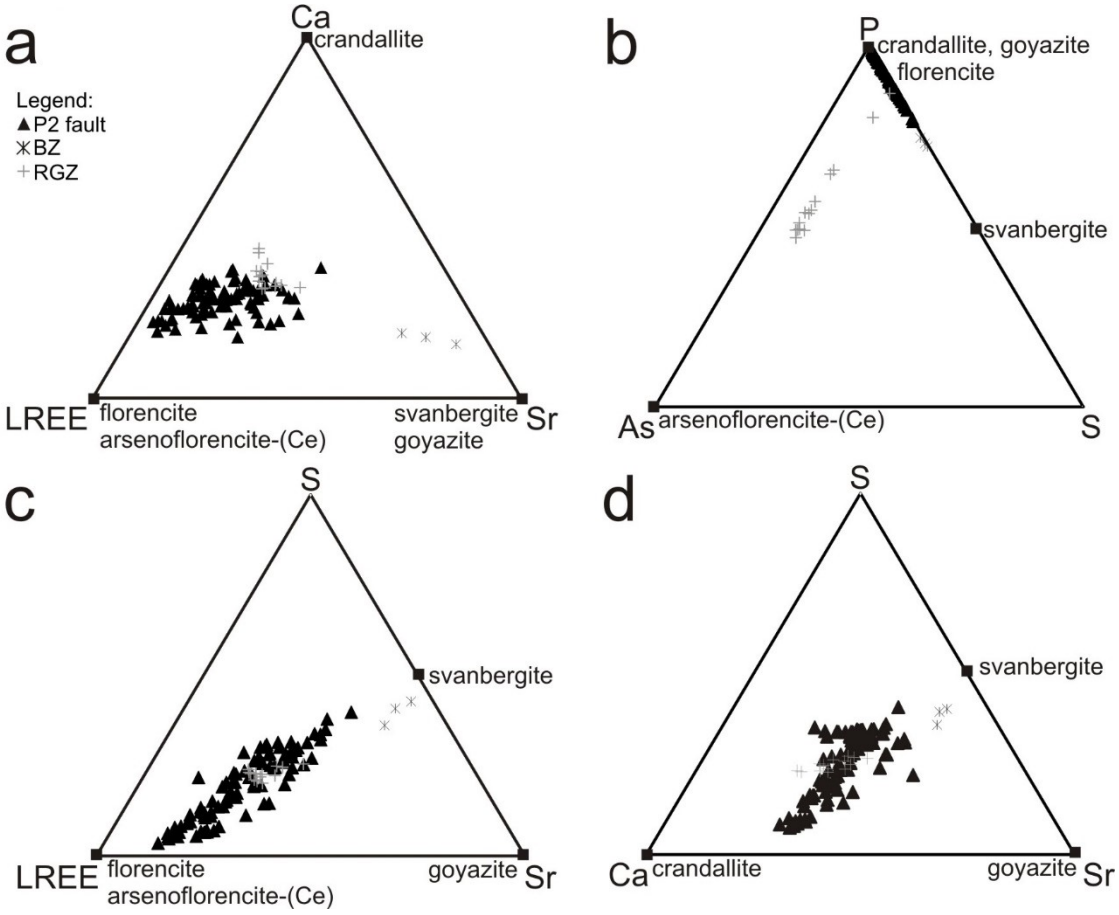

Figure 3.8. Compositions of APS minerals plotted on ternary diagrams. End member minerals are indicated. **(a)** Ca-Sr-LREE; **(b)** P-S-As; **(c)** S-Sr-LREE; **(d)** S-Sr-Ca. Each data point represents one grain. P2 fault = P2 fault samples (triangles). BZ = Bleached Zone sample (stars), RGZ = Red-Green Zone sample (crosses).

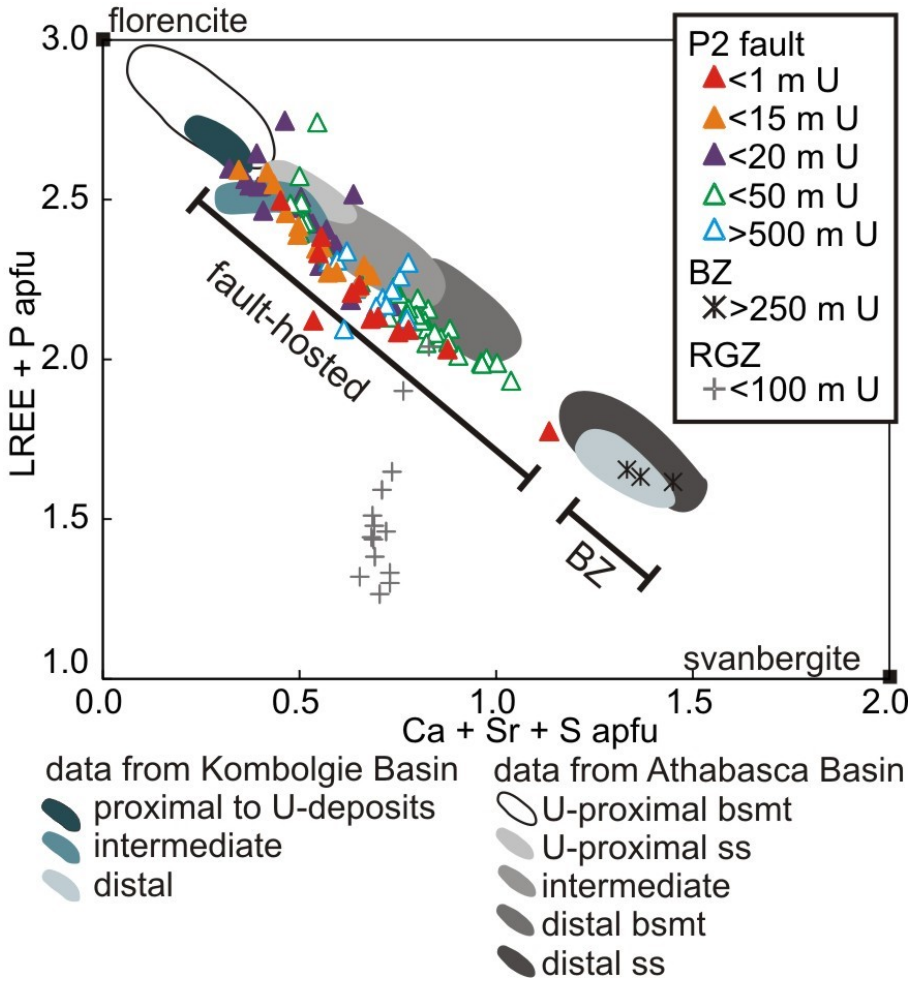

Figure 3.9. Cross-plot showing coupled substitution of Ca-Sr-S for LREE-P for APS minerals along the P2 fault (triangles), and within the Bleached Zone (BZ) (stars) and Red-Green Zone (RGZ) (crosses). P2 fault samples are color coded with respect to distance in metre from uranium mineralization (McArthur River deposit and low-grade): red filled triangles represents sample < 1 m from ore (MAC425 and MAC29), orange filled triangles were < 15 m from ore (MAC152), purple filled triangles were < 20 m from ore (MAC67 and MAC85), open green triangles were < 50 m from ore (MAC43, MAC44, MAC63 and MAC404) and open blue triangles were of unmineralized areas >500 m from the ore (MAC117 and MAC135). Each data point represents one grain. For comparison, the diagram shows the compositional ranges of APS minerals determined by Gaboreau et al (2005, 2007) from the Athabasca Basin (fields with various shades of gray) and Kombolgie Basin, Australia (field with various shades of blue).

APS minerals are abundant with kaolin and illite in one sample of the Bleached Zone (MAC17) along the unconformity. These grains are Sr- and S-rich and similar in composition within the sample but not with the APS minerals found along the P2 fault (Fig. 3.9). The average composition of the APS minerals is $Ca_{0.16}Sr_{0.68}Ce_{0.05}La_{0.03}Nd_{0.04}Pr_{0.01})(Al_{2.96}Fe^{3+}_{0.02})(PO_3O_{0.94}OH_{0.06})_{1.50}(SO_4)_{0.54}(AsO_4)_{0.01}(OH)_6$, svanbergite$_{0.54}$-crandallite$_{0.16}$-goyazite$_{0.14}$-florencite$_{0.13}$. The data are comparable to APS mineral compositions in distal sandstones by Gaboreau et al. (2007) (Fig. 3.9).

One Red-Green Zone sample of intensely altered metapelite (MAC412) footwall to the P2 fault, contain APS minerals with As- and Ce-rich cores and Ca, Sr, and S-rich rims together with clinochlore and sudoite. The grains show similar Ca, Sr, and S contents with varying LREE and P due to the presence of As that substitutes for P (Figs. 3.7a and 3.9). The average composition of these grains is $(Ca_{0.31}Sr_{0.22}Ce_{0.32}La_{0.04}Nd_{0.02}Fe^{3+}_{0.15})(Al_{2.92}Fe^{3+}_{0.08})(PO_3O_{0.83}OH_{0.17})_{1.11}(SO_4)_{0.18}(AsO_4)_{0.68}(OH)_6$, arsenoflorencite(-Ce)$_{0.39}$-crandallite$_{0.31}$-svanbergite$_{0.18}$-goyazite$_{0.12}$. This is the first documented occurrence of arsenoflorencite(-Ce) in the Athabasca Basin.

APS minerals from the McArthur River deposit and the P2 fault show cores of svanbergite-crandallite-goyazite rimmed by florencite (Figs. 3.4c-e,k,l, 3.5a). APS minerals from the Red-Green Zone contain arsenoflorencite-(Ce) cores rimmed by svanbergite-crandallite-goyazite (Figs. 3.4h, 3.5b, 3.8b). APS minerals of the Bleached Zone are svanbergite-crandallite-goyazite (Fig. 3.8). The zoning suggests the crystallization sequence of APS minerals in the study area. Early crystallization of arsenoflorencite(-Ce) was followed by svanbergite-crandallite-goyazite, and finally florencite.

3.5.3 Nature of fluids responsible for APS mineral formation

APS minerals in the Bleached Zone sample contain high SO_4^{2-} contents, up to 0.59 apfu (Figs. 3.7b,d, 3.8b-d), indicating relatively oxidizing conditions for their formation. These APS

minerals have close to svanbergite end-member composition, with a minor goyazite and crandallite component (Figs. 3.7b,d-e). The grains coexist with kaolin and illite (Fig. 3.4I), which is the diagenetic assemblage in the Athabasca Group sandstones (Hoeve and Quit 1984; Quirt 2001). The composition of the APS minerals is similar to those of diagenetic origin reported in Athabasca and Kombolgie sandstones (Gaboreau et al. 2005, 2007), and other sedimentary basins worldwide (Spötl, 1990; Gaboreau et al. 2005, 2007; Pe-Piper and Dolansky 2005; Gall and Donaldson 2006; Fig. 3.10). Therefore, the APS minerals of the Bleached Zone most likely crystallized from an oxidizing, Ca-, Sr- and SO_4-rich, diagenetic fluid of the overlying sandstones.

The oxidizing diagenetic fluids from the sandstones are recorded as relict cores of the APS minerals along the P2 fault in the basement (Figs. 3.4, 3.5a). These cores contain high Ca, Sr and S and are similar in composition to diagenetic APS minerals in sandstones described above. The S/P ratios of APS minerals as whole grains along the P2 fault are relatively low (< 0.16) compared to those of the Bleached Zone (0.36; Table 3.2, Fig. 3.11). The lowest S/P ratios (< 0.06) are found in areas of Zone 2 mineralization (Fig. 3.11b). The data show that the SO_4^{2-} contents in fluids decrease from the unconformity to the P2 fault and from non-mineralized areas along the P2 fault to ore zone. This indicates the change from a relatively oxidized to a relatively reduced environment. This modification of fluid chemistry likely took place due to interaction of fluids with the graphite-rich basement rocks, as has been suggested by Gaboreau et al (2007). Alternatively, it was caused by reduced fluids that originated from the graphite-rich basement rocks and supplied through faults. In either case, this redox change closer to the uranium ore is consistent with the reduction of U^{6+} to U^{4+} necessary for the precipitation of uraninite. Therefore, S/P ratios of APS minerals record the reduction of fluids associated with uranium mineralization.

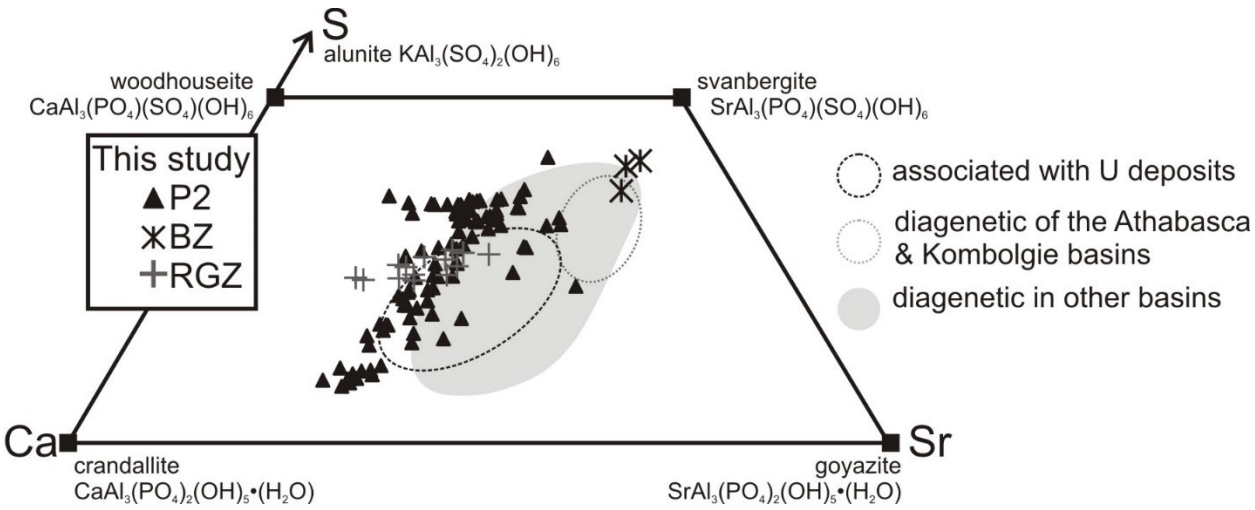

Figure 3.10. An alunite-goyazite-crandallite [S-Sr-Ca] ternary plot showing compositions of APS minerals from the P2 fault (P2; triangles), the Bleached Zone (BZ; stars), and the Red-Green Zone (RGZ; crosses). Each data point represents one grain. For comparison, the compositional ranges of diagenetic APS minerals from various sedimentary units are shown: diagenetic APS minerals of the Athabasca and Kombolgie basins are represented by grey dotted field (Gaboreau et al. 2005, 2007) and diagenetic APS minerals of the Chaswood Formation (Pe-Piper and Dolansky, 2005), Hornby Basin and Thelon Basins (Gall and Donaldson, 2006) and Mitterberg Formation (Spötl, 1990) are collectively represented by the grey field. APS minerals associated with uranium deposits of the Athabasca and Kombolgie Basin (Gaboreau et al. 2005, 2007) are represented by the black dashed field.

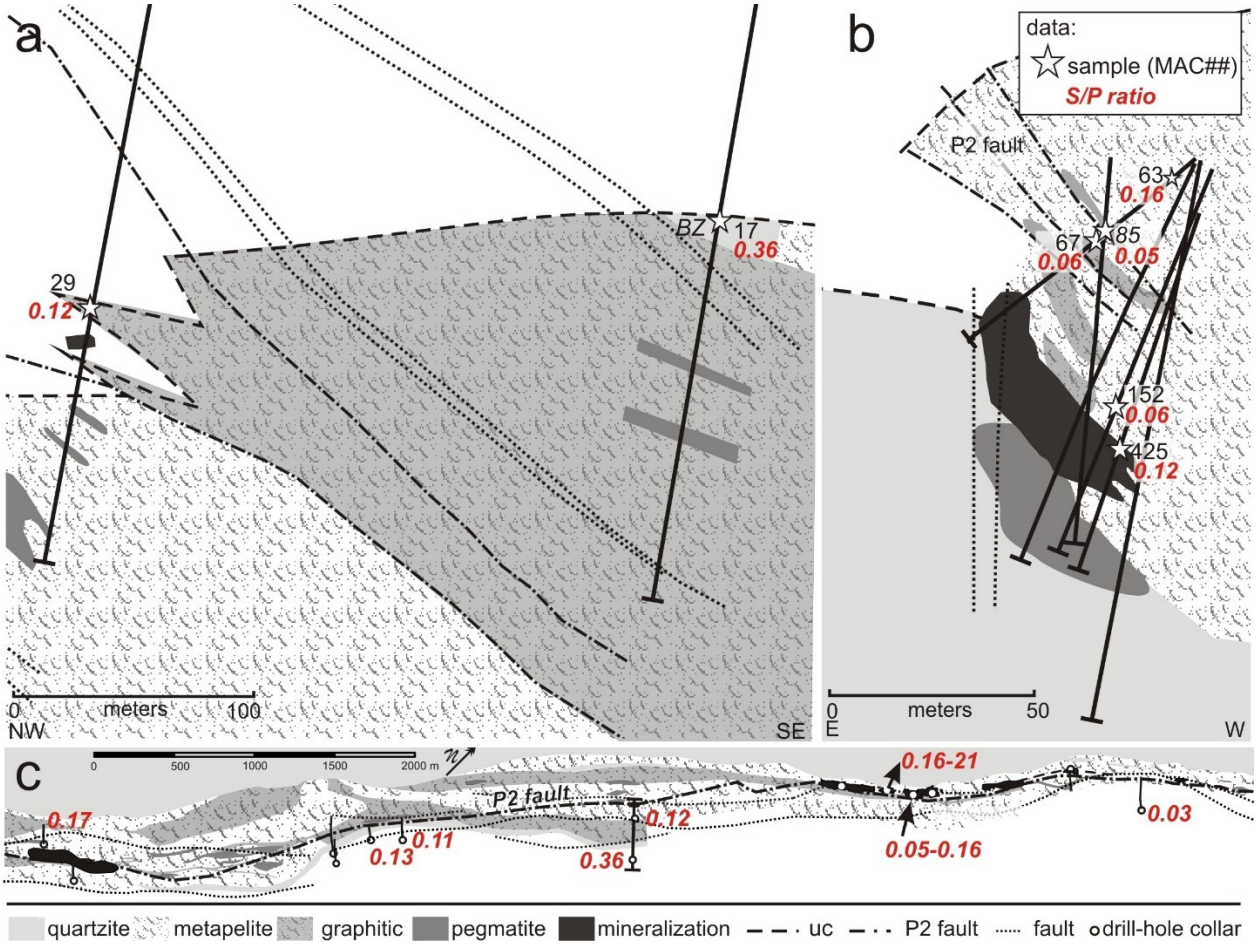

Figure 3.11. Spatial variation of S/P ratios for APS minerals. The average S/P ratio (mixed data, see Table 3.2) of APS minerals within a sample is expressed as a red, bold, italicized number next to its corresponding sample (a and b) or drill-core (c) location.

The spatial association of florencitic APS minerals with the McArthur River uranium deposit (Fig. 3.2b) and their abundance within the deposit suggest the close relationship between florencite and the uranium mineralization. This observation is consistent with that of Gaboreau (2007). The APS minerals in metapelite and pegmatite along the entire 7 km of the P2 fault studied are predominantly florencite with minor components of svanbergite-crandallite-goyazite (Figs. 3.4d-e, 9). The alteration assemblage of sudoite, magnesiofoitite and illite is also similar all along the P2 fault including the ore zone. The evidence suggests that similar fluids passed along the entire P2

fault. These fluids were likely uranium-bearing because APS minerals contain uranium (up to 16 ppm; Table 3.3).

The Red-Green Zone sample of metapelite (sample MAC412; Fig. 3.3d) contains As- and LREE-rich APS minerals (Figs. 3.7a,d, 8b; Table 3.2). Arsenic in APS minerals occurs as As^{5+}, replacing P^{5+} in the X-site of the crystal structure. These As-bearing crystals show prominent zoning with cores of arsenoflorencite-(Ce) and rims of crandallite-goyazite and svanbergite solid-solution (Figs. 3.5b, 7a,c, 8b; Table 3.2) with sharp boundaries. The zoning suggests that arsenoflorencite-(Ce) formed earlier than the svanbergite-crandallite-goyazite of diagenetic origin. This arsenoflorencite-(Ce) may have formed in the very early stage of diagenesis. If this is the case, As-rich APS minerals should be observed in sandstones. However, there is no record of As-rich APS minerals in the Athabasca sandstone. Furthermore, sharp boundaries between cores and rims suggests that As-rich APS minerals formed before the sandstone diagenesis. We suggest that arsenoflorencite(-Ce) cores may have formed during paleo-weathering before the deposition of the Athabasca sandstones. This proposed interpretation is further supported by the presence of As^{5+} in the APS minerals. Although As contents are high in organic-rich shale (e.g., Ketris and Yudovich 2009), As is mostly fixed in sulphide minerals (e.g., Ryan et al., 2013). For As to be incorporated in the APS minerals, it must be oxidized to As^{5+}, which is stable in oxidizing, near-surface conditions (Smedley and Kinniburgh 2002).

3.5.4 APS minerals related to uranium deposits and role of P2 fault

It has been suggested that APS minerals with florencitic compositions are contemporaneous with uranium mineralization based on their occurrences within uranium deposits (Quirt 1991; Gaboreau et al. 2005, 2007; Mercadier et al. 2011). Here we have shown that APS minerals of florencitic composition are found along a 7 km strike length of the P2 fault, even in areas barren of

mineralization (Table 3.2; Fig. 3.9); although, as previously discussed, APS minerals with the highest florencite component (reflecting relatively reducing conditions) are found in proximity to ore (Figs. 3.9, 11). The APS minerals also contain elevated uranium contents (Table 3.3; Fig. 3.6), suggesting that florencitic APS minerals crystallized from uranium-bearing fluids that became reduced. The evidence supports that florencite was contemporaneous with uranium mineralization.

Florencitic APS minerals are not found in the basement greater than ~50 m from the centre of the P2 fault (Table 3.1; Fig. 3.9). The distribution of the APS minerals constrains the extent of the fluid footprint, and suggests that the entire P2 fault was a conduit for an oxidizing uranium-bearing fluid during mineralization. The P2 fault was also a site of redox change where an initial oxidizing fluid became modified and relatively reducing.

3.6 Implication

APS minerals are very small in size, but ubiquitous in the altered metasedimentary rocks along the P2 fault, which hosts the McArthur River uranium deposit. Previous researchers noted the spatial association of florencitic APS minerals and uranium deposits and suggested their use as an exploration vector (e.g., Gaboreau et al. 2007). Our study reveals that APS minerals record the timing and characteristics of geological events, from paleoweathering, diagenesis to uraniferous hydrothermal activity. We conclude that oxidizing diagenetic fluids travelled along P2 fault and formed svanbergite-crandallite-goyazite. The fluid evolved to become reducing through interaction with the basement rocks and formed florencite rims. Our study shows that APS minerals are an excellent mineralogical tool to fingerprint fluid pathways. APS minerals with similar chemistry (high florencite component) are found along a 7 km of strike length of the P2 fault, including areas barren of uranium mineralization. This suggests that uranium-bearing fluids likely passed along the entire P2 fault, but only produced uranium mineralization in localized areas. This study confirms

that APS minerals are good indicators of alteration related to uranium mineralization, thus they may be useful in identifying fertile structures associated with uranium deposits.

Acknowledgments

This project was funded by Natural Resources of Canada through the Targeted Geoscience Initiative Four (TGI-4) program; a Research Affiliate Program Bursary to EEA and a grant to KH. We thank Eric G. Potter, science leader for the TGI-4 uranium ore system project, at the Geological Survey of Canada, for his continuous support. Cameco Corp provided their logistic support for our field work at the McArthur River mine. Special thanks extend to Gerard Zaluski and Tom Kotzer, as well as Aaron Brown, Doug Adams, Remi Labelle, and Brian McGill for their help and useful suggestions. We also thank Glenn Poirier of the Museum of Nature for his help with SEM and EMPA analysis, and Zhaoping Yang of the Geological Survey of Canada for her help during the LA ICP-MS analysis. We also extend many thanks to the Associate Editor, Julien Mercadier, and journal reviewers, David Quirt and unknown, of this manuscript.

References

Adlakha, E.E., Hattori, K., Zaluski, G., Kotzer, T., and Potter, E.G. (2014) Alteration within the basement rocks associated with the P2 fault and the McArthur River uranium deposit, Athabasca Basin. Geological Survey of Canada Open File 7462, 35 p, doi:10.4095/293364

Alexandre, P., Kyser, K., Polito, P., and Thomas, D. (2005) Alteration mineralogy and stable isotope geochemistry of Paleoproterozoic basement-hosted unconformity-type uranium deposits in the Athabasca Basin, Canada. Economic Geology, 100, 1547–1563.

Alexandre, P., Kyser, K., Jiricka, D., and Witt, G. (2012) Formation and evolution of the Centennial unconformity-related uranium deposit in the South-Central Athabasca Basin, Canada. Economic Geology, 107, 385 – 400.

Annesley, I. R., Madore, C., and Portella, P. (2005) Geology and thermotectonic evolution of the western margin of the Trans-Hudson Orogen: evidence from the eastern sub-Athabasca basement, Saskatchewan. Canadian Journal of Earth Sciences, 42(4), 573-597.

Beaufort, D., Patrier, P., Laverret, E., Bruneton, P., and Mondy, J. (2005) Clay alteration associated with Proterozoic unconformity-type uranium deposits in the East Alligator Rivers uranium field, Northern Territory, Australia. Economic Geology, 100(3), 515-536.

Bronkhorst, D., Mainville, A.G., Murdock, G.M., and Yesnik, L.D. (2012) McArthur River Operation Northern Saskatchewan, Canada: National Instrument 43-101 Technical Report.

Cuney, M., Brouand, M., Cathelineau, M., Derome, D., Freiberger, R., Hecht, L., Kister, P., Lobaev, V., Lorilleux, G., Peiffert, C. and Bastoul, A.M. (2003) What parameters control the high grade – large tonnage of the Proterozoic unconformity related uranium deposits?, in Cuney, M., ed., Uranium Geochemistry 2003, International Conference, April 13-16 2003, Proceedings: Unité Mixte de Recherche CNRS 7566 G2R, Université Henri Poincaré, Nancy, France, 123-126.

Derome, D., Cathelineau, M., Cuney, M., Fabre, C., Lhomme, T., and Banks, D. A. (2005) Mixing of sodic and calcic brines and uranium deposition at McArthur River, Saskatchewan, Canada: a Raman and laser-induced breakdown spectroscopic study of fluid inclusions. Economic Geology, 100(8), 1529-1545.

Dill, H.G. (2001) The geology of aluminium phosphates and sulfates of the alunite group minerals: a review. Earth-Science Reviews, 53(1), 35-93.

Gall, Q., and Donaldson, J.A. (2006) Diagenetic fluorapatite and aluminum phosphate sulfate in the Paleoproterozoic Thelon Formation and Hornby Bay Group, northwestern Canadian Shield. Canadian Journal of Earth Sciences, 43(5), 617-629.

Gaboreau, S., Beaufort, D., Vieillard, P., Patrier, P., and Bruneton, P. (2005) Aluminum phosphate–sulfate minerals associated with Proterozoic unconformity-type uranium deposits in the East Alligator River Uranium Field, Northern Territories, Australia. The Canadian Mineralogist, 43(2), 813-827.

Gaboreau, S., Cuney, M., Quirt, D., Beaufort, D., Patrier, P., and Mathieu, R. (2007) Significance of aluminum phosphate-sulfate minerals associated with U unconformity-type deposits: The Athabasca Basin, Canada. American Mineralogist, 92(2-3), 267-280.

Hajnal, Z., White, D.J., Takacs, E., Gyorfi, I., Annesley, I.R., Wood, G., and Nimeck, G. (2010) Application of modern 2-D and 3-D seismic-reflection techniques for uranium exploration in the Athabasca Basin. Canadian Journal of Earth Sciences, 47(5), 761-782.

Hoeve, J., and Sibbald, T. I. (1978) On the genesis of Rabbit Lake and other unconformity-type uranium deposits in northern Saskatchewan, Canada. Economic Geology, 73(8), 1450-1473.

Hoeve, J., Rawsthorne, K., and Quirt, D. (1981) Uranium metallogenetic studies: Collins Bay B Zone, II. Clay mineralogy. In: Summary of Investigations 1981, Saskatchewan Geological Survey, Miscellaneous Report 81(4), 73-76.

Hoeve, J., and Quirt, D.H. (1984) Mineralization and host-rock alteration in relation to clay mineral diagenesis and evolution of the Middle Proterozoic Athabasca Basin, Northern Saskatchewan, Canada. Saskatchewan Research Council, Technical Report 189, 189 p.

Jambor, J. L. (1999) Nomenclature of the alunite supergroup. The Canadian Mineralogist, 37, 1323-1341.

Jefferson, C.W., Thomas, D.J., Gandhi, S.S., Ramaekers, P., Delaney, G., Brisbin, D., Cutts, C., Portella, P., and Olson, R. A. (2007) Unconformity-associated uranium deposits of the Athabasca basin, Saskatchewan and Alberta; in EXTECH IV: Geology and Uranium EXploration TECHnology of the Proterozoic Athabasca Basin, Saskatchewan and Alberta, Geological Survey of Canada Bulletin, 588, 23-67.

Ketris, M.P., and Yudovich, Y.E. (2009) Estimations of Clarkes for carbonaceous biolithes: World averages for trace element contents in black shales and coals. International Journal of Coal Geology, 78(2), 135-148.

Laverret, E., Mas, P. P., Beaufort, D., Kister, P., Quirt, D., Bruneton, P., and Clauer, N. (2006) Mineralogy and geochemistry of the host-rock alterations associated with the Shea Creek unconformity-type uranium deposits (Athabasca Basin, Saskatchewan, Canada). Part 1. Spatial variation of illite properties. Clays and clay minerals, 54(3), 275-294.

Lewry, J.F., and Sibbald, T. (1980) Thermotectonic evolution of the Churchill province in northern Saskatchewan. Tectonophysics, 68, 45–82.

Longerich, H. P., Jackson, S. E., and Günther, D. (1996) Inter-laboratory note. Laser ablation inductively coupled plasma mass spectrometric transient signal data acquisition and analyte concentration calculation. Journal of Analytical Atomic Spectrometry, 11(9), 899-904.

Macdonald, C. (1985) Mineralogy and geochemistry of the sub-Athabasca regolith near Wollaston Lake. Geology of Uranium Deposits: Canadian Institute of Mining and Metallurgy Special, 32, 155-158.

McDonough, W.F., and Sun, S.S. (1995) The composition of the Earth. Chemical Geology, 120(3), 223-253.

McGill, B., Marlatt, J., Matthews, R., Sopuck, V., Homeniuk, L., and Hubregtse, J., (1993) The P2 North uranium deposit, Saskatchewan, Canada. Exploration and Mining Geology, 2(4), 321-333.

McKechnie, C. L., Annesley, I. R., and Ansdell, K. M. (2012) Medium-to low-pressure pelitic gneisses of Fraser Lakes Zone B, Wollaston Domain, northern Saskatchewan, Canada: mineral compositions, metamorphic P–T–t path, and implications for the genesis of radioactive abyssal granitic pegmatites. The Canadian Mineralogist, 50(6), 1669-1694.

Mercadier, J., Cuney, M., Cathelineau, M., and Lacorde, M. (2011) U redox fronts and kaolinisation in basement-hosted unconformity-related U ores of the Athabasca Basin (Canada): late U remobilisation by meteoric fluids. Mineralium Deposita, 46(2), 105-135.

Mercadier, J., Richard, A., and Cathelineau, M. (2012).Boron-and magnesium-rich marine brines at the origin of giant unconformity-related uranium deposits: δ11B evidence from Mg-tourmalines. Geology, 40(3), 231-234.

Quirt, D., Kotzer, T., and Kyser, T.K. (1991) Tourmaline, phosphate minerals, zircon and pitchblende in the Athabasca Group: Maw Zone and McArthur River areas. Saskatchewan. Summary of Investigations 1991, Saskatchewan Geological Survey Miscellaneous Report 91-4, 11.

Quirt D.H. (2001) Kaolinite and dickite in the Athabasca Sandstone, Northern Saskatchewan, Canada. Saskatchewan Research Council, Publication No. 10400-16D01.

Pe-Piper, G., and Dolansky, L.M. (2005) Early diagenetic origin of Al phosphate-sulfate minerals (woodhouseite and crandallite series) in terrestrial sandstones, Nova Scotia, Canada. American Mineralogist, 90(8-9), 1434-1441.

Ramaekers, P., Jefferson, C.W., Yeo, G.M., Collier, B., Long, D.G.F., Drever, G., McHardy, S., Jiricka, D., Cutts, C., Wheatley, K., Catuneau, O., Bernier, S., Kupsch, B., and Post, R.T. (2007) Revised geological map and stratigraphy of the Athabasca Group, Saskatchewan and Alberta; in EXTECH IV: Geology and Uranium EXploration TECHnology of the Proterozoic Athabasca Basin, Saskatchewan and Alberta. Geological Survey of Canada Bulletin, 588, 155-192.

Richard, A., Banks, D.A., Mercadier, J., Boiron, M.C., Cuney, M., and Cathelineau, M. (2011) An evaporated seawater origin for the ore-forming brines in unconformity-related uranium deposits (Athabasca Basin, Canada): Cl/Br and δ^{37}Cl analysis of fluid inclusions. Geochimica et Cosmochimica Acta, 75(10), 2792-2810.

Riegler, T., Lescuyer, J.L., Wollenberg, P., Quirt, D., and Beaufort, D. (2014) Alteration related to uranium deposits in the Kiggavik–Andrew Lake structural trend, Nunavut, Canada: New insights from petrography and clay mineralogy. The Canadian Mineralogist, 52, 27- 45.

Ryan, P, Kim, J, Hattori, K., and Thompson, A (2013) Dissolved arsenic in a fractured slate aquifer system, northern Appalachians, USA: Influence of bedrock geochemistry, groundwater flow paths, redox and ion exchange. Applied Geochemistry, 39, 181-192,

Spötl, C. (1990) Authigenic aluminium phosphate-sulfates in sandstones of the Mitterberg Formation, Northern Calcareous Alps, Austria. Sedimentology, 37(5), 837-845.

Smedley, P.L., and Kinniburgh, D.G. (2002) A review of the source, behaviour and distribution of arsenic in natural waters. Applied Geochemistry, 17(5), 517-568.

Stoffregen, R.E., Alpers, C.N., and Jambor, J.L. (2000) Alunite-jarosite crystallography, thermodynamics, and geochronology. Reviews in Mineralogy and Geochemistry, 40(1), 453-479.

Addendum

A discussion of the Ce and Eu anomalies exhibited by the APS minerals was requested by an examiner of this thesis. APS minerals presented in this paper exhibit different Ce and Eu anomalies: in the Red Green Zone, As-rich APS minerals exhibit strong positive Ce anomalies, in the Bleached Zone Sr-Ca-SO_4^{2-} rich APS minerals exhibit negative Ce anomalies, and along the P2 fault LREE-P rich APS minerals have slightly negative Ce anomalies and slightly positive Eu anomalies.

While most REE occur in the trivalent oxidative state, Ce and Eu are redox sensitive forming Ce^{3+}/Ce^{4+} and Eu^{2+}/Eu^{3+} cations, respectively. In solution, Ce and Eu anomalies are directly related to the redox conditions. However, several factors may control the anomalies in APS minerals; for example, ionic radii and preferential incorporation of ions by other minerals.

Rare earth elements are accommodated in the A-site of APS minerals [general chemical formula = $AB(XO_4)OH_4$]. According to Mordberg et al. (2008), larger ions are more compatible than smaller ions in the A-site. This suggests that Ce^{3+} and Eu^{2+} would most likely occupy the A site.

The geochemical properties of Ce^{4+} are similar to that of Mn^{4+}. Under oxidizing conditions at low temperatures, Ce^{4+} may be preferentially incorporated on Mn- and Fe-oxides. Thus the chondrite normalized REE data of APS minerals which co-precipitate with Mn- and Fe-oxides may exhibit negative Ce anomalies. Furthermore, Ce^{4+} is adsorbed on the surface of Fe-oxides and such Ce is resorbed easily during minor redox changes.

In the case of Eu, APS minerals formed under reducing conditions may exhibit positive Eu anomalies, as Eu^{2+} is accommodated over Eu^{3+}..

Table 3.3. Addendum. LA-ICPMS data of APS (ppm).

Sample:	**44**		**63**		**85**
# grains	3	1σ	3	1σ	1
Sm	2000	69	2200	440	2800
Eu	760	87	800	200	1300
Gd	820	68	450	69	810
Eu/Eu*	1.8		2.4		2.6

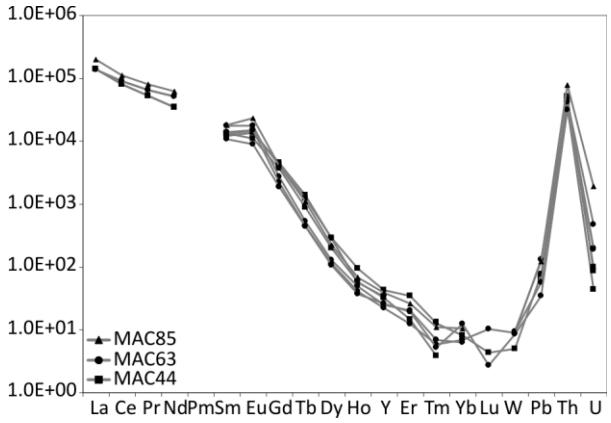

Figure 3.6 Addendum. A space representing Pm has been added to the elemental plot to illustrate the positive Eu anomaly.

Reference:

Mordberg, L. E., Stanley, C. J., & Germann, K. (2000). Rare earth element anomalies in crandallite group minerals from the Schugorsk bauxite deposit, Timan, Russia. European Journal of Mineralogy, 12(6), 1229-1243.

CHAPTER 4.

Paragenesis and composition of tourmaline types along the P2 fault and McArthur River uranium deposit, Athabasca Basin, Canada

Erin E. Adlakha and Keiko Hattori

The Canadian Mineralogist 2016, in press

Abstract

The P2 fault, a 13 km long steeply dipping reverse fault, is the main structural control of the McArthur River uranium deposit in the eastern Athabasca Basin, northern Saskatchewan, Canada. Three types of tourmaline were observed in the metasedimentary basement rocks along the P2 fault: early oxy-schörl [$(\square_{0.37}Na_{0.47}Ca_{0.16})(Mg_{0.72}Fe^{2+}_{1.30}Ti_{0.07}Al_{0.91})Al_6(Si_{5.79}Al_{0.21}O_{18})(BO_3)_3OH_3(F_{0.08}OH_{0.29}O_{0.63})$, where $\square$ = vacancy] of metamorphic-anatectic origin, and hydrothermal oxy-dravite [$(\square_{0.18}Na_{0.57}Ca_{0.23}K_{0.02})(Mg_{1.93}Fe^{2+}_{0.62}Ti_{0.15}Al_{0.29})Al_6(Si_{5.93}Al_{0.07}O_{18})(BO_3)_3OH_3(F_{0.20}OH_{0.23}O_{0.57})$] and magnesio-foitite [$(\square_{0.77}Na_{0.20}Ca_{0.02}K_{0.01})(Mg_{1.99}Fe^{3+}_{0.07}Al_{0.92})Al_{6.00}(Si_{6.00}O_{18})(BO_3)_3(OH_3)(F_{0.04}OH_{0.71}O_{0.25})$]. Oxy-schörl formed in granitic pegmatites, a partial melt product of the metasediments during their peak metamorphism. Oxy-dravite formed from hydrothermal fluids after the peak metamorphism but before deposition of the Athabasca sandstones, whereas magnesio-foitite is a product of later, low temperature hydrothermal activity. Both oxy-schörl and oxy-dravite are coarse-grained (from 500 μm, up to 1 cm), whereas magnesio-foitite occurs as radial aggregates of fine, prismatic crystals (<15 μm in width). Magnesio-foitite crystallized together with sudoite, illite and "APS" minerals (alunite-supergroup LREE-rich aluminum phosphate-sulphate minerals) along the entire studied length (~ 7km) of the P2 fault and is abundant in proximity to the Zone 2 ore body of the McArthur River deposit. In the ore zone, the assemblage occurs with uraninite and is partially overprinted by late, remobilized uraninite and sudoite. Therefore, magnesio-foitite is likely contemporaneous with the main stage of uranium mineralization. It is characterized by a high vacancy in its X-site (0.70 – 0.85 *apfu*) and high Al in its Y-site (0.70 – 1.12 *apfu*), suggesting that magnesio-foitite likely replaced pre-existing high Al phases, such as kaolin and sudoite. The occurrence of magnesio-foitite along the entire P2 fault, in areas of mineralization and apparently barren areas, suggests chemically similar fluids travelled along the entire P2 fault, but only produced

ore in localized areas.

4.0 Introduction

The Athabasca Basin hosts world-class unconformity-type uranium deposits, including the McArthur River deposit. Prevalent models for uranium mineralization invoke an oxidizing, highly saline brine (25 – 35 wt% NaCl equiv.), with a marine component, generated during basin development (*e.g.*, Hoeve & Sibbald 1978, Kotzer & Kyser 1995; Alexandre *et al*. 2005, Derome *et al.* 2005, Richard *et al.* 2011, Mercadier *et al.* 2012). Quartz-hosted fluid inclusions in ore breccias indicate that two types of fluids were present during mineralization, i) an earlier, acidic, NaCl-rich, uranium-bearing brine and ii) an evolved $CaCl_2$-rich brine assumed to have formed by the interaction of the earlier brine with basement rocks (Derome *et al.* 2005, Richard *et al.* 2010, Richard *et al.* 2011, Richard *et al.* 2012). Uranium deposition was caused by the reduction of U^{6+} to U^{4+} in the fluids. Proposed reductants include minerals (e.g., graphite, Fe^{2+}-bearing chlorite and sulphides) within the basement rocks and faults (*e.g.,* Hoeve & Sibbald 1978, Alexandre *et al*. 2005), and reducing fluids released from the basement (Hoeve & Sibbald 1978, Hoeve & Quirt, 1984, Kotzer & Kyser 1995, Kyser *et al.* 2000, Alexandre *et al.* 2005).

The uranium deposits commonly occur at the intersection of the unconformity with basement faults along graphite-bearing pelitic rocks (*e.g.* the P2 fault of the McArthur River deposit). Considering the spatial association of basement faults with mineralization, the faults are assumed to have acted as conduits for fluids of either basin or basement origin (*e.g.,* Hoeve and Quirt, 1984). However, detailed petrographic work of basement rocks along the faults are lacking. Therefore, the exact role of the faults during mineralization is not well understood.

Hydrothermal tourmaline is ubiquitous in close proximity to the Athabascan uranium deposits (i.e., Hoeve & Sibbald 1978, Alexandre *et al.* 2005, Rosenberg & Foit 2006, Cloutier *et al.*

2009, Mercadier et al. 2012), but it is not common in other uranium deposits. No tourmaline has been reported from unconformity-type uranium deposits in the Thelon Basin in northern Canada and the East Alligator Rivers district in northern Australia, both of which are considered to be similar in age and genesis to the deposits of the Athabasca Basin. Reported occurrences of tourmaline with uranium deposits are few, including the Mortimer Hills granitic pegmatite (Carter 1984) and the Jaduguda vein-type uranium (-Cu-Fe) deposit, India (Pal *et al.* 2010).

Tourmaline can accommodate many elements in its crystal structure (*e.g.*, Hawthorne & Dirlam 2011). Therefore, its composition is useful in evaluating the geological environments from which it crystallized (e.g., Copjakova *et al.* 2013, 2015). Two types of tourmaline have been reported in proximity to uranium deposits of the Athabasca Basin: an early dravitic tourmaline that occurs in the basement and as detrital grains in the sandstones of the Basin, and a later, hydrothermal alkali-deficient tourmaline (*e.g.* Rosenberg & Foit 2006, Mercadier *et al.* 2012, Ng *et al.* 2013). The timing of this later, hydrothermal tourmaline with respect to uranium deposition is contentious. Opinions range from pre-ore (Ng *et al.* 2013), syn-ore (Hoeve & Sibbald 1978, Kotzer & Kyser 1995, Fayek & Kyser 1997, Derome *et al.* 2005, Mercadier et al. 2012) to post-ore crystallization (Alexandre et al. 2005). This paper presents the occurrence and compositions of tourmaline in basement rocks along the P2 fault, Athabasca Basin, and discusses the i) timing and paragenesis of different types of tourmaline, ii) hydrothermal fluids responsible for tourmaline crystallization, and iii) role of the P2 fault during uranium mineralization. This information is useful in identifying fertile structures associated with uranium deposits.

4.1 Geological setting

4.1.1 Regional geology

The Mesoproterozoic Athabasca Basin is underlain by the Archean to Paleoproterozoic

western Rae and eastern Hearne Provinces (Figs 4.1A,B). The Hearne Province is comprised of accreted domains: (from west to east) the Peter Lake Domain, the Virgin River Domain, the Mudjatik Domain and the Wollaston Domain. The Paleoproterozoic Wollaston Domain is a NE-striking fold-thrust belt comprising Archean granitoids overlain by Paleoproterozoic metasediments of the Wollaston Group. The Wollaston Group hosts, or occurs immediately below, most uranium deposits of the eastern Athabsca Basin (Fig. 4.1B). It is a package of graphitic and non-graphitic pelite, semi-pelite and paragneiss with lenses of minor calc-silicate, arkose and quartzite (McGill et al. 1993), which was metamorphosed during the Trans-Hudson Orogeny (ca. 1.8-1.9 Ga; Lewry & Sibbald 1980) under upper amphibolite facies conditions (Annesley *et al.* 2005). Granitic pegmatite lenses in the metasedimentary rocks formed through local partial melting during peak metamorphism (Annesley *et al.* 2005). Since quartzite is resistant to weathering and erosion, it forms prominent "ridges", or paleo-topographic highs, which elevate the unconformity. It has been noted that many uranium deposits of the Athabasca Basin are spatially associated with quartzite ridges (Jefferson *et al.* 2007; Kerr, 2010).

Substantial weathering/erosion of the basement rocks beginning at ca. 1.73 Ga occurred before the deposition of the Athabasca Group sandstones (Kyser *et al.* 2000). The basement rocks at and below the unconformity show a vertical alteration profile comprising an uppermost Bleached Zone of kaolinite and illite, a Red Zone of hematite and kaolinite, and a lower Green Zone of sudoite and illite (Macdonald 1985, Adlakha *et al.* 2014).

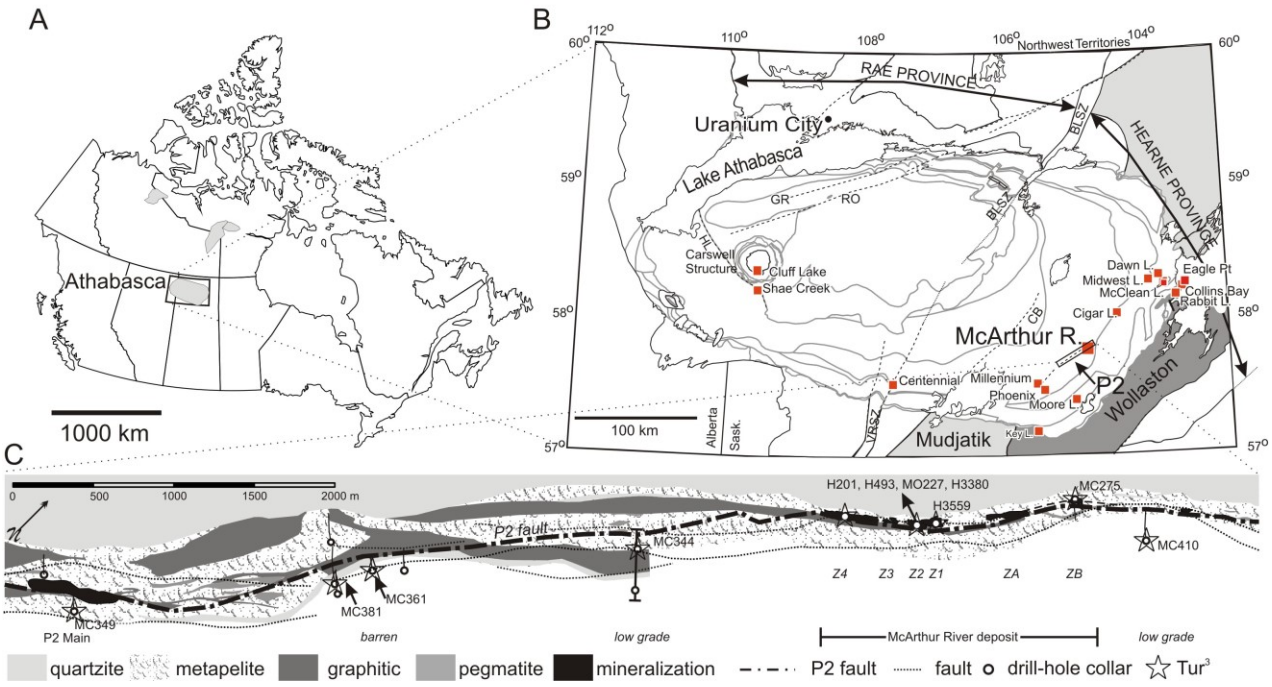

Figure 4.1. A) A map of Canada showing the location of the Athabasca Basin in Northern Saskatchewan. B) A map showing the location of the major uranium deposits, including the McArthur River deposit, and structures, including the P2 fault, in the Athabasca Basin (modified from Jefferson *et al*., 2007) The south-eastern margin of the Athabasca Basin is underlain by the Wollaston and Mudjatik Domains of the basement. Major shear zones: BB = Black Bay, BLSZ= Black Lake, CB = Cable Bay, GR = Grease River, RO = Robbilard, VRSZ = Virgin River. C) A schematic geological map of the basement rocks showing the P2 fault, and the locations of sampled drill-holes and mineralized zones. Drill-holes in unmineralised areas occur along the southwest P2 fault and drill-holes proximal to low-grade mineralization occur along the southwest and northeast portions of the P2 fault. Drill-holes containing Tur3 (associated with U mineralization) are starred. Studied drillholes are labelled and correspond to the samples listed in Table 4.1. Z# = Zone # ore body. Modified from Adlakha & Hattori (2015).

The Athabasca Basin is comprised of a succession of fluvial, to shallow marine arenite currently preserved at a maximum thickness of 1500 m in the centre of the basin (Ramaekers *et al.* 2007). At McArthur River, the Athabasca Group sandstones have a thickness of 500 m: quartz

arenite and basal quartz-pebble conglomerate of the Read Formation (RF), and the overlying sandstones of the Manitou Falls Formation which comprises the Bird Member (MFb), Collins Member (MFc) and Dunlop Member (MFd) in ascending order (Ramaekers *et al.* 2007).

4.1.2 Geology of the McArthur River deposit and P2 reverse fault

The McArthur River deposit contains six ore bodies (Zones 1-4, and A-B) with a collective strike over 1700 m (Fig. 4.1C). Uranium mineralization is constrained to the intersection of the P2 fault and the unconformity between the underlying metamorphic rocks of the Wollaston Group and overlying sandstones of the Athabasca Group. All ore bodies, with the exception of Zone 2, are hosted within the RF sandstone. The Zone 2 ore body is hosted predominately by graphitic pelites below the unconformity and is additionally bound by the Vertical Quartzite fault (VQ) to the west and 100 - 110° striking faults below the ore body. The VQ separates metapelites from a "quartzite ridge" near the unconformity (Fig. 4.1C). The ore bodies are enveloped by alteration haloes of sudoite, illite, tourmaline, and minor dickite (McGill *et al.* 1993).

The 13 km long P2 reverse fault, striking 040-045°/45°SE, is a broad deformation zone (McGill *et al.* 1993, Hajnal *et al.* 2007) along graphitic pelites that formed during the Trans-Hudson Orogeny (ca. 1.8-1.9 Ga; Lewry & Sibbald 1980). Reactivations of the fault produced splays in the Athabasca sandstones and resulted in the vertical displacement of the unconformity (up to 80 m) where the basement rocks were faulted over the lowermost sandstones (McGill *et al.* 1993). High-grade uranium mineralization of the McArthur River deposit is found at the nose of the uplifted basement (all except Zone 2) or within the basement wedge of the P2 fault (Zone 2).

Relatively unaltered basement rocks occur > 50 m from faults and the unconformity. They comprise garnet, biotite, feldspar, and quartz with or without pyrite, cordierite, graphite, and muscovite (Adlakha *et al.* 2014). They may contain accessory zircon, monazite and apatite and

commonly show minor alteration whereby cordierite and biotite are replaced by chlorite and feldspar by illite. The mineralogy of relatively unaltered pegmatite is biotite, feldspar and quartz with accessory zircon, monazite and apatite and with or without muscovite, garnet and pyrite.

The majority of rocks along the P2 fault are light green due to alteration forming sudoite (Al- and Mg-rich, di-trioctahedral chlorite), illite, tourmaline, sulphides and "APS" minerals (alunite-supergroup LREE-rich aluminum phosphate sulphate minerals) (McGill *et al.* 1993, Adlakha *et al.* 2014, Adlakha & Hattori 2015). Rocks are locally stained red by hematite, or buff white (frequently termed "bleached") due to high abundances of illite and/or kaolinite. Bleached rocks are common, especially in close proximity to mineralization and the unconformity (McGill *et al.* 1993). The area around the Zone 2 ore body is intensely altered to form sudoite and magnesio-foitite (Adlakha *et al.* 2014) and fault gouge is common.

4.2 Sampling & Methods

A total of 192 samples were collected from 27 drill cores along and within proximity to the P2 fault zone, spanning from the McArthur River mine site to approximately 7 km southwest (Fig. 4.1). Most samples are hydrothermally altered metasedimentary rocks, pegmatite and quartzite from the basement, with minor RF sandstone along the P2 fault. A total of 139 polished thin sections were made and were examined using a petrographic microscope with transmitted and reflected light sources.

Representative samples were selected for detailed mineralogical and textural analysis using a JEOL 6610LV scanning electron microscope at the University of Ottawa on carbon-coated sections because most alteration minerals are very fine-grained. Minerals were identified using energy-dispersive spectroscopy with a spectrum acquisition time of 40 seconds and an accelerating voltage of 20 kV.

Table 4.1. Sample descriptions.

area[a]	DDH	sample	rock type[a]	depth (m)[b]	proximity to ore	Tur occurrence	Mineralogy[c]
um	MC361	MAC109	pel/peg bx	587.6	> 500 m	Tur2 100 µm - 4 mm	Qz1,Qz2, Py1, Py2, Ilt1, Gr, Ms, Fe-ox, Sud1, Ilt2
	MC361	MAC110	pel bx	590	> 500 m	Tur2 100 µm Tur3 <50 µm	Qz1, Gr, Py1, Ms, APS, Ilt2, Sud,
	MC361	MAC111	peg	581.6	> 500 m	Tur2 100 µm	Qz1, Gr, Py1, Py2 Qz2, Ms, Ilt1, Fe-ox, Kln, Ilt2, APS, Sud1
	MC361	MAC122	ss	493	> 500 m	Tur3 vein 1 mm	Qz, Fe-ox, Kln, Ilt2, Sud1
	MC381	MAC436	peg	603	> 500 m	Tur2 < 100 µm Tur3 <50 µm	Qz1, Qz2, Ilt1, Gr, Ilt2, Sud, Rt
lg	MC370	MAC29	pel/peg bx	560.2	< 1 m	Tur3 aggregates & disseminations	Qz1, Ap, Zr, Gr, Ms, Kln, Fe-ox1, Ilt2, Sud1 APS, Fe-ox
	MC370	MAC32	ss bx	543	20 m	Tur3 veinlets (<500 µm)	Q*zd* , Ms*d* Z*rd* , Qz3, Kln, Il2, Sud1, APS
	MC349	MAC98	pel bx	578	< 10 m	Tur2 100 - 200 µm Tur3 vein 300 - 500 µm	Qz1, Qz2, Fe-ox, U1, U2, Kln, Ilt2, Sud1
	MC349	MAC99	pel/peg bx	573	< 10 m	Tur2 100 - 500 µm oriented vein Tur3 aggregates and veinlets <500 µm	Qz, Qz2, Py, Fe-ox, Ilt2, Sud, APS
Z1	H3559	MAC201	pel/peg bx	-	20 m	Tur2 <500 µm in Tur vein Tur3 aggregates <500 µm	Qz1, Qz2, Gr, Py1, Ms, Fe-ox, Ilt1, Sud1, Py2,
Z2	H201	MAC69	pel	-	< 20 m	Tur3 aggregates <500 µm	Qz1, Py1, Gr, Zr, Ilt1, Sud1, APS
	H201	MAC70	pel bx	-	< 20 m	Tur3 aggregates <100 µm	Qz1?, Gr, Ilt2, Sud1
	H493	MAC85	peg/pel bx	-	20 m	Zoned Tur1 Tur2 1 mm Tur3 <10 µm	Qz1, Qz2, Py1, APS, Sud1, Ilt2
	H493	MAC86	pel bx	-	10 m	Tur3 aggregates 200 µm	Qz1?, Ms, Gr, Py1, Ilt2, Sud1
	MO227	MAC146	peg bx	-	n.d.	Tur3 vein 2 mm	Qz1, Gr, Py, Sud1, Ilt2, Fe-ox,
	H3380	MAC423	pel	-	ore sample	Tur2 25 µm Tur3 aggregates >500 µm	Qz1, Bt, Qz2, Py1, Fe-Mg Chl, Ilt2, Sud1, U1, U2, Fe-ox, Py2 Sud2

(Extended to Next Page)

Table 4.1.— *Extended*

area[a]	DDH	sample	rock type[a]	depth (m)[b]	proximity to ore	Tur occurrence	Mineralogy[c]
	H3380	MAC425	pel	-	ore sample	Tur3 sphericules 100 µm	Qz1, Qz2, Ms, Fe-Mg Chl, Py1, Sud1,Ilt, U1, APS, U2, Py2
ZB	MC274	MAC440	ss	502.4	ore sample	Tur2 detrital Tur3 aggregates 150 µm	Qz*d* , Qz3, U1, Kln
MFd	MC274	MAC462	ss	93.1	> 400 m	Tur3 aggregates 150 µm	Qz*d* , Qz3, Kln

a: um = unmineralized, lg = low grade, Z1 = Zone 1, Z2 = Zone 2, ZB = Zone B, MFd = Maitous Falls Formation D, bx = breccia, peg = pegmatitie, pel = pelite
b: sample depth in drIlt-hole collared from surface. Depths are not shown for underground collared drilholes
c: Ap = apatite; APS = alumino-phosphate-sulphate minerals; Bt= biotite Clc = clinochlore; Dck = dickite; Fe-Mg chl = Fe-Mg Chlorite; fg = fine-grained; Gr = graphite; Ms = muscovite; Ilt = illite; Py = pyrite; Qz = quartz; Sud = sudoite, U = uraninite; Xtm = xenotime; Zrn = zircon
"*d* " after mineral abbreviations indicates detrital mineral.

Nineteen samples representing different environments were chosen for chemical analysis of tourmaline (Table 4.1): 5 samples (4 basement, 1 RF sandstone) from barren areas of the P2 fault (from DDH MC361 and MC381; Fig. 4.1), 4 samples (3 basement, 1 RF sandstone) from proximal (< 20 m) to sandstone-hosted low-grade mineralization (from DDH MC370, MC349; Fig. 4.1), 1 sample from the basement below the Zone 1 ore body, 7 samples from Zone 2 ore body and associated alteration halo, and 1 sample of the Zone B ore body (MC274; Fig. 4.1). One sandstone sample of MFd was selected for comparison (MC274; Fig. 4.1).

Major and minor element abundance in tourmaline was quantitatively determined at the University of Ottawa using a JEOL 8230 electron-probe microanalyzer (EPMA) at an accelerating voltage of 15 kV, and with a beam current of 20 nA and focused to 5-10 μm in diameter depending on grain size. Data collection times for peak and background were 20 s for all elements except for K and Si (10 s), and F and Cl (50 s). The standards are as follows: sanidine (Si$K\alpha$, Al$K\alpha$, K$K\alpha$), rutile (Ti$K\alpha$), hematite (Fe$K\alpha$), tephroite (Mn$K\alpha$), sphalerite (Zn$L\alpha$), diopside (Mg$K\alpha$, Ca$K\alpha$), albite (Na$K\alpha$), tugtupite (Cl$K\alpha$), sanbornite (Ba$L\alpha$), fluorite (F$K\alpha$), and celestine (Sr$L\alpha$). Data reduction was carried out using a ZAF routine.

The chemical formula of tourmaline was calculated based on the ideal formula $XY_3Z_6(T_6O_{18})(BO_3)_3V_3W$, which assumes 3 B in the B-site, 18 O forming the T-site and 3 OH in the V-site (Tables 4.2 & 4.3). As suggested by Rosenberg and Foit (2006), the stoichiometric proportions of tourmaline were normalized to 15 cations (Y + Z + T sites). For cation site assignment, the T-site was filled first with Si^{4+}, then Al^{3+} to sum 6 cations. The Z-site was occupied by Al^{3+}, and the remaining Al^{3+} was assigned to the Y-site. The Y-site was filled by Ti^{4+}, Fe^{2+} or Fe^{3+} and Mg^{2+}. All Ca^{2+}, K^+ and Na^+ were assigned to the X-site. The W-site accommodates F^-, OH^- and O^{2-}. The proportions of OH^- and O^{2-} were calculated to compensate for excess cation

charges. Fe was assumed to be Fe^{2+} for Tur1 and 2 (formula charge balance does not require Fe^{3+} which would further increase the already high $^{W}O^{2-}$), and Fe^{3+} for Tur3 (required due to low sum of formula positive charges resulting in anion deficiency). Moreover, the assignment of Fe^{2+} in Tur1 and Tur2 is supported by the following evidence; i) the fO_2 is expected to be low in metapelites due to the buffer by abundant graphite, and ii) any Fe^{3+}, if present, is preferentially incorporated into co-existing muscovite and biotite over tourmaline (Dyar *et al.* 2002). Rosenberg and Foit (2006) also suggested Fe^{3+} for Tur3 due to presence of abundant hematite in the hydrothermal assemblage.

4.3 Results

4.3.1 Tourmaline types and assemblages

Textural analysis indicates that three distinct types of tourmaline occur along the P2 fault. Tur1 is the least common tourmaline type and occurs only as relic grains (>2 mm), rimmed by Tur2, in a brecciated pegmatite lens (MAC85; Figs. 4.2A, 4.3A). It exhibits blue-green pleochroism under transmitted light microscope. It is difficult to evaluate the original mineral assemblage of Tur1 as it occurs as relic grains in altered pegmatite. However, the relic grains occur with plagioclase/feldspar, biotite and quartz (Qz1, Table 4.1) that were pseudomorphically replaced by illite and chlorite. The texture suggests that plagioclase/feldspar, biotite and quartz formed with Tur1.

Tur2 also occurs as relic grains and is most commonly found in altered pegmatite lenses, and quartz-tourmaline veins in metapelites (Figs. 4.2B, 4.3A-C). Less commonly, Tur 2 occurs as relic grains disseminated in altered metapelite (Figs. 4.3C,G). Tur2 is brown in hand specimens and exhibits brown-orange-yellow pleochroism in transmitted light (Figs. 4.3B,C). Tur2 forms subhedral-anhedral relic grains (0.2 – 2 mm) that display second order birefringence colours. Tur2

is associated with quartz (Fig. 4.3B); it commonly occurs as anhedral grains interlocked or completely surrounded by quartz (Qz2, Table 4.1) or as subhedral grains in quartz veins. It also commonly contains quartz inclusions (Fig. 4.3B). Tur2 shows a close spatial association with graphite and pyrite where graphite forms elongated, micaceous grains that commonly wrap around Tur2 grains (Figs. 4.3C,G). Anhedral to euhedral grains of pyrite (Py1, Table 4.1) occur in contact with Tur2 or quartz (Fig. 4.3A). The occurrence of Tur2 suggests that it formed in equilibrium with quartz, pyrite, and graphite. Some samples containing Tur2 contain relic biotite altered to "Fe-Mg chlorite" (intermediate composition between chamosite and clinochlore) and fine (>2 μm) to coarse-grained (>100 μm) illite (Fig. 4.3G). Fe-Mg chlorite and coarse-grained illite likely formed through the pseudomorphic replacement of earlier biotite and/or muscovite (Fig. 4.3G), although it is unclear whether this occurred contemporaneously with Tur2. Fine-grained illite replaces feldspar (Adlakha and Hattori 2014). The mineral assemblages of Tur1 and Tur2 are partially overprinted by Tur3 and associated minerals and the rims of Tur2 grains are commonly altered to fine-grained Tur3.

Tur3 forms aggregates of fine, prismatic to acicular crystals (up to 15 μm in width and 5 – 500 μm in length), which are blue in handspecimen and colorless in thin section (Figs. 4.2C, 4.3B-D). The aggregates are disseminated in clay minerals and form monomineralic veinlets (up to 0.5 cm; Figs. 4.2C, 4.3C,D). Aggregates of Tur3 may pseudomorphically replace earlier Tur2 or form around Tur2 grains with their c-axis perpendicular to the rim of Tur 2 (Figs. 4.3B,C). Along the P2 fault, Tur3 commonly occurs with sudoite (Sud1, Table 4.1), illite, and florencite-(Ce) (Figs. 4.3C,F-H; Table 4.1). The proportions of these minerals vary in locations, and illite is predominant in barren areas of the P2 fault, whereas sudoite is abundant proximal to mineralized areas including low-grade and high-grade mineralization. Quartz appears to be in disequilibrium

with Tur3 as it is resorbed in contact with Tur3 (Figs. 4.3B-D). Florencite occurs as small (> 20 μm) pseudocubes (Adlakha and Hattori 2015).

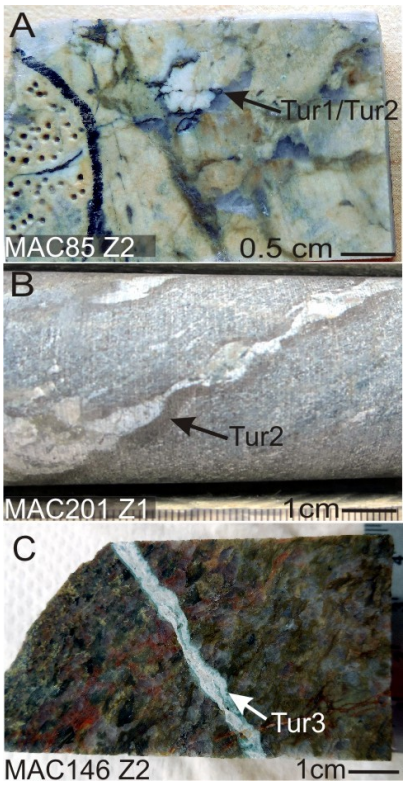

Figure 4.2. Photographs of drillcores containing tourmaline. A) Altered pegmatite (sample MAC85 from DDH H493 in Zone 2) containing zoned Tur1/Tur2 B) Tourmalinite (Tur2) vein in graphitic metapelite (sample MAC201 from DDH H3559 in Zone 1); C) Light blue Tur3 vein cross-cutting altered pegmatite (sample MAC146 from DDH H201 in Zone 2).

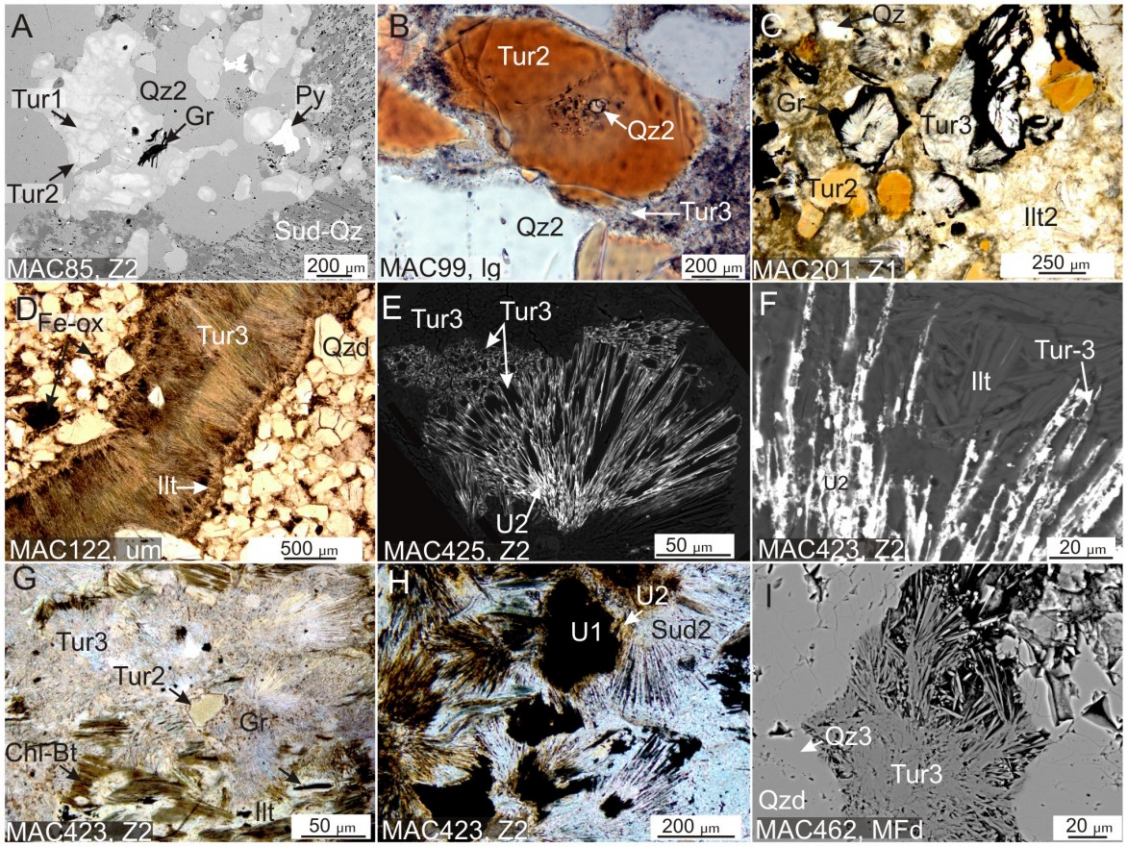

Figure 4.3. Photomicrographs and back-scattered electron (BSE) images of tourmaline. A) BSE image of rare zoned Tur2 with cores of Tur1 in pervasively altered pegmatite (sample MAC85 from DDH H493); B) Tur2 containing quartz inclusions, and rimmed by Tur3 in intensely altered metapelite from proximal to low grade mineralization (sample 99 from DDH MC349); C) Tur3 aggregates (likely pseudomorphs of earlier Tur2), partially resorbed Tur2 and quartz, and relic graphite (Gr) in illite of intensely altered metapelite (sample 201 from DDH H3559) below the Zone 1 ore body; D) Tur3 vein with marginal illite (Ilt) and Fe-oxide (Fe-ox) and partially resorbed quartz (Qz) in unmineralized (um) RF sandstone (sample MAC122 from MC361); E) Tur3 aggregate overprinted by remobilized uraninite (U2) in Zone 2 ore breccia (sample MAC425 from DDH 3380); F) Remobilized uraninite along grain boundaries between medium-grained illite and Tur3; G) An early assemblage of Tur2 with Fe-Mg chlorite (pseudomorphically replacing biotite; Chl-Bt), graphite and pyrite overprinted by Tur3 with recrystallized illite (sample MAC425 from DDH 3380); H) Brownish remobilized uraninite (U2) overprints opaque early uraninite (U1) and sudoite (Sud2) pseudomorphs of Tur3 (sample MAC423 from DDH H3380); I) BSE image of Tur3

interstitial to detrital quartz (Qz1) overgrown by quartz (Qz2) in MFd sandstone above Zone B ore body (sample MAC462 from DDH MC274).

Ore breccia from the Zone 2 ore body shows evidence for at least three distinct alteration events. The earliest produced Tur2 with quartz, pyrite, graphite, and Fe-Mg chlorite with fine-grained illite. This assemblage is partially overprinted by uraninite (U1, Table 4.1), sudoite (Sud1), coarse-grained illite (>10 μm in length), euhedral florencite, and rosettes of Tur3 (Figs. 4.3F-G). The final event appears significantly late and affected only local areas in limited scale. This is characterized by remobilized uraninite (U2) with sulphides (pyrite and lesser galena, Py2 in Table 4.1) and sudoite (Sud2) replacing Tur3 (Figs. 4.3E,F,H).

In the RF sandstones along the P2 fault, Tur2 occurs as detrital grains with quartz (Qz*d*, Table 4.1) and is overgrown by quartz (Qz3, Table 4.1), indicating that Tur2 formed before the deposition of the Athabasca sandstones. Tur3 in the RF forms monomineralic veinlets (MAC122; Fig. 4.3D; Table 4.1) or aggregates with sudoite, illite and APS minerals between detrital quartz grains (MAC32; Table 4.1). In the MFd, Tur3 occurs in pore space and embays quartz overgrowths of detrital quartz grains (Fig. 4.3I).

4.3.2 Distribution of tourmaline types along the P2 fault

Tur3 is more abundant than Tur2 in studied samples, although both types of tourmaline are found along the entire 7 km of the P2 fault studied. Tur3 is concentrated in intensely altered basement rocks near and within the Zone 2 ore body of the McArthur River deposit (observed in 21 of 30 samples and represented by MAC69, MAC70, MAC86, MAC146, MAC423, MAC425). Tur3 is sparse in barren areas of the P2 fault in the basement (3 of 18 barren samples and represented by MAC109, MAC110, MAC111). Tur3 proximal to low-grade mineralization is found in the basement rocks (MAC 29, MAC98, MAC99) along the P2 fault and within 5 m of the

unconformity (4 samples out of 13 proximal to low-grade mineralization contained Tur3).

For comparison, four tourmaline-bearing sandstones were studied. Three samples are of the lowermost RF sandstone from barren (MAC122), low-grade (MAC32) and mineralized (MAC440) areas of the P2 fault. The fourth sample (MAC462) is of the MFd sandstone directly above (>400 m) the Zone B deposit. Tur3 was observed in all four samples and Tur2 was observed in one sample of RF (MAC440). Tur1 was not observed in any of the sandstone samples.

4.3.3 Tourmaline composition

Tur1 is Fe-rich with an average formula of $(Na_{0.47}\square_{0.37}Ca_{0.16})(Fe^{2+}_{1.30}Al_{0.91}Mg_{0.7}Ti_{0.07})Al_6(Si_{5.79}Al_{0.21}O_{18})(BO_3)_3OH_3\ (O_{0.63}OH_{0.29}F_{0.08})$ where $\square$ is a vacancy. It contains high Na (Fig. 4.4A) and show considerable variations in Al (6.86 – 7.57 *apfu*), Fe (1.02 – 1.51 *apfu*) and Mg (0.34 – 1.17 *apfu*) (Table 4.2; Fig. 4.4).

Tur2 has an average composition of $(Na_{0.57}Ca_{0.23}\square_{0.18}K_{0.02})(Mg_{1.93}Fe^{2+}_{0.62}Al_{0.29}Ti_{0.15})Al_6(Si_{5.93}Al_{0.07}O_{18})(BO_3)_3OH_3(O_{0.57}OH_{0.23}F_{0.20})$ with little compositional variation among grains (n = 20) from different samples (Table 4.2). The composition of Tur2 grains is similar along the P2 fault independent of the distance from mineralization (Fig. 4.4).

Table 4.2. Average compositions of Tur1 and Tur2

Sample	MAC85cores		MAC85rim		MAC99		MAC109		MAC111		MAC201	
grains/pts	3/8		3/9		4/17		3/12		2/8		8/30	
	Tur1		Tur2		Tur2		Tur2		Tur2		Tur2	
	$\bar{x}$	1σ	$\bar{x}$	1σ	$\bar{x}$	1σ	$\bar{x}$	1σ	$\bar{x}$	1σ	$\bar{x}$	1σ
SiO_2	34.36	0.69	35.97	0.25	35.57	0.34	35.34	0.19	34.75	0.12	35.15	0.25
TiO_2	0.55	0.33	0.82	0.22	1.27	0.13	1.35	0.12	1.20	0.08	1.19	0.11
Al_2O_3	35.87	1.07	33.58	0.71	31.81	0.24	31.81	0.24	32.26	0.13	32.01	0.30
FeO	9.20	1.24	5.29	0.13	4.79	0.17	4.95	0.27	5.20	0.07	3.57	0.15
MnO	0.07	0.02	0.02	0.02	<0.01	0.02	0.03	0.01	0.02	0.01	<0.01	0.01
ZnO	0.07	0.02	0.04	0.02	<0.01	0.02	<0.01	0.01	0.02	0.03	<0.01	0.01
MgO	2.87	1.28	6.81	0.22	7.63	0.10	7.50	0.28	7.07	0.06	8.32	0.09
CaO	0.91	0.08	0.92	0.04	1.34	0.19	1.05	0.14	1.31	0.06	1.48	0.19
Na_2O	1.45	0.13	1.82	0.03	1.74	0.10	1.99	0.07	1.69	0.03	1.67	0.09
K_2O	0.05	0.01	0.05	0.01	0.07	0.01	0.07	0.01	0.08	0.01	0.07	0.01
F	0.15	0.07	0.40	0.05	0.53	0.08	0.24	0.07	0.42	0.08	0.45	0.06
Total	85.50	0.22	85.58	0.14	84.59	0.18	84.26	0.25	83.87	0.15	83.76	0.32
apfu												
T Si	5.79		5.95		5.97		5.94		5.88		5.91	
Al	0.21		0.05		0.03		0.06		0.12		0.09	
Z Al	6.00		6.00		6.00		6.00		6.00		6.00	
Y Al	0.91		0.49		0.26		0.24		0.32		0.26	
Ti	0.07		0.1		0.16		0.17		0.15		0.15	
Fe^{2+}	1.30		0.73		0.67		0.70		0.74		0.50	
Mg	0.72		1.68		1.91		1.88		1.79		2.09	
X Ca	0.16		0.16		0.24		0.19		0.24		0.27	
Na	0.47		0.58		0.56		0.65		0.56		0.54	
K					0.02		0.01		0.02		0.02	
W OH	0.29		0.26		0.12		0.32		0.22		0.19	
O	0.63		0.53		0.60		0.55		0.55		0.57	
F	0.08		0.21		0.28		0.13		0.23		0.24	

Notes:
Stoichiometric proportions are normalized to 15 cations (15 = T + Z + Y) and 3B and 3OH per formula unit were assigned
BaO and SrO below detection limit of 0.01 wt%

Table 4.3. Average compositions of Tur3

	Sample	MAC462		MAC110		MAC122		MAC436		MAC29		MAC32		MAC86		MAC99	
	n[a]	9		11		3		10		4		11		20		2	
	host rock[b]	MFd ss		pel		RF ss		pel		pel		RF ss		peg		peg/pel	
	area[c]	above ZB		P2, barren		P2, barren		P2, barren		P2, lg		P2, lg		P2, lg		P2, lg	
		$\bar{x}$	1σ	$\bar{x}$	1σ	$\bar{x}$	1σ	$\bar{x}$	1σ	$\bar{x}$	1σ	$\bar{x}$	1σ	$\bar{x}$	1σ	$\bar{x}$	1σ
	SiO_2	36.96	0.63	38.78	0.33	34.37	0.29	37.69	0.27	35.94	0.35	33.57	0.90	37.51	0.41	35.92	0.64
	Al_2O_3	36.52	0.74	36.21	0.39	33.29	0.91	36.83	0.27	36.85	0.63	37.92	0.39	35.42	0.41	33.03	1.41
	Fe_2O_3	0.21	0.04	1.71	0.70	2.33	0.22	0.54	0.17	1.35	0.08	0.87	0.13	0.14	0.04	1.68	0.13
	MgO	8.09	0.14	8.34	0.33	6.96	0.04	8.29	0.30	7.88	0.12	7.41	0.13	8.58	0.16	7.14	0.13
	CaO	0.13	0.01	0.03	0.01	0.05	0.01	0.10	0.02	0.09	0.01	0.23	0.04	0.08	0.04	0.07	0.01
	Na_2O	0.80	0.10	0.49	0.10	0.83	0.07	0.67	0.05	0.55	0.08	0.50	0.07	0.71	0.14	0.70	0.08
	K_2O	0.07	0.04	<0.01	<0.01	<0.01	<0.01	0.05	0.06	<0.01	<0.01	<0.01	<0.01	0.02	0.02	0.02	0.02
	F	0.13	0.04	0.12	0.09	0.18	0.09	0.07	0.04	0.05	0.03	0.06	0.05	0.04	0.04	0.23	0.14
	Total	82.85	0.89	85.36	0.29	77.77	0.93	84.21	0.37	82.64	0.43	80.48	0.79	82.50	0.46	78.47	2.41
	FeO^d	0.19	0.03	1.54	0.63	2.09	0.20	0.49	0.16	1.21	0.07	0.78	0.12	0.12	0.04	1.51	0.11
apfu																	
T	Si	6.01		6.11		6.01		6.02		5.85		5.60		6.11		6.21	
	Al									0.15		0.40					
Z	Al	6		6		6		6		6		6		6		6	
Y	Al	1		0.72		0.86		0.94		0.92		1.05		0.79		0.73	
	Mg	1.96		1.96		1.82		1.87		1.91		1.84		2.08		1.84	
	Fe^{3+}	0.02		0.2		0.31		0.03		0.16		0.11		0.02		0.22	
X	Na	0.25		0.15		0.28		0.21		0.17		0.16		0.23		0.23	
	Ca	0.02				0.01		0.02		0.02		0.04		0.01		0.01	
	K	0.01						0.01		0.00		0.00		0.00		0.01	
	X-vac	0.72		0.85		0.71		0.76		0.81		0.80		0.76		0.75	
W	F	0.07		0.06		0.10		0.04		0.03		0.03		0.02		0.13	
	O	0.32		0.27		0.49				0.12		0.00		0.29		0.64	
	OH	0.61		0.67		0.41		0.95		0.85		0.97		0.69		0.23	

Notes: *(Extended to Next Page)*

a: number of analyzed grains; b: peg = pegmatite, pel = pelite, ss = sandstone; c: lg = lowgrade, Z1 = Zone 1, Z2 = Zone 2; d: Fe contents if total Fe is FeO

Stoichiometric proportions are normalized to 15 cations (15 = T + Z + Y); 3B and 3OH per formula unit were assigned

TiO_2, MnO, SrO, BaO & Cl contents were below detection limit of 0.01 wt%

Table 4.3. —*Extended*

	Sample	MAC201		MAC69		MAC70		MAC146		MAC423		MAC425		MAC440	
	n[a]	7		21		16		4		9		8		7	
	host rock[b]	peg/pel		pel		pel		peg		pel		pel		RF ss	
	area[c]	P2, Z1		P2, Z2		P2, Z2		P2, Z2		P2, Z2		P2, Z2		P2, ZB	
		$\bar{x}$	1σ	$\bar{x}$	1σ	$\bar{x}$	1σ	$\bar{x}$	1σ	$\bar{x}$	1σ	$\bar{x}$	1σ	$\bar{x}$	1σ
	SiO_2	37.44	0.19	36.60	0.59	36.73	0.70	35.03	1.22	37.52	0.94	36.70	1.09	37.37	0.19
	Al_2O_3	34.50	0.84	35.50	0.45	35.80	0.53	34.85	0.88	36.22	1.05	37.13	1.58	36.78	0.81
	Fe_2O_3	0.23	0.03	0.15	0.04	0.11	0.03	1.61	0.37	0.22	0.17	0.68	0.66	0.41	0.09
	MgO	8.56	0.15	8.64	0.14	8.42	0.11	7.26	0.20	8.65	0.50	7.52	0.65	7.82	0.14
	CaO	0.02	0.01	0.11	0.03	0.11	0.02	0.11	0.04	0.08	0.03	0.17	0.04	0.10	0.01
	Na_2O	0.63	0.05	0.64	0.06	0.62	0.07	0.73	0.21	0.50	0.05	0.43	0.06	0.58	0.06
	K_2O	<0.01	<0.01	0.03	0.02	0.04	0.05	0.02	0.02	0.04	0.03	0.08	0.07	<0.01	<0.01
	F	0.04	0.05	0.08	0.04	0.06	0.04	0.04	0.02	<0.01	<0.01	0.03	0.04	0.09	0.05
	Total	81.43	0.70	81.76	0.65	81.90	0.73	79.51	1.51	83.32	0.73	82.73	1.25	83.09	1.02
	FeO^d	0.21	0.03	0.13	0.03	0.10	0.03	1.45	0.33	0.19	0.15	0.65	0.56	0.37	0.08
apfu															
T	Si	6.17		6.00		6.02		6.02		6.03		6.03		6.05	
	Al														
Z	Al	6		6		6		6		6		6		6	
Y	Al	0.70		0.87		0.91		1.05		0.87		1.12		1.01	
	Mg	2.10		2.11		2.06		1.86		2.07		1.76		1.89	
	Fe^{3+}	0.03		0.02		0.01		0.07		0.03		0.09		0.05	
X	Na	0.20		0.20		0.20		0.24		0.16		0.13		0.18	
	Ca	0.00		0.02		0.02		0.02		0.01		0.03		0.02	
	K	0.00		0.01		0.01		0.00		0.01		0.02			
	X-vac	0.80		0.77		0.78		0.74		0.82		0.82		0.80	
W	F	0.02		0.04		0.03		0.00		0.01		0.02		0.05	
	O	0.28		0.14		0.20		0.43		0.15		0.48		0.38	
	OH	0.70		0.82		0.77		0.57		0.84		0.50		0.57	

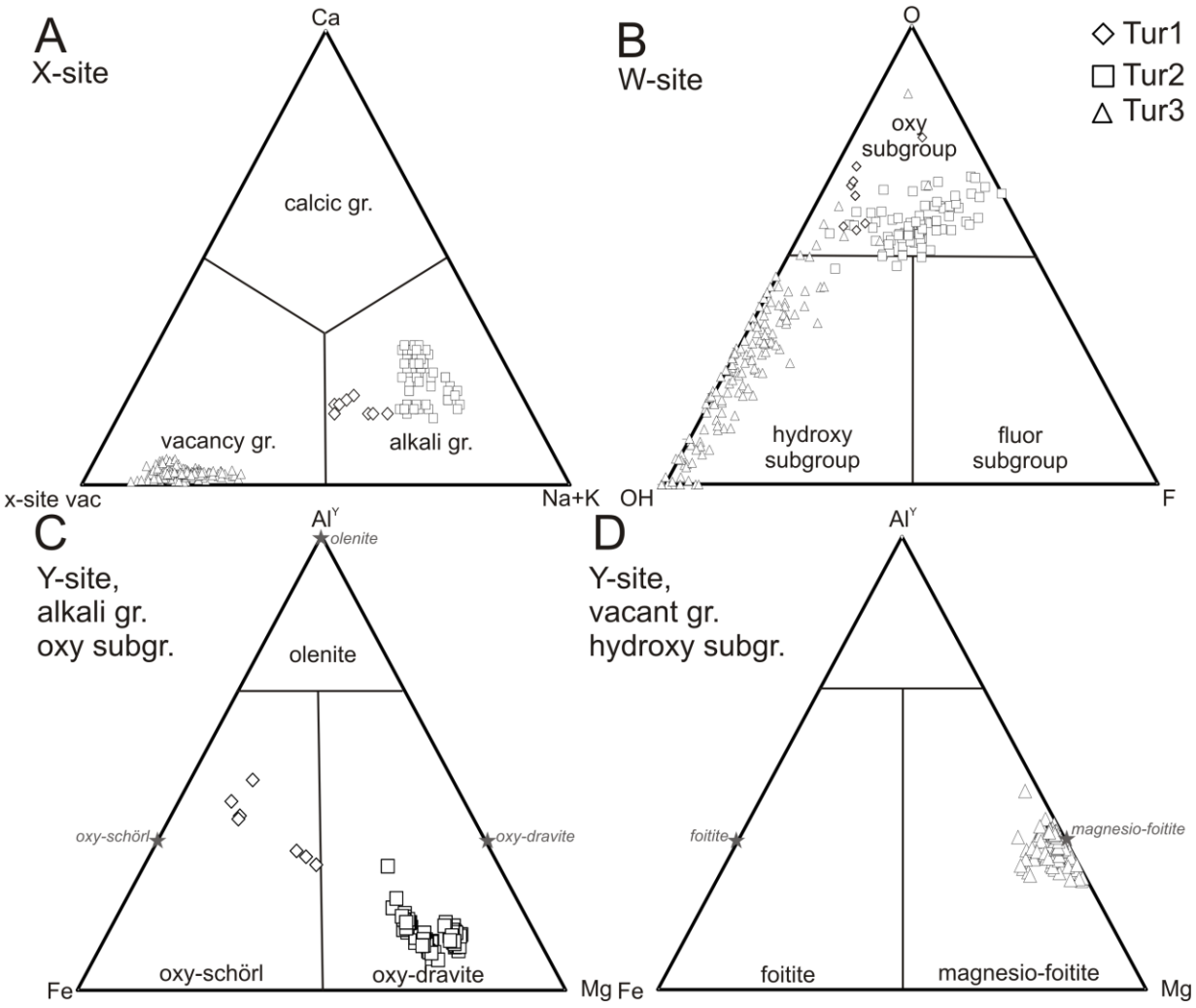

Figure 4.4. Tourmaline classification ternaries (Henry *et al*. 2011). A) X-site occupancy; B) W-site occupancy; C) Y-site occupancy for oxy species of alkali group and D) Y-site occupancy for hydroxy species of X-site vacant group

---

Tur3 has an average composition of $(\square_{0.77}Na_{0.20}Ca_{0.02}K_{0.01})(Mg_{1.99}Al_{0.92}Fe^{3+}_{0.07})Al_{6.00}(Si_{6.00}O_{18})(BO_3)_3(OH_3)(OH_{0.71}O_{0.25}F_{0.04})$ (Table 4.3). Tur3 both in the basement and sandstones is alkali deficient with X-site vacancies ranging from 0.70 – 0.85 *apfu* (Fig. 4.4A; Table 4.3). With the exception of sample MAC425, Tur3 from individual samples are similar as indicated by small standard deviations listed in Table 4.3. However, Tur3 exhibits significant ranges in Mg (1.59 – 2.22 *apfu*) and Al (6.44 – 7.58 *apfu*)

between samples (Fig. 4.4D). Tur3 from ore (samples MAC423 and MAC425 in Zone 2, sample MAC440 in Zone B) exhibit uniformly high X-site vacancy (0.82 – 0.83 *apfu*). Tur3 from the barren areas of the P2 fault (samples MAC110, MAC122, MAC436) display a wide range (0.70-0.85 *apfu*) of X-site vacancy.

4.4 Discussion

4.4.1 Evolution of tourmaline composition

The composition of Tur1 varies from oxy-schörl with high X-site vacancy (up to 0.4 *apfu*) to Mg-rich oxy-schörl with decreased vacancy at the X-site (Figs. 4.4A,C and 4.5A,B). The compositional variation of Tur1 is accompanied by a decrease of Al at the Y-site (Figs. 4.4B,C and 5A) and an increase in F of the W-site (Fig. 4.5C). The higher Mg and F, and lower Al contents is characteristic of Tur 2 which sometimes overgrows Tur1; therefore, the Mg-enriched analyses of Tur1 most likely represents transitional compositions of mixed Tur1+Tur2 due to partial dissolution of Tur1 during crystallization of Tur2 around it (Fig. 4.3A). It is therefore reasonable to assume that Tur1 was originally relatively homogeneous oxy-schörl with high X-site vacancy.

The composition of Tur2 corresponds to oxy-dravite (Fig. 4.4C) and is similar between samples with small variations in Ca and F contents (Fig. 4.5). The Ca and F show a broad positive correlation which suggests a fluor-uvite component in the samples (Fig. 4.5D). Positive correlation between $Al^{Y}/(Al^{Y} + Mg + Fe)$ and X-site vacancy (Fig. 4.5A) and negative correlation between Mg/(Mg+Fe) and X-site vacancy (Fig. 4.5B) suggest a coupled substitution $Na^{+} + Mg^{2+} = \square + Al^{3+}$.

The composition of Tur3 corresponds to magnesio-foitite (Fig. 4.4D) and is characterized by high Al and X-site vacancy (Fig. 4.5A). The data for Tur3 exhibits a positive correlation between Al in the Y-site and X-site vacancy and a negative correlation between Fe in the Y-site and X-site vacancy. This suggests coupled substitution of $\square + Al^{3+} = Na^{+} + Fe^{2+}$ (Figs. 4.5A,B).

The F contents are variable from <0.01 to 0.22 *apfu* and inversely correlate with X-site vacancy (Fig. 4.5C). The F contents do not correlate with Ca contents, which range from <0.01 to 0.05 *apfu* (Fig. 4.5D). Tur3 also shows a large range in the ratio of O/OH at the W-site (Fig. 4.4B) with an inverse correlation between Na^{+} and OH^{-} (Fig. 4.5E), suggesting a probable solid solution of dominant magnesio-foitite with oxy-dravite via substitution □ + OH^{-} = Na^{+} + O^{-2}. However, the small grain size of Tur3 led to low sums of oxides for analytical data with EPMA (Table 4.3, see Appendix 4 for full dataset). Since the contents of OH and O are calculated based on charge balance, uncertainty in the EPMA data propagate uncertainty in the evaluation of OH and O. Therefore, the values of O/OH ratio at the W site should be taken with caution.

The low sums of oxides in Tur3 and high Si-contents (cation normalization on T+Z+Y=15 *apfu* commonly leads to slight excess Si >6 apfu) might suggest the presence of other cations in the Y site. One possible cation is Li because it cannot be measured with EPMA. We consider that high Li is unlikely because Li-bearing tourmaline is not common outside Li-bearing pegmatites, although Richard et al. (2010) reported high Li contents (10^{2} - 10^{4} ppm) in fluid inclusions of quartz associated with uranium mineralization.

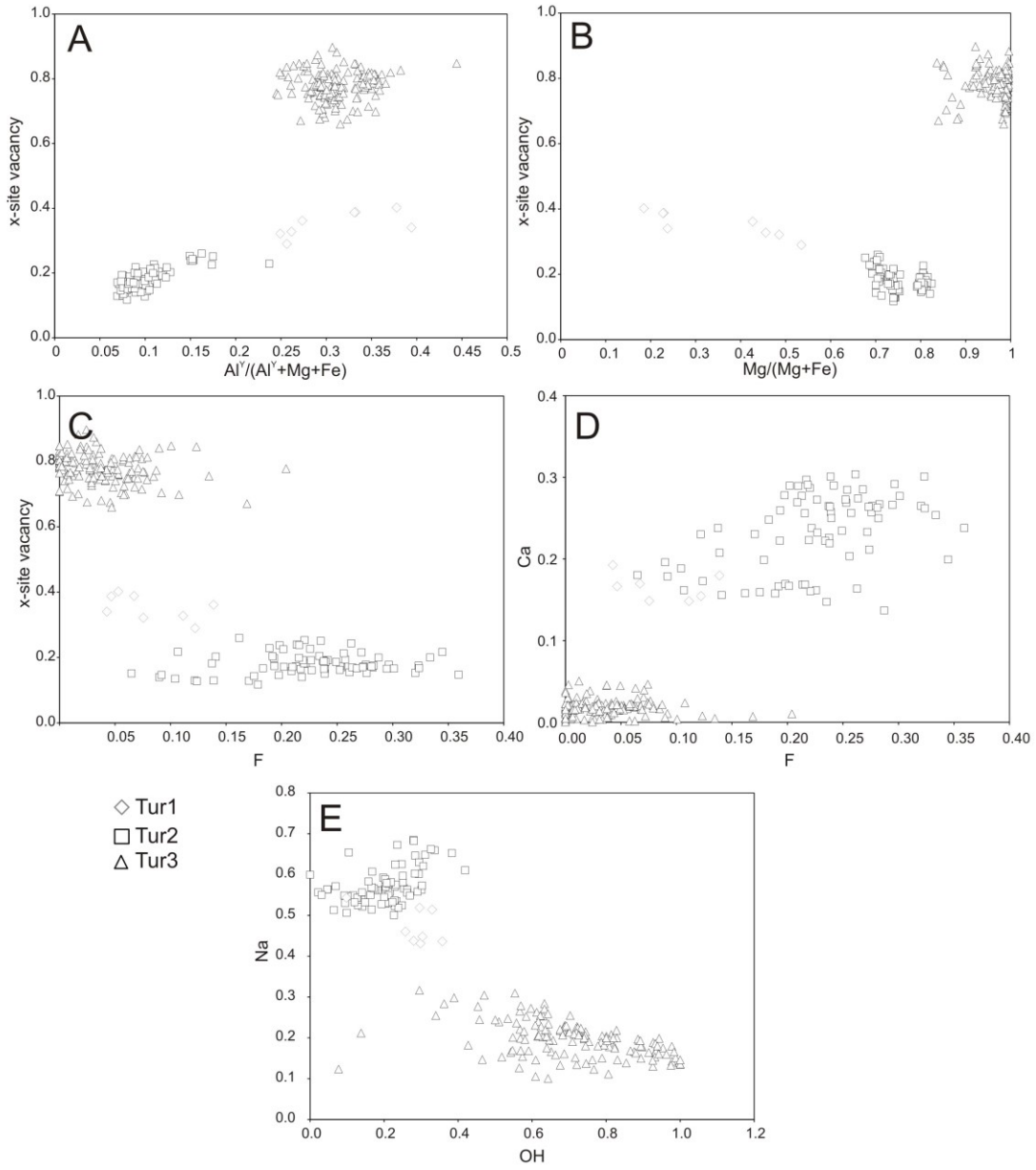

Figure 4.5. Binary plots displaying A) $Al^{Y}/(Al^{Y} + Mg + Fe)$ vs. X-site vacancy, B) Mg(Mg+Fe) vs. X-site vacancy, C) F vs. X-site vacancy, D) F vs. Ca, and E) OH vs. Na in Tur1 (diamonds), Tur2 (squares) and Tur3 (triangles). All data are calculated as atoms per formula unit.

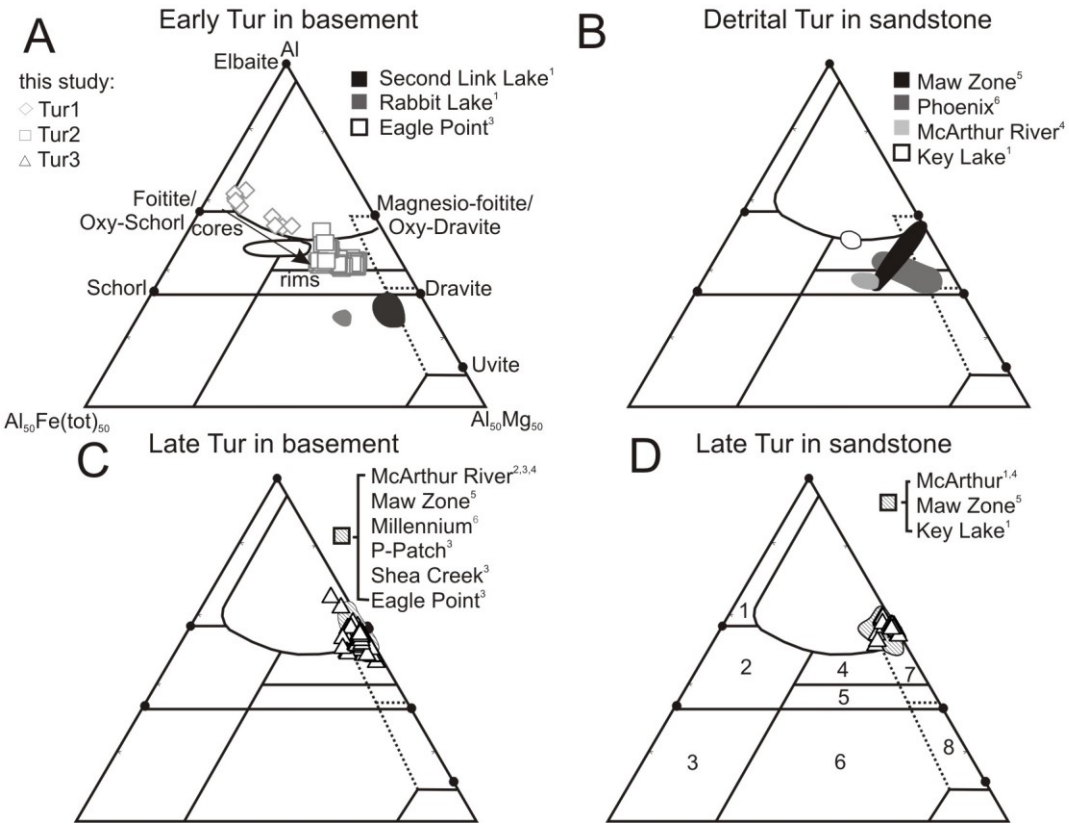

Figure 4.6. Tourmaline provenance diagrams of Henry & Guidotti (1985) comparing the composition of tourmaline in the basement and sandstone from the McArthur River mine (this study) and from other uranium deposits in the Athabasca Basin. A) Comparison with early-formed tourmalines in sub-Athabasca crystalline basement rocks at McArthur River (Tur1, Tur2); B) Reported compositions of detrital tourmaline of the Athabasca Group sandstone; C) Comparison with late-formed, hydrothermal tourmalines in sub-Athabasca crystalline basement rocks at McArthur River (Tur3); D) Comparison with late-formed, hydrothermal tourmalines in sandstones at McArthur River (Tur3). References: 1) Rosenberg & Foit (2006); 2) Kotzer, 1993; 3) Mercadier *et al*. (2012); 4) Ng, 2012; 5) Quirt *et al*. (1991); and 6) Dann, unpublished data. The numbered fields (shown in D) correspond to host rock-types (after Henry & Guidotti 1985): (l) Li-rich granitoid pegmatites and aplites, (2) Li-poor granitoids and their associated pegmatites and aplites, (3) Fe^{3+}-rich quartz-tourmaline rocks (hydrothermally altered granites), (4) Metapelites and metapsammites coexisting with an Al-saturating phase, (5) Metapelites and metapsammites not coexisting with an Al-saturating phase, (6) Fe^{3+}-rich quartz-tourmaline rocks, calc-silicate rocks, and

metapelites, (7) Low-Ca metaultramafics and Cr, V-rich metasediments, and (8) Metacarbonates and meta-pyroxenites.

4.4.2 Origin of Tur1 and Tur2

The presence of oxy-subgroup tourmaline in metamorphic rocks is well documented; oxy-schörl described by Bačík *et al.* (2013) occurs in metasomatically altered rhyolites from Slovak Republic and in muscovite-tourmaline orthogneiss in the Czech Republic, whereas oxy-dravite occurs in quartz-muscovite schist of the Narok district, Kenya (Bosi & Skogby 2013) and in graphitic quartzite at Bítovánky, Czech Republic (Cempírek et al. 2013). Oxy-schörl and Fe-rich oxy-dravite have been reported in pegmatites, from the Moldanubicum, Czech Republic, that are considered to be products of partial melting of metapelites (Novák *et al.* 2004), although Al-rich schörl and foitite are more common in pegmatites (Gadas et al. 2012).

In the tourmaline provenance diagram of Henry & Guidotti (1985), oxy-schörl (Tur1) examined in this study plots close to Fields 1 and 2 representing the composition of tourmaline in granitoid pegmatites (Fig. 4.6A). Our oxy-schörl occurs in altered pegmatite, which was originally composed of biotite, muscovite, feldspar and quartz prior to hydrothermal alteration. The occurrence suggests it is indeed of magmatic origin, and crystallized in pegmatites that are partial melting products of metasedimentary rocks as suggested by Annesley *et al.* (2005).

Coarse-grained dravitic tourmaline has been previously reported in the basement (Rosenberg and Foit 2006, Mercadier *et al.* 2012) and it is similar in composition to the oxy-dravite (Tur2) described in this study (Fig. 4.6A). Mercadier *et al.* (2012) also reported zoned dravitic tourmaline with schörlitic cores in basement pegmatite, similar in composition to zoned Tur2 of this study (Fig. 4.3A). The dravite occurs in the Eagle Point uranium deposit (Mercadier et al. 2012), and the Second Link Lake deposit and Rabbit Lake deposit (Rosenberg and Foit 2006), all of which occur in reactivated Hudsonian deformation zones (Hoeve & Sibbald 1978). Tourmaline

similar to the composition of Tur2 also occurs as detrital grains in the Athabasca sandstones (*e.g.*, Quirt *et al*. 1991, Rosenberg & Foit 2006, Mercadier *et al.* 2012, Ng *et al.* 2013, this study; Fig. 4.4B), confirming the crystallization before the Athabasca sandstone deposition.

The origin of this oxy-dravite is debated whether it is a metamorphic product (Adlakha *et al.* 2014) or a crystallization product of partial melts (Mercadier *et al.* 2012). Oxy-dravite of this study plots in Field 4 of the provenance diagram (Fig. 4.6A), suggesting its formation during metamorphism. However, oxy-dravite occurs in high abundance in pegmatite samples, which suggests its crystallization from a partial melt. As mentioned, Fe-rich oxy-dravite has been reported from pegmatites in Czech Republic, however it is not common and oxy-dravite of this study is more Mg-rich. The occurrence of zoned oxy-dravite grains, with cores of Tur1/oxy-schörl (Fig. 4.3A), within pegmatite suggests that oxy-dravite (Tur2) crystallized after peak metamorphism and solidification of partial melts. Furthermore, the oxy-dravite was not observed in the least altered metamorphic or pegmatitic rocks outside of the P2 fault (Adlakha et al. 2014, this study). These observations suggest that oxy-dravite crystallized late along the P2 fault, but before the deposition of the Athabasca Basin.

Mercadier *et al.* (2012) has shown similar B isotope composition of the cores and rims of zoned dravite. The isotopic signature may suggest the crystallization during the same event, possibly retrogression. Retrogression is consistent with the replacement of biotite with Fe-Mg chlorite and feldspar with illite, as observed in the oxy-dravite mineral assemblage. However, this interpretation is not consistent with high X_{Mg} of tourmaline. The X_{Mg} values of tourmaline commonly reflect temperatures, with retrogression products having lower X_{Mg} than the peak metamorphic products. For example, Van Hinsberg and Schumacher (2011) confirmed that in the Haut-Allier metamorphic suite, Massif Central, France, dravite formed during peak

metamorphism, around early schörlitic cores, and was later rimmed by schörl during retrogression.

It has been suggested that a significant hydrothermal event occurred after the peak metamorphism and prior to the deposition of Athabasca sandstones (Card 2012, 2014). Movement of faults likely provided conduits for focused fluids along graphitic pelite, and produced pyrite, and quartz along major basement structures. The hydrothermal fluids are considered to be responsible for the formation of anomalous quartz-rich rocks, such as silicified pegmatite and "quartzite ridges", in proximity to major basement faults (Card 2012, 2014). It is likely that Tur2 crystallized with quartz and pyrite during this hydrothermal event. The crystallization of Tur2 with pyrite is consistent with relatively low Fe contents in Tur2 as pyrite would preferentially incorporate Fe.

4.4.3 Origin of magnesio-foitite (Tur3)

It is noted here that tourmaline associated with uranium deposits in the Athabasca Basin has been commonly referred to as dravite, alkali-free dravite or alkali-deficient dravite, in the literature (*e.g.*, Quirt *et al*. 1991, Kotzer & Kyser 1995, Fayek & Kyser 1997, Jefferson *et al.* 2007). The compositions of these previously reported tourmaline plot near magnesio-foitite in the provenance diagram (Figs. 4.4C, D).

The timing of hydrothermal tourmaline with respect to uranium mineralization of the Athabasca Basin has been commonly debated (e.g., Hoeve & Sibbald 1978, Kotzer & Kyser 1995, Fayek & Kyser 1997, Derome *et al.* 2005, Cloutier *et al.* 2009, Mercadier *et al.* 2012, Ng 2012). The composition of magnesio-foitite in this study is similar to the hydrothermal tourmaline reported from other Athabasca uranium deposits (Figs. 4.4, 6), including Rabbit Lake, Second Link Lake, Key Lake, and Phoenix (Kotzer 1993, Rosenberg & Foit 2006, Mercadier *et al.* 2012, Ng 2012) and from the REE-rich Maw Zone (Quirt *et al.* 1991). Magnesio-foitite occurring in quartz

veins near the McArthur River Zone 4 ore body was suggested to be a pre-ore alteration by Ng *et al.* (2013) because it is overprinted by ore-related chlorite. Derome *et al.* (2005) suggests magnesio-foitite is synchronous with ore formation as it is associated with desilicification and occurs in the matrix of ore-hosting breccias. Other evidence supporting a syn-ore crystallization of magnesio-foitite is (i) close spatial association with ore (Hoeve & Sibbald 1978, Kotzer & Kyser 1995, Fayek & Kyser 1997, Derome *et al.* 2005) and (ii) δD and $\delta^{18}O$ values of magnesio-foitite suggesting it formed from the mixing of basinal and basement fluids when the mineralization took place (Kotzer & Kyser 1995). Magnesio-foitite has also been suggested as a post-ore alteration because of its occurrence in voids "created by pre-ore alteration but not filled with uraninite" (Alexandre *et al.* 2005) and it overprints pre-ore and syn-ore alteration assemblages (Cloutier *et al.* 2009).

The P2 fault is characterized by alteration forming magnesio-foitite, florencite, sudoite and illite. Magnesio-foitite grains are disseminated within these alteration minerals and their contacts with these alteration minerals show no reaction rim (*e.g.,* Fig. 4.3F), suggesting their equilibrium. Sudoite and illite are widely considered as syn-ore alteration minerals (*e.g.* Jefferson *et al.* and references therein). The assemblage of magnesio-foitite with sudoite, illite and florencite is especially prevalent around the Zone 2 ore body. In ore zone breccias, the assemblage occurs with uraninite of the main mineralization event. This assemblage is locally overprinted by remobilized uraninite and sudoite (Figs. 4.3E,F,H). The uraninite formed during the main event and the late recrystallized uraninite are easily differentiated because the compositions are different; the recrystallization product contains high Si, Ca, and Pb, which is similar to the late secondary uraninite reported by Fayek & Kyser (1997). The composition of uraninite and textural evidence suggest that magnesio-foitite and the main-stage uraninite are contemporaneous. Therefore, the

results of this study are in agreement with the prevailing interpretation of magnesio-foitite crystallizing from uraniferous fluids during the main-stage mineralization.

Significance of X-site vacancy:

The X-site of tourmaline accommodates alkalis and Ca^{2+}, and is partially vacant. The calculated mineral formula of magnesio-foitite indicates a consistently large X-site vacancy (Fig. 7; Table 4.3). The abundance of illite suggests reasonably high K^+ in hydrothermal fluids, yet tourmaline does not contain significant K (< 0.01 *apfu*). Although the X-site may accommodate alkalis, the ionic radius of K^+ is too large to replace Na^+ and Ca^{2+}. The rarity of K-tourmaline is considered to be due to the incompatibility of K^+ with the crystal structure of tourmaline and significant K in tourmaline is only reported in ultrahigh-pressure metamorphic rocks and rocks in close association with evaporites where K substitutes in the X-site of povondraite (Fe^{3+}-rich tourmaline) (*e.g.,* Bačík *et al.* 2008, Berryman *et al.* 2015).

As mentioned, previous workers have described two fluids during uranium mineralization: i) an earlier formed NaCl-rich, uranium-bearing brine and ii) an evolved $CaCl_2$-rich brine which formed by the interaction of the earlier brine with basement rocks (Derome *et al.* 2005, Richard *et al.* 2010, Richard *et al.* 2011). Experimental work by von Goerne *et al.* (2001) indicates that Na-deficient tourmaline primarily reflects low X_{Na} of the fluid. Therefore, the low Na^+ contents in tourmaline associated with Athabascan uranium deposits is surprising if the tourmaline formed from the NaCl-rich fluid. However, von Goerne et al (2001) also demonstrated that the X-site vacancy increases with decreasing temperatures. Uranium deposits of the Athabasca Basin are considered to have formed at low temperatures (< 200°C; *e.g.,* Kotzer & Kyser 1995). Therefore, it is possible that these low temperatures facilitated the formation of magnesio-foitite in lieu of dravite.

It is also possible that magnesio-foitite formed from a $CaCl_2$-rich brine instead of NaCl-rich brine. This is supported by the lack of Na-bearing phases associated with uranium mineralization, except for magnesio-foitite, which contains very low Na^+ (<0.83 wt% Na_2O; Table 4.3). This proposed interpretation is also consistent with depletion of Na in rocks proximal to the uranium deposits (*e.g.*, Sopuck *et al.* 1983). If this is the case it is reasonable to question why a Ca-rich tourmaline did not form. Calcium-rich tourmaline, such as uvite and ferruvite, do occur in nature, but their occurrences are rare, restricted to calcareous metasediments and calc-silicate rocks (Henry & Dutrow 1996) formed at high (> 400 °C) temperatures. Calcium-rich tourmaline has not been reported in rocks formed at low temperatures nor synthesized to date. Experimental work of von Goerne *et al.* (2001, 2011) found that X-site vacancy increased with increasing Ca/(Na+Ca) ratio of the fluid (with the exception of pure Ca fluid). Considering Na preferentially incorporates into tourmaline over Ca, this may explain why magnesio-foitite formed in lieu of a Ca-bearing tourmaline.

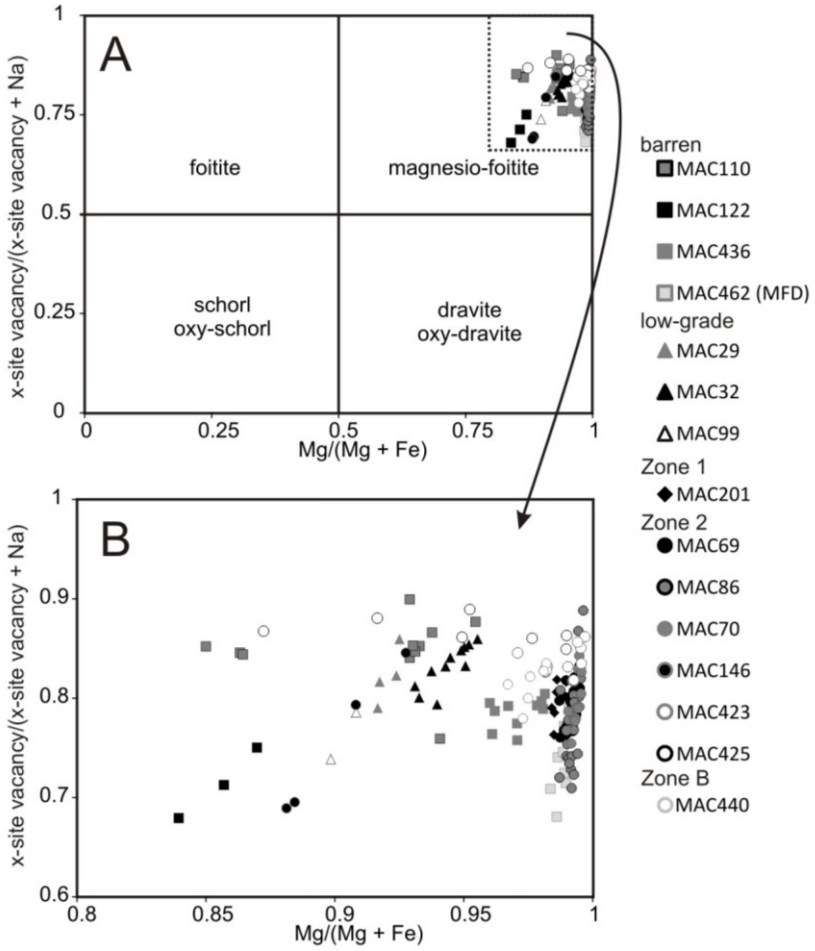

Figure 4.7. Binary diagrams of Tur3 data, Mg/(Mg + Fe) vs. x-site vacancy/(x-site vacancy + Na apfu), showing the alkali-deficiency of Tur3. Diagram B shows a smaller range and therefore a larger amount of detail than diagram A. Data of Tur3 from unmineralized areas are represented by squares, from low-grade areas by triangles, from Zone 1 by diamonds and from Zone 2 and B by circles. Tur3 from Zone 2 and B samples that contain uraninite are represented by open circles.

The high X-site vacancy of magnesio-foitite of the Athabasca Basin may also be partly attributed to the composition of the precursor phases of magnesio-foitite. The rocks in the area were extensively altered to form kaolin during weathering in the basement rocks and dickite during the diagenesis of sandstones before uranium mineralization. The X-site vacancy of magnesio-foitite is owed to coupled substitution of Al + □ = Na + Mg. High Al phases such as

dickite/kaolinite and sudoite are abundant in the sandstones and basement. Aluminum is not a highly mobile element in low temperature hydrothermal fluids. Tourmaline likely inherited high Al content of precursor minerals, thereby restricting the amount of Na^{+} and Ca^{2+} that was able to be accommodated into the mineral structure. We consider this proposed interpretation the most plausible mechanism explaining high vacancies in the X-site.

4.4.4 The role of the P2 fault and origin of mineral assemblages

In the basement, oxy-dravite and magnesio-foitite occur in close proximity (< 50 m) to the P2 fault and are absent in rocks of the footwall and hanging-wall of the structure. Oxy-dravite (Tur2) appears evenly distributed along the P2 fault, whereas magnesio-foitite (Tur3) is abundant in the alteration halo of the deposit and sparse in apparently barren areas of the fault. The occurrence of the two distinctly different types of tourmaline along the entire P2 fault, reflect different fluids in two separate events before and after the sandstone deposition. The observation suggests that the P2 fault served as a fluid conduit before and after the deposition of Athabasca sandstone. This interpretation is in agreement with those of Card (2014) who suggested that multiple events of hydrothermal activity over an extensive period of time, from pre-Athabasca to syn-mineralization, were facilitated by basement structures, such as the P2 fault.

The mineral assemblages of tourmaline along the P2 fault attests for multiple fluid events along structures of the basement rocks (Fig. 4.8). The earliest assemblage is of oxy-schörl (Tur1) with quartz, plagioclase/feldspar and biotite. Oxy-dravite (Tur2) then formed with quartz (Qz2), pyrite (Py1), and graphite. An assemblage of magnesio-foitite (Tur3), sudoite (Sud1), illite and florencite ± uraninite (U1) were formed during the main stage of uranium deposition. This assemblage was locally overprinted by remobilized uraninite (U1), sudoite (Sud2) and sulfide (Py2).

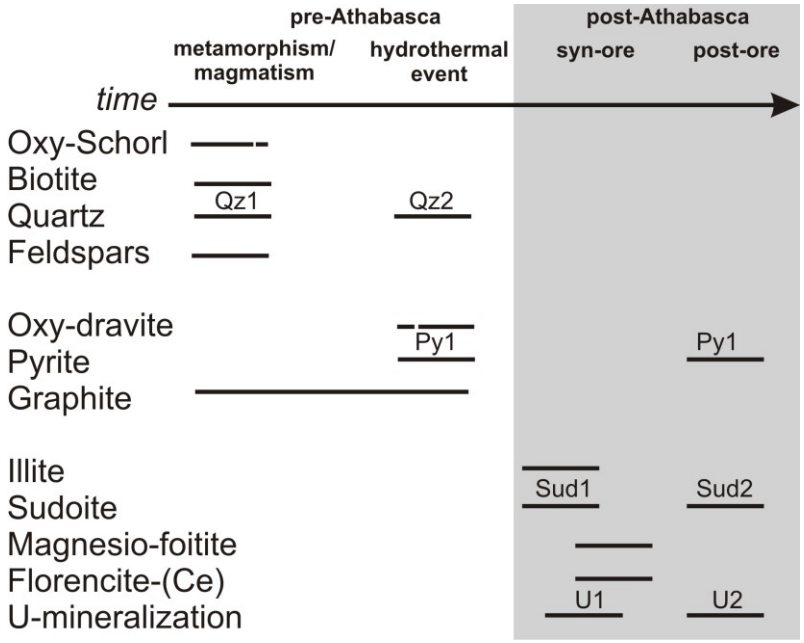

Figure 4.8. The paragenesis of mineral assemblages related to tourmaline in the basement rocks along the P2 fault at McArthur River. This figure is modified from Adlakha *et al.* (2014) and incorporates additional data from Adlakha and Hattori (2015).

The restricted distribution of magnesio-foitite (Tur3) along the P2 fault suggests that B-bearing fluids in the basement focused along the P2 fault during uranium mineralization. These fluids were likely uraniferous as magnesio-foitite and uraninite were contemporaneous, but uranium deposits only occur in specific areas of the P2 fault (Fig. 4.1C). Considering the occurrence of magnesio-foitite in both mineralized and barren areas, it is likely that the location of uranium mineralization was dependent upon the supply of a reducing fluid to these sites.

4.5 Conclusions

Three types of tourmaline occur in the basement rocks of the P2 fault. Early oxy-schörl (Tur1) crystallized as a primary phase in pegmatite. After peak metamorphism and before deposition of the Athabasca Group sediments, hydrothermal activity along the P2 fault produced oxy-dravite with quartz and pyrite. High Mg contents in oxy-dravite are explained by the removal

of Fe by the crystallization of pyrite. After deposition of the Athabasca Group sediments, uraniferous fluids crystallized magnesio-foitite with sudoite, illite and florencite along the entire P2 fault. The high X-site vacancy of magnesio-foitite is attributed to high Al content in the mineral, which is likely inherited from precursory high Al phases. This study demonstrates the important role of the P2 fault as the conduit for hydrothermal fluids before and during the uraniferous hydrothermal activity.

Acknowledgements

This project was funded by Natural Resources of Canada through the Targeted Geoscience Initiative Four (TGI-4) program, a Research Affiliate Program Bursary to EEA and a grant to KH. We thank Dr. Eric G. Potter, science leader for the TGI-4 U ore system project, at the Geological Survey of Canada, for his continuous support. Cameco Corporation provided their logistical support for our field work at the McArthur River mine. Special thanks extend to Gerard Zaluski and Tom Kotzer, as well as Aaron Brown, Doug Adams, Remi Labelle, and Brian McGill of Cameco Corp. for their help during the field work and useful suggestions. We also thank Glenn Poirier of the Museum of Nature for his help with SEM & EMPA analysis. Many thanks to the Associate Editor, Dr. Jan Cempírek, and reviewers, Dr. Radek Škoda and Dr. Peter Bačík, whose constructive comments improved this manuscript.

References

Adlakha, E. E., Hattori, K., Zaluski, G., Kotzer, T., & Potter, E.G. (2014). Alteration within the basement rocks associated with the P2 fault and the McArthur River uranium deposit, Athabasca Basin. Geological Survey of Canada Open File 7462, 35 pp.

Adlakha, E. E., & Hattori, K. (2015). Compositional variation and timing of aluminum phosphate-sulfate minerals in the basement rocks along the P2 fault and in association with the McArthur River uranium deposit, Athabasca Basin, Saskatchewan, Canada. American Mineralogist 100(7), 1386-1399.

Alexandre, P., Kyser, K., Polito, P., & Thomas, D. (2005). Alteration mineralogy and stable isotope geochemistry of Paleoproterozoic basement-hosted unconformity-type uranium deposits in the Athabasca Basin, Canada. Economic Geology 100(8), 1547-1563.

Annesley, I. R., Madore, C., & Portella, P. (2005). Geology and thermotectonic evolution of the western margin of the Trans-Hudson Orogen: evidence from the eastern sub-Athabasca basement, Saskatchewan. Canadian Journal of Earth Sciences 42(4), 573-597.

Bačík, P., Uher, P., Sýkora, M., & Lipka, J. (2008). Low-Al tourmalines of the schörl-dravite-povondraite series in redeposited tourmalinites from the Western Carpathians, Slovakia. The Canadian Mineralogist 46, 1117-1129.

Bačík, P., Cempírek, J., Uher, P., Novák, M., Ozdín, D., Filip, J., Škoda, R., Breiter, K., Klementová, M., Ďuďa, R. & Groat, L.A. (2013). Oxy-schörl, $Na(Fe^{2+}{}_2Al)Al_6Si_6O_{18}(BO_3)_3(OH)_3O$, a new mineral from Zlatá Idka, Slovak Republic and Přibyslavice, Czech Republic. American Mineralogist 98(2-3), 485-492.

Berryman, E. J., Wunder, B., Wirth, R., Rhede, D., Schettler, G., Franz, G., & Heinrich, W. (2015). An experimental study on K and Na incorporation in dravitic tourmaline and insight into the origin of diamondiferous tourmaline from the Kokchetav Massif, Kazakhstan. Contributions

to Mineralogy and Petrology, 169(3), 1-16.

Bosi, F., & Skogby, H. (2013). Oxy-dravite, $Na(Al_2Mg)(Al_5Mg)(Si_6O_{18})(BO_3)_3(OH)_3O$, a new mineral species of the tourmaline supergroup. American Mineralogist 98(8-9), 1442-1448.

Card, C. D. (2012). The Origins of Anomalously Graphitic Rocks and Quartzite Ridges in the Basement to the Southeastern Athabasca Basin. in Summary of Investigations 2012, Volume 2, Saskatchewan Geological Survey, Saskatchewan Ministry of the Economy, Miscellaneous Report, 2012-4.2, Paper A-6, 15pp.

Card, C. (2014). Altered Pelitic Gneisses and Associated "Quartzite Ridges" Beneath the Southeastern Athabasca Basin: Alteration Facies and their Relationship to Uranium Deposits along the Wollaston-Mudjatik Transition. in Summary of Investigations 2013, Volume 2, Saskatchewan Ministry of the Economy, Miscellaneous Report 2013-4.2, Paper A-4, 23pp

Carter, J. D. (1984). Mortimer Hills pegmatite uranium prospect—a Rossing-type uranium deposit in the Gascoyne Province. Western Australia Geological Survey Report 12, 27–31.

Cempírek, J., Stanislav, H., Novák, M., Groat, L., Selway, J., & Šrein, V. (2013) Crystal structure and compositional evolution of vanadium-rich oxy-dravite from graphite quartzite at Bítovánky, Czech Republic. Journal of Geosciences 58, 149–162.

Cloutier, J., Kyser, K., Olivo, G. R., Alexandre, P., & Halaburda, J. (2009). The Millennium uranium deposit, Athabasca Basin, Saskatchewan, Canada: an atypical basement-hosted unconformity-related uranium deposit. Economic Geology 104(6), 815-840.

Čopjaková, R., Škoda, R., Galiová, M. V., & Novák, M. (2013). Distributions of Y+ REE and Sc in tourmaline and their implications for the melt evolution; examples from NYF pegmatites of the Trebic Pluton, Moldanubian Zone, Czech Republic. Journal of Geosciences, 58(2), 113-131.

Čopjaková, R., Škoda, R., Galiová, M. V., Novák, M., & Cempírek, J. (2015). Sc-and REE-rich tourmaline replaced by Sc-rich REE-bearing epidote-group mineral from the mixed (NYF+ LCT) Kracovice pegmatite (Moldanubian Zone, Czech Republic). American Mineralogist, 100(7), 1434-1451.

Derome, D., Cathelineau, M., Cuney, M., Fabre, C., Lhomme, T. & Banks, D. A. (2005). Mixing of sodic and calcic brines and uranium deposition at McArthur River, Saskatchewan, Canada: a Raman and laser-induced breakdown spectroscopic study of fluid inclusions. Economic Geology 100, 1529–1545.

Dyar, M. D., Lowe, E. W., Guidotti, C. V., & Delaney, J. S. (2002). Fe^{3+} and Fe^{2+} partitioning among silicates in metapelites: A synchrotron micro-XANES study. American Mineralogist 87(4), 514-522.

Fayek, M., & Kyser, K., (1997). Characterization of multiple fluid-flow events and rare-earth elements mobility associated with formation of unconformity uranium deposits in the Athabasca basin, Saskatchewan. The Canadian Mineralogist 35, 627–658.

Gadas, P., Novák, M., Staněk, J., Filip, J. & Vašinová Galiová, M. (2012). Compositional evolution of zoned tourmaline crystals from pockets in common pegmatites, the Moldanubian Zone, Czech Republic. The Canadian Mineralogist 50, 895–912.

Hawthorne, F. C., & Dirlam, D. M. (2011). Tourmaline the indicator mineral: From atomic arrangement to Viking navigation. Elements 7(5), 307-312.

Hajnal, Z., Pandit, B., Reilkoff, B., Takacs, E., Annesley, I., & Wallster, D. (2007). Recent development in 2D and 3D seismic imaging of high-grade uranium ore deposit related environments, in the Eastern Athabasca Basin, Canada. In B. Milkereit (Ed.), Exploration in the new millennium: Proceedings of the Fifth Decennial International Conference on

Mineral Exploration, 1131-1135

Henry, D. J., & Guidotti, C. V. (1985). Tourmaline as a petrogenetic indicator mineral- An example from the staurolite-grade metapelites of NW Maine. American Mineralogist 70(1-2), 1-15.

Henry, D. J, & Dutrow, B. L. (1996). Metamorphic tourmaline and its petrologic applications. In: Grew E.S. Anovitz (eds) Boron: Mineralogy, Petrology and Geochemistry. Reviews in Mineralogy 33, 503-557.

Henry, D. J., Novák, M., Hawthorne, F. C., Ertl, A., Dutrow, B. L., Uher, P., & Pezzotta, F. (2011). Nomenclature of the tourmaline-supergroup minerals. American Mineralogist 96(5-6), 895-913.

Hoeve, J., & Sibbald, T. I. (1978). On the genesis of Rabbit Lake and other unconformity-type uranium deposits in northern Saskatchewan, Canada. Economic Geology 73(8), 1450-1473.

Hoeve, J., & Quirt D. (1984). Mineralisation and host rock alteration in relation to clay mineral diagenisis and evolution of the middle-Proterozoic, Athabasca Basin, northern Saskatchewan, Canada; Saskatchewan Research Council (SRC) Technical Report 187, 187 pp. .

Jefferson, C.W., Thomas, D.J., Gandhi, S.S., Ramaekers, P., Delaney, G., Brisbin, D., Cutts, C., Portella, P. & Olson, R.A., (2007). Unconformity-associated uranium deposits of the Athabasca basin, Saskatchewan and Alberta; in EXTECH IV: Geology and Uranium EXploration TECHnology of the Proterozoic Athabasca Basin, Saskatchewan and Alberta. Geological Survey of Canada Bulletin 588, 23-67.

Kerr, W.C. (2010). The discovery of the Phoenix Deposit; a new high-grade, Athabasca Basin unconformity-type uranium deposit, Saskatchewan, Canada. Society of Economic Geologists Special Publications 15, 703-728.

Kotzer, T. (1993). Fluid History of the Proterozoic Athabasca Basin. Unpublished PhD Thesis. University of Saskatchewan, 290 pp.

Kotzer, T. G., & Kyser, T. K. (1995). Petrogenesis of the Proterozoic Athabasca Basin, northern Saskatchewan, Canada, and its relation to diagenesis, hydrothermal uranium mineralisation and paleohydrogeology. Chemical Geology 120(1), 45-89.

Kyser, K., Hiatt, E., Renac, C., Durocher, K., Holk, G., & Deckart, K. (2000). Diagenetic fluids in Paleo- and Meso-Proterozoic sedimentary basins and their implications for long protracted fluid histories. In: Kyser T.K. (ed) Fluids and basin evolution. Mineralogical Association of Canada Short Course 28, 225-262.

Lewry, J.F., & Sibbald, T. (1980). Thermotectonic evolution of the Churchill province in northern Saskatchewan. Tectonophysics 68, 45–82.

Macdonald, C. (1985). Mineralogy and geochemistry of the sub-Athabasca regolith near Wollaston Lake. Geology of Uranium Deposits: Canadian Institute of Mining and Metallurgy Special 32, 155-158.

McGill, B., Marlatt, J., Matthews, R., Sopuck, V., Homeniuk, L., & Hubregtse, J., (1993). The P2 North uranium deposit Saskatchewan, Canada. Exploration Mining Geology 2(4), 321- 333.

Mercadier, J., Richard, A., & Cathelineau, M. (2012). Boron-and magnesium-rich marine brines at the origin of giant unconformity-related uranium deposits: $\delta^{11}B$ evidence from Mg-tourmalines. Geology 40(3), 231-234.

Ng, R. (2012). Geochemical and mineralogical evolution of the McArthur River Zone 4 unconformity-related uranium ore body and application of iron oxidation state in clay alteration as indicator of uranium mineralisation. Unpublished MSc thesis, Queen's University, 207 pp.

Ng, R., Alexandre, P., & Kyser, K. (2013). Mineralogical and Geochemical Evolution of the Unconformity-Related McArthur River Zone 4 Orebody in the Athabasca Basin, Canada: Implications of a Silicified Zone. Economic Geology 108(7), 1657-1689.

Novák, M., Povondra, P., & Selway, J.B. (2004). Schörl-oxy-schörl to dravite-oxy-dravite tourmaline from granitic pegmatites; examples from the Moldanubicum, Czech Republic. European Journal of Mineralogy 16, 323–333.

Pal, D., Trumbull, R., & Wiedenbeck, M. (2010). Chemical and boron isotope compositions of tourmaline from the Jaduguda U (–Cu–Fe) deposit, Singhbhum shear zone, India: Implications for the sources and evolution of mineralizing fluids. Chemical Geology 27, 245-260.

Quirt, D., Kotzer, T., & Kyser, T. K. (1991). Tourmaline, phosphate minerals, zircon and pitchblende in the Athabasca Group: Maw Zone and McArthur River areas. Saskatchewan: Summary of Investigations 1991, Saskatchewan Geological Survey Miscellaneous Report 91(4), 11 pp.

Ramaekers, P., Jefferson, C.W., Yeo, G.M., Collier, B., Long, D.G.F., Drever, G., McHardy, S., Jiricka, D., Cutts, C., Wheatley, K., Catuneau, O., Bernier, S., Kupsch, B & Post, R.T., (2007). Revised geological map and stratigraphy of the Athabasca Group, Saskatchewan and Alberta; in EXTECH IV: Geology and Uranium EXploration TECHnology of the Proterozoic Athabasca Basin, Saskatchewan and Alberta. Geological Survey of Canada Bulletin 588, 155-192.

Richard, A., Pettke, T., Cathelineau, M., Boiron, M. C., Mercadier, J., Cuney, M., & Derome, D. (2010). Brine–rock interaction in the Athabasca basement (McArthur River U deposit, Canada): consequences for fluid chemistry and uranium uptake. Terra Nova, 22(4), 303-308.

Richard, A., Banks, D. A., Mercadier, J., Boiron, M. C., Cuney, M., & Cathelineau, M. (2011). An evaporated seawater origin for the ore-forming brines in unconformity-related uranium deposits (Athabasca Basin, Canada): Cl/Br and $\delta^{37}Cl$ analysis of fluid inclusions. Geochimica et Cosmochimica Acta 75(10), 2792-2810.

Richard, A., Rozsypal, C., Mercadier, J., Banks, D. A., Cuney, M., Boiron, M. C., & Cathelineau, M. (2012). Giant uranium deposits formed from exceptionally uranium-rich acidic brines. Nature Geoscience, 5(2), 142-146.

Rosenberg, P. E., & Foit, F. F. (2006). Magnesio-foitite from the uranium deposits of the Athabasca Basin, Saskatchewan, Canada. The Canadian Mineralogist 44(4), 959-965.

Sopuck, V.J., deCarla, A., Wray, E.M., & Cooper, B. (1983). The application of lithogeochemistry in the search for unconformity-type uranium deposits, Northern Saskatchewan, Canada. Journal of Geochemical Exploration 19, 77-99.

van Hinsberg, V. J., & Schumacher, J. C. (2011). Tourmaline as a petrogenetic indicator mineral in the Haut-Allier metamorphic suite, Massif Central, France. The Canadian Mineralogist, 49(1), 177-194.

von Goerne, G., & Franz, G. (2000). Synthesis of Ca-tourmaline in the system CaO-MgO-Al_2O_3-SiO_2-B_2O_3-H_2O-HCl. Mineralogy and Petrology, 69(3-4), 161-182.

von Goerne, G., Franz, G., & Heinrich, W. (2001). Synthesis of tourmaline solid solutions in the system Na_2O-MgO-Al_2O_3-SiO_2-B_2O_3-H_2O. Contributions to Mineralogy and Petrology, 141(2), 160-173.

von Goerne, G., Franz, G., & van Hinsberg, V. J. (2011). Experimental determination of Na–Ca distribution between tourmaline and fluid in the system CaO–Na_2O–MgO–Al_2O_3–SiO_2–B_2O_3–H_2O. The Canadian Mineralogist, 49(1), 137-152.

CHAPTER 5.

Characterizing fluids associated with the McArthur River U deposit based on tourmaline trace element and stable (B, H) isotope compositions

Erin E. Adlakha, Keiko Hattori, William J. Davis, and Brandon Boucher

Submitted, Chemical Geology, December 2015

Abstract

Magnesio-foitite, an alkali-deficient Mg-rich tourmaline, occurs as disseminations and veinlets near the unconformity between Athabasca Group sandstones and crystalline basement, and along the P2 fault, a 13 km long reverse structure and the main structural control of the McArthur River U deposit. The tourmaline contains variable concentrations of REE (up to 46 ppm in total) and Y (up to 35 ppm), although most magnesio-foitite samples contain very low concentrations of REE (<2 ppm) and Y (<2 ppm). Early magnesio-foitite along the P2 fault, and within the uppermost sandstone unit, the MFd, exhibits high LREE relative to HREE ($Ce_N > Y_N$, Y as a proxy for HREE) and slight negative Eu anomalies, most likely due to the interaction of the fluid with the sandstones and felsic pegmatite in the basement. Later magnesio-foitite of the P2 fault is low in LREE ($Ce_N < Y_N$). This later magnesio-foitite exhibits similar chondrite-normalized REE patterns as uraninite ($Ce_N < Y_N$) of the deposit. The trace element data combined with textural observations suggest that the REE signature of this magnesio-foitite and uraninite is due to the co-crystallization of LREE-rich aluminum phosphate sulfate minerals. Low values of δD (-41 to -98 ‰) for magnesio-foitite suggest that the mineralizing fluids likely originated from groundwater, with a possible contribution of other fluids such as basinal and basement fluids. High values of $\delta^{11}B$ (+13.1 to +23.2 ‰) are explained by the dissolution of B from carbonate or evaporitic rocks and progressive enrichment of ^{11}B through preferential adsorption and incorporation of ^{10}B by illite and kaolinite.

5.0 Introduction

Tourmaline is a useful mineral in evaluating the composition and origin of hydrothermal fluids as tourmaline can accommodate a wide range of elements. Trace element abundances in tourmaline are of particular interest as studies suggest that they may provide insights into

hydrothermal and magmatic processes (e.g. Joliff et al. 1987, Taylor et al. 1999, Slack and Trumbell 2011, Čopjaková et al. 2013, 2015). For example, the trace element chemistry of tourmaline from different pegmatite units of the Třebíč Pluton, Moldanubian Zone, Czech Republic, reflects the evolution of different melts and the co-crystallization of phases: tourmaline within relatively primitive pegmatite contains much higher REE and Y compared to tourmaline occurring with REE-rich minerals (e.g. monazite and xenotime) in evolved pegmatite (Čopjaková et al. 2013).

In many hydrothermal ore deposits, including unconformity-type U deposits of the Athabasca Basin in northern Saskatchewan, Canada, tourmaline occurs as a common accessory mineral. Unconformity-type U deposits account for more than 33% of the world's U resources (Jefferson et al. 2007) and the Athabasca Basin hosts the world's largest high-grade U deposits, including the world-class McArthur River deposit. As such, a number of papers in the past 20 years have focussed on the geochemistry of tourmaline from the Athabasca Basin (e.g., Kotzer & Kyser 1995, Rosenberg & Foit 2006, Mercadier et al. 2012, Adlakha and Hattori 2016). Although the major element abundance and stable isotope geochemistry (B, H) of the tourmaline has been investigated in previous studies, its trace element abundances have not yet been reported.

In order to evaluate the nature and source of fluids responsible for U mineralization, we have determined the abundance of trace elements, as well as B and H isotope geochemistry, for tourmaline from well-characterized samples in proximity, and distal, to the McArthur River U deposit. For comparison, the trace element composition of a pre-Athabasca hydrothermal tourmaline, oxy-dravite, is also quantified and presented in this paper.

5.1 Geological context

5.1.2 Regional geology

Unconformity-type U deposits within the Athabasca Basin are spatially associated with the basal unconformity between the Athabasca Group sandstones and underlying crystalline basement rocks of the Rae and Hearne provinces (Fig. 5.1). The Hearne Province comprises four domains: Peter Lake, Virgin River, Mudjatik and Wollaston. Most U deposits, including the McArthur River deposit, are found within, or overlying, the metasedimentary rocks of the western Wollaston Domain near the transition-zone between the Wollaston and the Archean granitoid gneisses of the Mudjatik Domain. The Wollaston Domain is a NE-striking fold-thrust belt that comprises an Archean granitoids and overlying Paleoproterozoic metasedimentary rocks of the Wollaston Group (Lewry and Sibbald 1977). The Wollaston Group comprises graphitic and non-graphitic pelite, semi-pelite and paragneiss interlayered with minor calc-silicate, arkose and quartzite (McGill et al. 1993). These rocks are locally intruded by pegmatite lenses which formed by anatexis of the metasedimentary rocks during peak metamorphism (Annesley et al. 2005) associated with the Trans-Hudson Orogeny (~1.86 – 1.76 Ga; e.g. Annesley et al. 2005).

Sedimentation of the Athabasca Basin began after 1.76 Ga (Kyser et al. 2000) and continued until approximately 1.5 Ga (Raemakers et al. 2007). Sedimentary rocks of the Athabasca Group consist of basal, fluvial conglomerate and sandstone of the Read (Fig. 5.1) and Fair Point Formations (Raemakers et al. 1990). These units are overlain by fluvial to shallow marine quartz arenite, siltstones and phosphatic mudstone of the Manitou Falls, Lazenby Lake, Wolverine Point, Locker Lake, Otherside and Tuma Lake Formations. Capping the western portion of the basin are fine sandstones and shales of the Douglas Formation, and stromatolite and dolostone of the Carswell Formation (Fig. 5.1). The thickest preserved portion of the basin is 1500 m; however,

fluid inclusion studies by Pagel et al. (1980) suggest that the basin may have reached 5 – 7 km in thickness.

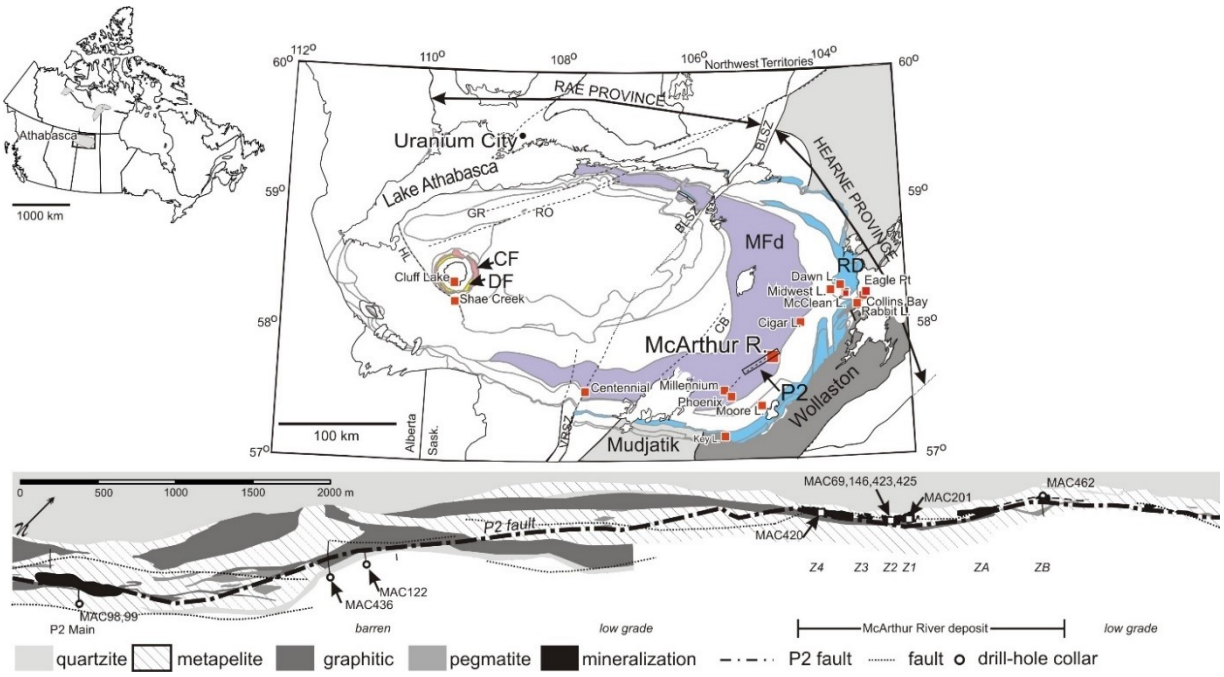

Figure 5.1. Top: A map showing the location of the major U deposits, including the McArthur River deposit, and structures, including the P2 fault, in the Athabasca Basin (modified from Jefferson et al. 2007 and Adlakha and Hattori 2015, 2016). The inset image of Canada (top left) shows the location of the Athabasca Basin. The units of the Athabasca Basin pertinent to this study are shown in colour: the Read Formation (RD) sandstone is shown in blue, the Dunlop Member of the Manitou Falls Formation (MFd) is purple, the Douglas Formation is yellow and the Carswell Formation (CF) is light pink. The south-eastern margin of the Athabasca Basin is underlain by the Wollaston (dark grey) and Mudjatik Domains (light grey) of the basement. Major shear zones: BB = Black Bay, BLSZ = Black Lake, CB = Cable Bay, GR = Grease River, RO = Robbilard, VRSZ = Virgin River. Modified from Jefferson et al. (2007), and Adlakha and Hattori (2015, 2016). Bottom: A plan view map showing the basement lithology at the unconformity and sample locations. Drillholes collared at surface are represented by open circle. Drillholes collared underground (i.e., within the McArthur River mine) are indicated by open squares. Modified from Adlakha and Hattori 2015, 2016).

5.1.2 Local geology

The least altered rocks of the Wollaston Group in proximity to the McArthur River deposit consist mainly of garnet ± cordierite paragneiss and graphitic pelite, intruded by granitic pegmatite units that range from centimetres to a few metres in width (McGill et al. 1993). A quartzite unit of the Wollaston Group occurs in proximity to the McArthur River deposit. The quartzite formed a paleo-topographic high before the deposition of Athabasca sandstones as the unit is resistive against weathering and erosion. The Athabasca Group in this area is approximately 500 m thick and comprises four quartz-rich sandstone units: the basal conglomeratic Read Formation (previously the Manitou Falls Formation A), and the three overlying sandstone members of the Manitou Falls Formation, including the conglomeratic Bird (MFb), sandy Collins (MFc) and uppermost clay-intraclast-bearing Dunlop (MFd) members (Raemakers et al. 2007) (Fig. 5.1).

The McArthur River deposit contains six ore bodies (Zones 1-4, A and B), all of which are located in the sandstones of the Read Formation, except for Zone 2 which is almost entirely hosted by the basement rocks of the Wollaston Group. The main stage of U mineralization is considered to have occurred ~1500 Ma, with subsequent remobilization at ~1150, 900 and 280 Ma (e.g. Fayek et al. 2002). All ore bodies are structurally controlled by the 13 km long P2 reverse fault (45°/045°), which displaces the basement rocks over the basal units of the Athabasca Group by up to 80 m (McGill et al. 1993). The P2 fault is constrained to graphitic pelite in the basement, and splays and fractures in the overlying sandstone. The fault likely began as a strike-slip ductile deformation zone during the Trans-Hudsonian Orogeny and was later reactivated as a reverse fault during sedimentation of the Athabasca Group (McGill et al. 1993, Hajnal et al. 2007).

The McArthur River deposit, and other U deposits of the Athabasca Basin, are enveloped by alteration halos consisting of sudoite, illite, and tourmaline (magnesio-foitite) with aluminum

phosphate-sulfate (APS) minerals (e.g., Kyser and Kotzer 1995, Gaboreau et al. 2007, Mercadier et al. 2012, Ng et al. 2013). Previous work shows that the hydrothermal alteration associated with the McArthur River deposit extends along the entire P2 fault (e.g., Adlakha and Hattori, 2015, 2016), although U mineralization is only found along 1.7 km of its NE portion.

Table 5.1. Sample list and descriptions.

	area[a]	DDH[b]	sample	depth[c] (m)	lithology[d]	Mgf occurrence
P2 fault samples	NM	MC361	MAC122	493	ss, RD	vein
	NM	MC381	MAC436	603	peg	vein/dissemination
	LG	MC349	MAC98	578	pel bx	vein/dissemination
	LG	MC349	MAC99	573	pel/peg bx	dissemination
	AH, Z2	H201	MAC69	>500	pel bx	dissemination
	AH, Z2	MO227	MAC146	>500	peg bx	vein
	AH, Z1	H3559	MAC201	>500	pel/peg bx	vein/dissemination
	AH, Z4	H677	MAC420	>500	pel	dissemination
	ORE, Z2	H3380	MAC423	>500	pel/ore	dissemination
	ORE, Z2	H3380	MAC425	>500	pel/ore	dissemination
	MFd	MC274	MAC462	93.1	ss, MFd	infill pore space

a: location: NM = non-mineralized, LG = low-grade,
AH = alteration halo, ORE= ore sample, Z#= Zone # ore body
b: Diamond Drillhole
c: sample depth from surface (note unconformity located ~ 500 m from surface),
basement samples with ">500 m" were collected from drillholes collared underground
d: bx = breccia, peg = pegmatite, pel = pelite, ss = sandstone, RD = Read Formation,
MFd = Dunlop member of Manitou Falls Formation

5.2 Occurrence of tourmaline and samples

Two species of hydrothermal tourmaline occur in the area: magnesio-foitite and oxy-dravite. Of greatest interest to this study is magnesio-foitite, which is syn-ore and most commonly found in proximity to U mineralization. Below the unconformity, magnesio-foitite is observed along the P2 fault and absent in basement rocks outside of the structure (Adlakha and Hattori 2016). Above the unconformity, magnesio-foitite occurs within the basal sandstone/conglomerate of the Read Formation and within the uppermost sandstone unit (MFd), 400 – 500 m above the unconformity (Ng et al. 2013, Adlakha & Hattori 2016). Magnesio-foitite forms aggregates of fine

(<15 µm in diameter), prismatic to acicular crystals which infill fractures, alter the rims of earlier oxy-dravite, and occur as disseminations with other clay sized minerals such as illite and/or sudoite (Fig. 5.2).

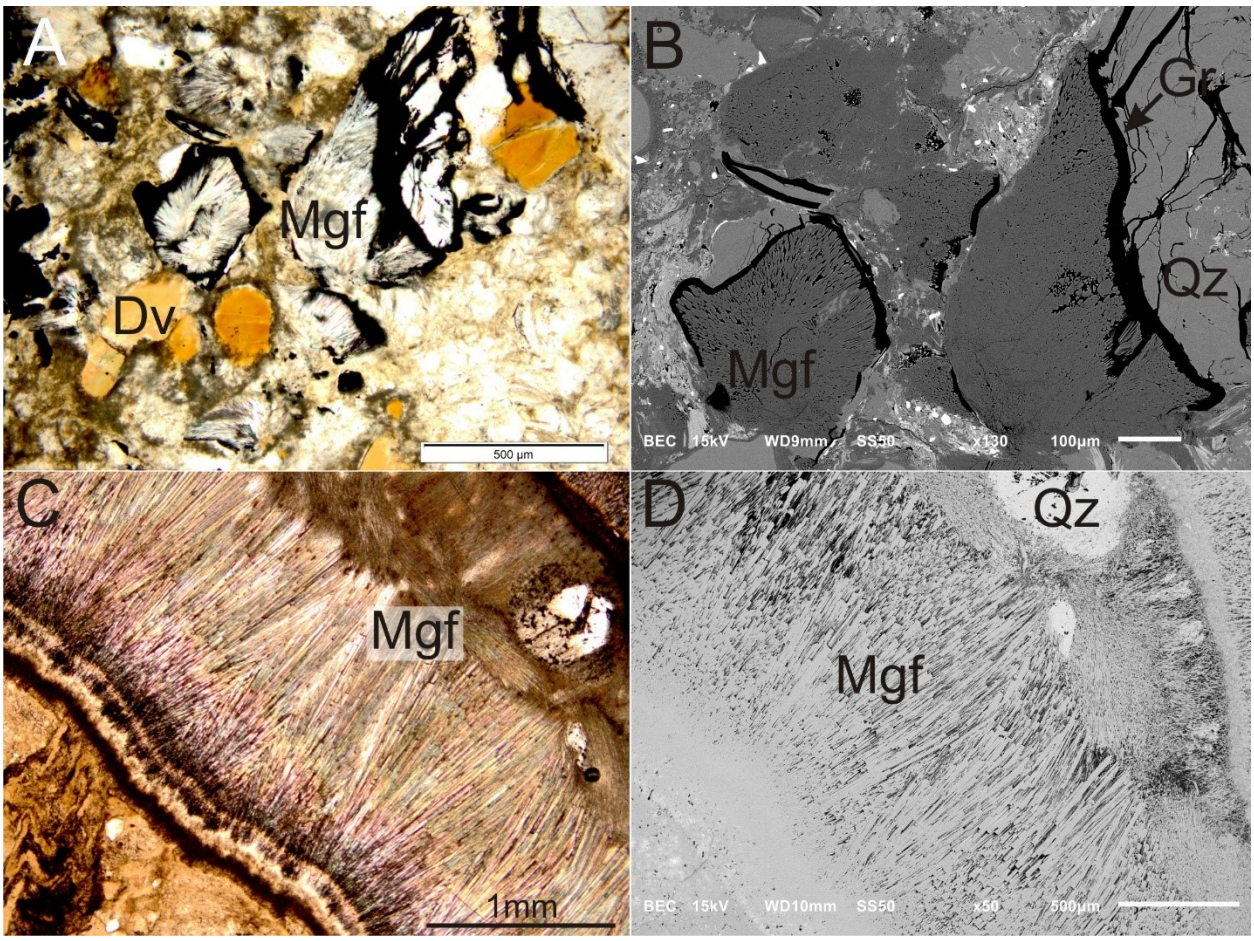

Figure 5.2. Photomicrographs (A, C) and back-scattered electron images (B, D) of magnesio-foitite (Mgf) as disseminated aggregates in sample MAC201 (A,B) and forming a veinlet in sample MAC146 (C,D). Gr = graphite, Ilt = illite, Sud = sudoite

Oxy-dravite is common in the basement rocks along the P2 fault. It forms brown, coarse grains up to 500 µm (Fig. 5.2A), and is associated with an assemblage of pyrite, graphite and quartz. It also occurs as detrital grains within the sandstones (e.g. Adlakha and Hattori 2016).

A total of 11 well-characterized magnesio-foitite samples were selected for this study, comprising 9 basement samples and 2 sandstone samples (Table 5.1). These samples were selected as they contain relatively large crystals, aggregates or monomineralic veinlets of magnesio-foitite suitable for analysis. The basement samples are representative of important areas of the P2 fault and include the Zone 2 ore body (MAC423, MAC425), the alteration halo of the Zone 2 ore body (MAC69, MAC146), below the sandstone-hosted Zone 1 (MAC201) and Zone 4 (MAC420) ore bodies, non-mineralized (apparently barren) areas (MAC436) and sub-economic (low-grade, <1 wt% U_3O_8) areas (MAC98, MAC99). One sample (MAC122) of the P2 fault in the Read Formation sandstone (non-mineralized) was also examined. Magnesio-foitite is absent in the basement outside the P2 fault; therefore, a MFd sample (MAC462) was analyzed for trace elements in order to be compared with the P2 fault samples. Samples MAC99 and MAC201 also contain oxy-dravite, which was analysed for trace element abundances.

5.3 Analytical methods

5.4.1 Trace elements

Tourmaline in polished thick (~ 50 μm) sections was first inspected using a scanning electron microscope (SEM) for the presence of mineral inclusions and to identify surrounding minerals. Prior to trace element analysis, the major element composition of tourmaline was quantified using an electron microprobe analyzer (EMPA). The EMPA method and data are reported in Adlakha and Hattori (2016).

Magnesio-foitite was analyzed at the University of New Brunswick using a COMPexPro 193nm excimer laser ablation system coupled to an Agilent 7700 quadrupole ICP-MS. Considering the small size of individual magnesio-foitite crystals, it was impossible to analyze single crystals. The laser was focussed to 26 μm for all samples except for MAC122 and MAC436 where a larger

spot size of 46 μm was used because tourmaline crystals are wide (up to 20 μm) and form large clean aggregates/veinlets (up to 0.5 cm wide). In general, a larger beam size provides lower detection limits. The elemental abundances were obtained based on the count ratios of select isotopes (^{7}Li, ^{45}Sc, ^{51}V, ^{52}Cr, ^{89}Y, ^{139}La, ^{140}Ce, ^{141}Pr, ^{146}Nd, ^{147}Sm, ^{175}Lu, ^{151}Eu, ^{157}Gd, ^{159}Tb, ^{163}Dy, ^{165}Ho, ^{166}Er, ^{169}Tm, ^{172}Yb, ^{175}Lu, ^{182}W) to ^{27}Al in the sample and the reference standards NIST-610 and NIST-612 from National Institute of Standards and Technology. Additionally, ^{10}B, ^{11}B and ^{31}P were collected to ensure that the data was collected from tourmaline, and not from inclusions of phosphate minerals (see section 5.1). Each sample was analysed 15 – 20 times and counts of each element were reviewed in time-series to verify the absence of mineral inclusions: the acquisition time for the data were adjusted appropriately (Appendix Figs A5.1A,B). Detailed analytical conditions are provided in Appendix Table A5.1. The data were imported into Iolite (Version 2.5) and the data reduction was carried out using the add-on IGOR Pro (Version 6.3.7, Wavemetrics Inc.). Analyses of reference BCR-2G (Columbia River basalt from USGS) shows an accuracy of ± 15 % for all elements (except for Y and Tb ± 20 %) and precision <10 %.

Oxy-dravite was analyzed for trace elements at the Geological Survey of Canada using a 193 nm ArF excimer laser focused to 34 μm on the sample surface with a repetition rate of 10 Hz. Isotopes were measured using an Agilent 7700 ICP-MS. During the analysis ~40 s of background signal was collected with the laser turned off and then ablation was performed for ~60 s for a total time of 100 s for one analytical cycle. Counts of all elements were monitored during the analysis to make sure mineral inclusions are not incorporated in the analysis. The elemental abundances were obtained based on the count ratios of select isotopes (^{7}Li, ^{45}Sc, ^{51}V, ^{52}Cr, ^{89}Y, ^{139}La, ^{140}Ce, ^{141}Pr, ^{146}Nd, ^{147}Sm, ^{175}Lu, ^{151}Eu, ^{157}Gd, ^{159}Tb, ^{163}Dy, ^{165}Ho, ^{166}Er, ^{169}Tm, ^{172}Yb, ^{175}Lu, ^{182}W) to ^{25}Mg in the sample and the USGS reference standard GSD-1G (synthetic basalt glass). Analyses

of reference BCR-2G shows accuracy of ± 10 % for all elements (except for Cr at ±14 %, Tb at ±11% and Tm at ±12%). The analysis of GSD-1G shows counting precision of <5 % for all elements.

5.4.2 Hydrogen isotope compositions

The δD values of magnesio-foitite were obtained at the University of Ottawa, using an Elementar Vario Pyro Cube for sample pyrolysis and a Thermo-Finnigan DELTAplus XP Isotope Ratio Mass Spectrometer (IRMS) for isotope ratio measurement (Vario Pyo Cube instruction manual, V1.3, Elementar, Germany). Tourmaline mineral separates were prepared using a micro-drill to separate material from monomineralic tourmaline veinlets in drill cores. Sample purity of magnesio-foitite is greater than 95%, based on visual inspection of the veinlets using optical and scanning electron microscopes, with possible presence of quartz, illite and sudoite. Individual samples of illite and sudoite, and mixtures of illite and sudoite were also analysed. The samples and standards were weighed in silver capsules and then placed in an auto-sampler carousel. The samples were combusted in a pyrolysis reactor at 1450 °C to produce H_2 for mass spectrometric analysis. Duplicate analysis of samples gives precision of ± 1 ‰. The data were normalised to VSMOW using an internal standard, kaolinite, and an international standard, polyethylene foil of CH-7 from International Atomic Energy Agency. The data are reported as standard delta notation per mil (‰).

5.4.3 Boron isotope compositions:

Grains for B isotope analysis were selected using SEM back-scattered electron imaging in polished thick sections. The select areas were cored and set in a one-inch epoxy mount for the isotope analysis. The B isotope composition of tourmaline was measured using a sensitive high-resolution ion microprobe (SHRIMP II) at the Geological Survey of Canada, Ottawa. Slit openings

were set at 150 μm at the source and 400 μm at the collector to provide flat top peaks with a mass resolution of ~1500, adequate to resolve BH hydride peaks. No energy filtering was employed. Analyses were carried out using Faraday cups with 10^{11} ohm resistors. Each analysis consisted of 3 sets of 10 scans collecting counts at three mass stations at ^{10}B (6 s), ^{11}B (3 s) and background (10 s) for a total analytical time of 20 minutes. Elevated backgrounds were not noted. Peak centering was performed after each set of 10 analyses and measured intensities were normalized to the total secondary beam. The data were reduced using the software POXI. Internal precision was typically 0.1 - 0.2 ‰ for individual analyses of standard tourmalines with external reproducibility at 0.4 - 0.6 ‰ (95% confidence). Instrumental mass fractionation was evaluated and corrected using dravite reference material (H108796) (Dyar et al. 2001, Leeman and Tonarini 2001). Results for three other tourmaline reference materials (elbaite H98144, dravite, and schorl IAEA-B-4; Tonarini et al. 2003) indicate matrix-related instrumental mass fractionation differences at the ±1 ‰ level. The B isotope compositions are reported as a standard per mil (‰) notation.

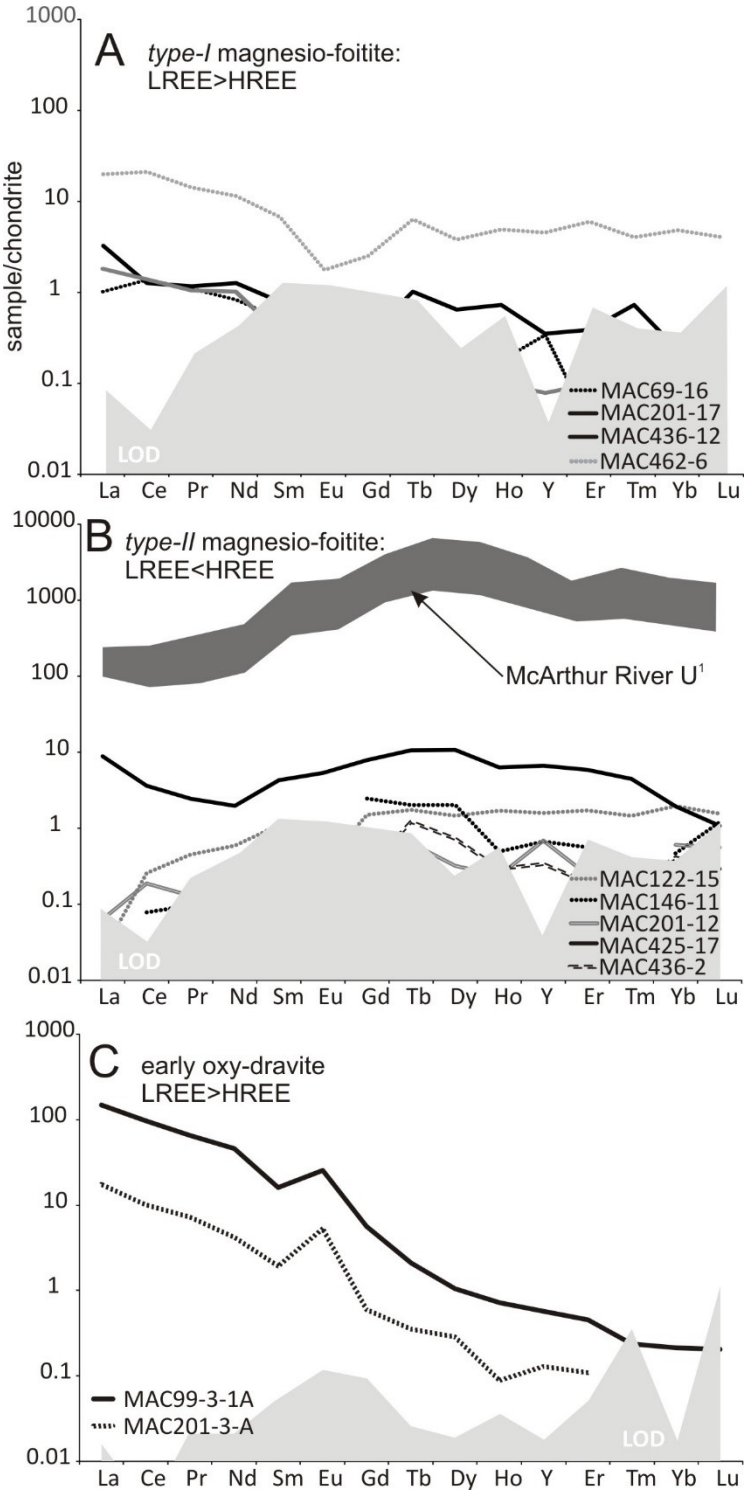

Figure 5.3. Chondrite normalized REE+Y diagrams for representative measurements of magnesio-foitite and oxy-dravite presented in Table 5.2. A) *type-I* magnesio-foitite exhibits slighter higher LREE relative to HREE with negative Eu anomalies, B) *type-II* magnesio-foitite exhibits high HREE relative to LREE, and C) oxy-dravite displays high LREE relative

to HREE and negative Eu anomalies. Data for McArthur River uraninite (Fayek and Kyser 1997) is shown as a dark grey field in diagram B. The limit of detection (LOD) is shown as a light grey field. Chondrite values are from McDonough and Sun (1995).

5.4 Results

5.4.1 Trace elements

A total of one hundred and seven measurements of trace elements were conducted on seven magnesio-foitite samples and six measurements of the 2 samples of oxy-dravite (Appendix Tables 5.A.2 and A.3). Magnesio-foitite in five samples along the P2 fault (MAC69, MAC122, MAC146, MAC201, MAC436), from non-mineralized and mineralized areas, contain very low concentrations of total REE (<2 ppm, Table 5.2, La - Lu) and Y (<2.5 ppm). The Eu anomalies of magnesio-foitite from these five samples could not be determined as the concentrations of LREE are below detection limits.

Magnesio-foitite in ore sample MAC425 and MFd sample MAC462 contains high and variable concentrations of total REE (3.8 – 46 ppm and 0.2 – 68 ppm, respectively) and Y (2.5 – 35 ppm and 0.32 – 7.1 ppm, respectively). Europium anomalies from sample MAC425 range from negative (as low as 0.2) to positive (up to 1.9), however most are close to 1. Magnesio-foitite from MAC462 exhibits negative Eu anomalies (as low as 0.4; Fig. 5.3).

Considering the small grain size of magnesio-foitite and the very low concentrations of REE in magnesio-foitite, it is possible that surrounding or intergrain minerals contributed LREE to the analysis. Surrounding minerals (e.g., chlorite and illite) contain essentially no REE and do not contribute to the magnesio-foitite data (Appendix Fig. A5.1C). This implies surrounding minerals could have diluted the REE data obtained for magnesio-foitite. Counts of ^{10}B and ^{11}B were collected during analysis to confirm that the data were acquired from magnesio-foitite. To

ensure that intergrain minerals did not contribute REE, counts of ^{31}P were collected during the analysis because APS minerals, xenotime, monazite and apatite are the main REE-bearing phases in the study area. There is no correlation between LREE or HREE and P (Appendix Fig. A5.1D), thus it is unlikely that minute grains of these phosphates contributed to REE results. Therefore, we consider the measured trace element abundances to represent those of magnesio-foitite.

Two types of magnesio-foitite are recognised based on abundances of REE and Y: *type-I* exhibits a negatively sloped chondrite normalized REE pattern with higher LREE relative to HREE ($Ce_N > Y_N$) and slightly negative Eu anomalies (Fig. 5.3A), *type-II* shows a positively sloped normalized pattern with lower LREE relative to HREE ($Ce_N < Y_N$; Fig. 5.3B). Some magnesio-foitite from MAC201 contain REE concentrations lower than detection limits and could not be classified (see Appendix Table A5.2 for LOD). Both types of magnesio-foitite occur as disseminations but *type-II* forms monomineralic veinlets. Both *type-I* and *-II* magnesio-foitite occur in samples along the P2 fault, although *type-II* is far more abundant (Appendix Table A5.2). Sandstone MFd sample contains predominately *type-I.*

Four P2 fault samples (MAC122, MAC146, MAC201, MAC436) contain relatively low Li (up to 34.7 ppm), V (up to 156 ppm), Cr (86.7 ppm) and W (up to 0.25 ppm). Magnesio-foitite of sample MAC69 contains variable concentrations of Li (up to 449 ppm), V (208 to 1030 ppm), and Cr (48.6 – 170 ppm). The highest values were observed in ore sample MAC425, with Li ranging from 502 – 1110 ppm, V from 1240 – 3420 ppm, Cr from 126 – 198 ppm, and W up to 6.80 ppm. In contrast, magnesio-foitite in the uppermost sandstone (MAC462), MFd, contains relatively low V (16.4 – 29.3 ppm), Cr (1 – 40.6 ppm) and W (up to 2.12 ppm).

Table 5.2. Representative analysis of trace elements in tourmaline (ppm)

	magnesio-foitite									oxy-dravite	
	Type I: $Ce_N > Y_N$				*Type II: $Ce_N < Y_N$*						
	MAC69	MAC201	MAC436	MAC462	MAC122	MAC146	MAC201	MAC425	MAC436	MAC99	MAC201
Li	449	13.9	6.3	n.d.	34.7	n.d.	33.1	765	11.4	10.42	11.8
Sc	21.2	23.2	10.6	7.8	12.6	23.2	39.3	21.9	9.82	65.5	57.2
V	1030	81.9	117	29.3	118	79.3	82.8	2680	95.8	1030	1160
Cr	170	15.1	94	32.7	27.9	13.9	6.3	180	73.7	478	315
Y	0.553	0.55	0.126	7.1	2.49	1.05	1.08	10.4	0.532	0.89	0.509
La	0.251	0.77	0.45	4.7	<0.02	<0.02	<0.02	2.09	<0.02	34.7	7.47
Ce	0.92	0.8	0.94	13.5	0.164	0.05	0.12	2.31	<0.02	61.62	13.9
Pr	0.107	0.109	0.102	1.32	0.042	<0.02	<0.02	0.23	<0.02	6.06	1.43
Nd	0.4	0.58	<0.2	5.2	<0.2	<0.2	<0.2	0.90	<0.2	20.9	4.81
Sm	0.084	<0.2	0.057	1.04	<0.2	<0.2	<0.2	0.66	<0.2	2.47	0.72
Eu	<0.07	<0.07	<0.07	0.10	<0.07	<0.07	<0.07	0.31	<0.07	1.48	0.503
Gd	<0.2	0.066	<0.2	0.5	0.3	0.49	<0.2	1.57	<0.2	1.13	0.313
Tb	<0.03	0.037	<0.03	0.23	0.063	0.073	<0.03	0.38	0.044	0.076	0.039
Dy	<0.06	0.16	<0.06	0.94	0.36	0.5	0.079	2.64	0.179	0.257	0.097
Ho	<0.03	0.04	<0.03	0.27	0.093	<0.03	<0.03	0.34	<0.03	0.039	0.025
Er	<0.11	<0.11	<0.11	0.96	0.275	<0.11	<0.11	0.94	<0.11	0.072	0.060
Tm	<0.01	0.018	<0.01	<0.01	0.036	<0.01	<0.01	0.11	<0.01	0.006	0.006
Yb	<0.06	<0.06	<0.06	0.8	0.324	<0.06	0.1	0.32	0.068	0.035	0.013
Lu	<0.03	<0.03	<0.03	0.101	0.039	<0.03	<0.03	<0.03	<0.03	0.005	0.025
W	<0.06	<0.06	<0.06	0.23	0.132	0.098	<0.06	0.17	<0.06	<0.02	<0.04
∑REE	1.76	2.58	1.55	29.66	1.70	1.11	0.30	12.81	0.29	128.81	29.41
Y_N/Ce_N	0.24	0.28	0.05	0.21	6.17	8.53	3.66	1.84	>1	0.01	0.01

n.d. = no data

Early oxy-dravite contains relatively high REE (15 – 130 ppm; Table 5.2) and low Y (0.25 – 0.89 ppm), with negatively sloped normalized REE patterns expressed as Ce_N/Y_N = 67 – 170, and positive Eu anomalies (Eu/Eu* = 2.7 – 6.5). Contents of Li (8.8 – 13.1 ppm) and W (<0.02 ppm) are low, whereas Cr (293 – 478 ppm) and V (588 – 1160 ppm) are relatively high. Oxy-dravite contains 54.3 – 65.5 ppm Sc.

5.4.2 Hydrogen isotope composition of tourmaline and fluid

Three samples of magnesio-foitite were analysed for hydrogen isotopes: MAC122 from the non-mineralized RF, MAC146 of the Zone 2 ore body alteration halo and MAC420 of the Zone 4 ore body alteration halo. Samples MAC122 and MAC146 contain monomineralic veinlets of magnesio-foitite (Fig. 5.2C,D) and sample MAC420 contains massive aggregates of magnesio-

foitite with very minor sudoite. Both MAC122 and MAC146 have similar δD values of -44.0 ‰ and -44.4 ‰, respectively. In contrast, MAC420 has a lower δD value of -93.0 ‰.

Although the mineral separates were collected from monomineralic veins and aggregates, it is likely that they contained minor illite, sudoite and/or quartz. Quartz does not contain H; however, illite and sudoite contain H. Illite and sudoite show δD values of -60 ‰ and -66 ‰, respectively, which are in agreement with data from the McArthur River area determined by Kotzer and Kyser (1995) (-60 ± 20 (1σ) ‰ and -75 to ± 16 (1σ) ‰, respectively). Assuming that the magnesio-foitite samples contain 2.5% each of sudoite and illite (conservative estimate of purity, which is more than 95%) and that the minerals contain ideal H contents (1.35 wt% for illite, 1.46 wt% for sudoite, and 0.43 wt% for magnesio-foitite), the calculated H isotope composition of magnesio-foitite in samples MAC122, MAC146 and MAC420 is ~-41, ~-41 and ~-98 ‰, respectively. Clearly, contamination does not significantly impact the data. We also note that our δD values for magnesio-foitite are similar to the range of -49 to -143 ‰ reported by Kotzer and Kotzer (1995).

The δD ratio of a fluid in equilibrium with tourmaline is calculated using the empirical fractionation factor of -21 and -28 ‰ at 170 and 200 °C, respectively, determined by Kotzer et al. (1993). This temperature range encompasses the range of temperatures estimated for ore deposition (Derome et al. 2005) and tourmaline formation (Kotzer and Kyser 1995). The δD values of fluids range from -13 to -20 ‰ for monomineralic magnesio-foitite veins in MAC122 and MAC146, and from -70 to -77 ‰ for magnesio-foitite aggregates associated with sudoite in MAC420.

5.4.3 Boron isotope composition of tourmaline and fluid

A total of seventeen measurements of $\delta^{11}B$ were collected from 7 different samples (Table 5.3). Magnesio-foitite from non-mineralized areas of the P2 fault zone (MAC122), areas of low-grade mineralization (MAC98, MAC99), areas proximal (i.e. alteration halo) to Zone 1 (MAC201) and Zone 2 (MAC69) ore bodies, and from the Zone 2 ore body (MAC423 and MAC425) have $\delta^{11}B$ values ranging from +13.1 to +23.2 ‰ (Table 5.3). Magnesio-foitite co-existing with uraninite from two samples shows a large range in $\delta^{11}B$ values from +13.0 to +19.8 ‰. Magnesio-foitite from alteration haloes of the Zone 1 and Zone 2 ore bodies also exhibits a large range from +16.8 to +23.2 ‰. In the two samples near low-grade mineralization along the P2 fault, magnesio-foitite has a narrower range of $\delta^{11}B$ values, from +15.7 to +18.3 ‰. In the non-mineralized sample, magnesio-foitite shows $\delta^{11}B$ ranging from +15.0 to +15.8 ‰.

The $\delta^{11}B$ values of a fluid in equilibrium with tourmaline were calculated using the fractionation factor between tourmaline and water of Meyer et al. (2008) at temperatures between 170 and 200 °C. All B in the fluid is assumed to be boric acid, as boric acid is predominant in fluids during tourmaline formation (Morgan and London 1989). The fractionation factor of -6.0 to -5.4 ‰, yields $\delta^{11}B$ values of a co-existing fluid ranging from +18.4 to +29.2‰ $\delta^{11}B$ (Table 5.3; Fig. 5.4).

5.5 Discussion

5.5.1 Composition of hydrothermal fluids

Two different species of hydrothermal tourmaline occur in the basement along the P2 fault: earlier oxy-dravite related to pre-Athabasca hydrothermal activity and later magnesio-foitite related to uraniferous hydrothermal activity (Adlakha and Hattori 2016). This study reveals that oxy-dravite is characterized by overall high REE contents (14 – 130 ppm) with high LREE relative

to HREE ($Ce_N >> Y_N$, where Y is used for the proxy of HREE). On the other hand, magnesio-foitite is characterized by very low REE contents (usually <2 ppm), except for grains in the ore zone. Two types of magnesio-foitite exist along the P2 fault, based on relative abundance of LREE and HREE. Most magnesio-foitite along the P2 fault are *type-II,* with low LREE relative to HREE ($Ce_N < Y_N$, Fig. 5.3, Table 5.2). *Type-I* magnesio-foitite also occurs along the P2 fault, containing higher LREE than HREE ($Ce_N > Y_N$). Tourmaline does not preferentially incorporate specific REE; therefore, the REE patterns of tourmaline reflect the composition of the fluid (Joliff et al. 1987). As such, the different REE abundances of oxy-dravite, *type-I* and *type-II* magnesio-foitite are attributed to the different compositions of fluids from which they crystallized.

Crustal hydrothermal fluids are commonly enriched in LREE because they are more mobile than HREE (Faure 1998). Therefore, hydrothermal tourmaline commonly contains relatively high LREE, similar to oxy-dravite and *type-I* magnesio-foitite in this study. Oxy-dravite exhibits positive Eu anomalies (Fig. 5.3C) indicating that the fluid likely interacted with plagioclase-bearing mafic rocks (e.g. metabasite of the Wollaston Domain). This is also supported by high Cr contents in oxy-dravite (Table 5.1). In contrast, *type-I* magnesio-foitite exhibits a flatter pattern with minor negative Eu anomalies, indicating the interaction of the fluid with felsic rocks. Granitic pegmatite lenses are abundant in the Wollaston Group in the basement (Annesley et al. 2005) and provided clasts for sediments in the Athabasca Basin; therefore, it is likely that this REE pattern reflects the interaction of the fluid with felsic rocks in the basement, as well as fragments and clasts of such rocks in the Athabasca Basin.

The low LREE (relative to HREE) in *type-II* magnesio-foitite along the P2 fault zone is unusual for hydrothermal tourmaline. The P2 fault experienced high water/rock ratios during hydrothermal activity considering the pervasive alteration (sudoite, illite, magnesio-foitite and

APS minerals) observed along the entire 13 km long fault (Adlakha and Hattori 2015, 2016). Therefore, the host rock cannot be responsible for the REE pattern of *type-II* magnesio-foitite. Instead, the high HREE, relative to LREE, of tourmaline is attributed to the co-crystallization of tourmaline with a LREE-rich phase. Previous studies indicate that magnesio-foitite forms an assemblage with LREE-rich (up to 15 wt% LREE) APS minerals (florencite; Adlakha and Hattori 2015). The chondrite-normalized REE pattern of florencite is steep and negatively sloped due to high LREE contents and relatively low HREE contents (50 – 150 ppm HREE; Adlakha and Hattori 2015). Therefore, the depletion of LREE in *type-II* magnesio-foitite is credited to its co-precipitation with florencite. The effect of contemporaneous REE-bearing minerals on the REE composition of tourmaline has also been demonstrated in magmatic systems by Čopjaková et al. (2013).

Both *type-I* and *-II* magnesio-foitite occur in four different samples of the P2 fault, independent of rock type, in areas of mineralization and non-mineralized areas. Only *type-II* magnesio-foitite occurs as veinlets within the P2 fault zone. The presence of both types of magnesio-foitite along the P2 fault is explained by the evolution of fluids along the fault. Early fluid along the P2 fault, and in the MFd, contained higher LREE than HREE and crystallized *type-I* magnesio-foitite. This enrichment in LREE is most likely due to reactions with felsic material, such as clasts of pegmatites in sandstones and pegmatite lenses in the basement rocks. When the crystallization of florencite began along the P2 fault, *type-II* LREE-depleted magnesio-foitite was produced.

Type-II magnesio-foitite along the P2 fault exhibits similar normalized REE patterns to uraninite from the McArthur River deposit, where HREE contents are greater than LREE (Fig. 5.3B, Fayek and Kyser 1997). This observation supports the interpretation that magnesio-foitite,

florencite and uraninite crystallized together. Florencite in the Athabasca Basin forms very small (<20 μm) grains but contains high LREE. Thus, the crystallization of this mineral has a profound effect on the chemistry of fluids. It is also noted that uraninite contains much higher overall concentrations of REE (up to 12,000 ppm) than magnesio-foitite. This is because REE^{3+} has a similar ionic radius to U^{4+}.

Magnesio-foitite within the Zone 2 ore zone contains up to two orders of magnitude higher REE than tourmaline from areas outside of the ore zone (Table 5.2), indicating that fluids in the ore zone had higher concentrations of REE than elsewhere along the fault. Genetic models for unconformity-type U deposits invoke the mixing of two fluids during mineralization: i) an oxidizing, U^{6+}-bearing fluid and ii) a reducing, REE-rich basement-derived fluid (e.g. Kotzer and Kyser 1995, Fayek and Kyser 1997). The basement rocks are the most likely source of REE considering the abundance of REE-bearing minerals in pegmatite and pelite such as garnet, zircon, apatite, and monazite (Fayek and Kyser 1997). Although some of these minerals are reported in the Athabasca Group sandstone (Fayek and Kyser 1997), they occur as minor to trace amounts and show minor alteration (e.g. Hecht and Cuney 2000). Given that U precipitaiton required a reducing basement fluid, it is possible that the relatively low total REE in magnesio-foitite was due to the co-precipitation of florencitic APS minerals from a REE-rich basement fluid. This observation is consistent with Adlakha and Hattori (2015) who observed that LREE-bearing APS minerals were much more abundant in proximity to the ore zone and contained higher REE than APS minerals in areas distal to the ore zone.

Magnesio-foitite of the MFd also contains comparatively high REE (Table 5.2). This observation is consistent with reports of REE enrichment of the MFd sandstones (Chen et al. 2015).

5.5.2 Stable isotope compositions of magnesio-foitite forming fluid

The δD values of two monomineralic magnesio-foitite veinlets are essentially identical (δD = -44 %), although the samples are from two different areas of the P2 fault: the alteration halo of the Zone 2 ore body and the non-mineralized sandstone of the Read Formation, ~4 km SW of Zone 2. Furthermore, magnesio-foitite from the two samples exhibit very similar REE and trace element contents, as well as only *type-II* magnesio-foitite (Table 5.2). It is too fortuitous to have such similarities in these samples. Furthermore, APS minerals associated with magnesio-foitite have similar compositions along the P2 fault (Adlakha and Hattori, 2015). The data suggest that these alteration minerals crystallized from the same fluid that travelled along the P2 fault.

The δD values of the magnesio-foitite suggest that fluids range from -77 to -13 ‰ δD. The possible fluids during formation of the tourmaline include (i) seawater, (ii) evaporating seawater, (iii) a basinal fluid, and (iv) groundwater. Seawater has a δD value of ~0 ‰ throughout geological time and evaporated seawater has a δD > 0 ‰ (Fig. 5.4), as D is enriched in water during the evaporation (Faure 1998). The negative δD values of the fluids that formed magnesio-foitite suggest that seawater and evaporating seawater were not solely responsible for the formation of tourmaline. Theoretically, negative δD can be achieved through extreme evaporation of seawater, where >90 % of water is lost to evaporation after NaCl crystallization (Holser 1979). To achieve δD below -10 ‰, the water would have to be evaporated even further. This type of fluid has been postulated as the origin of halite-hosted fluid inclusions (Knauth and Beeunas 1986). If the fluids achieved negative δD values by such extreme evaporation, the original volume of seawater must be more than 20 times of the uraniferous fluids. Considering the extent of hydrothermal alteration associated with the U deposits and size of U deposits, this appears to be an unlikely proposition. The above precludes (i) seawater, (ii) evaporating seawater or extremely evolved seawater as the

sole fluid responsible for the crystallization of tourmaline. The third possibility is (iii) a basinal fluid which formed during the deposition and diagenesis of the Athabasca Basin. The upper part of the Athabasca Basin mostly comprises shallow marine sediments; therefore, the ultimate source of basinal fluid is seawater. In general, basinal fluids in thick marine sedimentary basins show δD values comparable to, or higher than, seawater (Clayton et al. 1966). Through diagenesis and the formation of kaolin and illite, the basinal fluid would be enriched in D, because H is preferentially incorporated into hydrous minerals such as kaolin and illite (e.g., Suzuoki and Epstein 1976). This indicates that the basinal fluid alone probably did not produce magnesio-foitite. The fourth possibility is (iv) groundwater. During its deposition, the Athabasca Basin was located on the paleo-continent Laurentia at latitudes of 30 to 50° (Irving et al. 2004). At these latitudes, groundwater of the Athabasca Basin likely had δD values between -70 to -30 ‰ (Fig. 5.4; Taylor 1974), and progressively lower values as Laurentia drifted to higher latitude. Therefore, groundwater as the main source of fluid is consistent with the δD values of the fluids responsible for the magnesio-foitite crystallization, although this interpretation does not preclude possible contribution of other fluids.

The $\delta^{11}B$ values of magnesio-foitite presented in this study (+13.0 to +23.2 ‰) indicate its equilibrium with fluids with $\delta^{11}B$ = +18.4 to +29.2 ‰ (Fig. 5.4). Here, we examine possible sources of B for the hydrothermal fluids responsible for magnesio-foitite. They include B dissolved in seawater, evaporated seawater and groundwater, and B in marine evaporite minerals. The $\delta^{11}B$ of seawater and evaporated seawater is ≈ +40 ‰ or higher (e.g., Vengosh et al. 1992) (Fig. 5.4). The values are much higher than those estimated for B in fluids for magnesio-foitite, indicating that these are probably not the major sources for B. The $\delta^{11}B$ of groundwater is variable (Fig. 5.4) and is influenced by the $\delta^{11}B$ values of aquifer rocks and the degree of B adsorption on clay

minerals (Vengosh et al. 1989, 1991, Vengosh 1990). If B in groundwater of the Athabasca Basin is sourced from Athabasca sediments (metamorphic and magmatic provenance) the fluid should have relatively low $\delta^{11}B$ values. However, detrital clays adsorb ^{10}B onto mineral surfaces and detrital minerals are altered to form sheet silicate minerals, which preferentially incorporate ^{10}B, during water-rock interaction (e.g. Palmer et al., 1987; Vengosh et al. 1992, Williams et al., 2001). Therefore, fluid can become enriched in ^{11}B.

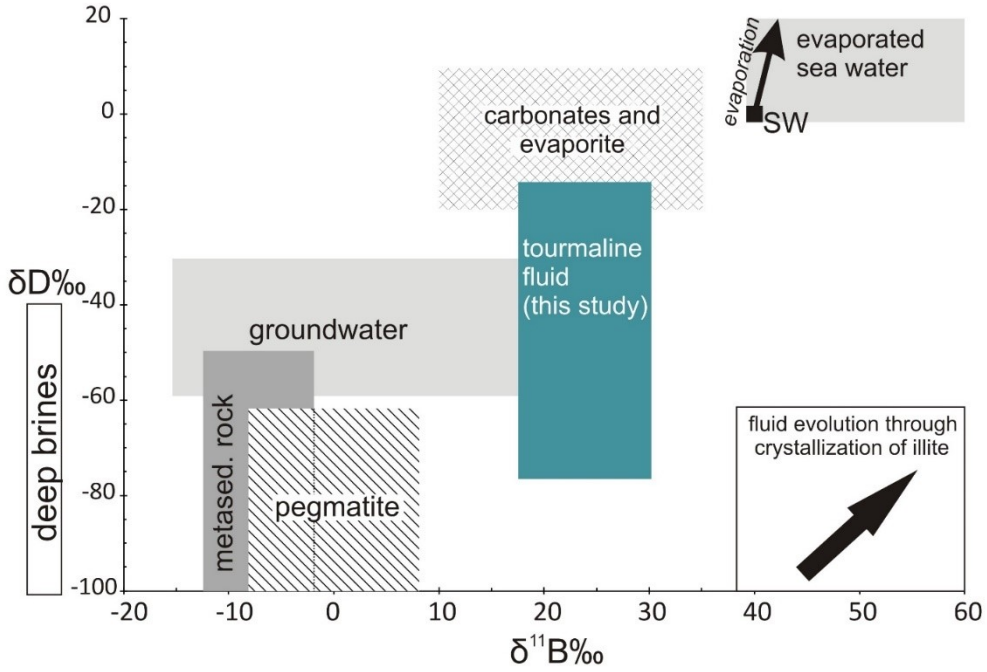

Figure 5.4. Schematic diagram of $\delta^{11}B$ and δD values of the fluid in equilibrium with magnesio-foitite presented in this study (Table 5.3) and of various fluids with ^{11}B and □D. The □^{11}B data were sourced from Barth (1993, and references therein) and Trumbell et al. (2008) and δD data from Taylor (1974) and Frape et al. (1984). An arrow from seawater values shows the expected change in isotope composition during evaporation. The bottom right inset shows fluid evolution during crystallization of illite (e.g., Suzuoki and Epstein 1976, Palmer et al., 1987). SW = seawater

---

The calculated $\delta^{11}B$ of the fluid is similar to that of evaporite and carbonate rocks ($\delta^{11}B$ = +13 to +31 ‰, Swihart et al. 1986) (Fig. 5.4) and brines formed through the dissolution of these

rocks (Kloppman et al. 2001). Carbonate is preserved within the dolomitic Carswell Formation, the youngest unit of the Athabasca Group in the western part of the Athabasca Basin (Raemakers, 1990; Fig. 5.1). Evaporites are not present in the area, although there are reports of stromatolites and salt casts within the Carswell Formation (Raemakers, 1990). The occurrence of carbonates may indicate that the paleo-environment was favorable for the formation of evaporites. It is possible that these rocks existed during deposition of the Basin but were eroded. Dissolution of evaporitic components of these rocks would provide high ^{11}B to the fluid. The high $\delta^{11}B$ and low δD values of magnesio-foitite presented here are consistent with tourmaline that crystallized from a brine formed through the dissolution of evaporites and/or carbonates by groundwater (Fig. 5.4). A contribution of evaporite to groundwater has been invoked by many researchers based on the high salinities of fluids in the Athabasca Basin (e.g., Kotzer and Kyser 1995; Kyser et al. 2000; Derome et al. 2005).

The $\delta^{11}B$ values of magnesio-foitite presented in this study are significantly lower than those reported by Mercadier et al. (2012) (McArthur River deposit = +23.1 to +28.7 ‰, Shea Creek = +19.6 to +32.2 ‰, P-Patch = +23.8 to +34.6 ‰, and Eagle Point = +29.7 to +36.5 ‰). The wide range in $\delta^{11}B$ data for tourmaline observed by Mercadier et al and in this study from the Athabasca Basin suggests that an additional process likely affected the isotope composition of the fluid. Two possibilities include the mixing of fluids and/or fractionation of B from the fluid.

Table 5.3. B-isotope data of magnesio-foitite

				$\delta^{11}B_{FLUID}$[b] (‰)	
Zone[a]	Sample	$11B_{TUR}$ (‰)	*T °C*	*170*	*200*
NM	MAC122	15.8		21.8	21.2
	MAC122	15.0		21.0	20.4
LG	MAC98	17.2		23.2	22.6
	MAC98	18.3		24.2	23.6
LG	MAC99	15.7		21.7	21.1
	MAC99	17.1		23.0	22.4
AH	MAC201	19.9		25.9	25.3
	MAC201	23.2		29.2	28.6
	MAC201	22.9		28.8	28.2
AH	MAC69	16.8		22.8	22.2
	MAC69	17.1		23.1	22.5
ORE	MAC423	13.0		19.0	18.4
	MAC423	18.9		24.9	24.3
	MAC423	18.3		24.3	23.7
	MAC423	18.6		24.6	24.0
ORE	MAC425	17.3		23.2	22.6
	MAC425	19.8		25.8	25.2

Notes
a: proximity to mineralization; NM = non-mineralized, LG = low-grade, AH = alteration halo, ORE= ore sample
b: calculated using fractionation factors by Meyer et al. (2008); approximately -6.0 at 170°C and -5.4 at 200°C

Here we consider possible mixing of two fluids: a basinal brine and a basement fluid. The basinal fluid containing B from dissolved evaporite, or seawater, has high ^{11}B. The basement fluid has a low $\delta^{11}B$ value as B is sourced from the dissolution of pegmatite and metapelite, both of which contain low $\delta^{11}B$ (Fig. 4). Therefore, the mixing of these two fluids could have produced the range of $\delta^{11}B$ values for magnesio-foitite. This is supported by the relatively high REE contents in magnesio-foitite of the ore zone suggesting the contribution of a basement fluid. It is also consistent with a large chemical variation in the APS minerals in the ore zone from Sr-Ca-SO_4^{2-}

rich to LREE-P rich varieties (Gaboreau et al. 2007, Adlakha and Hattori 2015). The compositional change reflects two fluids: oxidizing basinal and less oxidizing basement fluids.

In addition, the range in $\delta^{11}B$ values of magnesio-foitite may be explained by the fractionation of B isotopes during fluid-rock interaction. As previously mentioned, the adsorption of ^{10}B on the surfaces of clay minerals results in enrichment of ^{11}B in fluids. Furthermore, sheet silicate minerals preferentially incorporate ^{10}B into the tetrahedral site during their crystallization (e.g., Williams et al., 2001). Clay-sized sheet silicates, such as illite and kaolinite, are ubiquitous in the Athabasca Group sandstones and basement rocks, especially near U deposits. To demonstrate the effect of illite crystallization on the B isotope value of fluids, the evolution of the $\delta^{11}B$ of the fluid was modelled using Raleigh fractionation using the fractionation factor of ca. -20 ‰ at 200 °C between illite-fluid determined by Williams et al. (2001) (Fig. 5.5). The results indicate that it is possible to substantially increase the $\delta^{11}B$ of a fluid through the crystallization of illite. Therefore, the range in B isotope data observed for tourmaline in the proximity of U deposits could be due to the removal of ^{10}B through the progressive crystallization of clay minerals during the hydrothermal activity related to the U mineralization.

5.6 Conclusion

Magnesio-foitite shows different trace element signatures depending on the occurrence: magnesio-foitite in the MFd, the uppermost sandstone, contains high LREE relative to HREE, whereas magnesio-foitite of the P2 fault exhibits two different REE signatures; one with relatively high LREE and the predominant, second type with relatively low LREE. Initial fluids along the P2 fault carried high LREE and produced magnesio-foitite with LREE>HREE. The fluid became enriched in REE through interaction with the basement rocks. The co-precipitation of magnesio-foitite with florencite, a LREE-bearing APS mineral, formed fluids with low LREE from which

magnesio-foitite and uraninite crystallized. Magnesio-foitite of the ore zone contains higher REE than magnesio-foitite in other areas of the fault, possibly due to the presence of a REE-rich basement fluid or that less florencite co-precipitated. The δD values of magnesio-foitite suggest that the dominant source of fluids is groundwater although a contribution of sea water cannot be ruled out. The high $\delta^{11}B$ values of magnesio-foitite indicate that the groundwater dissolved carbonates and/or evaporites and produced an ^{11}B-rich fluid. The large range in B isotope composition of tourmaline from various U deposits in the area may be due to the preferential incorporation of ^{10}B into illite and kaolinite during their crystallization or mixing of various sourced fluids including basinal and basement fluids.

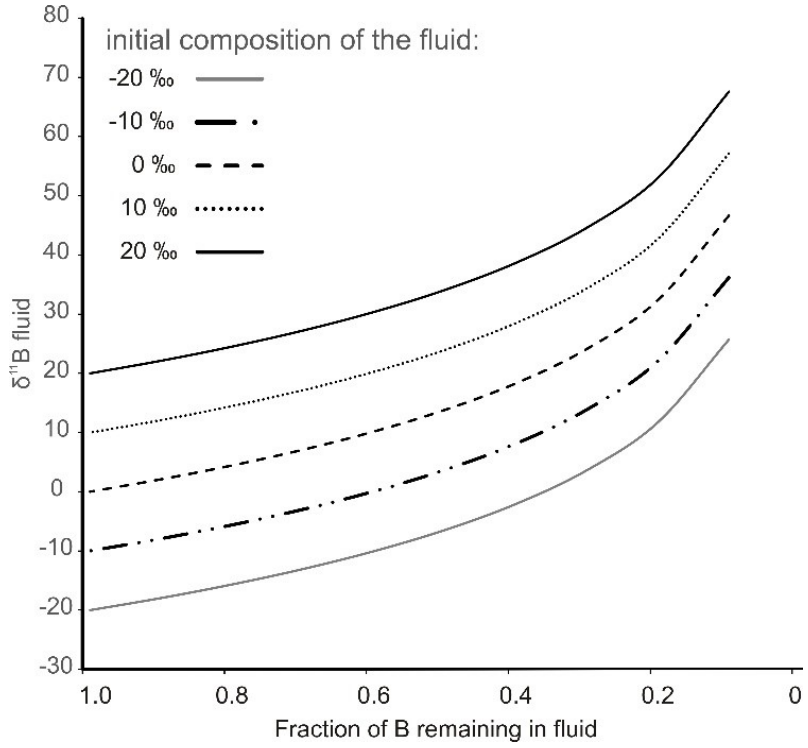

Figure 5.5. Rayleigh fractionation models of a fluid, with various initial $\delta^{11}B$ (ranging from -20 to +20 ‰), which has undergone fractionation of B isotopes due to the crystallization of illite. The fractionation factor of -20 ‰ (at 200 °C) is used for the calculations (Williams et al. 2001).

Acknowledgements:

This project was funded by Natural Resources of Canada through the Targeted Geoscience Initiative Four (TGI-4) program, a Research Affiliate Program Bursary to EEA and a grant to KH. We thank Dr. Eric G. Potter, science leader for the TGI-4 U ore system project, at the Geological Survey of Canada, for his continuous support. Cameco Corporation provided their logistical support for our field work at the McArthur River mine. Special thanks extend to Gerard Zaluski and Tom Kotzer, as well as Aaron Brown, Doug Adams, Remi Labelle, and Brian McGill of Cameco Corp. for their help during the field work and useful suggestions. We thank Zhaoping Yang of the GSC for her assistance with LA-ICP-MS analysis of oxy-dravite. Many thanks extend to Tom Pestaj and Pat Hunt of the GSC for their assistance with sample preparation for B isotope analysis. We also thank Paul Middlestead of the University of Ottawa for his assistance with H isotope analysis.

References

Adlakha, E. E., & Hattori, K. (2015). Compositional variation and timing of aluminum phosphate-sulfate minerals in the basement rocks along the P2 fault and in association with the McArthur River U deposit, Athabasca Basin, Saskatchewan, Canada. American Mineralogist, 100(7), 1386-1399.

Adlakha, E., and Hattori, K. (2016). Paragenesis and composition of tourmaline types along the P2 fault and McArthur River U deposit, Athabasca Basin, Canada. The Canadian Mineralogist, in press.

Annesley, I. R., Madore, C., & Portella, P. (2005). Geology and thermotectonic evolution of the western margin of the Trans-Hudson Orogen: evidence from the eastern sub-Athabasca basement, Saskatchewan. Canadian Journal of Earth Sciences, 42(4), 573-597.

Barth, S. (1993). Boron isotope variations in nature: a synthesis. Geologische Rundschau, 82(4), 640-651.

Chen, S., Hattori, K., Grunsky, E.C., and Liu, Y., (2015). Geomathematical Study of Sandstones Overlying the Phoenix Uranium Deposits and the REE-rich Maw Zone, Athabasca Basin, Saskatchewan, in Targeted Geoscience Initiative 4: unconformity-related uranium systems, (ed.) E.G. Potter and D.M. Wright; Geological Survey of Canada, Open File 7791, 21–31

Clayton, R. N., Friedman, I., Graf, D. L., Mayeda, T. K., Meents, W. F., & Shimp, N. F. (1966). The origin of saline formation waters: 1. Isotopic composition. Journal of Geophysical Research, 71(16), 3869-3882.

Čopjaková, R., Škoda, R., Galiová, M. V., & Novák, M. (2013). Distributions of Y+ REE and Sc in tourmaline and their implications for the melt evolution; examples from NYF pegmatites of the Třebíč Pluton, Moldanubian Zone, Czech Republic. Journal of Geosciences, 58(2).

Čopjaková, R., Škoda, R., Galiová, M. V., Novák, M., & Cempírek, J. (2015). Sc-and REE-rich tourmaline replaced by Sc-rich REE-bearing epidote-group mineral from the mixed (NYF+ LCT) Kracovice pegmatite (Moldanubian Zone, Czech Republic). American Mineralogist, 100(7), 1434-1451.

Derome, D., Cathelineau, M., Cuney, M., Fabre, C., Lhomme, T., & Banks, D. A. (2005). Mixing of sodic and calcic brines and U deposition at McArthur River, Saskatchewan, Canada: a Raman and laser-induced breakdown spectroscopic study of fluid inclusions. Economic Geology, 100(8), 1529-1545.

Dyar, M.D., Wiedenbeck, M., Robertson, D., Cross, L.R., Delaney, J.S., Ferguson, K., Francis, C.A., Grew, E.S., Guidotti, C.V., Hervig, R.L., Hughes, J.M., Husler, J., Leeman, W., McGuire, A.V., Rhede, D., Rothe, H., Paul, R., Richards, I., & Yates, M. (2001). Reference minerals for the microanalysis of light elements. Geostandards Newsletter, 25(2-3), 441-463.

Faure, G. (1998). Principles and applications of geochemistry: a comprehensive textbook for geology students. Prentice Hall.

Fayek, M., & Kyser, T.K. (1997). Multiple fluid events and rare earth elements associated with unconformity-type U mineralization from the Athabasca Basin, Saskatchewan, Canada. The Canadian Mineralogist, 35, 327 – 658.

Fayek, M., Kyser, T. K., & Riciputi, L. R. (2002). U and Pb isotope analysis of U minerals by ion microprobe and the geochronology of the McArthur River and Sue Zone U deposits, Saskatchewan, Canada. The Canadian Mineralogist, 40(6), 1553-1570.

Frape, S. K., Fritz, P., & McNutt, R. T. (1984). Water-rock interaction and chemistry of groundwaters from the Canadian Shield. Geochimica et Cosmochimica Acta, 48(8), 1617-1627.

Gaboreau, S., Cuney, M., Quirt, D., Patrier, P., & Mathieu, R. (2007). Significance of aluminum phosphate-sulfate minerals associated with U unconformity-type deposits: The Athabasca basin, Canada. American Mineralogist, 92(2-3), 267-280.

Tonarini, S., Pennisi, M., Adorni-Braccesi, A., Dini, A., Ferrara, G., Gonfiantini, R., Wiedenbeck, Gröning, M., (2003). Intercomparison of boron isotope and concentration measurements. Part II: evaluation of results. Geostandards Newsletter, 27(1), 41-57.

Hajnal, Z., Pandit, B., Reilkoff, B., Takacs, E., Annesley, I., & Wallster, D. (2007). Recent development in 2D and 3D seismic imaging of high-grade U ore deposit related environments, in the Eastern Athabasca Basin, Canada. In Exploration in the new millennium: Proceedings of the Fifth Decennial International Conference on Mineral Exploration, 1131-1135.

Hecht, L., & Cuney, M. (2000). Hydrothermal alteration of monazite in the Precambrian crystalline basement of the Athabasca Basin (Saskatchewan, Canada): implications for the formation of unconformity-related U deposits. Mineralium Deposita, 35(8), 791-795.

Holser, W. (1979). Trace elements and isotopes in evaporites. In Marine Minerals (ed. R. G. Burns) Reviews in Mineralogy, Mineral Society of America, pp. 295-346.

Irving, E. (1979). Paleopoles and paleolatitudes of North America and speculations about displaced terrains. Canadian Journal of Earth Sciences, 16(3), 669-694.

Jefferson, C.W., Thomas, D.J., Gandhi, S.S., Ramaekers, P., Delaney, G., Brisbin, D., Cutts, C., Quirt, D., Portella, P., and Olson, R.A., (2007). Unconformity associated U deposits of the Athabasca Basin, Saskatchewan and Alberta, In: Goodfellow, W.D. (ed.) Mineral Deposits of Canada: A Synthesis of Major Deposit-Types, District Metallogeny, the Evolution of Geological Provinces, and Exploration Methods: Geological Association of Canada, Mineral Deposits Division, Special Publication No. 5, 273-305.

Jolliff, B. L., Papike, J. J., & Shearer, C. K. (1987). Fractionation trends in mica and tourmaline as indicators of pegmatite internal evolution: Bob Ingersoll pegmatite, Black Hills, South Dakota. Geochimica et Cosmochimica Acta, 51(3), 519-534.

Kloppmann, W., Négrel, P., Casanova, J., Klinge, H., Schelkes, K., & Guerrot, C. (2001). Halite dissolution derived brines in the vicinity of a Permian salt dome (N German Basin). Evidence from boron, strontium, oxygen, and hydrogen isotopes. Geochimica et Cosmochimica Acta, 65(22), 4087-4101.

Knauth, L. P., & Beeunas, M. A. (1986). Isotope geochemistry of fluid inclusions in Permian halite with implications for the isotopic history of ocean water and the origin of saline formation waters. Geochimica et Cosmochimica Acta, 50(3), 419-433.

Kotzer, T. G., Kyser, T. K., King, R. W., & Kerrich, R. (1993). An empirical oxygen-and hydrogen-isotope geothermometer for quartz-tourmaline and tourmaline-water. Geochimica et Cosmochimica Acta, 57(14), 3421-3426.

Kotzer, T. G., & Kyser, T. K. (1995). Petrogenesis of the Proterozoic Athabasca Basin, northern Saskatchewan, Canada, and its relation to diagenesis, hydrothermal U mineralization and paleohydrogeology. Chemical Geology, 120(1), 45-89.

Kyser, K., Hiatt, E., Renac, C., Durocher, K., Holk, G., & Deckart, K. (2000). Diagenetic fluids in Paleo-and Meso-Proterozoic sedimentary basins and their implications for long protracted fluid histories. Fluids and Basin Evolution, 28, 225-262.

Leeman, W. P., & Tonarini, S. (2001). Boron isotopic analysis of proposed borosilicate mineral reference samples. Geostandards Newsletter, 25(2-3), 399-403.

Lewry, J. F., & Sibbald, T. I. (1977). Variation in lithology and tectonometamorphic relationships in the Precambrian basement of northern Saskatchewan. Canadian Journal of Earth Sciences, 14(6), 1453-1467.

McDonough, W. F., & Sun, S. S. (1995). The composition of the Earth. Chemical geology, 120(3), 223-253.

McGill, B. D., Marlatt, J. L., Matthews, R. B., Sopuck, V. J., Homeniuk, L. A., & Hubregtse, J. J. (1993). The P2 North U deposit, Saskatchewan, Canada. Exploration and Mining Geology, 2(4), 321-331.

Mercadier, J., Richard, A., & Cathelineau, M. (2012). Boron-and magnesium-rich marine brines at the origin of giant unconformity-related U deposits: δ11B evidence from Mg-tourmalines. Geology, 40(3), 231-234.

Meyer, C., Wunder, B., Meixner, A., Romer, R. L., & Heinrich, W. (2008). Boron-isotope fractionation between tourmaline and fluid: an experimental re-investigation. Contributions to Mineralogy and Petrology, 156(2), 259-267.

Morgan, G. B., & London, D. (1989). Experimental reactions of amphibolite with boron-bearing aqueous fluids at 200 MPa: implications for tourmaline stability and partial melting in mafic rocks. Contributions to Mineralogy and Petrology, 102(3), 281-297.

Ng, R., Alexandre, P., & Kyser, K. (2013). Mineralogical and geochemical evolution of the unconformity-related McArthur River Zone 4 orebody in the Athabasca Basin, Canada: implications of a silicified zone. Economic Geology, 108(7), 1657-1689.

Pagel, M., Poty, B., & Sheppard, S. M. F. (1980). Contribution to some Saskatchewan U deposits mainly from fluid inclusion and isotopic data. In: Ferguson S, Goleby A (eds.) U in the Pine Creek Geosyncline. IAEA, Vienna, 639 – 654.

Palmer, M. R., Spivack, A. J., & Edmond, J. M. (1987). Temperature and pH controls over isotopic fractionation during adsorption of boron on marine clay. Geochimica et Cosmochimica Acta, 51(9), 2319-2323.

Ramaekers, P. (1990). Geology of the Athabasca Group (Helikian) in Northern Saskatchewan. Saskatchewan Energy and Mines, Saskatchewan Geological Survey, Report 195, 48 p.

Ramaekers, P., Jefferson, C. W., Yeo, G. M., Collier, B., Long, D. G. F., Drever, G., McHardy, S., Jiricka, D., Cutts, C., Wheatley, K., Catuneanu, O., Bernier, S., Kupsch, B., Post, R. (2007) Revised geological map and stratigraphy of the Athabasca Group, Saskatchewan and Alberta. In: Jefferson, C W, Delaney, G (eds.) EXTECH IV: Geology and U EXploration TECHnology of the Proterozoic Athabasca Basin, Saskatchewan and Alberta, Geological Survey of Canada, Bulletin no. 588, 155-191.

Rosenberg, P. E., & Foit, F. F. (2006). Magnesiofoitite from the U deposits of the Athabasca Basin, Saskatchewan, Canada. The Canadian Mineralogist, 44(4), 959-965.

Slack, J. F., & Trumbull, R. B. (2011). Tourmaline as a recorder of ore-forming processes. Elements, 7(5), 321-326.

Suzuoki, T., & Epstein, S. (1976). Hydrogen isotope fractionation between OH-bearing minerals and water. Geochimica et Cosmochimica Acta, 40(10), 1229-1240.

Swihart, G. H., Moore, P. B., & Callis, E. L. (1986). Boron isotopic composition of marine and nonmarine evaporite borates. Geochimica et Cosmochimica Acta, 50(6), 1297-1301.

Taylor, H. P. (1974). The application of oxygen and hydrogen isotope studies to problems of hydrothermal alteration and ore deposition. Economic geology, 69(6), 843-883.

Taylor, B. E., Palmer, M. R., & Slack, J. F. (1999). Mineralizing fluids in the Kidd Creek massive sulfide deposit, Ontario: evidence from oxygen, hydrogen, and boron isotopes in tourmaline. Economic Geology Monograph, 10, 389-414.

Trumbull, R. B., Krienitz, M. S., Gottesmann, B., & Wiedenbeck, M. (2008). Chemical and boron-isotope variations in tourmalines from an S-type granite and its source rocks: the Erongo granite and tourmalinites in the Damara Belt, Namibia. Contributions to Mineralogy and Petrology, 155(1), 1-18.

Vengosh, A., Chivas, A. R., & McCulloch, M. T. (1989). Direct determination of boron and chlorine isotopic compositions in geological materials by negative thermal-ionization mass spectrometry. Chemical Geology: Isotope Geoscience section, 79(4), 333-343.

Vengosh, A., Chivas, A. R., McCulloch, M. T., Starinsky, A., & Kolodny, Y. (1991). Boron isotope geochemistry of Australian salt lakes. Geochimica et Cosmochimica Acta, 55(9), 2591-2606.

Vengosh, A., Starinsky, A., Kolodny, Y., Chivas, A. R., & Raab, M. (1992). Boron isotope variations during fractional evaporation of sea water: New constraints on the marine vs. nonmarine debate. Geology, 20(9), 799-802.

Williams, L. B., Hervig, R. L., Holloway, J. R., Hutcheon, I., (2001). Boron isotope geochemistry during diagenesis. Part I. Experimental determination of fractionation during illitization of smectite. Geochimica et Cosmochimica Acta 65, 1769-1782.

CHAPTER 6.

Geochemistry and U-Pb Geochronology of Ti oxides in association with the P2 fault and McArthur River U Deposit, Athabasca Basin, SK.

Abstract

Two TiO_2 polymorphs occur near the unconformity between the Athabasca Group sandstones and crystalline basement, and along the P2 fault, a 13 km long reverse structure and the host of the McArthur River uranium deposit: i) rutile occurs with zircon and quartz in basement metapelite and formed during metamorphism of the basement and ii) anatase occurs with hematite (± dolomite, kaolin, illite and aluminum phosphate sulfate minerals) in basement rocks and sandstone, and formed under oxidizing, late diagenetic to early hydrothermal activity. The composition of rutile is heterogeneous with variable concentrations of Nb (up to 3.86 wt% Nb_2O_5), V (up to 2.12 wt% V_2O_3) and W (up to 2.54 wt% WO_3), suggesting low water/rock ratios during crystallization. The Zr contents of rutile suggest equilibration temperatures of rutile-quartz-zircon between 740 – 890 °C, reflecting granulite facies conditions during metamorphism. However, the U-Pb ages of rutile range from 1726 – 1771 Ma and post-dates the Trans Hudson Orogeny, which metamorphosed the basement rocks at ~1.8 Ga. Considering that the blocking temperature of rutile is approximately 600 °C, the rutile ages represent either i) cooling of the lower crust during post-orogenic uplift, or ii) a thermal event (possibly related to the nearby ~1.75 Ga anorogenic Neultin Suite) after the regional metamorphism. The presence of anatase in basement samples well below the unconformity, with younger ages of 1569 ± 31 Ma, indicate the onset of oxidizing hydrothermal activity below the Athabasca Basin.

6.0 Introduction

Rutile is a common mineral in metamorphic and sedimentary rocks, and has also been reported in a variety of hydrothermal ore deposits (e.g., porphyry, VMS; Schandl et al. 1990, Rabbia et al 2009). It can accommodate a wide variety of minor elements such as V, Cr, Fe, Zr, Nb, Hf, Ta and W, and its chemistry reflects that of host rocks and/or fluids from which it formed

(e.g., Meinhold 2010). Therefore, it is a useful mineral in the study of ore deposits as its minor elements reflect ore forming processes (e.g. Rabbia et al. 2009, Clark and Williams-Jones 2004) and the provenance of siliciclastic sediments (e.g. Zack et al. 2002). Additionally, it can be utilized for U-Pb geochronology and Zr-in-rutile geothermometry (Zack et al. 2004).

In the Athabasca Basin, rutile has been reported in crystalline basement rocks and Athabasca sandstones in proximity to unconformity-type uranium deposits (e.g., Kotzer and Kyser 1995, Fayek and Kyser 1997, Alexandre et al. 2005, 2009; Cloutier et al. 2010). However, the timing of rutile crystallization is unclear and it has been suggested to be a pre-, syn and post ore phase in different studies (e.g., Kotzer and Kyser 1995, Fayek and Kyser 1997, Alexandre et al. 2005, 2009; Cloutier et al. 2010). In addition, there has been no detailed study on rutile. This chapter reports Ti oxide phases, major and trace element abundances, crystallization temperatures, and U-Pb ages of TiO_2 in metamorphic, magmatic and sedimentary rocks along the P2 fault, the main ore-hosting structure of the McArthur River uranium deposit in the eastern Athabasca Basin, in order to evaluate their origin.

6.1 Geology and sampling

The P2 fault is a ~13 km long reverse structure (~050°/45-60°) along graphitic metapelite of the Wollaston domain, a supracrustal package of Archean to Paleoproterozoic, upper amphibolite to granulite facies, metasedimentary (predominately metapelite, semi-pelite and arkose) rocks and magmatic rocks which comprise the basement of the eastern Athabasca Basin (Fig. 6.1). The P2 fault was originally a ductile structure during the metamorphism of the basement (1.8 – 1.9 Ga; Lewry and Sibbald 1980) and underwent brittle reactivations after deposition of the unconformably overlying, Paleoproterozoic, conglomeratic sandstones of the Athabasca Basin (e.g., McGill et al. 1993). Vertical movement along the P2 fault of up to 80 m is responsible for

displacement of the basement over the sandstones (McGill et al. 1993). In the area, the Athabasca Basin comprises ~500 m of fluvial to marine quartz dominated strata, consisting of four major sequences: the lower Read Formation, and the Manitou Falls Formations B, C and D. The P2 fault extends into the lower sandstone units as splays and fractures. The sandstones are quartz dominated and contain a diagenetic assemblage of hematite, kaolinite, illite and Sr-SO_4^{2-}rich aluminum phosphate sulfate (APS) minerals (e.g., Gaboreau 2007).

Extensive alteration occurs along the P2 fault in the basement and extends up to 50 m into the hanging wall and footwall rocks (e.g., McGill et al. 1993, Adlakha and Hattori 2015, 2016). The earliest alteration comprises an assemblage of oxy-dravite, graphite, pyrite and quartz and is associated with a hydrothermal event that postdates metamorphism but predates the Athabasca Basin sediments and uraniferous activity (Adlakha and Hattori 2016). The most common alteration assemblage along the fault comprises illite, sudoite, magnesio-foitite and LREE-rich APS minerals, and is associated with hydrothermal activity that produced the McArthur River deposit (Adlakha and Hattori 2015, 2016). The assemblage also forms alteration halos that envelope the ore bodies of the McArthur River deposit.

The McArthur River deposit comprises six ore bodies (Zones 1-4, and A-B) which collectively strike ~1.7 km and are structurally controlled by the P2 fault and unconformity. All ore bodies are hosted within the Read Formation of the Athabasca Basin, with the exception of Zone 2 which is almost completely hosted within the basement rocks. The McArthur River deposit is the largest high-grade uranium deposit yet discovered, with an average grade of ~10.94 % U_3O_8. Low grade, or sub-economic, (<1% U_3O_8) mineralization is found sporadically along the fault.

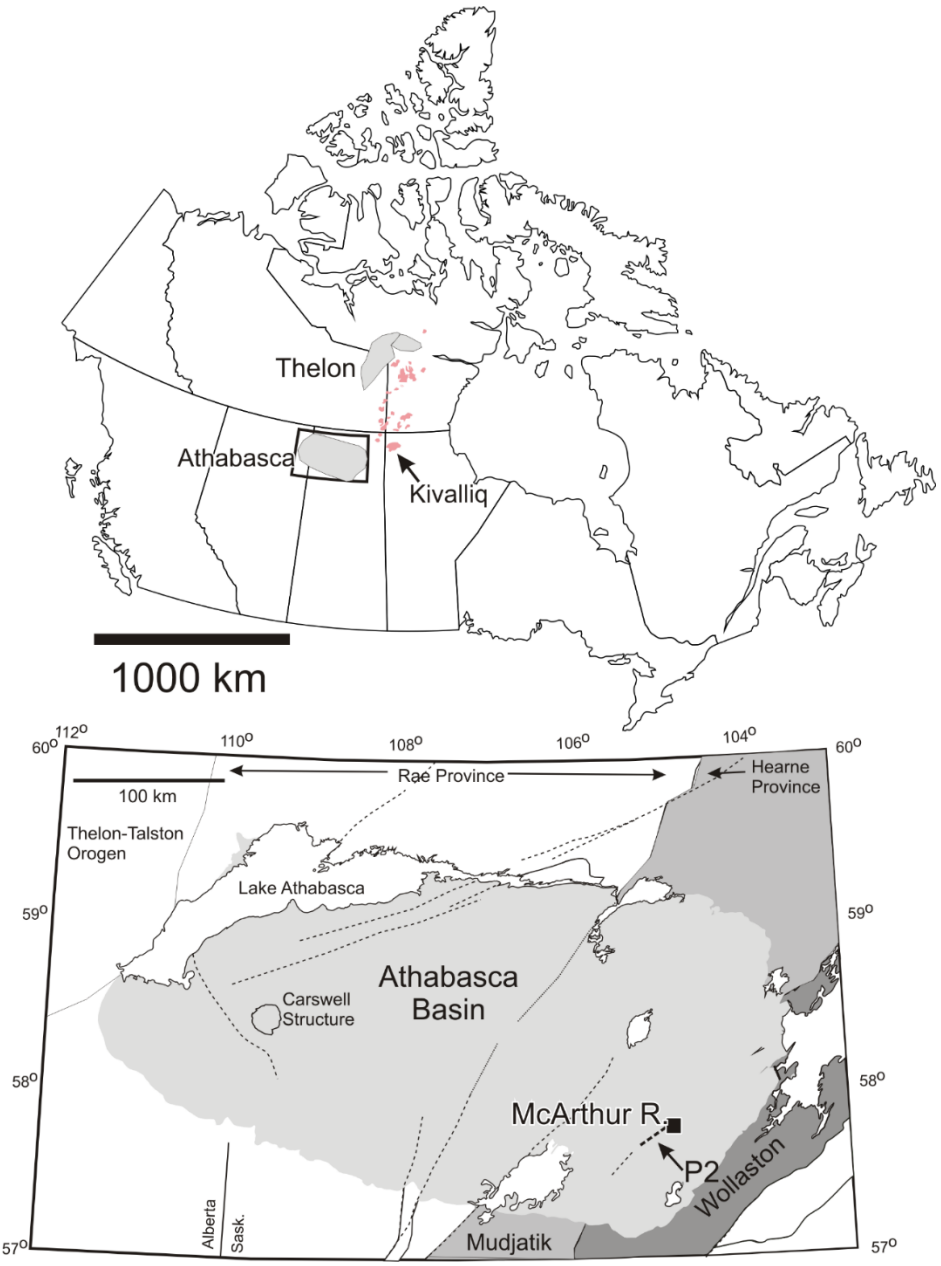

Figure 6.1. Top: A map of Canada with location of the Athabasca and Thelon Basins and the 1.75 Ga anorogenic Kivalliq Suite (pink; Kivalliq locations from Peterson et al. 2015). Bottom: A simplified map of the Athabasca Basin (after Jefferson et al. 2007 and modified from Adlakha and Hattori 2015, 2016) showing the location of the P2 fault, McArthur River deposit, and Wollaston Domain. Dashed lines represent major shear zones of the basement.

A total of 16 samples containing TiO_2 phases were selected for this study (Table 6.1). The samples range from basement metapelite and pegmatite to the lowermost sandstone unit of the Athabasca Basin. The samples also range in location along the P2 fault, from areas of mineralization (proximal to the Zone 1, 2 and 4 ore bodies), to areas of sub-economic mineralization, to apparently barren or unmineralized areas.

Table 6.1. Sample list and descriptions

DDH[a]	Sample	Depth (m)[b]	Lithology[c]	Area[d]	TiO_2 mineral species[e]
MC349	MAC98	578	PEL BX/GOUGE	SUB-EC	Rt, Ant
	MAC99	573	PEL BX	SUB-EC	Rt
H3559	MAC201	-	GR PEL	Z1	Rt
H3576	MAC203	-	GR PEL	Z1	Rt
H203	MAC152	-	PEL BX	Z2	Rt
	MAC444	-	PEL PEG	Z2	Rt
H201	MAC70	-	GR BX	Z2	Rt
	MAC441	-	PEL	Z2	Rt
H493	MAC84	-	PEL GR BX	Z2	Rt
	MAC86	-	PEL GR BX	Z2	Rt
H677	MAC420	-	PEL	Z4	Rt, Ant
MC410	MAC406	527.7	SS	SUB-EC	Rt, Ant
MC362	MAC127	602.3	PEL/PEG BX	P2 BARREN	Rt
MC359	MAC426	581.6	PEL	P2 BARREN	Rt
	MAC430	494	SS	P2 BARREN	Rt, Ant
MC381	MAC436	603	PEG	P2 BARREN	Rt, Ant

(-) = collared underground

a: diamond drill-hole; b: depth from surface; c: pel = metapelite, peg = pegmatite, ss = sandstone, gr = graphitic, bx = breccia; d: Area of the P2 fault, sub-ec = sub-economic area, Z1-4 = Zone # ore body of the McArthur River deposit; e: Rt = Rutile, Ant = anatase

6.2 Methodology

Mineral identification, detailed textural analysis and imaging were carried out using a petrographic microscope in both transmitted and reflected light on polished thick (~100 μm)

sections, followed by a TESCAN MIRA 3 LMU Variable Pressure Schottky Field Emission Scanning Electron Microscope (SEM) at Saint Mary's University, Halifax, Nova Scotia.

Polymorphs of TiO_2 were identified using a Jobin-Yvon Horiba LabRam HR confocal laser Raman microspectrometer at Saint Mary's University, Halifax, Nova Scotia. Identification used characteristic Raman shifts at 242, 449 and 614 cm^{-1} for rutile, and 199, 400, 517 and 642 cm^{-1} for anatase. No brookite was observed. Analyses were performed using a 532 nm (green) Nd-YAG laser (105 mW laser power at objective) focused through a 100x objective. Spectra were collected using a 600 grooves/mm grating, a 50 μm confocal hole size, and a Synapse 1024 x 256 pixel CCD detector. Spectra collection was performed using an acquisition duration of 10s with 3 accumulations. Frequency calibration was performed using a pure silicon wafer.

Major and minor elements were quantified by wavelength dispersive X-ray spectrometry using a JEOL 8230 SuperProbe at the University of Ottawa, Ottawa, Ontario. The working conditions of the electron probe micro-analyser (EPMA) were set to an accelerating voltage of 20 kV with a 40 nA beam current focussed to a 5 μm spot size. Data collection time was 40 s with 20 s background time for all elements. Analytical standards include chromite (Cr_2O_3, Al_2O_3; Kα), Mn columbite (Nb_2O_5; Lα), ThO_2 (ThO_2; Mα), zircon (ZrO_2; Lα), $NiTa_2O_6$ (Ta_2O_5; Mα), rutile (TiO_2; Kα), cassiterite (SnO_2; Lα), $CoWO_4$ (WO_3; Mα), UO_2 (UO_2; Mα), Powellite (MoO_3; Lα), Vanadinite (V_2O_3; Kα), Hematite (FeO; Kα), Tephroite (MnO; Kα), Chromite (MgO; Kα), and Diopside (SiO_2; Kα). Data reduction was completed using ZAF program.

Trace element abundances and U-Pb ages were determined using a Resonetics S-155-LR 193nm Excimer laser ablation system coupled to an Agilent 7700x quadrupole ICP-MS at the

University of New Brunswick, Fredericton, New Brunswick. Detailed running conditions of the LA-ICPMS for each experiment are listed in Appendix Tables 6.1 and 6.2. All grains were examined for inclusions before analysis, and time-sequence intensity graphs of the data were inspected for possible inclusions. The data were imported into Iolite (Version 2.5) and the data reduction was carried out using the add-on IGOR Pro (Version 6.3.7, Wavemetrics Inc.). The calibration standard NIST610 (National Institute of Standards and Technology, synthetic glass) and ratio of each isotope to counts of Ti were used to quantify trace element abundances. Analysis of BCR-2G (Columbia River Basalt, USGS) indicates accuracy of >90% and precision of >95% for the trace elements. Analysis of the same grains using LAICPMS and EPMA yielded similar results for elements Nb, W, and Cr (Appendix Fig. A6.1). Data of V produced by LAICPMS yields higher values (by ~1000 ppm) than EPMA. Data of Zr acquired by LAICPMS has a broad positive correlation with EPMA data. There is no correlation between Si and Zr; therefore, the Zr values did not originate from zircon inclusions. The rutile reference R10 (Luvizotto et al. 2009) was used to calibrate U-Pb geochronology data and reference R13 was used for quality control and indicate an accuracy and precision of >95%.

6.3 Results

6.3.1 TiO_2 polymorph occurrences

Raman spectroscopy work identifies two TiO_2 polymorphs (Fig. 6.2, Table 6.1): i) rutile occurs in basement rocks and ii) anatase occurs in both sandstone and basement samples. Anatase is a low temperature/pressure TiO_2 phase whereas rutile is stable at high temperature and pressure conditions such as upper-amphibolite to granulite metamorphic conditions (e.g., Dachille et al. 1968).

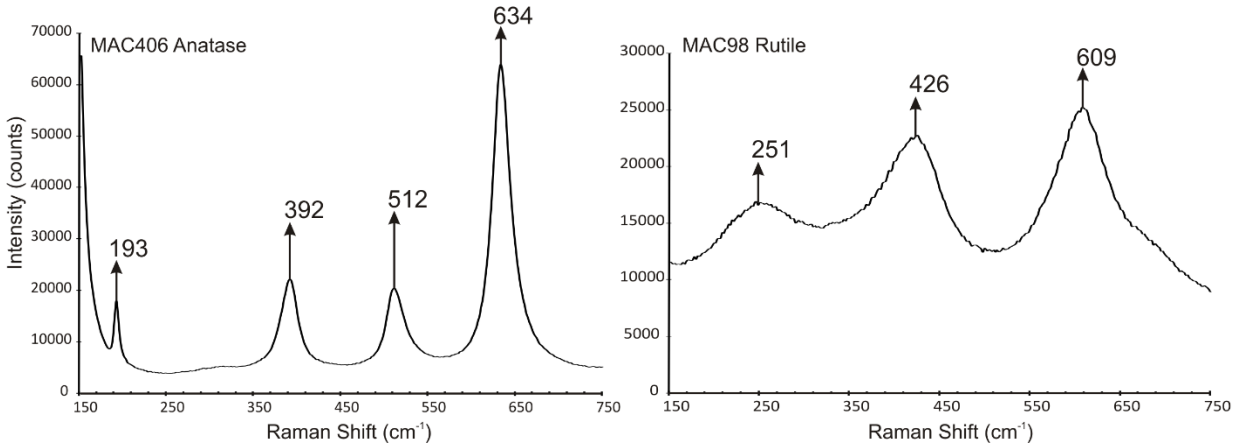

Figure 6.2. Raman spectra for A) Anatase and B) Rutile.

Rutile occurs as a relict accessory mineral in hydrothermally altered metasedimentary gneisses and pegmatite along the P2 fault (Table 6.1). In section, rutile is dark brown to opaque under transmitted light, and moderately reflective and grey with a bluish tint in reflected light. Rutile typically occurs in trace amounts as fractured, anhedral grains ranging from 20 – 500 μm in diameter (Fig. 6.2). However, one sample (MAC436) contains relatively abundant, disseminated, euhedral-subhedral rutile grains (Fig. 6.3A). It is also noted that needles of rutile within chlorite laths occur in the basement. This rutile likely formed during the retrograde alteration of biotite to chlorite and this type was not incorporated in this study.

Rutile commonly occurs with an assemblage of oxy-dravite, quartz, graphite, pyrite and zircon, as shown in samples MAC99, MAC201, and MAC436. In this assemblage, rutile forms inclusions within oxy-dravite, or partially surrounded by oxy-dravite (Fig. 6.3C). Zircon, quartz and graphite also form inclusions within oxy-dravite. Rutile frequently contains inclusions of zircon from 10 – 50 μm in diameter, and apatite and zircon commonly occur in proximity to rutile grains (Fig. 6.3B).

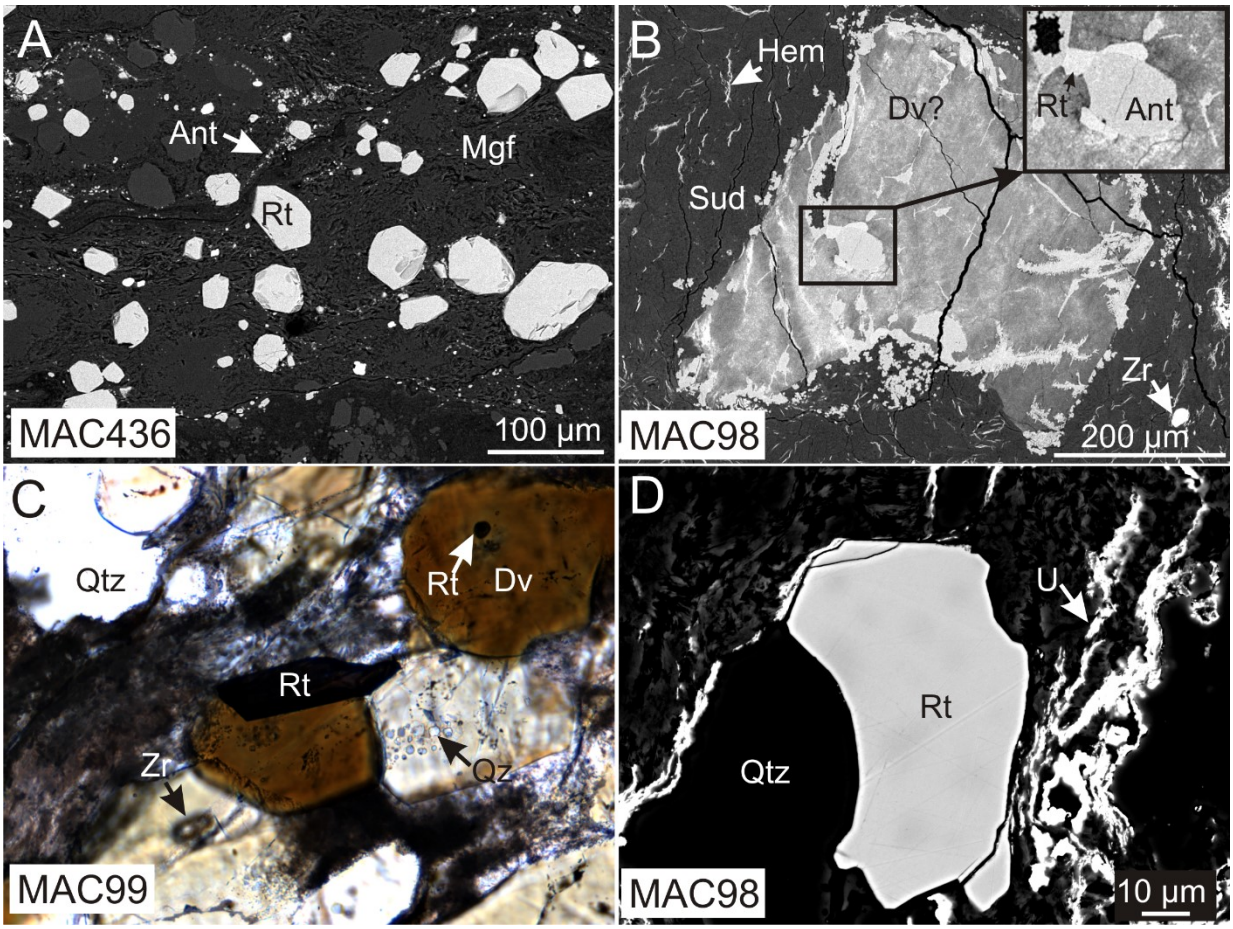

Figure 6.3. Rutile (Rt) in basement samples. A) A backscattered electron (BSE) image of disseminated, subhedral to euhedral rutile grains surrounded by magnesio-foitite and fine-grained anatase (Ant), B) a BSE image of rutile and anatase infilling fractures of and oxy-dravite pseudomorph, surrounded by sudoite (Sud) and stringers of hematite (Hem), C) a photomicrograph in plane polarized light of rutile, quartz (Qtz) and zircon (Zr) inclusions in oxy-dravite (Dv), and D) a SEM-BSE image of fractured rutile surrounded by a mixture of fine-grained uranium oxide (U), sudoite, and magnesio-foitite.

The most common mineral assemblage in the studied rocks consist of sudoite, illite, and magnesio-foitite. This assemblage typically surrounds and infills fractured grains of rutile (Fig. 6.3A). Additionally, rutile in sample MAC98 occurs as fractured grains surrounded by late U-oxide (Fig. 6.3D). Notably, a small amount of rutile in MAC98 occurs with anatase along fractures of oxy-dravite, which is replaced by sudoite (Fig. 6.3B). Oxy-dravite contains up to 1.50 wt.%

TiO_2 (Adlakha and Hattori 2016); therefore, this rutile (and anatase) may have been produced by the alteration of oxy-dravite to sudoite, as sudoite contains very low TiO_2 (<0.19 wt%; e.g., Adlakha et al. 2014).

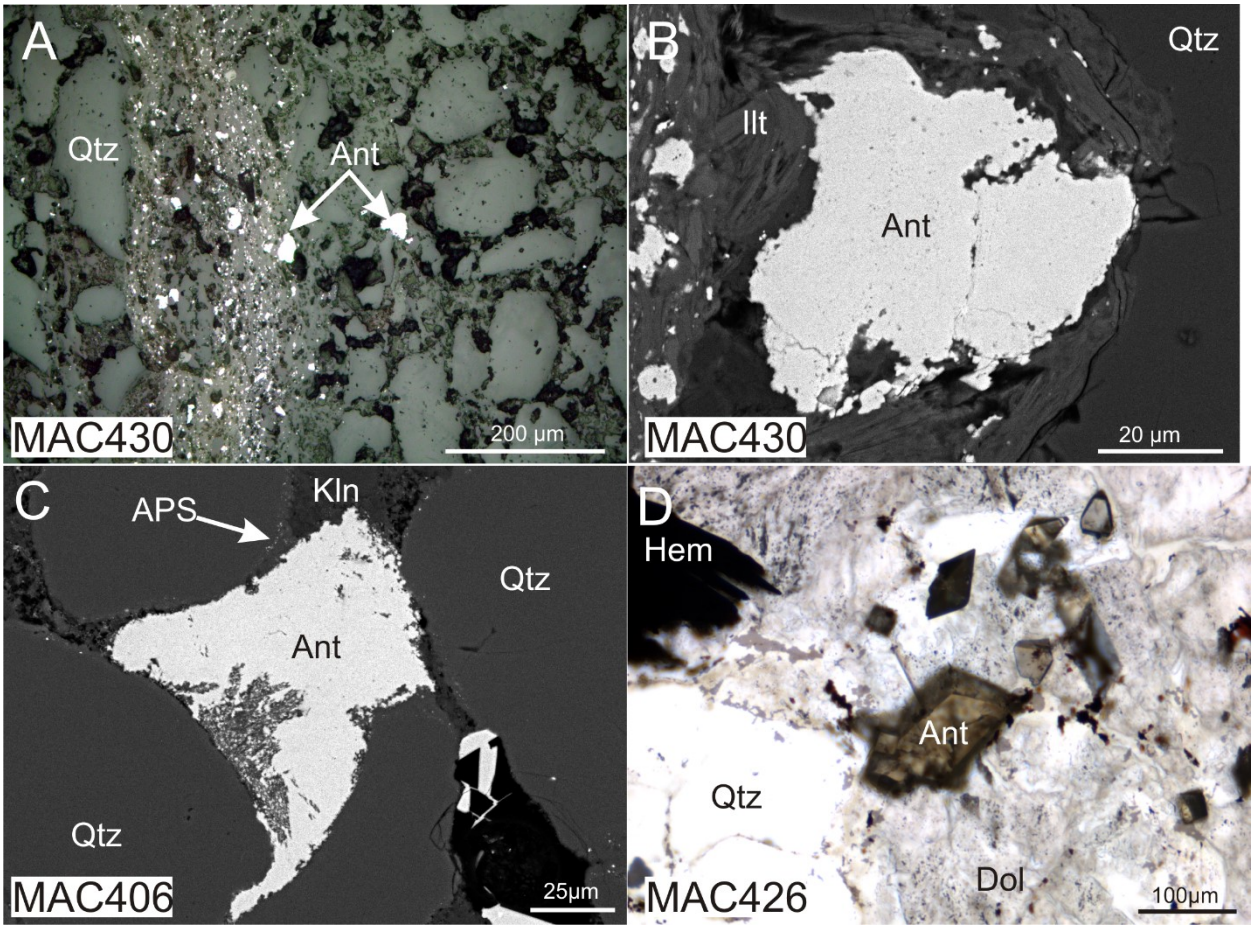

Figure 6.4. A) A reflected light image of a silty seam containing anatase (Ant) in quartz (Qtz) sandstone, B) A SEM-BSE image of anatase with authigenic illite (Ilt) within quartz sandstone, C) A SEM-BSE image of anatase with kaolin (Kln) infilling pore space between detrital quartz grains (rimmed by quartz overgrowths containing APS minerals) in sandstone, D) A photomicrograph in plane-polarized light of anatase with dolomite and crystalline hematite (Hem) within basement metapelite.

Anatase occurs locally in sandstone and the basement along the P2 fault (Table 6.1, Figs. 6.3, 6.4). It is brown-blue and translucent in transmitted light and moderately reflective and grey in reflected light (Fig. 6.4D). In sandstone samples (MAC406 and MAC430), anatase is concentrated in silty beds comprising detrital quartz and zircon, and authigenic kaolinite, illite, APS minerals and hematite (Fig. 6.4A). Anatase grains, which are anhedral and patchy, overprint kaolinite and crosscut corroded diagenetic overgrowths of detrital quartz grains that contain Sr and SO_4^{2-} -rich APS minerals (Figs. 6.4B, C).

The occurrence of anatase in basement samples (MAC98, MAC426, MAC436) is varied. In sample MAC436, anatase forms small (< 15 μm), anhedral grains disseminated with larger euhedral rutile in fine-grained magnesio-foitite (Fig. 6.3A). In sample MAC98, anatase forms anhedral grains (< 15 μm) with stringers of hematite and U-oxide in sudoite and magnesio-foitite, and with rutile and the altered oxy-dravite (Fig. 6.3B). In MAC426, anatase forms euhedral to anhedral grains (up to 100 μm) and occurs in a vein of dolomite and crystalline hematite (Fig. 6.4D).

6.3.2 Minor element abundance

Rutile compositions determined by EPMA show variably high Nb_2O_5 (≤ 3.86 wt%), Ta_2O_5 (≤ 0.42 wt%), Cr_2O_3 (≤ 0.48 wt%), ZrO_2 (≤ 0.49 wt%), WO_3 (≤ 2.54 wt%), and V_2O_3 (≤ 2.12 wt%) (Table 6.2). In individual samples, rutile grains have similar composition as evidenced by low standard deviations of averaged values (Table 6.2), with the exception of WO_3 and V_2O_5, which can vary significantly between grains in one sample (e.g., MAC84, MAC98). Notably, rutile of sample MAC98 contains exceptionally high Nb (average 3.29 wt%).

Compared to rutile, anatase contains very low concentrations of minor elements: up to 0.79 wt% Nb_2O_5, 0.03 wt% Ta_2O_5, 0.16 wt% Cr_2O_3, 0.13 wt% WO_3, and 0.46 wt% V_2O_3 (Table 6.3). Most anatase grains contain low ZrO_2 (<0.10 wt% in most grains, <0.49 wt% in MAC426). The FeO content is variable (up to 1.77 wt%).

6.3.3 Trace element composition and geothermometry by LA-ICPMS

Representative trace element concentrations of rutile and anatase are listed in Tables 6.4 and 5, respectively (for full data sets see Appendix Tables A6.3 and A6.4). Trace element analysis indicates that rutile contains variable Ca (< 810 ppm), Sc (5.8 – 1050 ppm), Co (< 102 ppm), Se (< 170 ppm) Sn (< 440 ppm), Hf (1.96 – 127 ppm), Th (< 140 ppm), and U (9.06 – 668 ppm). Rutile contains low Mo (<33 ppm), Y (<21 ppm) and Pb (<7.4 ppm).

Anatase contains variable concentrations of Ca (<9760 ppm), Sn (<130 ppm), Hf (< 160 ppm), Ta (< 190 ppm), Th (< 68.7 ppm), Pb (< 32 ppm) and U (< 180 ppm). Anatase contains low concentrations of Ga (< 2.59 ppm), Y (< 9.5 ppm), and Mo (< 8.8 ppm).

Zircon and quartz are common in proximity to rutile grains of the basement (Fig. 6.3B,C). Quartz and rutile commonly share grain boundaries and zircon commonly occurs as inclusions in, or along grain boundaries of, rutile (Fig. 6.5). Assuming rutile, zircon and quartz were in equilibrium, the Zr content of rutile yields equilibrium temperatures between 740 – 890 °C (with an uncertainty of ± 50 °C; Table 6.4), using the equation $T\,(\text{in }℃) = 127.8 \times \ln(\text{Zr in ppm}) - 10$ proposed by Zack et al. (2004).

Table 6.2. Averaged electron microprobe results for rutile in wt%.

Sample	MAC152 (48/11)		MAC201 (33/8)		MAC70 (19/7)		MAC86 (27/9)		MAC420 (18/8)		MAC441 (22/8)		MAC84 (27/9)		MAC127 (27/12)		MAC203 (6/2)		MAC79 (12/3)		MAC98 (18/9)		MAC99 (20/10)		MAC444 (12/5)		MAC426 (2/1)		MAC436 (12/7)	
	x̄	±	x̄	±	x̄	±	x̄	±	x̄	±	x̄	±	x̄	±	x̄	±	x̄	±	x̄	±	x̄	±	x̄	±	x̄	±	x̄	±	x̄	±
Cr_2O_3	0.22	0.14	0.05	0.02	0.19	0.03	0.16	0.05	0.19	0.05	0.17	0.03	0.10	0.05	0.18	0.04	0.05	0.04	0.18	0.03	0.19	0.06	0.04	0.02	0.27	0.05	0.21	0.04	0.15	0.03
Nb_2O_5	0.45	0.07	0.47	0.13	0.47	0.14	0.42	0.13	0.43	0.19	0.59	0.14	0.37	0.03	0.32	0.17	0.99	0.16	1.31	0.16	3.29	0.50	1.10	0.12	0.35	0.10	0.28	0.01	0.35	0.07
ZrO_2	0.10	0.03	0.11	0.03	0.08	0.02	0.09	0.02	0.09	0.04	0.11	0.03	0.09	0.02	0.10	0.02	0.16	0.03	0.11	0.04	0.08	0.04	0.09	0.02	0.09	0.02	0.19	0.00	0.10	0.02
Al_2O_3	0.05	0.03	0.05	0.01	0.06	0.03	0.03	0.04	0.02	0.01	0.08	0.20	0.01	0.01	0.02	0.02	0.10	0.02	0.07	0.06	0.12	0.06	0.08	0.02	0.01	0.01	0.07	0.01	0.04	0.01
Ta_2O_5	<0.01		<0.01		<0.01		<0.01		<0.01		<0.01		<0.01		<0.01		0.07	0.02	0.07	0.09	0.13	0.13	<0.01		<0.01		<0.01		<0.01	
TiO_2	98.94	0.32	99.27	0.36	99.19	0.41	98.95	0.29	99.30	0.44	98.99	0.94	98.03	0.53	99.07	0.41	98.41	0.34	97.90	0.36	94.33	1.12	98.48	0.28	98.71	0.26	95.41	0.33	98.76	0.40
SnO_2	0.02	0.01	0.01	0.01	0.02	0.01	0.03	0.01	0.02	0.01	0.02	0.01	0.05	0.01	0.02	0.01	0.03	0.01	0.03	0.01	0.04	0.01	0.01	0.01	0.02	0.01	0.02	0.01	0.03	0.01
WO_3	0.10	0.03	0.27	0.06	0.07	0.04	0.08	0.03	0.09	0.06	0.05	0.03	0.49	0.06	0.03	0.03	0.21	0.05	0.10	0.03	0.34	0.23	0.06	0.04	0.07	0.04	2.18	0.36	0.22	0.04
V_2O_3	0.33	0.17	0.40	0.04	0.43	0.05	0.86	0.20	0.45	0.14	0.26	0.04	1.45	0.34	0.86	0.15	0.14	0.07	0.15	0.08	1.35	0.24	0.20	0.04	0.93	0.22	0.00	0.00	0.72	0.08
FeO	0.14	0.06	0.20	0.03	0.09	0.03	0.06	0.03	0.11	0.05	0.19	0.05	0.06	0.02	0.08	0.02	0.38	0.08	0.48	0.09	0.68	0.28	0.48	0.09	0.05	0.02	1.38	0.10	0.05	0.01
SiO_2	0.01	0.03	0.00	0.01	0.05	0.05	0.06	0.07	0.02	0.02	0.06	0.21	0.00	0.01	0.01	0.01	0.00	0.00	0.03	0.02	0.04	0.07	0.02	0.02	0.01	0.01	0.11	0.11	0.01	0.01
Total	100.41	0.20	100.86	0.26	100.66	0.39	100.75	0.25	100.75	0.14	100.59	0.63	100.67	0.29	100.70	0.30	100.55	0.20	100.48	0.28	100.62	0.46	100.60	0.22	100.56	0.11	99.91	0.27	100.46	0.46

Note: ThO_2, UO_2, MnO_2, MoO_3 <0.01 wt%. Number in parentheses below sample numbers indicate: (number of data points/ number of grains) analysed.

Table 6.3. Averaged electron microprobe results for anatase in wt%.

Sample	MAC426 (11/5)		MAC436 (5/3)		MAC98 (18/9)		MAC430 (12/6)		MAC406 (20/9)	
	x̄	±	x̄	±	x̄	±	x̄	±	x̄	±
Cr_2O_3	0.06	0.08	0.11	0.11	0.04	0.04	<0.01		<0.01	
Nb_2O_5	0.25	0.03	0.13	0.10	0.09	0.05	0.39	0.18	0.33	0.03
ZrO_2	0.26	0.12	<0.01		<0.01		0.08	0.05	0.04	0.03
Al_2O_3	<0.01		0.16	0.17	0.23	0.26	0.06	0.05	0.17	0.22
TiO_2	99.59	0.34	99.80	0.61	98.49	1.90	98.89	0.78	98.61	1.00
WO_3	0.15	0.18	0.03	0.01	0.02	0.02	<0.01		<0.01	
UO_2	<0.01		<0.01		0.04	0.04	<0.01		0.02	0.01
V_2O_3	<0.01		<0.01		0.08	0.14	<0.01		<0.01	0.00
FeO	0.31	0.17	0.15	0.11	0.51	0.43	0.58	0.23	0.59	0.28
MgO	<0.01	0.00	0.02	0.02	0.05	0.06	<0.01	0.00	<0.01	0.00
SiO_2	<0.01	0.01	0.14	0.10	0.21	0.25	0.09	0.09	0.21	0.28
Total	100.68	0.14	100.47	0.41	99.79	1.14	100.15	0.26	100.01	0.43

Note: MnO, MoO_3, SnO_2, Ta_2O_5, ThO_2 <0.01 wt%

Number in parentheses below sample numbers indicate: (number of data points/ number of grains) analysed.

Table 6.4. Representative trace element compositions of rutile obtained by LA-ICPMS (in ppm)

	MAC84	MAC99	MAC79	MAC152	MAC127	MAC203	MAC444	MAC201	MAC98	MAC86	MAC70	MAC436	MAC420
Sc	110	85.5	93.9	105	117	813	54.2	103	148	88.1	103	91.2	113
V	15700	2480	2450	2130	7880	1560	5330	4030	11400	7260	4680	4400	5270
Cr	1350	335	1250	1330	1260	219	849	374	1770	1270	1470	1010	1530
Fe	9.3	3010	2670	1100	458	3180	292	1300	4610	229	1120	374	790
Co	<0.0314	<0.0314	0.04	<0.0314	<0.0314	<0.0314	<0.0314	<0.0314	<0.0314	<0.0314	1.87	<0.0314	6.4
Ni	<0.893	<0.893	<0.893	<0.893	<0.893	<0.893	<0.893	<0.893	<0.893	<0.893	2.86	<0.893	1.49
Cu	1.08	1.22	1.9	1.59	0.84	1.08	0.86	1.16	1.5	1.64	6.19	1.17	0.99
Zn	4.3	5.3	5.3	6.5	4.2	<4.16	<4.16	7.3	<4.16	<4.16	9.1	<4.16	<4.16
Ga	<0.0783	0.8	1.18	0.46	1.25	2.76	<0.0783	0.39	1.34	0.37	3.67	0.203	0.091
Se	<3.11	<3.11	44	<3.11	<3.11	6	<3.11	110	<3.11	<3.11	<3.11	73	<3.11
Y	0.02	0.065	0.3	0.045	0.06	0.059	0.079	0.069	0.06	0.38	5.12	0.089	0.02
Zr	653	677	597	818	685	983	583	895	567	670	474	742	879
Nb	2410	7330	8570	2590	3010	7800	2750	3460	23200	3030	3810	3410	4150
Mo	16.4	4.35	32.9	7.78	24.4	14.2	1.04	8.31	2.57	13.4	17.5	0.46	16
Sn	419	54.2	218	217	169	255	146	93	310	213	176	211	195
Hf	38.9	35.1	31.9	49	36	50.1	31.5	48.6	33	37	29.9	38.3	52
Ta	212	610	749	292	297	1020	372	238	2640	228	240	628	390
W	4240	531	1250	987	215	2580	267	2740	3790	850	844	1300	1370
Pb	<0.198	<0.198	<0.198	<0.198	<0.198	<0.198	<0.198	<0.198	<0.198	1.29	7.36	<0.198	<0.198
Th	<0.1	<0.1	<0.1	<0.1	<0.1	<0.1	<0.1	<0.1	<0.1	5.9	43.7	<0.1	<0.1
U	97.4	11.8	45.6	67.6	74.3	21.8	13.8	42.5	27.4	69.6	47	36.8	41.1
Nb/Cı	1.8	21.9	6.9	1.9	2.4	35.6	3.2	9.3	13.1	2.4	2.6	3.4	2.7
T°C*	818	823	807	847	824	871	804	859	800	822	777	835	856

*calculated using geothermometer by Zack et al. (2004), uncertainty of ± 50 °C

Table 6.5. Representative trace element compositions of anatase (in ppm)

	MAC98	MAC406	MAC426	MAC426	MAC430	MAC436
Ca	<151	197	227	<151	<151	<151
Sc	42.6	67.4	9.87	24.8	57.8	2.29
V	117	79.6	50.8	33.3	29.5	12.9
Cr	259	209	889	148	12.2	2
Fe	1560	6650	1600	1070	2850	505
Co	<0.0314	0.033	<0.0314	<0.0314	<0.0314	0.035
Ni	<0.893	<0.893	<0.893	<0.893	<0.893	1.97
Cu	1.89	1.85	1	1.09	1.44	1.58
Zn	4.7	6.4	<4.16	<4.16	<4.16	<4.16
Ga	0.22	0.75	<0.0783	<0.0783	0.19	1.72
Ge	<3.42	<3.42	<3.42	<3.42	<3.42	<3.42
Se	<3.11	<3.11	25	<3.11	<3.11	<3.11
Y	0.112	7.64	0.58	0.04	1.05	0.111
Zr	170	537	1860	1890	662	11.4
Nb	836	1970	1780	1920	1940	1160
Mo	3.1	7.6	0	0	1.27	0
Sn	0.39	2.89	107	56.9	0.81	0.55
Hf	2.81	17.3	117	135	17	0.76
Ta	58.7	80.5	160	145	102	35.2
W	93.8	25.5	369	237	80.9	51.9
Pb	0.82	30.4	6.17	0.088	7.77	0.21
Th	3.61	39.1	45.4	0.36	2.2	0.38
U	115	180	9.17	0.58	49.3	1.49

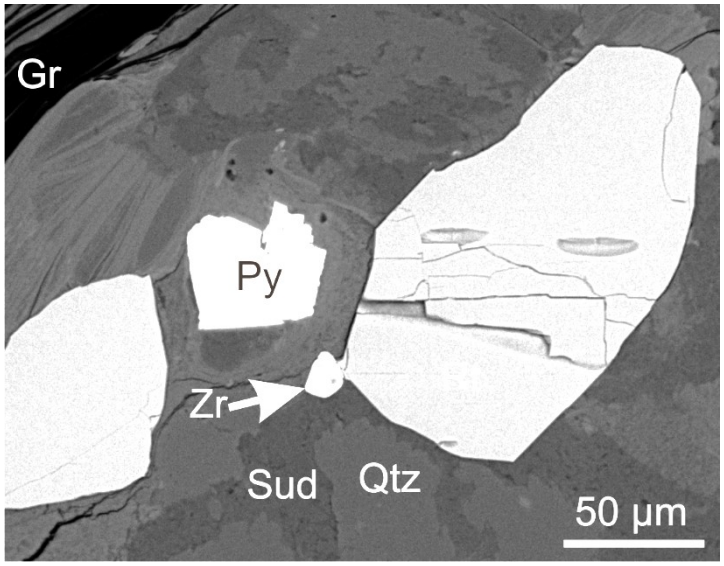

Figure 6.5. A rutile grain (Rt) sharing a grain boundary with zircon (Zr) in sample MAC127. Quartz likely shared grain boundaries with both rutile and zircon; however, sudoite (Sud) partially dissolved quartz during later hydrothermal activity. Py = pyrite, Gr = graphite

6.3.4 U-Pb Geochronology

The U-Pb data collected for rutile and anatase are listed in Appendix Table 6.3. All grains contained negligible ^{204}Pb; therefore, no common Pb correction was applied. Using the MS Excel add-on Isoplot 4.15, $^{206}Pb/^{238}U$ and $^{207}Pb/^{235}U$ for rutile and anatase were plotted on Concordia diagrams (e.g., Fig. 6.6; see Appendix Fig. 6.3 for all Concordia diagrams) and the Concordant ages were calculated (Table 6.6). Rutile yields Concordant ages that range from 1726 ± 12 Ma to 1771.3 Ma ± 9.8 (Table 6.6). The MSWD associated with each age is low (< 2.5) and is therefore likely due to analytical uncertainties.

Anatase from sample MAC426 yields a Concordant age of 1569 ± 31 Ma with a MSWD of 0.30 (Fig. 6.6). The large uncertainty of 31 Ma is attributed to relatively low concentrations of uranium (typically <6 ppm; Appendix Table A6.3).

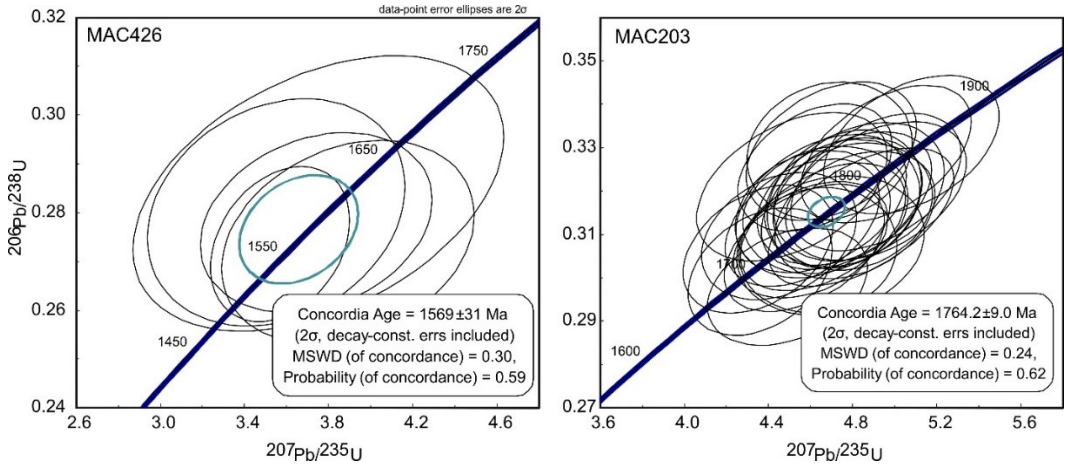

Figure 6.6. Concordia diagrams (constructed using Isoplot 4.15) for samples MAC426 (anatase) and MAC426 (rutile).

Table 6.6. U-Pb ages for anatase and rutile

Sample	n	Age	±	MSWD	Probability
MAC426*	5	1569	31	0.3	0.59
MAC420	11	1726	12	0.027	0.87
MAC99	22	1726	11	2.8	0.093
MAC84	28	1741	12	1.3	0.26
MAC201	43	1749	7.8	0.89	0.35
MAC79	12	1750	14	1.8	0.18
MAC127	25	1750	8.4	0.0075	0.93
MAC436	10	1751	14	0.014	0.91
MAC70	15	1759	13	0.075	0.78
MAC152	14	1762	12	0.22	0.64
MAC203	29	1764	9	0.24	0.62
MAC444	26	1771	9.8	2	0.15

*anatase; n = number of data points used for Concordia age
See Appendix Fig. 6.3 for Concordia diagrams

6.4 Discussion

6.4.1 The Origin of Rutile

Rutile occurs as an accessory mineral in metapelitic and pegmatitic rocks along the P2 fault. Textural evidence suggests that rutile pre-dates the hydrothermal assemblage of magnesio-foitite, sudoite and illite produced by uraniferous fluids. Rutile commonly occurs with an assemblage of oxy-dravite, pyrite, quartz, graphite and zircon (Figs. 6.3C, 6.5). The textural evidence also suggests that rutile either slightly predates or is synchronous with the hydrothermal assemblage of oxy-dravite. Adlakha and Hattori (2016) interpreted oxy-dravite to have formed during a post-metamorphic, hydrothermal event before deposition of the Athabasca Basin, based on the evidence that oxy-dravite has similar compositions (high Mg) among different samples, and restricted to the P2 fault, and postdates schörl in anatectic pegmatite lenses. However, it is unclear whether rutile formed coevally with oxy-dravite during this hydrothermal event, or whether it formed during metamorphism and was resistive during the later event that produced the tourmaline. To evaluate the origin of rutile, we examine i) the chemical composition of rutile, ii) Zr-in-rutile thermometry and iii) U-Pb ages of rutile.

Rutile along the P2 fault is heterogeneous in composition and contains very high concentrations of HFSE (high field strength elements, such as Nb, Ta, Hf, Zr, W, U and Th) and metals (e.g., Cr, V) (Table 6.4). Rutile in metapelite is discriminated based on high Nb/Cr ratios (e.g, Zack et al. 2004, Meinhold et al. 2008). During metamorphism of sedimentary rocks, rutile is formed at the expense of Ti-bearing minerals such as ilmenite and biotite (e.g., Luvizotto et al. 2009). Ilmenite and biotite may also contain high Nb, which rutile preferentially incorporates over other phases due to its high affinity for Nb (Zack et al. 2004). However, Cr is not selectively incorporated into most metamorphic minerals and is generally considered to be equally distributed

between metamorphic phases (Zack et al. 2004). Rutile from the P2 fault contains high Nb/Cr ratios (Table 6.4) supporting the interpretation that rutile is of metamorphic origin and primary with respect to the metapelites. The variably high concentrations of minor elements in rutile may be explained by low water/rock ratios during its formation (i.e. the local host rock is governing mineral chemistry). The metapelites formed under granulite conditions during the Trans-Hudson orogeny (e.g., Annesley et al. 1997) and experimental work by Brenan et al. (1994) indicates high partitioning coefficients for HFSE between rutile and fluid. Therefore, the variable rutile compositions along the P2 fault may be explained by local compositional variations of the metapelite.

Zirconium-in-rutile temperatures were calculated as 740 – 890 °C (±50 °C) (Table 6.4). These temperatures coincide with granulite facies metamorphism and therefore support rutile formation during metamorphism of the Wollaston Domain. These temperatures are based on the assumption that rutile, zircon and quartz were in equilibrium during their formations. Ideally, equilibration would be confirmed by the observation of shared grain boundaries between all three minerals in the same sample. Unfortunately, the rocks along the P2 fault have been extensively altered by later hydrothermal events. Therefore, many original textures have been overprinted and obscured by later clay-sized minerals. This is illustrated in Figure 6.5, where rutile, zircon and quartz may have originally shared grain boundaries, but later sudoite replaced quartz and obscured the original texture. Zircon commonly forms inclusions and shares grain boundaries with rutile, and quartz is commonly in contact with rutile; therefore, we are confident that the three minerals originally formed an equilibrium assemblage and that the Zr-in-rutile temperatures reflect the temperature during rutile crystallization.

Rutile along the P2 fault yield Concordant U-Pb ages that range from 1726 ± 12 Ma to 1771.3 Ma ± 9.8 (Table 6.6). The Trans-Hudson Orogeny that metamorphosed the Wollaston Domain occurred at ~1.8 Ga (Lewry & Sibbald 1980). Therefore, the rutile ages obtained in this study post-date the Trans-Hudson Orogeny by up to 75 Ma.

Similar 1.75 Ga ages have been observed in the area: Alexandre et al. (2009) gave Ar/Ar ages of ~1.75 for muscovite from the McArthur River deposit, work by Krogh and Clark (1987) identified 1.75 Ga aged metamorphic zircon below the eastern Athabasca Basin, and Orrell et al. (1999) reported ages of 1.75 Ga for rutile in the Mudjatik Domain (Fig. 6.1). Considering the closure temperature of rutile at ~600 °C for 200 μm grains (Cherniak 2000), rutile ages and the ages reported in the aforementioned studies suggest that the basement rocks of the Athabasca Basin were experiencing high temperatures, between 1726 – 1771 Ma. These ages indicate that rutile either formed i) during metamorphism but the basement rocks were in the lower crust and remained hot well after metamorphism, or ii) during a later event at 1.75 Ga.

Previous studies suggest that 1.75 Ga ages of basement hosted minerals below the eastern Athabasca Basin represent rapid uplift and exhumation of the basement (e.g., Ornell et al. 1999, Kyser et al. 2000 and Alexandre et al. 2009). Kyser et al. (2000) suggests that this age also represents a maximum age for initial sedimentation of the Athabasca Basin as the exhumed basement rocks to the east of the basin were most likely the source rocks of the basin. The 1.75 Ga ages of rutile in this study may be explained by cooling due to post-orogenic uplift.

Alternatively, rutile may have been reset or formed during a thermal event at 1.75 Ga. North-east of the Athabasca Basin outcrops the ~1.75 Ga aged Kivalliq Igneous Suite (Fig. 6.1). This bimodal, anorgenic province is dominated by rapakivi granites of the Neultin suite, which were generated by crustal melting in response to basaltic underplating at the lower to middle crust

(Petts et al. 2014, Peterson et al. 2015). Work by Peterson et al. (2015) show that the 1.75 Ga ages are widespread in the western Churchill Province (Fig. 6.1). The authors suggest that the entire western Churchill Province was subjected to the high temperature thermal event produced by Neultin-related basaltic magmatism and that this event is responsible for the resetting of zircon ages below the Athabasca Basin. Therefore, it is possible that metamorphic rutile of the P2 fault was also reset during this event Alternatively, the rutile may have formed during this event.

Although rutile does occur together with oxy-dravite, we interpret oxy-dravite as a product of later hydrothermal activity (Adlakha and Hattori, 2016), possibly related to the 1.75 Ga thermal event. The occurrence of rutile with oxy-dravite is explained by the immobility of Ti during hydrothermal activity. Rutile was likely stable during the hydrothermal activity that crystallized oxy-dravite. Alternatively, rutile and oxy-dravite may have crystallized together during metamorphism and under conditions of low water/rock ratios. The homogeneity and high Mg content of tourmaline, in this case, can be explained by the crystallization of pyrite from the fluids, which likely lowered Fe in the fluids. Regardless of whether rutile and/or oxy-dravite formed during metamorphism or the 1.75 Ga thermal event, it is clearly evident that rutile pre-dates the formation of the Athabasca Basin and the uraniferous hydrothermal event.

6.4.2 The Origin of Anatase

Anatase occurs in hematitized sandstone along the unconformity and P2 fault, and in the basement along the P2 fault. In the sandstone samples, anatase cross-cuts the early diagenetic assemblage of quartz overgrowths with kaolinite and Sr-SO_4^{2-} -rich APS minerals, suggesting anatase formation during later diagenesis or early hydrothermal activity. Anatase is the low temperature/pressure TiO_2 phase and Ti is not mobile at low temperatures; therefore, anatase in sandstones likely formed from local detrital rutile in these samples.

Anatase was observed in basement samples of the P2 fault near uranium mineralization and in apparently barren areas (Table 6.1). In these samples, anatase typically forms fine-grained (< 15 μm), disseminations with magnesio-foitite, sudoite and relict rutile ± uraninite. The textural evidence suggests that anatase formed from the alteration of rutile (Figs. 6.3A,B), either before or during hydrothermal activity that produced magnesio-foitite, sudoite and uraninite.

In the basement, anatase also forms euhedral grains in dolomite with hematite. Although veins of dolomite plus quartz are found locally in proximity to uranium deposits (e.g., Pagel et al 1980, Kotzer and Kyser 1995, Derome et al. 2005), this particular sample occurs in an apparently barren area of the P2 fault, ~80 m below the unconformity (Table 6.1). The occurrence of anatase with hematite in both basement and sandstone samples suggests that fluids were oxidizing, which is consistent with the interpretation that anatase formed by diagenetic fluids of the sandstones or early hydrothermal fluids.

The dolomite-hosted anatase produced a Concordant U-Pb ages of 1569 ± 31 Ma. The main mineralization event of the McArthur River uranium deposit is suggested to have occurred between 1520 – 1540 Ma, based on the oldest discordant ages of uraninite (McGill et al. 1993, Alexandre et al. 2009). The U-Pb age of anatase is older than any uraninite ages, suggesting that anatase formed prior to uraninite, but was stable during the uraniferous hydrothermal event. Its occurrence together with hematite may indicate that this age represents the onset of oxidizing hydrothermal activity in the basement along the P2 fault and that may be related to the formation of the McArthur River deposit.

6.5 Conclusions

- Two TiO_2 polymorphs occur along the P2 fault: i) rutile in basement samples and anatase in both sandstone and basement samples.
- Textural evidence combined with chemical data suggests that rutile formed with zircon, graphite and quartz under low water/rock ratios during metamorphism.
- The Zr contents of rutile coexisting with zircon and quartz indicate equilibrium temperatures between 740 – 890 °C (±50 °C), under granulite facies metamorphic conditions.
- The U-Pb ages of rutile range from 1726 – 1771 Ma and post-date the peak metamorphism of the host rocks. Rutile ages either represent cooling of the lower crust during post-orogenic uplift or basaltic underplating at the lower to middle crust at 1.75 Ga.
- Anatase crystallized during low temperature, oxidizing hydrothermal activity in both sandstone and basement. The occurrence of anatase with dolomite and hematite well below the unconformity in barren areas of the P2 fault attests to oxidizing fluid circulation along the fault.
- The U-Pb age of anatase (1569 ± 31 Ma) indicates the onset of oxidizing hydrothermal activity in the basement that may be related to the McArthur River deposit.

Acknowledgements

This project was funded by Natural Resources of Canada through the Targeted Geoscience Initiative Four (TGI-4) program, a Research Affiliate Program Bursary to EEA and a grant to KH. We thank Dr. Eric G. Potter, science leader for the TGI-4 U ore system project, at the Geological Survey of Canada, for his continuous support. Cameco Corporation provided their logistical support for our field work at the McArthur River mine. Special thanks extend to Gerard Zaluski

and Tom Kotzer, as well as Aaron Brown, Doug Adams, Remi Labelle, and Brian McGill of Cameco Corp. for their help during the field work. We thank Xiang Yang of SMU for his assistance with SEM work, Mitchell Kerr of SMU for help with Raman work, and Glenn Poirier and David Deikrup of the University of Ottawa for their assistance with EPMA work. Lastly, we thank Brandon Boucher and Chris McFarlane of UNB for his assistance with LAICPMS work.

References

Adlakha, E. E., & Hattori, K. (2015). Compositional variation and timing of aluminum phosphate-sulfate minerals in the basement rocks along the P2 fault and in association with the McArthur River uranium deposit, Athabasca Basin, Saskatchewan, Canada. American Mineralogist, 100(7), 1386-1399.

Adlakha, E., and Hattori, K. (2016). Paragenesis and composition of tourmaline types along the P2 fault and McArthur River U deposit, Athabasca Basin, Canada. The Canadian Mineralogist, in press.

Alexandre, P., Kyser, K., Polito, P., & Thomas, D. (2005). Alteration mineralogy and stable isotope geochemistry of Paleoproterozoic basement-hosted unconformity-type uranium deposits in the Athabasca Basin, Canada. Economic Geology, 100(8), 1547-1563.

Alexandre, P., Kyser, K., Thomas, D., Polito, P., & Marlat, J. (2009). Geochronology of unconformity-related uranium deposits in the Athabasca Basin, Saskatchewan, Canada and their integration in the evolution of the basin. Mineralium Deposita, 44(1), 41-59.

Annesley, I.R., Madore, C., Shi, R., and Krogh, T.E. (1997). U–Pb geochronology of thermotectonic events in the Wollaston Lake area, Wollaston Domain: a summary of 1994–1996 results. Summary of investigations, 97-4.

Brenan, J. M., Shaw, H. F., Phinney, D. L., & Ryerson, F. J. (1994). Rutile-aqueous fluid partitioning of Nb, Ta, Hf, Zr, U and Th: implications for high field strength element depletions in island-arc basalts. Earth and Planetary Science Letters, 128(3), 327-339.

Cherniak, D. J. (2000). Pb diffusion in rutile. Contributions to Mineralogy and Petrology, 139(2), 198-207.

Cloutier, J., Kyser, K., Olivo, G. R., & Alexandre, P. (2010). Contrasting patterns of alteration at the wheeler river area, Athabasca basin, Saskatchewan, Canada: insights into the apparently uranium-barren zone K alteration system. Economic Geology, 105(2), 303-324.

Clark, J. R., & Williams-Jones, A. E. (2004). Rutile as a potential indicator mineral for metamorphosed metallic ore deposits. Rapport Final de DIVEX, Sous-projet SC2, Montréal, Canada, 17.

Dachille, F., Simons, P. Y., & Roy, R. (1968). Pressure-temperature studies of anatase, brookite, rutile and TiO2-II. Am Mineral, 53, 1929-1939.

Derome, D., Cathelineau, M., Cuney, M., Fabre, C., Lhomme, T., & Banks, D. A. (2005). Mixing of sodic and calcic brines and uranium deposition at McArthur River, Saskatchewan, Canada: a Raman and laser-induced breakdown spectroscopic study of fluid inclusions. Economic Geology, 100(8), 1529-1545.

Fayek, M., & Kyser, T.K. (1997). Multiple fluid events and rare earth elements associated with unconformity-type U mineralization from the Athabasca Basin, Saskatchewan, Canada. The Canadian Mineralogist, 35, 327 – 658.

Gaboreau, S., Cuney, M., Quirt, D., Patrier, P., & Mathieu, R. (2007). Significance of aluminum phosphate-sulfate minerals associated with U unconformity-type deposits: The Athabasca basin, Canada. American Mineralogist, 92(2-3), 267-280.

Jefferson, C.W., Thomas, D.J., Gandhi, S.S., Ramaekers, P., Delaney, G., Brisbin, D., Cutts, C., Quirt, D., Portella, P., and Olson, R.A., (2007). Unconformity associated U deposits of the Athabasca Basin, Saskatchewan and Alberta, In: Goodfellow, W.D. (ed.) Mineral Deposits of Canada: A Synthesis of Major Deposit-Types, District Metallogeny, the Evolution of

Geological Provinces, and Exploration Methods: Geological Association of Canada, Mineral Deposits Division, Special Publication No. 5, 273-305.

Kotzer, T. G., & Kyser, T. K. (1995). Petrogenesis of the Proterozoic Athabasca Basin, northern Saskatchewan, Canada, and its relation to diagenesis, hydrothermal uranium mineralization and paleohydrogeology. Chemical Geology, 120(1), 45-89.

Krogh, T.E., and Clark, L.A. (1987). Zircon Dating of Sub-Athabasca Granitoid Rocks, Saskatchewan. Geological Association of Canada Annual Meeting Abstracts 12, 64.

Kyser, K., Hiatt, E., Renac, C., Durocher, K., Holk, G., & Deckart, K. (2000). Diagenetic fluids in Paleo-and Meso-Proterozoic sedimentary basins and their implications for long protracted fluid histories. Fluids and Basin Evolution, 28, 225-262.

Lewry, J. F., & Sibbald, T. I. (1980). Thermotectonic evolution of the Churchill Province in northern Saskatchewan. Tectonophysics, 68(1), 45-82.

Luvizotto, G. L., Zack, T., Meyer, H. P., Ludwig, T., Triebold, S., Kronz, A., Münker, C., Stockli, D.F., Prowatke, S., Klemme, S., Jacob, D.E., and von Eynatten, H. (2009). Rutile crystals as potential trace element and isotope mineral standards for microanalysis. Chemical Geology, 261(3), 346-369.

McGill, B. D., Marlatt, J. L., Matthews, R. B., Sopuck, V. J., Homeniuk, L. A., & Hubregtse, J. J. (1993). The P2 North U deposit, Saskatchewan, Canada. Exploration and Mining Geology, 2(4), 321-331.

Meinhold, G., Anders, B., Kostopoulos, D., & Reischmann, T. (2008). Rutile chemistry and thermometry as provenance indicator: an example from Chios Island, Greece. Sedimentary Geology, 203(1), 98-111.

Meinhold, G. (2010). Rutile and its applications in earth sciences. Earth-Science Reviews, 102(1), 1-28.

Orrell, S. E., Bickford, M. E., & Lewry, J. F. (1999). Crustal evolution and age of thermotectonic reworking in the western hinterland of the Trans-Hudson Orogen, northern Saskatchewan. Precambrian Research, 95(3), 187-223.

Pagel, M., Poty, B., & Sheppard, S. M. F. (1980). Contribution to some Saskatchewan uranium deposits mainly from fluid inclusion and isotopic data. In Uranium in the Pine Creek Geosyncline.

Peterson, T. D., Scott, J. M., LeCheminant, A. N., Jefferson, C. W., & Pehrsson, S. J. (2015). The Kivalliq Igneous Suite: Anorogenic bimodal magmatism at 1.75 Ga in the western Churchill Province, Canada. Precambrian Research, 262, 101-119.

Petts, D. C., Davis, W. J., Moser, D. E., & Longstaffe, F. J. (2014). Age and evolution of the lower crust beneath the western Churchill Province: U–Pb zircon geochronology of kimberlite-hosted granulite xenoliths, Nunavut, Canada. Precambrian Research, 241, 129-145.

Rabbia, O. M., Hernández, L. B., French, D. H., King, R. W., & Ayers, J. C. (2009). The El Teniente porphyry Cu–Mo deposit from a hydrothermal rutile perspective. Mineralium Deposita, 44(8), 849-866.

Schandl, E. S., Davis, D. W., & Krogh, T. E. (1990). Are the alteration halos of massive sulfide deposits syngenetic? Evidence from U-Pb dating of hydrothermal rutile at the Kidd volcanic center, Abitibi subprovince, Canada. Geology, 18(6), 505-508.

Zack, T., Kronz, A., Foley, S. F., & Rivers, T. (2002). Trace element abundances in rutiles from eclogites and associated garnet mica schists. Chemical Geology, 184(1), 97-122.

Zack, T., Von Eynatten, H., & Kronz, A. (2004). Rutile geochemistry and its potential use in quantitative provenance studies. Sedimentary Geology, 171(1), 37-58.

Zack, T., Moraes, R., & Kronz, A. (2004). Temperature dependence of Zr in rutile: empirical calibration of a rutile thermometer. Contributions to Mineralogy and Petrology, 148(4), 471-488.

CHAPTER 7.

Global Summary & Conclusions

7.0 Preface

This thesis has unravelled the long history of hydrothermal activity that altered the basement rocks in the McArthur River area through detailed textural analysis of alteration mineral assemblages. As a result, a paragenetic sequence of these alteration events has been developed and fertile alteration has been identified. This information may be useful for identifying basement faults that contributed to the mineralization. Additionally, the chemistry of the alteration minerals has been used to evaluate fluid source and chemistry. This information provides a better understanding of the role of basement rocks and basement faults during the mineralization of the world-class McArthur River deposit. This chapter provides a summary of the work documented in the thesis. The summary is described in chronological order of geologic events and makes reference to the chapters where more detailed information is located. The events are also summarized in Table 7.1, which also lists petrographic observations and makes reference to figures throughout the thesis.

7.1 Summary

The metapelitic rocks and pegmatite along the P2 fault have been extensively altered through multiple generations of hydrothermal activity. The mineral assemblages produced during metamorphism and associated partial melting are observed in “least altered” rocks found well below the unconformity (> 100 m) and outside of the fault zone (>50 m) (Chapter 2). Metapelitic rocks originally comprised an assemblage of quartz, feldspar, biotite ± garnet, cordierite, muscovite, pyrite, plagioclase, monazite, apatite, and zircon. The P2 fault occurs along graphite-rich metapelite. Anatectic pegmatite, formed through partial melting of the metasediments, comprised a similar assemblage with the addition of schorl but without cordierite and garnet.

Table 7.1. Summary table of petrographic observations and paragenetic interpretations of basement rocks

Event	Assemblage	Petrographic Observation	Example Locations/Samples	Reference Figure
Metamorphism (~1.8 Ga)	K-feldspar (Kfs)	anhedral-subhedral < 1 mm	Least altered rocks outside P2 fault & below alteration profile (e.g, MAC3 of MC344, MAC18 of MC370)	Fig. 2.2E1-4, 2.7J
	Biotite (Bt)	subhedral laths <1 mm		
	Garnet (Gt)	subhedral to anhedral grains		
	Cordierite (Crd)	altered to Sud		
	Quartz (Qtz)	euhedral to anhedral grains < 1mm	Relict (i.e. resistive to later hydothermal alteration) along the P2 fault (e.g., MAC85 of H493)	Fig. 6.3
	Rutile (Rt)	anhedral-subhedral grains <0.5 mm		
	Zircon (Zr)	euhedral grains as inclusions in rutile and oxy-dravite		
	Graphite (Gr)	elongate micaceous "stringers"		
	Oxy-schorl (Sch)	cores of oxy-dravite		Figs. 2.9G, 4.3A
HE1 (~1.75 Ga)	Oxy-dravite (Dv)	euhedral-subhedral prismatic grains < 1 mm	Many rocks along P2 fault (e.g., MAC99 of MC349, MAC201 of H3559)	Fig. 2.8, 4.3, 5.2 & 6.3
	Pyrite* (Py)	euhedral-anheadral grains, inclusions in Dv		
	Quartz	euhedral to anhedral grains < 1mm		
	Rutile	relict of metamorphism		
	Graphite	relict of metamorphism		
R-met	Fe-Mg Chlorite (Chl)	replaced Bt, Grt, and Crd, or as radial aggregates in veinlets	Best preserved in least altered rocks outside P2 fault and below alteration profile, persists in lower GZ (e.g., MAC9 of MC344)	Figs. 2.2D, 2.11A Fig. 2.2E1-4
	Illite (Ilt)	replaced Fsp		
PW	Kaolin (Kln)	aggregate "books" of fine-grained plates	RZ outside P2 fault, below u/c (e.g., MAC14 of MC344 and MAC55-56 of MC385) and RGZ	Fig. 2.2B, Fig. 2.4D,E
	Hematite (Hem)	fine-grained, along fractures in quartz		
	As-rich APS	Cores of zoned pseudocubic APS minerals	Transitional RGZ (e.g., MAC412 of MC346)	Figs. 3.3D, 3.4H
	Clinochlore (Cln)	Forms fine-grained aggregates		
	Sudoite (Sud)	Forms fine-grained aggregate, replaced Gt and Fe-Mg chlorite	GZ (e.g., MAC13 of MC344)	Fig. 2.2C
Early Diagenesis	Sr-Ca-SO_4^{2-}-APS minerals	pseudocubes in BZ, rims of As-rich APS in RGZ, and cores to LREE-P APS along P2	Best preserved in BZ that overprints RZ along u/c outside P2 fault (e.g., MAC17 of MC344, MAC57-59 of MC385). Preserved as Sr-Ca-SO42-APS cores in LREE-P rich APS along P2 fault.	Figs. 2.4A, 3.4I
	Illite	alters kaolin of RZ, forms laths in BZ		
	Kaolin/Dickite	aggregate "books" of fine-grained plates		
	Hematite	Fine-grained, overprints earlier minerals	Preserved in RZ, removed in BZ (e.g., MAC57-59 of MC385)	Figs. 2.4C,D
Late Dgs Early HE2? (~1.57 Ga)	Anatase (Ant)	anhedral fine-grains (<15 μm) to euhedral grains (up to 100 μm)	Locally along P2 fault (e.g., MAC426 of MC359)	Fig. 6.4
	Dolomite (Dlm)	massive in vein		
	Hematite	crystalline needles in veins		
HE2 - U min	Magnesio-foitite (Mgf)	Radial aggregates, veinlets, overgrowths on oxy-dravite.	P2 fault samples	Figs. 3.4, 4.3, 5.2
	LREE-P APS minerals	Pseudocobic grains (<15 μm), zoned with Dgs type cores		
	Sudoite	Forms fine-grained aggregates, mixtures with illite		
	Illite	Forms fine-grained aggregates, mixtures with sudoite		
	Uraninite (U1)	Massive replacements, remobilized veinlets	Ore zone samples (e.g., MAC423 and MAC425 of H3380)	Figs. 4.3E-H
Rmb	Sudoite	pseudomorphs earlier Mgf at margins of U2	Locally along P2 (e.g., MAC98 of MC349) and in ore zone (e.g., MAC425 H3380)	Fig. 4.3E-H
	Uraninite (U2)	veinlets and stringers		

Notes: HE = Hydrothermal Event, R-met= retrograde metamorphism, PW= paleo-weathering, Dgs = diagenesis, Rmb = Remobilization, GZ = Green Zone, RGZ = Red Green Zone, RZ = Red Zone, BZ = Bleached Zone

Sample numbers = MAC###, Diamond Drillhole Numbers = MC### or H##, See Fig. 1.1 for drill hole locations along P2, and Appendix 1 for sample depths.

*see Emberley (2014, uOttawa BSc thesis) for pyrite study

The earliest, assemblage preserved along the P2 fault is of rutile, oxy-dravite, zircon, quartz, pyrite, and graphite (Chapter 6). Rutile, zircon, and quartz likely formed during metamorphism and possibly pre-date oxy-dravite and pyrite. Rutile forms fractured anhedral grains and commonly forms inclusions within hydrothermal oxy-dravite. Chemical analysis indicates rutile is heterogeneous, with varying concentrations of Nb (up to 3.86 wt% Nb_2O_5), V (up to 2.12 wt% V_2O_5) and W (up to 2.4 wt% WO_3) which suggests its formation under conditions with low water/rock ratios (Chapter 6). Zirconium-in-rutile thermometry indicates equilibration between rutile, quartz and zircon at temperatures ranging 740 – 890 °C (± 50 °C), reflecting granulite metamorphic conditions. The U-Pb ages of rutile grains range from 1726 – 1771 Ma. This range is notably younger than the Trans-Hudson Orogeny (~1.8 – 1.9 Ga) that produced the metamorphic and anatectic rocks. Considering the closure temperature of rutile at 600 °C, these ages indicate that the basement rocks were subjected to high temperatures well after peak metamorphism. We conclude that this age represents either cooling of the lower crust during post-orogenic uplift, or a later thermal event, possibly related to basaltic underplating and the emplacement of the nearby 1.75 Ga Nueltin Suite granites. Oxy-dravite likely formed during a hydrothermal event before deposition of the Athabasca Basin. Evidence for the hydrothermal origin of oxy-dravite includes the presence of zoned oxy-dravite with cores of early schorl, its presence only in rocks along the P2 fault, its ubiquity in veins, and its homogenous composition along the entire fault (Chapter 4). The trace element composition of oxy-dravite is characterized by relatively high REE contents (up to 130 ppm total REE, $Ce_N > Y_N$), a positive Eu anomaly, and high Cr and V content (Chapter 5). The positive Eu anomaly with high Cr and V contents of oxy-dravite indicates that the hydrothermal fluid interacted with plagioclase-bearing mafic rocks.

Alternatively, oxy-dravite formed during metamorphism with rutile and its composition was controlled by the co-precipitation of pyrite which removed available Fe.

The least altered rocks outside of the P2 fault have undergone retrograde metamorphism. Retrogression produced Fe-Mg chlorite (intermediate of chamosite and clinochlore) and rutile needles at the expense of biotite, and fine-grained illite at the expense of feldspar. This information is important in order to discriminate these phases from the various chlorite species and illite types produced by later hydrothermal alteration.

The basement rocks outside of the P2 fault and near the unconformity exhibit a laterally extensive alteration consisting of an upper Bleached Zone of illite, kaolinite and dickite along the unconformity, a middle Red Zone of pervasive hematite and kaolinite, and a lower Green Zone of chlorite. The Red and Green Zones have previously been interpreted as a paleo-weathering profile and the Bleached Zone formed after paleo-weathering from interaction of reducing fluids of the overlying basin. Field observations and a preliminary paragenetic sequence of these rocks, revealed inconsistencies with the previous interpretation (Chapter 2). The new data suggests that in the study area, the Red and Green Zones have been enhanced and overprinted by diagenetic and/or hydrothermal fluids. In some areas the Red and Green Zones are physically mingled indicating fluid mixing, or multiple generations of hydrothermal alteration. This new interpretation was confirmed by the identification of compositionally zoned APS minerals in the mingled Red-Green Zone and unzoned APS minerals in the Bleached Zone (Chapter 3). The cores of the zoned APS minerals are As- and Ce-rich, corresponding to the end member arsenoflorencite(-Ce). Pelites typically contain elevated concentrations of As which is fixed in sulfides. In oxidizing near surface conditions, As^{5+} is stable and may be incorporated into APS minerals. It is likely that the As-rich cores formed during paleo-weathering. The rims of the APS minerals are Sr-Ca-SO_4^{2-} rich, close

to svanbergite composition with a minor crandallite component. The APS minerals of the Bleached Zone are also Sr-Ca-SO_4^{2-} rich and occur with kaolin, dickite and illite. This assemblage has been well documented as a diagenetic assemblage within the Athabasca Basin by previous researchers. Therefore, the presence of the Sr-Ca-SO_4^{2-} rich APS minerals in the Bleached Zone and Red-Green Zone supports the interpretation that diagenetic fluids produced the Bleached Zone and enhanced the Red and Green Zones in the basement. This observation is evidence for extensive interaction of basinal fluids with the basement and may support claims that the illite, dravite and chlorite alteration corridors of the Athabasca Basin in the McArthur River and Key Lake area were produced by fluids that that interacted with the basement.

The presence of anatase along the P2 fault was documented in this study (Chapter 6). It forms anhedral grains with kaolinite, illite and hematite in the sandstone unit immediately above the unconformity. Anatase was also observed along the P2 fault in the basement and near the unconformity with sudoite, magnesio-foitite and remobilized uraninite, and in an unmineralized portion of the P2 fault, ~80 m below the unconformity, with dolomite and hematite. Texturally, anatase post-dates desilicification and diagenesis of the Athabasca sandstones as it cross-cuts corroded diagenetic quartz overgrowths that contain APS minerals. One sample of anatase in the basement yields a U-Pb age of 1569 ± 31 Ma placing it 30-50 Ma before the main mineralizing event of the McArthur River deposit. Therefore, the presence of anatase may indicate the onset of oxidizing hydrothermal activity along the P2 fault associated with the McArthur River deposit.

The most common alteration assemblage along the P2 fault comprises sudoite, illite, magnesio-foitite and aluminum-phosphate sulfate (APS) minerals. This assemblage is present along the entire P2 fault and is genetically linked to the main hydrothermal event that produced the McArthur River deposit. Sudoite and illite are common alteration minerals within the

basement, regardless of their proximity to the P2 fault, therefore their usefulness in targeting basement structures is limited. This study focussed on the occurrence and chemical variation of APS minerals (Chapter 3) and magnesio-foitite (Chapters 4 and 5) of the basement and sandstone.

Along the P2 fault, APS minerals are zoned and contain Ca-Sr-SO_4^{2-} rich cores, similar in composition to APS minerals of the Red-Green and Bleached Zones. The presence of this type of APS minerals along the entire fault suggests that oxidizing diagenetic fluids entered the basement along the fault. It is likely that kaolinite formed with Ca-Sr-SO_4^{2-} rich APS but was replaced by subsequent hydrothermal alteration. The rims of the APS minerals are LREE- (predominately Ce) and P-rich, similar in composition to florencite(-Ce). In proximity to U mineralization, the APS minerals exhibit a large chemical variation, with SO_4/PO_4 molar ratios of 0.05 - 0.21, whereas APS minerals in unmineralized areas of the fault have a relatively narrow range in composition with moderate SO_4/PO_4 ratios of 0.11 - 0.13. The large range of S/P ratios in the ore zone are attributed to fluid evolution. Initial fluids were oxidizing and high in SO_4^{2-}. Through interaction with the basement, or possibly mixing with a basement sourced fluid, SO_4^{2-} was reduced to sulfide and the S/P ratio was lowered. This interpretation is supported by the chemical zoning of the APS minerals and the presence of ubiquitous sulfide in the basement.

Although different types of APS minerals occur in basement rocks outside the P2 fault, magnesio-foitite was only observed along the fault (Chapter 4). Magnesio-foitite forms aggregates of fine-grained (<15 μm), acicular to prismatic crystals, which occur as matrix to breccia, infill veins or replace earlier oxy-dravite. The chemical composition of magnesio-foitite is similar along the entire P2 fault, suggesting high water/rock ratios. Magnesio-foitite exhibits a high X-site vacancy (0.70 - 0.85 apfu) and high Al in the Y-site (0.70 – 1.12 apfu), indicating that magnesio-foitite replaced Al-rich minerals such as kaolinite and/or sudoite. The trace element composition

of magnesio-foitite is varied, although most contain low REE and Y (<2 ppm) (Chapter 5). Magnesio-foitite can be subdivided into two groups based on trace element abundances. The earliest and least common magnesio-foitite is characterized by high LREE relative to HREE ($Ce_N > Y_N$) with slightly negative Eu anomalies. This type of magnesio-foitite was also documented in the MFd, or uppermost sandstone unit, above the McArthur River deposit. Considering the REE composition, this magnesio-foitite likely formed from a fluid that interacted with felsic clasts in the Athabasca Basin and pegmatite of the basement. The most common type of magnesio-foitite along the fault is characterized by high HREE relative to LREE ($Ce_N < Y_N$). This magnesio-foitite shares a similar chondrite normalized REE pattern as uraninite from McArthur River. The RE pattern is attributed to co-crystallization with LREE-rich APS minerals. Magnesio-foitite exhibits low δD values of -41 to -98 ‰, indicating that the mineralizing fluid was likely groundwater with contribution of basement and or basinal fluids (Chapter 5). Magnesio-foitite also exhibits high values of δB (+13.1 to +23.2 ‰) indicating a marine contribution, either through the dissolution of evaporitic rocks or mixing of seawater. The large range in δB values suggests B fractionation during the progressive crystallization of illite and kaolinite.

The latest event along the P2 fault involves the local remobilization of U-oxide and alteration of magnesio-foitite to sudoite. The U-oxide forms stringers that contain low Pb, variable Ca and Si. Sudoite pseudomorphically replaces magnesio-foitite along the margins of remobilized uraninite.

7.2 Conclusions and Implications

- Multiple overprinting alteration assemblages occur along the P2 fault:
    i. Oxy-dravite, graphite, pyrite, quartz, and rutile formed before deposition of the Athabasca Basin,

ii. Fe-Mg chlorite and illite formed during retrograde metamorphism,

iii. Sr-Ca-SO_4^{2-} rich APS minerals (+kaolinite) formed from diagenetic fluids that entered the basement along the P2 fault,

iv. Anatase formed locally along the P2 fault from early, oxidizing hydrothermal fluids,

v. Magnesio-foitite, and LREE+P rich APS minerals crystallized with sudoite and illite during uraniferous hydrothermal activity related to the formation of the McArthur River deposit,

vi. Late stage remobilization of uraninite and alteration of magnesio-foitite to sudoite occurred locally along the fault.

- Early rutile formed under granulite facies metamorphic conditions, at temperatures up to 890 °C (± 50 °C), as indicated by Zr-in-rutile thermometry. Post-metamorphic ages (between 1726 and 1771 Ma) produced by rutile indicate either cooling of the lower crust or emplacement of the nearby Nueltin Suite granites.
- The onset of post-Athabasca hydrothermal activity along the P2 fault was initiated at 1569 ± 31 Ma, evident by anatase U-Pb ages.
- The assemblage of sudoite, illite, magnesio-foitite and APS minerals, along the entire 7 km studied section of the P2 fault indicates that the alteration halo of the McArthur River deposit extends laterally along the fault.
- The chemistry of LREE-rich APS minerals may be useful for exploration as a large range in S/P ratios (0.05 - 0.21) was observed in APS minerals proximal to U mineralization, whereas moderate S/P ratios (0.11 – 0.13) were observed in unmineralized areas.
- The major chemistry of magnesio-foitite does not vary with proximity to ore, indicating that high water/rock ratios persisted along the fault. Rare, early magnesio-foitite contains high

LREE relative to HREE and positive Eu anomalies, indicative of fluids that interacted with felsic clasts of the sandstone and pegmatite of the basement. Later magnesio-foitite exhibits high HREE relative to LREE, similar to uraninite, due to the co-crystallization of LREE rich APS minerals.

- The presence of LREE+P rich APS and magnesio-foitite along basement faults may help exploration regimes vector toward unconformity-type uranium deposits.
- The mineralizing fluid was likely groundwater with contributions of dissolved evaporites and basinal brines. The mineralizing fluid travelled along the entire P2 fault but evolved in the ore zone likely due to interactions with the basement or mixing with a basement fluid.
- This thesis demonstrates that the P2 fault was a site of multiple hydrothermal events starting before the Athabasca Basin formation and during the evolution of the diagenetic-hydrothermal system of the Athabasca Basin.

APPENDICES.

Appendix 1 Supplementary Material for Chapter 1

Sample List

Line/Area	Drill-hole	Sample	Depth	Lithology	Zone	Thin Section
L9225N (Zone B)	MC274	U1	536	UO	P2 ZB	Y
	MC335	U2	589	UO		Y
260+00E	MC344	MAC3	651.5	PELITE	HW	Y
sub-ec background	MC344	MAC4	641.4	PELITE	HW	N
	MC344	MAC5	634.3	PEG	HW	Y
	MC344	MAC6	630	PELITE	HW	N
	MC344	MAC7	587.7	PEG	HW	N
	MC344	MAC8	576.7	PEG	HW	Y
	MC344	MAC9	628.2	PELITE	HW	Y
	MC344	MAC10	611	PELITE	HW	N
	MC344	MAC11	546.75	PEG/PEL	HW	N
	MC344	MAC12	541.7	PELITE	HW	Y
	MC344	MAC13	525.9	PEG/PEL	HW	Y
	MC344	MAC14	520.4	PELITE	HW	Y
	MC344	MAC15	536.7	PEG/PEL	HW	N
	MC344	MAC16	507.4	PEG/PEL	HW	N
	MC344	MAC17	499.4	QTZ	HW	Y
260+00E	MC370	MAC18	630.8	PEG/PEL	FW	Y
sub-ec P2	MC370	MAC19	617	PEG/PEL	FW	N
	MC370	MAC20	609.4	PELITE	FW	N
	MC370	MAC21	606.9	PELITE	FW	Y
	MC370	MAC22	578.45	PEG	P2 LG	N
	MC370	MAC23	593.5	PEG	P2 LG	Y
	MC370	MAC24	605.5	PELITE	FW	N
	MC370	MAC25	590	PELITE	FW	Y
	MC370	MAC26	569	MFA	P2, MFA	Y
	MC370	MAC27	558.8	PELITE	P2 LG	N
	MC370	MAC28	561.5	MFA	P2 LG	N
	MC370	MAC29	560.2	DRAV BX	P2 LG	Y
	MC370	MAC30	552.5	PELITE	P2 LG	N
	MC370	MAC31	551	PELITE	P2 LG	N
	MC370	MAC32	543	MFA	P2, MFA	Y
	MC370	MAC33	533.2	PELITE	P2 LG	Y
	MC370	MAC34	534.5	CHLOR BX	P2 LG	N

Line/Area	Drill-hole	Sample	Depth	Lithology	Zone	Thin Section
Underground	H729	MAC35	9.5	PELITE	P2 Z3	Y
McArthur	H729	MAC36	8.9	PELITE	P2 Z3	N
	H729	MAC37	18.2	PEG	P2 Z3	Y
	H729	MAC38	31	PEL/PEG	P2 Z3	Y
	H729	MAC39	38.6	GRAPH	P2 Z3	N
	H729	MAC40	43.8	PEG	P2 Z3	N
	H729	MAC41	64.1	PELITE	FW	N
	H729	MAC42	65.6	PELITE	FW	N
	H729	MAC43	49.5	PELITE	P2 Z3	Y
	H729	MAC44	64.5	PEG	P2 Z3	Y
	H729	MAC45	57.6	PEG	P2 Z3	Y
	H729	MAC46	43.3	PEL	P2 Z3	Y
	H729	MAC47	49.4	PEL	P2 Z3	Y
	H729	MAC48	65	PEL	P2 Z3	Y
	H729	MAC49	69.9	PEL/PEG	P2 Z3	N
	H729	MAC50	76.4	PEL	VQ Z3	N
	H729	MAC51	78.4	PEL	VQ Z3	Y
	H729	MAC52	116	PEG	VQ Z3	Y
	H729	MAC53	118	QTZ	VQ Z3	Y
	H729	MAC54	115.9	PEGPEL	VQ Z3	N
L241+00E	MC385	MAC55	686	PEL	FW	Y
barren background	MC385	MAC56	680.2	PEL	FW	Y
	MC385	MAC57	678.8	PEG	FW	Y
	MC385	MAC58	674.3	QTZ	FW	Y
	MC385	MAC59	664.3	PEG	FW	Y
	MC385	MAC60	661.2	QTZ	FW	N
	MC385	MAC61	657	MFA	MFA	Y
	MC385	MAC62	652.2	MFA	MFA	Y
Underground	H201	MAC63	7.6	PEG/PEL	P2 Z2	Y
McArthur 8273	H201	MAC64	18.9	PELITE	P2 Z2	N
	H201	MAC65	18.4	PELITE	P2 Z2	N
	H201	MAC66	24.7	PELITE BX	P2 Z2	Y
	H201	MAC67	30.8	PEG/PEL	P2 Z2	Y
	H201	MAC68	36.1	PELITE	P2 Z2	N
	H201	MAC69	38.1	PELITE	P2 Z2	Y
	H201	MAC70	34.3	GRAPH BX	P2 Z2	Y
	H201	MAC441	46.5	pel	P2 Z2	Y
	H201	MAC442	58.8	fault	P2 Z2	x
	H201	MAC443	65.4	ss	P2 Z2	Y

Line/Area		Drill-hole	Sample	Depth	Lithology	Zone	Thin Section
Underground		H347	MAC71	11.2	PEG/PEL	P2 Z2	N
McArthur 8273		H347	MAC71-1	38.7	PELITE	P2 Z2	Y
		H347	MAC72	33.4	PEG	P2 Z2	N
		H347	MAC73	43.6	PELITE	P2 Z2	Y
		H347	MAC74	40.8	PEG/PEL CHL BX	P2 Z2	Y
		H347	MAC75	46.8	PEG BX	P2 Z2	Y
		H347	MAC76	44	P2 FAULT	P2 Z2	N
		H347	MAC77	58.3	PEG	P2 Z2	Y
		H347	MAC78	107.5	QTZ	P2 Z2	Y
		H347	MAC79	106	QTZ	P2 Z2	Y
Underground		H493	MAC80	14	PELITE	P2 Z2	Y
McArthur 8273		H493	MAC81	15.3	PEG BX	P2 Z2	Y
		H493	MAC82	23.8	P2	P2 Z2	N
		H493	MAC83	30	PEG GRPH BX	P2 Z2	Y
		H493	MAC84	24.5	PELITE	P2 Z2	Y
		H493	MAC85	17.7	PEL/PEG	P2 Z2	Y
		H493	MAC86	31.7	PEL GRPH BX	P2 Z2	Y
L300+00N		MC349	MAC87	659	PELITE	FW	Y
P2 Main		MC349	MAC88	657.5	PEL/PEG	FW	Y
		MC349	MAC89	645.5	PEG	FW	Y
	6398000	MC349	MAC90	647.4	PEG	FW	Y
	492353	MC349	MAC91	626.3	PEL CHL BX	P2 LG	Y
		MC349	MAC92	619.4	SHEAR	P2 LG	N
		MC349	MAC93	611.5	SHEAR	P2 LG	N
		MC349	MAC94	601.1	PEG BX	P2 LG	Y
		MC349	MAC95	599.6	PELITE	P2 LG	Y
		MC349	MAC96	599	PEL/PEG BX	P2 LG	Y
		MC349	MAC97	581.4	PEG/PEL	P2 LG	Y
		MC349	MAC98	578	SHEAR	P2 LG	Y
		MC349	MAC99	573	PEL/PEG BX	P2 LG	Y
L243+00E		MC361	MAC100	652.9	PELITE	FW	Y
barren P2		MC361	MAC101	652.2	PELITE	FW	Y
		MC361	MAC102	646	PELITE	FW	Y
		MC361	MAC103	643	PELITE	FW	N
		MC361	MAC104	641	PEG	FW	Y
		MC361	MAC105	627.7	PELITE	FW	Y
		MC361	MAC106	606.3	PELITE	P2 Barren	Y
		MC361	MAC107	603.7	PEG BX	P2 Barren	N
		MC361	MAC108	697	FRACTURE ZONE	P2 Barren	N
		MC361	MAC109	587.6	PELITE/PEG	P2 Barren	Y
		MC361	MAC110	590	PELITE	P2 Barren	Y
		MC361	MAC111	581.6	PEG	P2 Barren	Y
		MC361	MAC112	565.5	FRACTURE ZONE	P2 Barren	N
		MC361	MAC113	559	FRACTURE ZONE	P2 Barren	N

Line/Area	Drill-hole	Sample	Depth	Lithology	Zone	Thin Section
	MC361	MAC114	560	PELITE	P2 Barren	Y
	MC361	MAC115	556	PEG	P2 Barren	Y
	MC361	MAC116	528.5	PEG	P2 Barren	Y
	MC361	MAC117	523.3	PEG	P2 Barren	Y
	MC361	MAC118	522.1	FRACTURE ZONE	P2 Barren	N
	MC361	MAC119	510.5	PELITE	P2 Barren	N
	MC361	MAC120	504	PELITE/PEG	P2 Barren	Y
	MC361	MAC121	496	MFA	MFA	Y
	MC361	MAC122	493	MFA	MFA	Y
L050+50N	MC362	MAC122-1	643.9	PELITE	FW	N
barren P2	MC362	MAC123	637.9	PELITE BX	FW	N
	MC362	MAC124	625.3	PELITE	P2 Barren	N
	MC362	MAC125	640.8	PEG	P2 Barren	N
	MC362	MAC126	615.8	PELITE BX	P2 Barren	N
	MC362	MAC127	602.3	PEG/PEL BX	P2 Barren	Y
	MC362	MAC128	597.2	PELITE BX	P2 Barren	N
	MC362	MAC129	?	PEG	P2 Barren	Y
	MC362	MAC130	582.2	PELITE BX	P2 Barren	Y
	MC362	MAC131	555.8	PELITE	P2 Barren	N
	MC362	MAC132	548.5	PEG	P2 Barren	N
	MC362	MAC133	534	PEG BX	P2 Barren	N
	MC362	MAC134	533.5	PEG BX	P2 Barren	Y
	MC362	MAC135	520.2	PEG	P2 Barren	Y
	MC362	MAC136		PEL	HW	Y
	H231	MAC137	82.8	PEG BX	VQ Z2	Y
BX ZONE	H231	MAC138	81	PEL BX	VQ Z2	Y
	H231	MAC139	85.2	PEL BX	VQ Z2	N
	H231	MAC140	86.7	PEL BX	VQ Z2	N
	H231	MAC141	90.1	PEL BX	VQ Z2	Y
	H231	MAC142	91.2	PEL BX	VQ Z2	N
	H231	MAC143	89	QTZ BX	VQ Z2	N
8240	H203	MAC144	55.5	PEL BX	P2 Z2	Y
damage zone below ore body	H203	MAC151	52.3	PELITE	P2 Z2	Y
	H203	MAC152	62	PEL BX	P2 Z2	Y
	H203	MAC153	61.5	PEG BX	P2 Z2	Y
	H203	MAC154	54.5	FAULT	P2 Z2	N
	H203	MAC444	69.7	pel/peg	P2 Z2	Y
	H203	MAC445	90.1	pel	P2 Z2	Y
	MO227	MAC145	52.3	PEG BX	P2 Z2	N
	MO227	MAC146	52.6	PEG BX	P2 Z2	Y
	MO227	MAC147	55.8	PEL BX	P2 Z2	N
	MO227	MAC149	58.4	PEL BX	P2 Z2	N
	MO227	MAC150	86.9	QTZ BX	VQ Z2	N

Line/Area	Drill-hole	Sample	Depth	Lithology	Zone	Thin Section
	H3559	MAC201	20.5	PELITE	P2 Z1	Y
P2	H3559	MAC202		P2	P2 Z1	Y
	H3576	MAC203	55.7	PELITE	P2 Z1	Y
	MC410-2	MAC400	790.9	qtz/peg	FW	Y
	MC410-2	MAC401	782.7	pel	FW	Y
	MC410-2	MAC402	761.6	peg	FW	Y
	MC410-2	MAC403	738.5	peg	P2 LG	Y
	MC410-2	MAC404	542.7	peg/pel	P2 LG	Y
	MC410-2	MAC405	545.7	peg/pel	P2 LG	Y
	MC410-2	MAC406	527.7	ss	MFA	Y
	MC344	MAC407	501.1	quartzite	HW	N
	MC346	MAC408	737.1	peg	FW	Y
L28 50	MC346	MAC409	725.4	pel	FW	Y
background	MC346	MAC410	682.5	qtz	FW	Y
	MC346	MAC411	674.1	pel	FW	Y
	MC346	MAC412	669	pel	FW	Y
	MC346	MAC413	653.7	peg	FW	Y
	MC346	MAC414	619.5	pel	FW	Y
	MC346	MAC415	603.5	ss	MFA	Y
	MC346	MAC416	580.5	congl.	MFA	Y
ZONE 4	H677	MAC417	80.4	Fault	P2 Z4	x
	H677	MAC418A	77.1	UO	P2 Z4	Y
	H677	MAC418B	59.3	UO BX	P2 Z4	Y
	H677	MAC419	58.1	FAULT	P2 Z4	x
	H677	MAC420	57.1	pel	P2 Z4	Y
Z2 8270	H3380	MAC421	79.3	qtz	VQ Z2	Y
	H3380	MAC422	74.7	FAULT	VQ Z2	x
	H3380	MAC423	52.9	pel	P2 Z2	Y
	H3380	MAC424	50.9	pel	P2 Z2	Y
	H3380	MAC425	57.1	pel	P2 Z2	Y
Barren P2	MC359	MAC426	581.6	pel	P2 Barren	Y
	MC359	MAC427	546	pel	P2 Barren	Y
	MC359	MAC428	520	pel	HW	Y
	MC359	MAC429	513.5	pel	HW	Y
	MC359	MAC430	494	ss	MFA	Y
	MC359	MAC431	626.1	peg	P2 Barren	Y
	MC359	MAC432	491	ss	MFA	Y
L241	MC381	MAC433	660.5	pel	FW	Y
FW to P2	MC381	MAC434	656	peg	FW	Y
P2 at u/c	MC381	MAC435	621	pel	FW	Y
	MC381	MAC436	603	peg	P2 Barren	Y

Line/Area	Drill-hole	Sample	Depth	Lithology	Zone	Thin Section
9224N	MC274	MAC437	598	pel	FW	Y
	MC274	MAC438	618.3	pel	FW	Y
	MC274	MAC439	615.3	pel	FW	Y
	MC274	MAC440	502.4	ss	P2 ZB	Y
	MC274	MAC461	62.8	ss	MFD	Y
	MC274	MAC462	93.1	ss	MFD	Y
	MC232	MAC447	465.6	ss	MFA	N
	MC232	MAC448	461	ss	MFA	N
	MC232	MAC449	336.4	ss	MFB	Y
	MC232	MAC450	85	ss	MFD	N
	MC232	MAC451	45	ss	MFD	Y
	MC238	MAC452	506.8	congl	MFA	Y
	MC241	MAC453	129.5	ss		N
	MC241	MAC454	141.8	ss		N
	MC241	MAC455	152.5	ss	MFD	Y
	MC241	MAC463	39.7	ss	MFD	Y
	MC388	MAC456	517	congl	MFA	Y
	MC388	MAC457	519.8	congl	MFA	Y
	MC388	MAC458	561	ss	MFA	N
	MC388	MAC459	563.6	ss	MFA	N
	MC388	MAC460	520.1	ss		Y

Drillhole locations (UTM)

HoleID	Easting	Northing
H203	496706.68	6402036.94
H227	496661.75	6401997.46
H231	496662.49	6401996.63
H347	496725.55	6402060.37
H3576	496912.30	6402209.09
H493	496715.84	6402080.27
H677	496483.03	6401838.18
H729	496617.58	6401956.20
MC232	496405.92	6401861.56
MC238	496412.35	6401853.57
MC241	496418.56	6401845.57
MC274	497267.50	6402877.13
MC335	497394.60	6402814.80
MC344	495727.95	6400552.50
MC346	493075.22	6398009.57
MC359	494441.91	6399221.16
MC362	494625.31	6399624.84
MC370	495563.37	6400737.66
MC381	494386.13	6399253.88
MC385	494185.50	6399419.01
MC388	495512.07	6400778.98

SGA 2013 (Extended Abstract)

The paragenesis and chemistry of alteration minerals within the basement rocks associated with the P2 fault and the McArthur River uranium deposit, Athabasca Basin

E.E. Adlakha*; K. Hattori

*Department of Earth Science, University of Ottawa, Ottawa, Ontario, Canada, K1N 6N5 *eadla028@uottawa.ca*

E.G. Potter

Geological Survey of Canada, Booth Street Complex, Ottawa, Ontario

Abstract. The main ore body (Zone 2) of the McArthur River deposit, Athabasca Basin, is almost completely hosted in the basement rocks immediately below the Athabasca sandstones, and is spatially associated with the P2 reverse fault. The Paleoproterozoic basement rocks have undergone upper-amphibolite facies metamorphism, retrograde metamorphism, paleo-weathering, diagenetic effects from the overlying sandstones and multiple episodes of hydrothermal alteration. Peak metamorphism produced garnet-biotite-cordierite assemblages in paragneiss and metapelite, plus quartzite. Three distinct horizons occur below the unconformity: i) a lowermost Green Zone formed through retrogression then paleo-weathering and is characterized by the chloritization of ferromagnesian minerals and illitization of K-feldspar, ii) an overlying Red Zone of pervasive hematite and kaolinite alteration due to paleo-weathering, and iii) a Bleached Zone that formed along the unconformity from K-bearing, diagenetic, basinal fluids that crystallized coarse-grain illite and altered kaolinite to dickite. Multiple stages of hydrothermal activity overprinted earlier alteration minerals, particularly along the P2 Fault and proximal to the ore body. Two generations of tourmaline occur along the P2 Fault Zone: an earlier, coarse-grained dravite, and later, fine-grained magnesiofoitite. A second chlorite-forming event, a third illite-forming event, and a second hematitization-rutilization event have also occurred along the P2 fault within the basement.

Keywords. Uranium, Athabasca Basin, McArthur River, Alteration, Fault

1 Introduction & Background

The basement rocks below the eastern Athabasca Basin are part of the Wollaston Group and host the McArthur River deposit (Fig. 1), the largest known high-grade uranium deposit. The Wollaston Group consists of pelite, semi-pelite, arkose, calc-silicate and quartzite that was were subsequently metamorphosed during the Tran-Hudson orogeny (ca. 1.8-1.9 Ga; Lewry and Sibbald 1980) under upper amphibolite facies conditions. Granitic pegmatite lenses intrude the metasediments and likely formed from local partial melting after peak metamorphism. Substantial erosion during exhumation of the basement rocks developed a paleo-weathering profile before the deposition and subsequent diagenesis of the Athabasca Group sandstones (beginning at ca. 1.73 Ga; Kyser et al. 2000). The Athabasca Group sandstones consist of a succession of fluvial to marine quartz-dominated sediments, currently preserved at a maximum thickness of 1500 m in the centre of the basin. Above the McArthur River deposit, the preserved thickness of the sandstones is approximately 500 m. Immediately above the deposit, the sandstone has been intensively silicified.

The Zone 2 ore body (primary mineralization at 1521 ± 8 Ma; McGill et al. 1993) is the main deposit at McArthur River and is almost entirely hosted within the basement rocks immediately below the unconformity. The ore body is structurally controlled by two faults: the P2 reverse fault

and the Vertical Quartzite fault. The P2 reverse fault is one of the most prominent structures within the Athabasca Basin is responsible for thrusting the basement rocks above the overlying sandstones by as much as 80 m (McGill et al. 1993). The structure, trending 045°/45°SE, is predominantly hosted within graphitic pelite in the basement but is also expressed as a series of splays in the overlying sandstones due to the later reactivations of the fault. Hydrothermal alteration has been documented to be structurally controlled along the P2 Fault, as it occurs along the shear zone, splay faults, and fractures (Jefferson et al. 2007). The Vertical Quartzite (VQ) fault is a steeply dipping structure between the footwall quartzite and cordierite-bearing pelite. The rocks adjacent to the P2 and below the ore body show evidence of extensive fluid/rock interaction as they are highly brecciated and altered. Therefore, the P2 Fault may have served as a fluid pathway for uraniferous fluids to permeate the basement rocks and precipitate the ore.

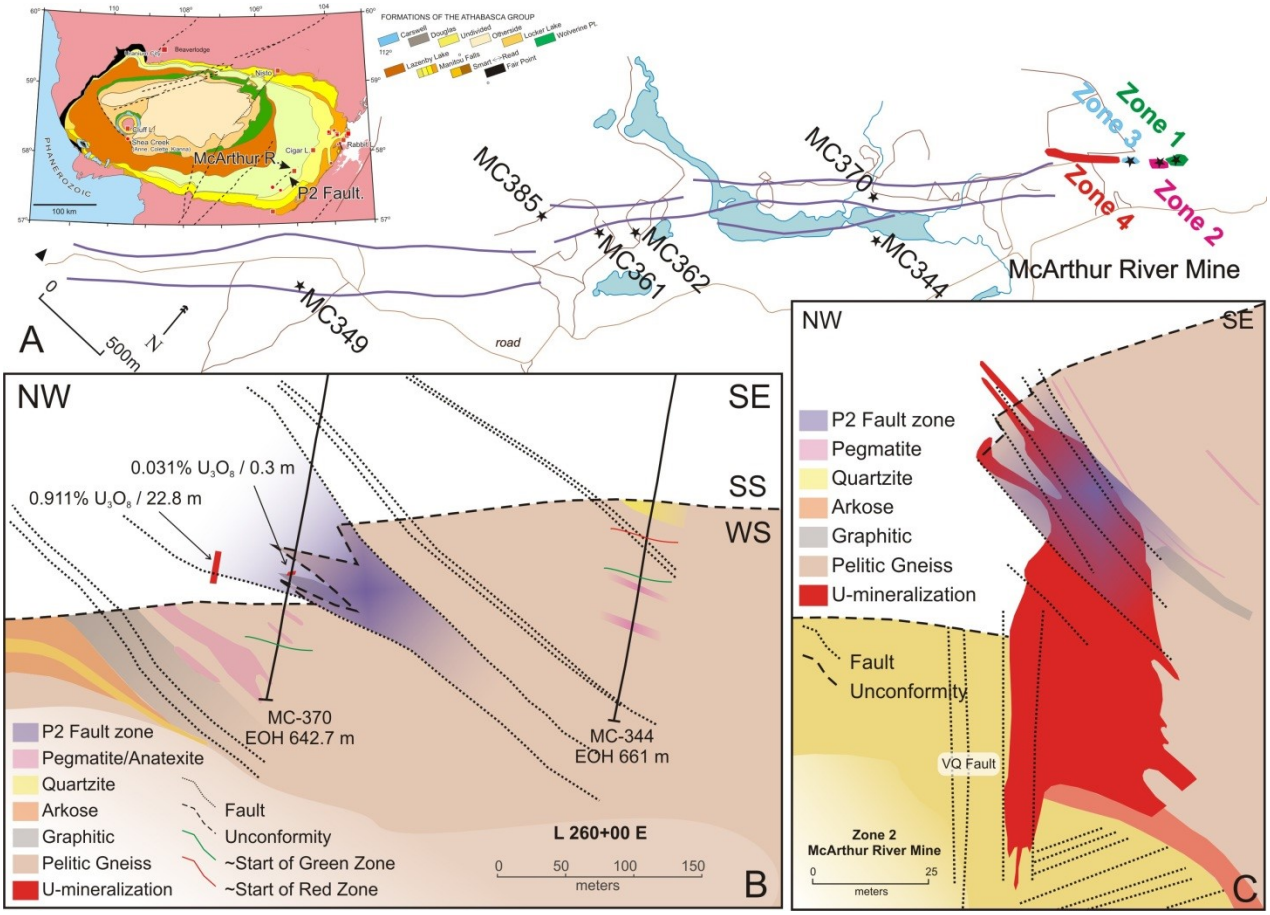

Figure 1. A) A plan-view map showing the P2 Fault surface expression, respective sample drill collars, and the McArthur River mine site. A regional map (adapted from Jefferson et al., 2007) of the Athabasca Basin is in the upper left corner and shows high-grade uranium deposits and major structural features including the P2 reverse fault (highlighted in white). **B)** Cross-sections (NW-SE) of exploration line 260E showing sampled drill holes MC-370 & MC-344 and **C)** the Zone 2 ore-body from McArthur River Mine. The P2 Fault Zone is highlighted in both sections.

2 Sampling & Methods

Field work was conducted in August, 2012, and consisted of the sampling of drill-core along the P2 structure and within the McArthur River underground mine (Fig. 1). Two background holes (non-mineralized and not intersecting the P2 Fault: MC-344 and -385) and four drill-holes along the P2 Fault were sampled: two are non-mineralized and cross-cut the P2 Fault (MC-361/2), and two are sub-economic holes that cross-cut the P2 (MC-370, -349). Twelve drill-holes were

sampled from the McArthur River mine site: two from Zone 1, nine from Zone 2 (the main ore body), and one from Zone 3. Thin section petrography using transmitted and reflective light microscopy was used to identify minerals and to characterize textural relationships in polished thin sections. Qualitative identification of alteration minerals was carried out by Terraspec short-wave infrared spectroscopy (SWIR) on drill-core samples and electron dispersive spectroscopy (EDS) using a JEOL 6610LV scanning electron microscope (SEM) at the University of Ottawa on carbon-coated polished thin sections. Textural relationships between alteration phases were determined through back-scattered electron (BSE) imaging. Quantitative analysis of biotite, garnet, illite, chlorite, and tourmaline for major and minor element constituents (SiO_2, TiO_2, Al_2O_3, FeO, MnO, ZnO, MgO, CaO, Na_2O, K_2O, Cl, BaO, F and SrO) were measured using a JEOL 8230 electron-probe microanalyzer (EMPA) at the University of Ottawa. EMPA data for magnesiofoitite is presented in Table 1.

3 Results

3.1 Alteration preceding the uranium mineralization

In order to understand the alteration associated with the P2 fault and the McArthur River ore body, detailed work focused on two drill-cores approximately 150 – 200 m away from the P2 Fault (and any apparent mineralization) to characterize regional alteration.

Below the unconformity (200-300 m) the rocks show a laterally extensive alteration profile consisting of overprinting zones: a lower Green Zone, a middle Red Zone, and a Bleached Zone that occurs along the unconformity. Relatively unaltered metapelite is found well below the unconformity and contains pink garnet, fresh to slightly chloritized biotite, chloritized cordierite, slightly illitized K-feldspar, and quartz (Fig. 2A). BSE-images of cordierite show evidence of illitization at grain boundaries and fractures (Fig. 2C). The least-altered rocks gradationally transition into the overlying Green Zone that records chloritization due to retrogression, which was enhanced during paleo weathering and hydrothermal activity. The Green Zone is dominated by two generations of chlorite: i) Al-chlorite (sudoite) that completely replaces garnet and cordierite, and ii) Fe-chlorite that occurs as coarse (300 μm) radial aggregates and that replaces biotite. The feldspar in the Green Zone is completely replaced by fine-grain illite. There is also evidence for the addition of K within chloritized garnets as illite occurs as discrete fine-grained aggregates within the altered grains (Fig. 2B). The Green Zone is overprinted by the Red Zone that developed during the weathering of the basement rocks. Hematite and kaolinite are abundant within the Red Zone and alter Fe-bearing minerals and illite, respectively (Fig. 2D). The presence of kaolinite and hematite alteration is consistent with alteration that would result from a low temperature, oxidizing, and surficial fluid. The Bleached Zone occurs above and below the unconformity as fine grained white-yellow clay alteration that overprints the Red Zone in drill-core. Samples from the Bleached Zone (Fig. 2F) show that alteration is dominated by fine-grained dickite and two generations of illite: early, fine-grained illite and late, coarse-grained illite. Coarse-grained illite also persists to the Red Zone along the P2 Fault. SWIR spectral analyses of the Red and Bleached Zone suggest a mixture of illite-kaolinite and illite-dickite, respectively. The presence of dickite in the Bleached Zone indicates that the fluid responsible for its formation was higher temperature than the fluid that produced the kaolinite in the Red Zone. Therefore, the Bleached Zone was probably formed by a higher temperature, K-bearing, diagenetic, basinal fluid that reacted with the basement rocks and propagated along the P2 during the lithification of the Athabasca sandstones.

Table 1: Chemical composition of dravite and magnesiofoitite within rocks along the P2 Fault. Atom proportions are O = 24.5

drill-hole		MO227 (mineralized)	MC3559 (mineralized)		MC362 (barren)	MC361 (barren)	MC349 (sub-ec)
sample (depth)		146 (Zone 2 u/g)	201 (Zone 1 u/g)		122 (637.9 m)	109 (587.6 m)	99 (~578 m)
host rock		*pelite*	*graphitic pelite*		*bleached SS*	*pegmatite*	*brecciated pelite*
		magnesiofoitite	magnesiofoitite	dravite	magnesiofoitite	dravite	dravite
		x̄ 1σ	x̄ 1σ	x̄ 1σ	x̄ 1σ	x̄ 1σ	x̄ 1σ
wt%	SiO2	35.03 1.22	35.68 3.31	35.35 0.31	34.37 0.29	35.34 0.09	35.52 0.26
	TiO2	<0.02	<0.02	1.06 0.15	<0.02	1.36 0.08	1.29 0.08
	Al2O3	34.85 0.88	34.06 1.25	32.06 0.15	33.29 0.91	31.75 0.15	31.83 0.19
	FeO (T)	1.45 0.33	0.20 0.02	3.56 0.02	2.10 0.20	4.77 0.02	4.68 0.18
	MnO	<0.02	<0.02	0.01 0.01	<0.02	0.03 0.01	0.02 0.02
	ZnO	<0.02	<0.02	0.01 0.01	<0.02	0.00 0.01	0.01 0.02
	MgO	7.26 0.20	8.11 0.80	8.34 0.06	6.96 0.04	7.63 0.04	7.68 0.06
	CaO	0.11 0.04	0.02 0.01	1.27 0.25	0.05 0.01	1.01 0.05	1.36 0.12
	Na2O	0.73 0.21	0.59 0.04	1.71 0.11	0.83 0.07	2.05 0.04	1.73 0.07
	K2O	0.02 0.02	<0.02	0.07 0.01	<0.02	0.07 0.01	0.07 0.01
	Cl	<0.02	<0.02	<0.02	<0.02	<0.02	<0.02
	BaO	0.02 0.02	<0.02	0.01 0.01	<0.02	0.02 0.02	0.01 0.01
	F	0.04 0.02	0.14 0.22	0.42 0.03	0.18 0.09	0.22 0.08	0.57 0.08
	SrO	<0.02	<0.02	0.00 0.01	0.03 0.04	0.01 0.01	0.02 0.02
	Total	79.51 1.51	78.79 5.22	83.70 0.22	77.77 0.93	84.15 0.13	84.56 0.13
	F/Cl	12	80	134	24	246	557
apfu							
T:	Si	5.81	5.92	5.75	5.87	5.76	5.77
	Al	0.19	0.08	0.25	0.13	0.24	0.23
ΣT		6.00	6.00	6.00	6.00	6.00	6.00
Z:	Al	6.00	6.00	5.90	6.00	5.85	5.86
	Fe			0.10		0.15	0.14
Y:	Al	0.64	0.60		0.56		
	Fe	0.20	0.03	0.39	0.30	0.50	0.49
	Ti			0.13		0.17	0.16
	Mg	1.80	2.00	2.02	1.77	1.85	1.86
	Ca			0.22		0.18	0.24
	□	0.40	0.36	0.24	0.36	0.31	0.26
ΣY		3.03	3.00	3.00	2.99	3.00	3.00
X:	Na	0.23	0.19	0.54	0.28	0.65	0.55
	K	0.01	0.01	0.01	0.01	0.01	0.02
	□	0.76	0.80	0.44	0.71	0.34	0.44
ΣX		1.00	1.00	1.00	1.00	1.00	1.00
B:	B*	3.00	3.00	3.00	3.00	3.00	3.00
O:	OH*	3.98	3.93	3.79	3.90	3.89	3.71
	F	0.02	0.07	0.21	0.10	0.11	0.29
ΣO		4.00	4.00	4.00	4.00	4.00	4.00

□ = vacancy; u/g = underground collared hole; * determined by stoichiometry; FeO (T) = total Fe

3.2 Alteration associated with the P2 fault

Two generations of Mg-tourmaline occur consistently along the P2 Fault (within 50 m) and are absent from the aforementioned regional alteration profile: early dravite and later magnesiofoitite (alkali-deficient dravite). Euhedral-subhedral, coarse-grained (up to 0.5 mm), dravite $[(\square_{0.4}Na_{0.6})(\square_{0.2}Mg_{1.9}Fe_{0.5}Ca_{0.2}Ti_{0.2})(Al_{5.9}Fe_{0.1})(Si_{5.7}Al_{0.3}O_{18})(BO_3)_3(OH_{3.8}F_{0.2})]$ forms wide (1-2 cm) veins (Fig. 3A) or isolated grains, and radial aggregates of fine-grained (<0.2 mm) magnesiofoitite $[(\square_{0.75}K_{0.08}Na_{0.17})(\square_{0.23}Ca_{0.02}Fe_{0.04}Mg_{2.10}Al_{0.61})Al_6(Al_{0.22}Si_{5.78}O_{18})(BO_3)_3(F_{0.02}OH_{3.98})]$ occur as thin veinlets (< 2 mm), as overgrowths on earlier dravite (Fig. 3C) or disseminated within fine-grained illite (Fig. 3F). Both species of tourmaline show high atomic ratios of F/Cl. Discrete alteration events also

occur along fractures and as veinlets along the P2 Fault Zone: i) late chlorite and illite assemblage occurs as veins and cross-cut tourmaline alteration (Fig. 3F) adjacent to the Zone 2 orebody (H493), and ii) a second oxidation event (hematite + rutile) restricted to fractures within the P2 zone overprints tourmaline (Fig. 3D) proximal to sub-economic mineralization (MC349).

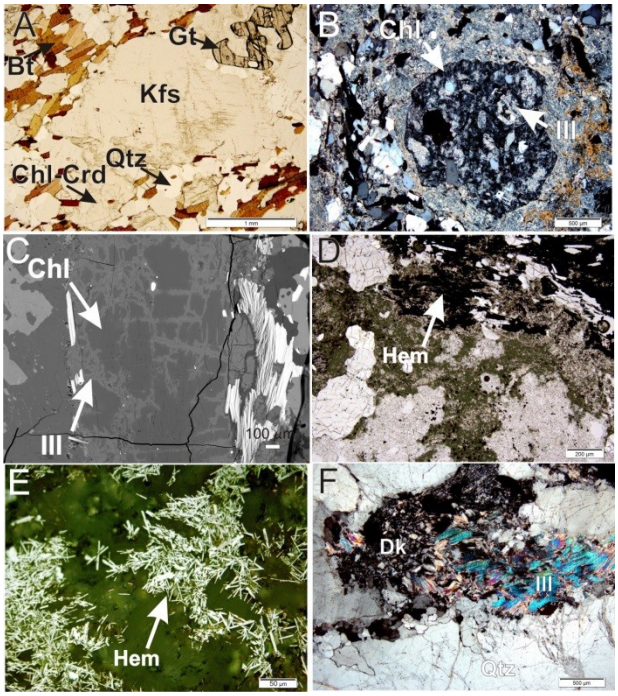

Figure 2. Microphotographs showing representative mineralogy of the alteration profile observed within the basement rocks. **A)** Unaltered biotite (Bt) and garnet (Gt), slightly illitized K-feldspar (Kfs), chloritized cordierite (Chl-Crd) and quartz within metapelite (MC344, 651.5 m). **B)** Chloritized and illitized garnet, and **C)** chloritized cordierite (BSE image) showing illitization along fractures from a metapelite (MC344, 525.9 m) of the Green Zone. **D&E)** Hematite overprinting metapelite in the Red Zone (MC385, 678.8 m). **F)** Coarse-grain illite and dickite overprint fine-grain illite within basal quartzite (MC344, 499.4 m).

4 Summary

The alteration along the P2 fault cross-cuts the chlorite and illite alteration of the Green Zone that formed by retrogression and paleo-weathering fluids, the hematite and kaolinite alteration of the Red Zone that formed from paleo-weathering of the basement regolith, and the dickite and illite alteration of the Bleached Zone that formed from a diagenetic K-bearing fluid. Two generations of tourmaline occur along the entire length of the P2 and their major chemistry is consistent regardless of their position relative to mineralization. A late chlorite and illite event overprints the tourmaline formation proximal to the Zone 2 ore body, and a hematite + rutile oxidation event overprints the tourmaline proximal to sub-economic mineralization farther along the P2. Intense alteration is concentrated within the P2 structure adjacent to the McArthur River deposit, confirming that the P2 fault was a conduit for an uraniferous hydrothermal fluid. Further investigation into the chemistry and paragenesis of alteration associated with mineralization is in progress to elucidate the reactions during the uranium mineralization event.

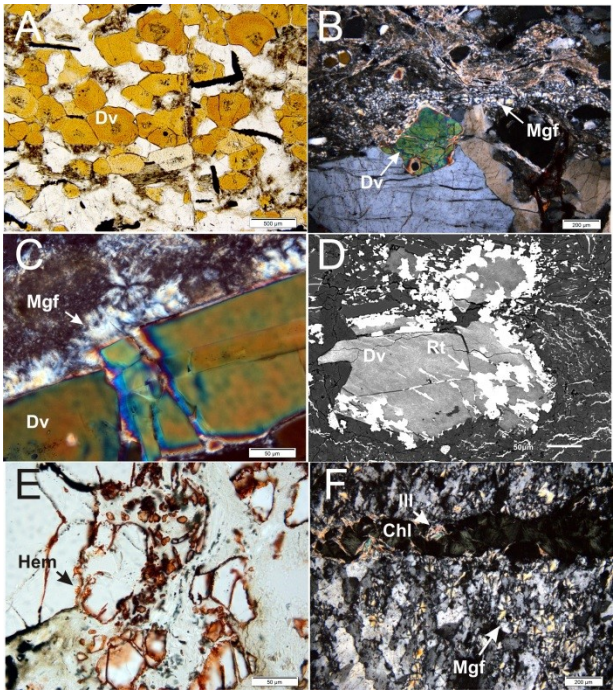

Figure 3. Microphotographs that show alteration phases along the P2 Fault and the host rocks the ore body. **A)** An early dravite (Dv) vein (see Table 1 for chemical analysis) along the P2 in Zone 1 (H3559, 20.5 m). **B&C)** Two generations of tourmaline: early coarse grain dravite and later fine-grain aggregates of magnesiofoitite (Mgf) that occur as veinlets and overgrowths (MC349, 575 m). **D&E)** Rutilization of early dravite along grain boundaries and fractures (BSE-image) and hematite overprinting quartz in metapelite along the P2 Fault (MC349, 578 m). **F)** A chlorite/illite veinlet that crosscuts magnesiofoitite alteration within a chlorite breccia along the P2 fault proximal to the Zone 2 ore-body (H347, 45 m).

Acknowledgements

We thank Jeanne Percival of the Geological Survey of Canada for her help with SWIR data and Athabasca clay standards; G. Poirier of the Museum of Nature for his help during SEM & Probe analysis; and to Cameco

Geologists G. Zaluski, T. Kotzer, V. Sopuck, G. Witt, D. Adams and B. McGill for all of their assistance. We acknowledge a bursary to EEA and a grant to KH through the Natural Resources Canada TGI-4 project.

References

Jefferson CW, Thomas DJ, Gandhi SS, Ramaekers P, Delaney G, Brisbin D, Cutts C, Quirt D, Portella P, Olson RA (2007c) Unconformity-associated uranium deposits of the Athabasca Basin, Saskatchewan and Alberta. Mineral Deposits of Canada: A Synthesis of Major Deposit Types, District Metallogeny, the Evolution of Geological Provinces, and Exploration Methods. Geological Association of Canada, Mineral Deposits Division, Special Publication No 5:273-305

Kyser K, Hiatt E, Renac C, Durocher K, Holk G, Deckart K (2000) Diagenetic fluids in Paleo- and Meso-Proterozoic sedimentary basins and their implications for long protracted fluid histories. Mineralogical Association of Canada Short Course 28:225–262

Lewry JF, Sibbald TII (1980) Thermotectonic evolution of the Churchill province in northern Saskatchewan. Tectonophysics 68:45–82

MacDonald C (1980) Mineralogy and geochemistry of a Precambrian regolith in the Athabasca Basin. Dissertation. University of Saskatchewan

McGill B, Marlatt J, Matthews R, Sopuck V, Homeniuk L, Hubregtse J (1993) The P2 North uranium deposit Saskatchewan, Canada. Exploration Mining Geology 2(4):321

Goldschmidt 2013

Fluid evolution recorded by alteration minerals along the P2 reverse fault and associated with the McArthur River U-deposit

E. E. ADLAKHA*[1]; K. HATTORI[1]; E.G. POTTER[2]

[1]Department of Earth Science, University of Ottawa, Ottawa, Ontario, Canada, K1N 6N5 (*correspondance: eadla028@uottawa.ca); (keiko.hattori@uottawa.ca)

[2]Geological Survey of Canada, Ottawa, Ontario, Canada, K1A 0E8; (eric.potter@nrcan-rncan.gc.ca)

The basement rocks along the P2 fault are extensively altered, particularly where they host the McArthur River Zone 2 uranium ore body. Two generations of tourmaline occur along the P2: i) early, euhedral-subhedral, coarse-grained (>0.5 mm), 1-2 cm wide veins and isolated grains of dravite (Mg-tourmaline), and ii) later fine-grained (<0.2 mm), radial magnesiofoitite (alkali-deficient dravite) forms veinlets (< 2 mm), overgrowths on earlier dravite, and grains disseminated within fine-grain illite. Fe-clinochlore, coarse-grain illite, rutile and hematite are ubiquitous along the P2 and occur as pervasive replacement minerals or veins, and post-date dravite crystallization.

To ensure minerals were free of inclusions, individual grains were first inspected with BSE-SEM at highest magnification and elemental peaks were then carefully monitored during trace element analysis (LA-ICPMS). Dravite $[(\square_{0.4}Na_{0.6})(\square_{0.2}Mg_{1.9}Fe_{0.5}Ca_{0.2}Ti_{0.2})(Al_{5.9}Fe_{0.1})(Si_{5.7}\ Al_{0.3}O_{18})(BO_3)_3(OH_{3.8}F_{0.2})]$ contains 1.24 (± 0.09, 1σ) wt% TiO_2, 89 – 280 ppm Zn, 51 - 630 ppm Cr, 190 - 1500 ppm V, and atomic F/Cl ratios range 98 – 11000. Magnesiofoitite $[(\square_{0.7}K_{0.1}Na_{0.2})(\square_{0.4}Fe_{0.1}Mg_{2.0}Al_{0.5})Al_6(Al_{0.1}Si_{5.9}O_{18})(BO_3)_3(F_{0.02}OH_{3.98})]$ contains 65 – 260 ppm V, 2.9 - 110 ppm Cr, 0.2 – 3.7 ppm U, and 0.2 – 34 ppm Th, and ranges 3.2 - 80 atomic F/Cl. Dravite and magnesiofoitite contain low Li (< 12 ppm) and high Ni (1 – 28, 13 – 250 ppm, respectively); however, they also show contrasting trace element behaviours: dravite is enriched in LREE relative to HREE $([Ce]_N/[Ce]^*_N) > 1$, and has a positive Eu anomaly, whereas, magnesiofoitite is enriched in HREE relative to LREE $([Ce]_N/[Ce]^*_N) < 1$, and has a negative Eu anomaly. Chlorite $[(Fe_{1.9}Mg_{2.6}Al_{1.4})(Si_{2.7}\ Al_{1.3}O_{10})(OH)_8]$ contains significant Li (40 - 669 ppm), and Mn (803 – 4083 ppm); illite $[(K_{0.9})(Al_{1.8}Mg_{0.1}Fe_{0.1})(Si_{3.2}Al_{0.8}O_{10})(OH)_2]$ contains significant B (17 – 250 ppm), Li (<4.9 – 144 ppm), Ti (36 – 14500 ppm), Rb (343 - 692 ppm), U (<0.01 – 0.6 ppm), Sn (1.2 – 148 ppm), and Ba (78 – 1670 ppm); and both minerals show atomic F/Cl ratios > 10. High F/Cl, U, Th and B, and a negative Eu anomaly in alteration phases suggests a contribution of pegmatite to the fluid.

SK Open House 2013

Unraveling the alteration history of basement rocks along the P2 Fault Zone and that host the McArthur River uranium deposit

E. ADLAKHA[1], K. HATTORI[1], G. ZALUSKI[2], T. KOTZER[2], and E. POTTER[3]

[1]Department of Earth Science, University of Ottawa, Ottawa, Ontario, Canada, K1N 6N5 (*correspondance: eadla028@uottawa.ca; keiko.hattori@uottawa.ca)
[2] Cameco Corporation, Exploration Office, Saskatoon, SK. Canada, S7M 1J3 (gerard_zaluski@cameco.com; tom_kotzer@cameco.com)
[3]Geological Survey of Canada, Ottawa, Ontario, Canada, K1A 0E8; (eric.potter@nrcan-rncan.gc.ca)

The P2 reverse fault in the basement rocks below the southeastern Athabasca Basin hosts the Zone 2 ore body of the McArthur River uranium deposit, the largest high-grade unconformity-type uranium deposit yet discovered. This study is to document alteration within and near the P2 deformation zone and the Zone 2 ore body using field observations, and petrographic and geochemical data on carefully selected drill core samples in order to evaluate the role of the P2 fault as the conduit for basinal and basement fluids. The P2 fault is constrained to chloritized graphitic metapelite and traced seismically as a listric structure down at least 2 km from the unconformity and up to 1.5 km along the strike. Alteration immediately below the unconformity is laterally extensive along strike and consists of a lower Green Zone with sudoite and illite (±Fe-Mg chlorite), middle Red Zone with hematite and kaolinite, and Bleached Zone of illite and kaolinite right along the unconformity. The vertical zonation of alteration from Bleached, Red, and Green Zones is also observed along the unconformity in the P2 fault zone; however, the lateral distribution of alteration is not continuous within and in proximity to the fault because the Red and Green Zones are intermittently mingled and sporadically overprinted by illite of Bleached Zone-type alteration. It has been previously suggested that the Red Zone represents a pre-Athabascan paleoweathering horizon, with lowermost depths delineated by the chloritic Green Zone. However, we observe at least two generations of hematite in the Red Zone. Furthermore, along the P2 fault pervasive hematitic and bleaching alteration are observed at depths up to 200 m below the unconformity and the Red and Bleached Zone alteration (±sudoite) is apparent in the immediately overlying sandstone and conglomerates. These observations clearly suggest that the alteration is not simply due to weathering.

Magnesiofoitite (alkali-deficient Mg-tourmaline) is ubiquitous in rocks along the P2 fault, especially those proximal to mineralization and the unconformity. Magnesiofoitite is late in the alteration sequence as it crosscuts and/or replaces all aforementioned alteration; it is likely related to uranium mineralization as it is spatially associated with high grade ore. In addition, textural evidence and the abundance of REE suggest that magnesiofoitite is coeval with aluminum phosphate sulfate minerals (APS). Alteration surrounding the Zone 2 ore body is dominated by sudoite, illite and magnesiofoitite with minor sulfides, and late Fe-Mg chlorite veins. Minor, localized late hematite is restricted to veins (±pitchblende) and fractures. Preliminary data indicate that multiple overprinting events from paleo-weathering through diagenetic to late hydrothermal fluids altered the rocks in and proximal to the P2 fault zone. We suggest that the paleo-weathering (characterized by hematite I in the Red Zone) made the basement rocks more susceptible to fluid-rock interactions and was overprinted by later alteration (hematite II, Green and Bleached Zone-type). To date our observations indicate that the P2 fault allowed for oxidizing fluids related to basinal diagenesis of the Athabasca Group sandstones and later uraniferous hydrothermal fluids to enter deep in the basement and interact with the basement rocks.

Ore fluids recorded in the compositions of magnesiofoitite and alumino-phosphate-sulfate (APS) minerals in the basement along the P2 structure and the McArthur River deposit, Athabasca Basin.

E. E. ADLAKHA[1], K. HATTORI[1], G. ZALUSKI[2], T. KOTZER[2], and E. POTTER[3]

[1]Department of Earth Science, University of Ottawa, Ottawa, Ontario, Canada, K1N 6N5 (*correspondance: eadla028@uottawa.ca; keiko.hattori@uottawa.ca)
[2] Cameco Corporation, Exploration Office, Saskatoon, SK. Canada, S7M 1J3 (gerard_zaluski@cameco.com; tom_kotzer@cameco.com)
[3]Geological Survey of Canada, Ottawa, Ontario, Canada, K1A 0E8; (eric.potter@nrcan-rncan.gc.ca)

The P2 reverse fault is a reactivated structure in the southeastern Athabasca Basin that hosts the McArthur River uranium deposit, the largest high-grade unconformity-type uranium deposit yet discovered. This study is to document alteration below the unconformity, specifically within and near the P2 deformation zone and the basement-hosted Zone 2 ore body, in order to evaluate the role of the P2 fault as the conduit for basinal and basement fluids and identify fertile alteration. The results of this study show that the P2 structure is the site of multiple stages of diagenetic-hydrothermal alteration, which produced illite, sudoite, Fe-Mg chlorite, clinochlore, kaolinite, aluminum phosphate-sulfate minerals (APS) and tourmaline. Below the unconformity, the assemblage of illite plus sudoite is common in pelite and pegmatite regardless of proximity to the P2 fault, and kaolinite is distributed along the unconformity; however, the assemblage of magnesiofoitite (alkali-deficient Mg-tourmaline) plus LREE-rich APS has only been found in close proximity to the P2 structure.

Along the P2 fault, magnesiofoitite forms fine-grained (<0.2 mm) matrix, aggregates, overgrowths on metamorphic/magmatic dravite (< 2 mm), and veinlets (< 2 mm) that cross-cut sudoite and illite. APS form zoned pseudo-cubes (1 – 20 μm), disseminated and clustered within fine-grained matrix in altered metapelite and pegmatite and vary compositionally from LREE-rich, to Ca- or Sr-rich. Magnesiofoitite contains low contents of LREE ($[LREE]_N/[HREE]_N$) ≈ 0.2), yet significant amounts of U (0.2 – 3.7 ppm), Cr (2.9 - 110 ppm), V (65 – 260 ppm) and W (0.03 – 0.347 ppm). The low LREE in magnesiofoitite is consistent with its close proximity to LREE-rich APS, implying that the two minerals are contemporaneous. Some crystals of magnesiofoitite are essentially free of alkalis. Overall, low alkalis (<0.3 in apfu) and high U plus W in magnesiofoitite suggests that the fluids were acidic and oxidized in order to transport soluble complexes of U^{6+} and W^{6+}. This fluid character is further supported by the co-precipitation of APS: significant Al solubility requires acidic fluids and the presence of SO_4^{2-} confirms the oxidized nature of the fluids.

The presence of these co-genetic minerals along the P2 structure suggests that the P2 fault was a conduit for uraniferous fluids; however, the fluids did not form uranium deposits all along the P2. The evidence further substantiates models in which the localization of large deposits required the focusing of an ascending reduced fluid to precipitate uraninite from the descending oxidized uraniferous fluid.

Tourmaline in the metasedimentary country rocks of the McArthur River uranium deposit, Saskatchewan

Erin Adlakha and Keiko Hattori

Address: Department of Earth Sciences, University of Ottawa, Ottawa, Ontario, K1N 6n5

e-mail: Eadla028@uottawa.ca

Tourmaline is a common alteration mineral of many hydrothermal deposits and its composition and species reflect the nature of the mineralizing fluids. Therefore, characterization of tourmaline in hydrothermal deposits is important. In the Athabasca Basin, the occurrence of dravite (Mg-rich tourmaline) has been reported as a regional alteration mineral and also in and around uranium deposits. The results of a detailed study of alteration minerals in the McArthur River uranium deposit, the world largest high-grade uranium deposit, reveals three different species of tourmaline. The majority of tourmaline around the McArthur River deposit is magnesiofoitite (alkali-deficient tourmaline), as reported from the Rabbit Lake by Rosenberg and Foit (2006). Magnesiofoitite is paragenetically late as it forms overgrowths on earlier tourmaline of dravite. Dravite likely formed during the regional metamorphism of sedimentary rocks under upper amphibolite facies conditions and associated injection of pegmatite.

They form dark brown to black grains in metapelites and pegmatite. In thin section they are light brown to yellow pleochroic euhedral-subhedral, coarse-grains (>0.5 mm), and form wide (1-2 cm) oriented veins and isolated grains surrounded by fine-grained magnesiofoitite, and/or illite. They show little compositional variation among different grains, $[(\square_{0.4}Na_{0.6})(\square_{0.2}Mg_{1.9}Fe_{0.5}Ca_{0.2}Ti_{0.2})(Al_{5.9}\ Fe_{0.1})(Si_{5.7}Al_{0.3}O_{18})(BO_3)_3(OH_{3.8}F_{0.2})$; □ = vacancy], although a few grains show Fe-rich cores (high schorl component) and dravitic rims. Dravite contains 1.24 (± 0.09, 1σ) wt% TiO_2, 89 – 280 ppm Zn, 51 - 630 ppm Cr, 190 - 1500 ppm V, and atomic F/Cl ratios range 98 – 11000. Dravite contain high LREE ($[LREE]_N/[HREE]_N$) > 7), and has a positive Eu anomaly.

Paragenetically late tourmaline, magnesiofoitite (alkali-deficient dravite; $[(\square_{0.7}K_{0.1}Na_{0.2})(\square_{0.4}Fe_{0.1}Mg_{2.0}Al_{0.5})Al_6(Al_{0.1}Si_{5.9}O_{18})(BO_3)_3(F_{0.02}OH_{3.98})]$; □ = vacancy), has a vacancy (0.7-0.86 apfu) in the x-site (alkali site). They are fine-grained (<0.2 mm), and form radial aggregates around earlier dravite, within veinlets (<2 mm) or as matrix. Magnesiofoitite is bluish white in hand specimens and clear in thin section. The distribution of magnesiofoitite and its close spatial association with the U mineralization and ore-bearing basement faults (P2 fault) suggest that it formed from uraniferous fluids. The presence of U (up to 3.7 ppm U) in magnesiofoitite supports this interpretation.

Rosenberg, P.E., & Foit, F.F., Jr., 2006. Magnesiofoitite from the uranium deposits of the Athabasca Basin, Saskatchewan; The Canadian Mineralogist 44: 959-965

Fluid evolution recorded in the chemistry of tourmaline and aluminum sulfate-phosphate minerals along the P2 fault, McArthur River uranium deposit, Saskatchewan

E. E. ADLAKHA[1], K. HATTORI[1], G. ZALUSKI[2], T. KOTZER[2], and E. POTTER[3]

[1]Department of Earth Science, University of Ottawa, Ottawa, Ontario, Canada, K1N 6N5 (*correspondance: eadla028@uottawa.ca; keiko.hattori@uottawa.ca)
[2] Cameco Corporation, Exploration Office, Saskatoon, SK. Canada, S7M 1J3 (gerard_zaluski@cameco.com; tom_kotzer@cameco.com)
[3]Geological Survey of Canada, Ottawa, Ontario, Canada, K1A 0E8; (eric.potter@nrcan-rncan.gc.ca)

The P2 fault is a 13 km reverse basement structure hosted in graphitic metapelite of the eastern Athabasca Basin and hosts the world-class McArthur River uranium deposit. An assemblage of magnesiofoitite (alkali-deficient tourmaline) and LREE-rich aluminum sulfate-phosphate minerals (APS) occur along the entire P2 fault. These minerals are found in highest abundance in proximity to the McArthur River deposit. In the basement, magnesiofoitite was found only along the P2 fault. Magnesiofoitite forms aggregates of fine-grained (typically < 0.2 mm) needles that are intermixed with sudoite and/or illite, or in veinlets (< 2 mm). Magnesiofoitite is similar in composition along the entire P2 fault, independent of mineralization, and contains a high vacancy in its alkali site (0.70 – 0.85 apfu), suggesting low Na/H+ in the fluids. Magnesiofoitite is slightly enriched in HREE relative to LREE ($[LREE]_N/[HREE]_N \approx 0.7$). APS occur within and outside the P2 fault, but the compositions vary depending on the locations. Along the fault, APS form zoned pseudo-cubes (> 20 μm), with Sr- Ca- and SO_4^{2-}-rich cores (svanbergite composition) and LREE- and P-rich rims (florencite composition). These APS contain up to 16 ppm U, suggesting the fluids were uraniferous. Outside the fault, APS occur along the unconformity with kaolin and are svanbergitic. Magnesiofoitite and florencite show complementary REE patterns implying that the two minerals are contemporaneous. APS mineral cores contain high SO_4^{2-} suggesting an earlier oxidized fluid, whereas SO_4^{2-}-poor rims, especially near the ore, indicate that the fluid became relatively reduced. The data suggests that the uraniferous fluids passed through the entire P2 fault, but the mineralization took place only when the fluids were reduced.

The chemistry and paragenesis of alteration minerals within the basement rocks that host of the McArthur River uranium deposit and the P2 reverse fault, Athabasca Basin, Saskatchewan.

E. Adlakha[1]; K. Hattori[1] & E. Potter[2]

[1]Department of Earth Sciences, University of Ottawa, Ottawa, Ontario, K1N 6N5, Canada

[2]Geological Survey of Canada, Booth Street Complex, Ottawa, Ontario

The main ore body (Zone 2) within the McArthur River deposit, Athabasca Basin, is unique as it is almost completely hosted within the basement rocks immediately below the unconformably overlying Athabasca sandstones, and is bound by two faults: the P2 reverse fault and the Vertical Quartzite fault. The Paleoproterozoic age basement rocks (Wollaston Supergroup) are variable in composition and lithology, and have a long geologic history: upper-amphibolite metamorphism, retrograde metamorphism, paleo-weathering, diagenetic effects from the deposition of the overlying sandstones and multiple episodes of hydrothermal alteration. Three distinct colour horizons occur below the unconformity: a lowermost Green Zone, a Red Zone, and a Bleached Zone that occurs along the unconformity. The Green Zone formed from the retrogression (enhanced by meteoric fluids) of Fe-garnet ($Fe_{81}Mg_{19}$), biotite ($Fe_{48}Mg_{52}$) and cordierite to chlorite (X_{Fe}=0.10, 0.47, & 0.33, respectively) and the destruction of k-feldspar to fine-grain illite $[(K_{0.74}Na_{0.02}[H3O]_{0.24})(Mg_{0.19}Fe_{0.11}Al_{1.23})(Al_{1.09}Si_{2.91}O_{10})(F_{0.02}[OH]_{1.98}[H_2O])]$. The Red Zone represents paleo-weathering as oxidizing fluids during the erosion of the basement rocks lead to hematization of chlorite and kaolinization of fine-grain illite. The Bleached Zone occurs along the unconformity and formed from diagenetic basinal fluids that crystallized abundant coarse-grain illite $[(K_{0.76}Na_{0.04}[H3O]_{0.2})(Mg_{0.18}Fe_{0.06}Al_{1.28})(Al_{1.2}Si_{2.8}O_{10})(F_{0.03}[OH]_{1.97}[H_2O])]$ and altered kaolinite to dickite (identified using short-wave infrared spectroscopy). Coarse-grain illite persists to the lower units of the basement rocks proximal to P2 and textural evidence suggests it to be recrystallized within fine-grain illite. Chloritized garnet and cordierite also shows illite alteration as chlorite contains K and illite replacement is texturally evident with BSE imaging along grain fractures. Many hydrothermal alteration events overprint the colour profile of the basement rocks, particularly within the area bound between the P2 & VQ faults, below the ore body. Two generations of tourmaline occur within the P2 fault zone: an earlier, euhedral-subhedral coarse-grain tourmaline that is oriented within thick veins, and later fine-grain magnesiofoitite $[(\square_{0.75}K_{0.08}Na_{0.17})(\square_{0.23}Ca_{0.02}Fe_{0.04}Mg_{2.10}Al_{0.61})Al_6(Al_{0.22}Si_{5.78}O_{18})(BO_3)_3(F_{0.02}OH_{3.98})]$ that occurs as radial aggregates within veins, as rims upon earlier tourmaline and disseminated within fine-grain illite. A second chlorite event (X_{Fe}=0.46), a third illite event and a second hematite event persists throughout the basement rocks as veins and cross-cuts tourmaline alteration.

FERTILE ALTERATION IN BASEMENT ROCKS ALONG THE P2 STRUCTURE THAT HOSTS THE MCARTHUR RIVER DEPOSIT, ATHABASCA BASIN: INSIGHTS ON THE CHARACTERISTICS OF THE MINERALIZING FLUID.

E. E. Adlakha[1], K. Hattori[1], G. Zaluski[2], T. Kotzer[2], and E. Potter[3]

[1]Department of Earth Science, University of Ottawa, Ottawa, Ontario, Canada, K1N 6N5 (*correspondance: eadla028@uottawa.ca; keiko.hattori@uottawa.ca)
[2] Cameco Corporation, Exploration Office, Saskatoon, SK. Canada, S7M 1J3 (gerard_zaluski@cameco.com; tom_kotzer@cameco.com)
[3]Geological Survey of Canada, Ottawa, Ontario, Canada, K1A 0E8; (eric.potter@nrcan-rncan.gc.ca)

The P2 reverse fault is a reactivated structure in the southeastern Athabasca Basin that hosts the McArthur River uranium deposit, the largest high-grade unconformity-type uranium deposit yet discovered. This study is to document alteration below the unconformity, specifically within and near the P2 deformation zone and the basement-hosted Zone 2 ore body, in order to evaluate the role of the P2 fault as the conduit for basinal and basement fluids and identify fertile alteration. The results of this study show that the P2 structure is the site of multiple stages of diagenetic-hydrothermal alteration, which produced illite, sudoite, Fe-Mg chlorite, clinochlore, kaolinite, aluminum phosphate-sulfate minerals (APS) and tourmaline. Below the unconformity, the assemblage of illite plus sudoite is common in pelite and pegmatite regardless of proximity to the P2 fault, and kaolinite is distributed along the unconformity; however, the assemblage of magnesiofoitite (alkali-deficient Mg-tourmaline) plus LREE-rich APS has only been found in close proximity to the P2 structure.

Along the P2 fault, magnesiofoitite forms fine-grained (<0.2 mm) matrix, aggregates, overgrowths on metamorphic/magmatic dravite (< 2 mm), and veinlets (< 2 mm) that cross-cut sudoite and illite. APS form zoned pseudo-cubes (1 – 20 μm), disseminated and clustered within fine-grained matrix in altered metapelite and pegmatite and vary compositionally from LREE-rich, to Ca- or Sr-rich. Magnesiofoitite contains low contents of LREE ($[LREE]_N/[HREE]_N$) ≈ 0.2), yet significant amounts of U (0.2 – 3.7 ppm), Cr (2.9 - 110 ppm), V (65 – 260 ppm) and W (0.03 – 0.347 ppm). The low LREE in magnesiofoitite is consistent with its close proximity to LREE-rich APS, implying that the two minerals are contemporaneous. Some crystals of magnesiofoitite are essentially free of alkalis. Overall, low alkalis (<0.3 in apfu) and high U plus W in magnesiofoitite suggests that the fluids were acidic and oxidized in order to transport soluble complexes of U^{6+} and W^{6+}. This fluid character is further supported by the co-precipitation of APS: significant Al solubility requires acidic fluids and the presence of SO_4^{2-} confirms the oxidized nature of the fluids.

The presence of these co-genetic minerals along the P2 structure suggests that the P2 fault was a conduit for uraniferous fluids; however, the fluids did not form uranium deposits all along the P2. The evidence further substantiates models in which the localization of large deposits required the focusing of an ascending reduced fluid to precipitate uraninite from the descending oxidized uraniferous fluid.

Adlakha, E E; Hattori, K; Zaluski, G; Kotzer, T G; Potter, E G (2015) Mineralogy of a fertile fluid conduit related to unconformity-type uranium deposits in the Athabasca Basin, Saskatchewan. Presentations of the 2014 TGI-4 unconformity-related uranium workshop; by Potter, E G (ed.); Geological Survey of Canada, Scientific Presentation 34, 2015; p. 41-67 (Appendix 1)

Available for free download at:

http://ftp.maps.canada.ca/pub/nrcan_rncan/publications/ess_sst/296/296519/sp_0034_gsc.pdf

Adlakha, E.E., Hattori, K., Zaluski, G., Kotzer, T.G., Davis, W.J., and Potter, E.G., (2015) Mineralogy of a fertile fluid conduit related to unconformity-type U deposits in the Athabasca Basin, Saskatchewan, in Targeted Geoscience Initiative 4: unconformity-related U systems, (ed.) E.G. Potter and D.M. Wright; Geological Survey of Canada, Open File 7791, p. 74–82. doi:10.4095/295776 (Appendix 1.3)

Available for free download at:

http://ftp.maps.canada.ca/pub/nrcan_rncan/publications/ess_sst/295/295776/of_7791.pdf

E E; Hattori, K; Potter, E G; Sopuck, V. (2013) The paragenesis and chemistry of alteration associated with the P2 fault in metamorphic rocks underlying the Athabasca Basin; Adlakha, Geological Survey of Canada, Open File 7365; 1 sheet, doi:10.4095/292559

Available for free download at:

http://ftp.maps.canada.ca/pub/nrcan_rncan/publications/ess_sst/292/292559/gscof_7365_e_2013_pr01.pdf

Appendix 2 Supplementary Material for Chapter 2

Table A2.1. Data set for EPMA analysis (wt% oxide)

sample	SiO2	TiO2	Al2O3	FeO	MnO	ZnO	MgO	CaO	Na2O	K2O	Cl	BaO	F	SrO	P2O5	Total
17-1-illite1	45.688	0.244	35.603	0.749	0.02	0	0.635	0	0.522	10.532	0.002	0.055	0.094	0.019		94.123
17-1-illite3	45.589	0.05	36.546	0.584	0.005	0	0.207	0	0.463	10.946	0.001	0	0.04	0		94.414
17-1-illite4	46.538	0.432	34.658	0.99	0.03	0.037	0.72	0	0.222	11.166	0.002	0.014	0.139	0		94.889
17-1-illite5	45.469	0.023	36.579	0.63	0.009	0.055	0.241	0	0.434	11.039	0	0.064	0.025	0.014		94.571
17-1-illite6	45.987	0.473	35.018	0.968	0.005	0.006	0.66	0	0.407	11.107	0.003	0.021	0.099	0		94.711
17-1-dark1	46.236	0	37.332	0.163	0	0.016	0.039	0	0.049	2.023	0.013	0	0	0		85.868
17-1-dark2	46.02	0.02	36.311	0.216	0.019	0	0.109	0	0.054	2.121	0.009	0.034	0.22	0		85.038
17-1-dark3	46.517	0.005	37.385	0.151	0	0	0.089	0	0.073	1.646	0.01	0.02	0.034	0		85.914
17-2-illite1	46.083	0.695	35.018	1.001	0.018	0.01	0.662	0	0.289	11.156	0.003	0.023	0.045	0		94.983
17-2-illite2	45.688	0.218	36.745	0.543	0	0	0.158	0	0.503	10.786	0.005	0	0.084	0.027		94.721
17-2-illite3	45.911	0.064	36.926	0.559	0.007	0	0.254	0	0.504	10.919	0.007	0.094	0.114	0		95.309
17-2-illite4	46.443	0.201	35.306	0.869	0	0	0.696	0	0.301	10.99	0.013	0.034	0.01	0		94.856
17-2-illite5	46.188	0.277	35.513	0.965	0.019	0	0.637	0	0.348	11.081	0.004	0.017	0.099	0.058		95.163
17-2-illite6	45.294	0.215	37.16	0.542	0	0.021	0.177	0	0.599	10.793	0	0.061	0.04	0		94.885
17-3-illite1	45.31	0.011	37.903	0.05	0	0	0.021	0	0.305	11.08	0.005	0.072	0.02	0		94.768
17-3-illite2	45.971	0.015	37.613	0.131	0	0.036	0.109	0	0.278	11.006	0.004	0	0	0		95.162
17-3-illite3	46.143	0.005	37.03	0.16	0	0.043	0.108	0	0.269	10.878	0.013	0	0	0.052		94.698
17-3-illite4	46.067	0.015	38.164	0.087	0	0.004	0.021	0	0.283	10.98	0.007	0.04	0.1	0.005		95.729
17-3-illite5	46.126	0.039	37.597	0.137	0	0.01	0.079	0	0.296	10.96	0.007	0.007	0.09	0		95.308
17-3-darkinillit	45.764	0	36.73	0.18	0.014	0.006	0.064	0	0.042	2.737	0.013	0.018	0.073	0.049		85.656
17-3-darkinillit	45.728	0.311	34.417	0.634	0.007	0	0.432	0	0.123	5.227	0.015	0.008	0	0		86.899
17-3-kao1	46.252	0	37.902	0.135	0	0.03	0.046	0	0.029	1.024	0.003	0.016	0.19	0.006		85.552
17-3-kao2	46.362	0.009	37.301	0.119	0.013	0	0.008	0.005	0.027	0.374	0.005	0	0.102	0		84.281
17-3-kao3	46.432	0.039	34.636	0.303	0.005	0.019	0.144	0	0.049	2.162	0.012	0	0.122	0.005		83.874
17-3-kao4	45.77	0	38.967	0.065	0.008	0.026	0.003	0.017	0.015	0.234	0.007	0	0.112	0		85.175
17-3-kao5	45.854	0	36.632	0.105	0.019	0.037	0.048	0	0.038	1.294	0.01	0	0	0		84.035
17-4-illite1	46.203	0.01	37.361	0.477	0.026	0	0.027	0	0.228	10.957	0	0.115	0.05	0		95.433
17-4-illite2	46.55	0.042	36.56	0.513	0	0	0.017	0	0.252	11.054	0	0.018	0.055	0		95.038
17-4-illite3	46.189	0.028	37.657	0.223	0	0.045	0.018	0	0.224	10.675	0	0.087	0	0.003		95.149
17-4-illite4	46.781	0.203	36.363	1.147	0	0	0.18	0	0.274	11.094	0.003	0.018	0.114	0		96.128
17-4-illite5	46.389	0.022	37.877	0.146	0.023	0	0.015	0	0.221	8.707	0.004	0.046	0.06	0.033		93.517
17-4-kao1	46.883	0	37.746	0.142	0	0.001	0.014	0	0.009	0.938	0.012	0	0.127	0.024		85.84
17-4-kao2	46.572	0	37.427	0.098	0.003	0	0.03	0	0.016	0.617	0.006	0	0.015	0		84.777
17-4-kao3	47.394	0.004	36.915	0.073	0.023	0.031	0.015	0	0.015	0.898	0.004	0	0	0		85.371
17-4-kao4	46.327	0	38.013	0.091	0.003	0.017	0.033	0	0.026	0.717	0.001	0.002	0.146	0		85.315
17-4-kao5	47.268	0.005	37.727	0.112	0.007	0	0.026	0.016	0.027	0.505	0.004	0.007	0.175	0.055		85.859
17-4-kao6	46.348	0	36.953	0.215	0.002	0	0.07	0	0.034	1.234	0.005	0.029	0	0		84.889
13-2-gm1	48.723	0.005	32.439	2.209	0.006	0	2.009	0	0.046	9.391	0.001	0.017	0.113	0.054		94.965
13-2-gm2	48.603	0	33.056	1.677	0	0.042	1.083	0	0.024	11.026	0.006	0.02	0.074	0.097		95.676
13-2-gm3	48.067	0.004	32.616	2.382	0	0	2.326	0	0.028	9.181	0.008	0.002	0.015	0		94.621
13-2-gm4	48.701	0.027	32.02	2.336	0.025	0.028	1.688	0	0.017	9.587	0.002	0	0.152	0.013		94.532
13-2-gm5	47.531	0.02	32.552	2.32	0.006	0	2.168	0	0.012	9.427	0.007	0	0.049	0.021		94.09
13-2-gm6	49.844	0.014	32.534	1.319	0.016	0.037	1.449	0	0.028	10.182	0.005	0	0.099	0		95.484
13-3-illiteb1	49.622	0.002	31.906	1.503	0.009	0.026	1.2	0	0.024	9.641	0.016	0.044	0.104	0.043		94.092
13-3-illiteb2	50.128	0.014	32.065	1.545	0.018	0.04	1.235	0	0.032	9.902	0.012	0.03	0.148	0		95.104
13-3-illiteb3	49.511	0.011	32.789	1.303	0	0	0.972	0	0.026	9.807	0.007	0	0.134	0.006		94.508
13-3-illiteb4	49.648	0.027	32.127	1.601	0	0	1.211	0	0.046	9.714	0.008	0	0.207	0		94.5
13-3-illitef1	48.951	0.003	32.942	1.597	0	0	1.142	0	0.01	10.04	0.003	0.066	0.005	0.023		94.779
13-3-illitef2	48.852	0	33.562	1.279	0.021	0	0.899	0	0.016	10.435	0.005	0.009	0.01	0		95.083
13-3-illitef3	46.505	0.012	33.462	2.343	0	0	1.865	0	0.017	8.527	0.009	0	0.029	0		92.755
13-3-illitef4	48.415	0.008	34.197	1.474	0.004	0.03	0.944	0	0.033	10.279	0.002	0.025	0.049	0		95.439
13-3-illitef5	46.707	0.003	33.703	3.009	0	0	2.273	0	0.029	9.173	0.011	0	0.194	0		95.018
13-4-ill1	49.947	0	31.954	1.646	0.003	0	1.911	0	0.08	8.449	0.013	0.006	0.088	0.008		94.065
13-4-ill2	49.601	0.013	32.301	1.487	0	0	1.533	0	0.03	9.883	0.007	0	0.192	0.032		94.996
13-4-ill3	47.527	0.03	33.389	2.079	0	0	1.602	0	0.01	9.54	0.004	0.019	0.044	0		94.224
13-4-ill4	49.521	0.015	32.335	1.539	0	0.032	1.192	0	0.026	9.857	0.007	0.035	0.163	0.032		94.683
13-4-ill5	47.419	0.052	33.245	2.275	0.005	0	2.083	0	0.024	8.565	0.01	0	0.102	0		93.735

9-1-fgill1	48.317	0.045	31.259	2.887	0.008	0.018	2.008	0	0.105	10.081	0.01	0.211	0.199	0.001		95.063
9-1-fgill2	48.909	0.002	31.194	2.656	0.034	0.031	1.747	0	0.159	9.656	0.01	0.22	0.209	0		94.737
9-1-fgill3	47.997	0.025	31.624	2.872	0.01	0.029	2.08	0	0.104	10.329	0.008	0.186	0.344	0		95.461
9-1-fgill4	48.717	0.001	31.694	2.267	0.029	0.04	2.224	0	0.097	10.257	0.011	0.213	0.186	0.007		95.663
9-1-fgill5	49.118	0.011	31.717	2.482	0.016	0.002	1.807	0	0.104	9.925	0.007	0.211	0.185	0		95.505
9-4-ill1	46.997	0.003	31.37	2.572	0.015	0	2.455	0	0.138	8.869	0.02	0.282	0.106	0		92.777
9-4-ill2	45.958	0.009	31.93	2.689	0	0	2.579	0	0.152	9.143	0.027	0.396	0.197	0.067		93.058
9-4-ill3	45.443	0.011	31.407	2.88	0.008	0.035	2.949	0	0.14	9.059	0.029	0.268	0.25	0		92.367
9-4-ill4	46.921	0.002	31.71	1.635	0.023	0	2.209	0	0.129	9.642	0.022	0.334	0.112	0.025		92.712
9-4-ill5	47.962	0.007	32.289	1.165	0	0.002	1.676	0	0.172	9.066	0.014	0.189	0.177	0.007		92.648
9-4-ill6	45.833	0.004	31.78	2.737	0.005	0	2.47	0	0.163	9.152	0.023	0.614	0.192	0.084		92.971
13-1cord1	48.254	0.032	31.979	2.064	0		1.511	0	0.135	9.322					0.021	93.318
13-1cord2	49.353	0.015	31.715	2.017	0		1.464	0	0.133	9.023					0.002	93.722
13-1cord3	49.391	0.034	31.088	2.056	0.015		1.632	0	0.111	9.179					0.025	93.531
13-1cord4	47.622	0.044	32.123	2.356	0.016		1.544	0	0.105	9.232					0.038	93.08
13-1cord5	47.664	0.027	31.58	2.105	0		1.439	0	0.131	9.115					0.015	92.076
13-1cord6	47.467	0.022	31.675	2.144	0.013		1.495	0	0.113	9.097					0	92.026
13-1black1	0.141	0.012	0.095	0.005	0		0.014	0.02	0	0.022					0	0.309
13-1black2	0.21	0	0.144	0.002	0.001		0.006	0.007	0	0.029					0.004	0.403
13-1black3	1.173	0.018	0.772	0.069	0		0.076	0.011	0.024	0.175					0.023	2.341
9-3-gt1	36.992	0.005	21.32	34.516	2.773		3.976	0.932	0	0					0.094	100.608
9-3-gt2	36.722	0	21.195	34.278	2.999		3.947	0.922	0.027	0.001					0.114	100.205
9-3-gt3	36.646	0	21.245	34.278	2.859		3.804	0.929	0.016	0					0.131	99.908
9-3-gt4	36.767	0.013	21.375	34.248	2.839		3.997	0.948	0.024	0					0.053	100.264
9-3-gt5	36.687	0	21.184	34.173	2.822		4.155	0.954	0.034	0					0.143	100.152
9-3-gt6	36.645	0	21.243	34.356	2.85		3.927	0.919	0.027	0.015					0.051	100.033
3-2-cordlight1	37.02	0	28.631	8.251	0.061		7.112	0.369	0.064	2.813					0.011	84.332
3-2-cordlight2	37.55	0.021	28.289	8.288	0.056		7.318	0.312	0.052	2.853					0	84.739
3-2-cordlight3	38.013	0	28.484	8.377	0.05		7.167	0.157	0.118	2.686					0.006	85.058
3-2-cordlight4	37.532	0	27.948	8.105	0.042		7.327	0.361	0.071	2.875					0	84.261
3-2-cordlight5	36.555	0.014	28.581	8.218	0.043		7.911	0.425	0.052	1.851					0	83.65
3-2-corddark1	37.913	0	30.257	5.386	0.045		6.631	0.365	0.064	2.106					0	82.767
3-2-corddark2	37.9	0.01	30.09	5.378	0.05		6.782	0.323	0.073	2.086					0	82.692
3-2-corddark3	38.116	0	30.301	5.506	0.052		6.974	0.338	0.079	2.079					0	83.445
3-2-corddark4	39.062	0	30.21	4.933	0.048		6.365	0.299	0.064	2.311					0	83.292
3-2-corddark5	37.97	0.027	29.825	5.443	0.04		7.053	0.357	0.046	1.943					0	82.704
3-3-gt	37.083	0.006	21.349	33.394	1.284		5.083	0.983	0.001	0					0.086	99.269
3-3-gt2	36.756	0.013	21.444	33.737	1.394		4.823	1.005	0.012	0.01					0.035	99.229
3-3-gt3	36.921	0	21.365	33.798	1.31		5.045	0.967	0.008	0.004					0.02	99.438
3-3-gt4	36.98	0.012	21.496	33.876	1.292		5.127	1.007	0.016	0					0.035	99.841
3-3-gt5	37.107	0.022	21.45	33.81	1.289		5.114	0.982	0.014	0					0.047	99.835
3-3-gt6	37.29	0	21.612	34.042	1.337		5.1	0.954	0.044	0					0.078	100.457
3-1-corddark1	38.036	0	28.803	7.7	0.043		9.15	0.466	0.011	0.885					0	85.094
3-1-corddark2	37.684	0.019	29.305	7.709	0.055		9.079	0.472	0.048	0.892					0	85.263
3-1-corddark3	37.232	0.003	28.709	8.814	0.044		9.365	0.459	0.039	0.783					0	85.448
3-1-corddark4	38.273	0	28.946	7.867	0.063		9.193	0.462	0.027	0.94					0	85.771
3-1-corddark5	38.026	0	28.745	7.621	0.068		9.629	0.46	0.035	0.61					0	85.194
3-1-cordlight1	36.939	0.006	27.747	10.028	0.084		9.438	0.477	0.016	1.081					0.03	85.846
3-1-cordlight2	37.608	0	28.84	9.345	0.081		8.151	0.402	0.043	1.735					0.036	86.241
3-1-cordlight3	38.746	0.006	28.578	8.45	0.051		7.876	0.304	0.042	2.562					0.008	86.623
3-1-cordlight4	37.024	0.015	28.204	9.503	0.057		9.106	0.459	0.005	1.193					0.002	85.568
3-1-cordlight5	36.863	0	28.947	8.961	0.072		9.287	0.481	0.041	0.954					0.047	85.653
13-3-gtchldark	37.271	0.01	32.809	2.152	0	0.011	13.184	0	0	0.796	0.015	0.042	0.028	0		86.303
13-3-chldark2	38.232	0.017	31.411	3.147	0	0	12.058	0.063	0.01	0.832	0.03	0.015	0.078	0		85.853
13-3-chldark3	37.844	0.01	32.335	3.218	0.017	0	11.265	0.048	0.006	1.04	0.027	0.013	0.073	0		85.859
13-3-chldark4	38.805	0	31.4	2.762	0.006	0.042	11.945	0	0.007	1.174	0.034	0.009	0.101	0.012		86.246
13-3-chldark5	36.355	0	32.36	2.349	0	0	13.102	0.338	0.014	0.585	0.019	0	0.055	0		85.15
13-4-chlgt1	38.488	0.009	32.061	2.362	0	0.003	11.86	0.031	0.022	1.037	0.026	0	0	0		85.893
13-4-chlgt2	38.397	0.008	32.507	2.199	0	0	11.731	0.035	0.024	1.077	0.038	0.003	0	0		86.01
13-4-chlgt3	36.651	0.006	32.014	2.4	0	0	13.977	0.006	0.01	0.418	0.043	0.014	0.041	0.005		85.558
13-4-chlgt4	38.236	0.039	32.639	2.371	0	0	11.996	0.012	0.004	1	0.034	0.032	0.051	0		86.385
13-4-chlgt5	38.149	0	32.112	2.432	0.005	0	11.872	0.009	0.015	0.925	0.033	0	0.046	0		85.572

9-1-chlbt1	27.381	0.105	21.564	25.335	0.119	0	13.991	0.015	0	0.165	0.006	0.029	0.123	0	88.78
9-1-chlbt2	28.398	0.364	21.397	23.798	0.096	0	13.351	0.003	0	0.711	0.007	0	0.163	0.027	88.244
9-1-chlbt3	26.941	0.056	21.278	25.4	0.105	0.029	14.375	0.013	0	0.029	0.006	0	0.108	0.011	88.305
9-2-chlbt1	27.501	0.058	20.833	24.985	0.108	0.019	15.206	0.008	0.008	0.021	0.002	0	0.245	0.024	88.915
9-2-chlbt2	27.61	0.104	21.124	25.309	0.138	0.077	14.708	0	0.005	0.071	0	0.023	0.164	0.012	89.276
9-2-chlbt3	28.328	0.187	20.972	24.591	0.125	0.03	14.185	0	0.019	0.438	0.01	0	0.034	0.013	88.916
9-2-chlbt4	27.766	0.068	21.279	24.905	0.131	0.034	14.646	0.017	0.007	0.221	0.003	0.035	0.198	0	89.226
9-2-chlbt5	27.956	0.134	20.848	24.956	0.098	0	14.705	0	0.016	0.125	0.001	0.019	0.187	0	88.966
9-2-chlbt6	28.367	0.095	20.81	24.687	0.132	0	14.417	0	0.001	0.272	0.002	0.041	0.176	0	88.926
9-3-chlbt1	27.158	0.04	21.047	25.253	0.126	0.028	14.791	0.003	0	0.027	0.004	0	0.27	0	88.632
9-3-chlbt2	27.664	0.072	20.739	24.712	0.166	0.067	15.174	0.031	0.007	0.06	0.009	0.039	0.146	0	88.823
9-3-chlbt3	28.368	0.309	20.869	24.126	0.117	0.03	14.408	0	0	0.656	0.01	0	0.211	0	89.013
9-3-chlbt4	31.288	0.24	22.103	21.192	0.088	0.087	12.63	0	0	1.778	0.009	0	0.219	0	89.54
9-3-chlgt1	37.409	0.283	23.641	15.815	0.142	0	9.759	0	0.021	4.078	0.005	0	0.261	0	91.303
9-3-chlgt2	41.903	0.031	30.03	9.905	0.078	0.011	5.418	0	0.1	6.839	0.065	0.012	0.063	0	94.413
9-3-chlgt3	42.657	0.025	30.221	9.854	0.078	0.006	5.357	0	0.092	6.366	0.072	0.095	0.171	0.001	94.907
9-3-chlgt4	27.508	0.015	21.505	27.296	0.426	0	12.34	0.125	0	0.069	0.013	0	0.033	0	89.313
9-3-chlgt5	33.04	0	22.687	28.831	1.649	0	8.562	0.498	0.018	0.237	0.021	0	0.077	0.035	95.618
9-3-chlgt6	24.052	0.016	21.954	39.088	0.556	0.032	5.35	0.022	0	0.016	0.086	0	0	0	91.153
3-2-bt1	35.503	4.01	19.268	19.479	0.023	0.017	9.267	0	0.098	9.309	0.078	0.047	0.407	0	97.317
3-2-bt2	35.75	4.064	19.163	19.46	0.021	0.087	8.698	0	0.136	9.91	0.066	0.019	0.306	0	97.536
3-2-bt3	37.101	2.364	24.861	14.41	0.042	0	7.108	0	0.071	6.311	0.047	0.034	0.289	0	92.505
3-2-bt4	35.101	3.925	19.796	19.18	0.055	0.036	8.899	0	0.088	9.063	0.058	0.042	0.236	0	96.367
3-2-bt5	35.8	3.957	18.972	19.685	0.055	0.058	8.951	0	0.128	9.76	0.065	0.001	0.394	0	97.645
3-3-bt1	36.306	0.455	20.157	14.615	0.022	0.015	14.795	0	0.438	8.348	0.026	0	0.601	0	95.519
3-3-bt2	36.747	0.299	20.098	14.647	0.041	0.128	14.894	0	0.338	8.711	0.016	0.087	0.643	0	96.374
3-3-bt3	35.332	2.416	19.25	18.475	0.042	0.099	10.611	0	0.15	9.543	0.057	0.06	0.521	0	96.324
3-3-bt4	36.138	1.71	18.951	18.632	0.04	0.073	11.326	0	0.131	9.508	0.059	0.1	0.446	0.014	96.927
3-3-bt5	36.822	1.609	19.095	16.597	0.051	0.048	12.493	0	0.148	9.4	0.06	0.065	0.512	0	96.67
3-1-bt	35.717	4.047	19.047	19.168	0.044	0.06	9.148	0	0.085	9.407	0.062	0.056	0.369	0	97.041
3-1-bt2	35.848	3.642	19.239	19.255	0.016	0.057	9	0	0.111	9.84	0.065	0.068	0.403	0	97.359
3-1-bt3	36.112	4.013	18.945	19.344	0.072	0.062	9.091	0	0.078	9.904	0.069	0.101	0.413	0	98.014
3-1-bt4	35.873	3.903	18.741	19.739	0.046	0.015	9.079	0	0.105	9.909	0.075	0.019	0.428	0	97.735
9-4-chl1	27.557	0.014	21.342	22.399	0.085	0.08	15.899	0.034	0.008	0.007	0.016	0.002	0.128	0	87.513
9-4-chl2	25.941	0.007	22.032	23.14	0.102	0	16.352	0	0.007	0.024	0.031	0.008	0.093	0.008	87.699
9-4-chl3	25.956	0.003	22.28	22.769	0.081	0	16.359	0	0.016	0.006	0.03	0.014	0.026	0.04	87.562
9-4-chl4	26.365	0	21.422	21.333	0.073	0.024	17.6	0.004	0	0.004	0.032	0	0.14	0	86.931
9-4-chl5	26.595	0	21.626	21.891	0.104	0	17.027	0	0.021	0.001	0.053	0	0.057	0	87.339
9-4-chl6	26.196	0	21.579	21.517	0.074	0.009	17.02	0.026	0.008	0.021	0.037	0.004	0.079	0.028	86.557

Appendix 3 Supplementary Material for Chapter 3

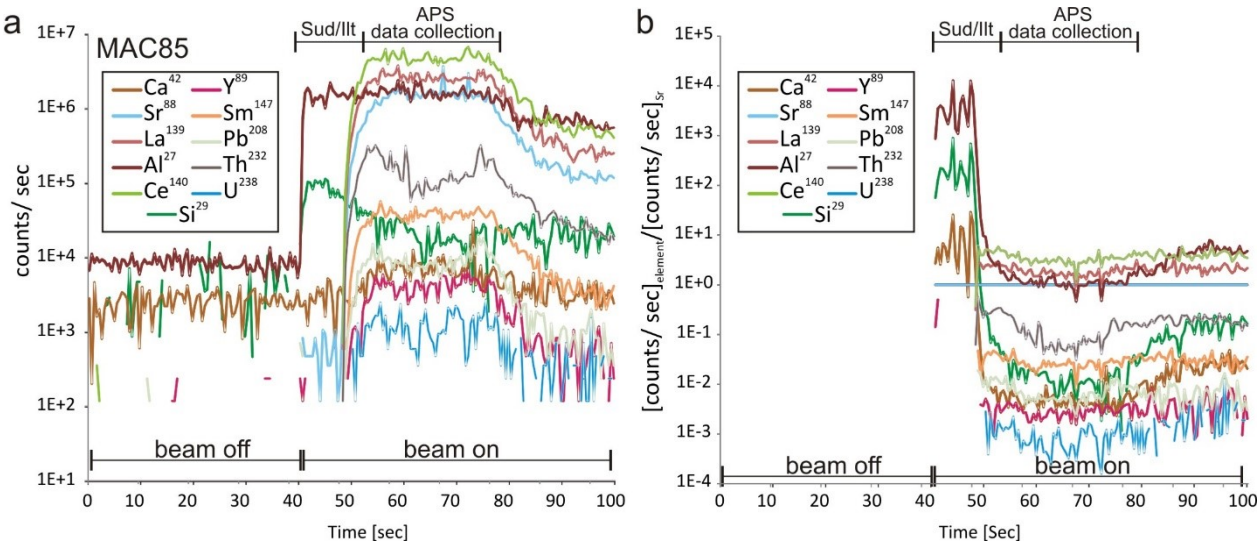

Figure A3.1. (a) A graph of the LA-ICP-MS analysis of an APS grain from sample MAC85 showing element counts (major and trace) vs. time in seconds. High counts of Y, Th and U correlate with high counts of the major elements in APS minerals (eg., Ce, La, Al, and Sr). This graph clearly shows that trace elements (such as Y, Th and U) are incorporated in the APS crystal structure and were not present as inclusions or contributed by surrounding minerals of sudoite (Sud) or illite (Ilt). **(b)** The same graph as shown in (a) but counts/sec of each element is normalized to that of Sr.

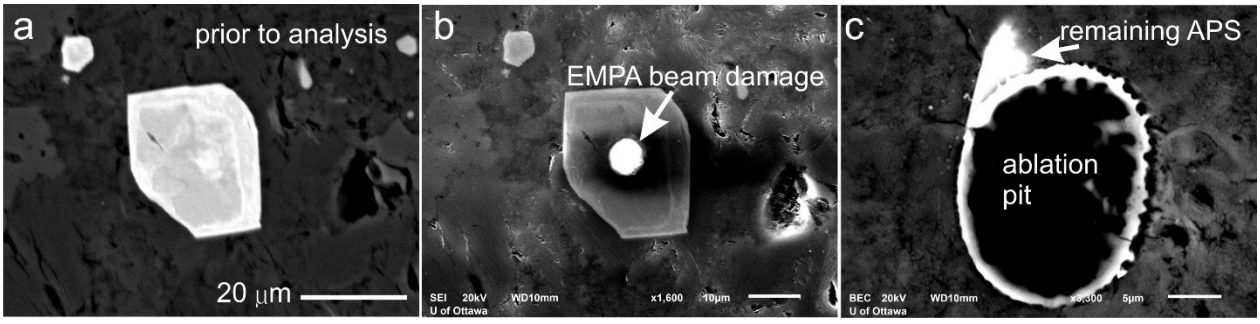

Figure A3.2. An APS mineral **(a)** before EMPA analysis and **(b)** after analysis showing beam damage. **(c)** A laser pit after LA ICP-MS analysis. (a) and (c) are BSE images and (b) is a secondary electron image.

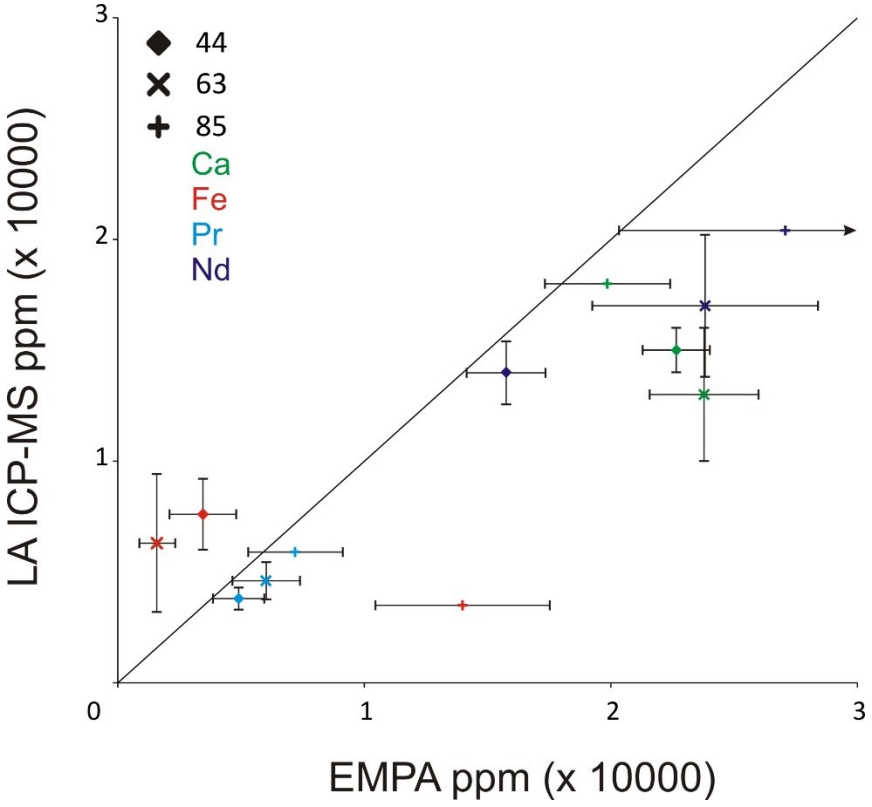

Figure A3.3. A binary plot comparing the average concentrations of Ca (green), Fe (red), Pr (cyan) and Nd (blue) in APS mineral grains from samples MAC44 (diamonds), MAC63 (x), and MAC85 (crosses) obtained with EMPA (Table 2) and LA ICP-MS (Table 3). Horizontal and vertical bars represent one standard deviation of the data (Tables 2 and 3). LA ICP-MS data of sample MAC85 is of one grain.

Table A3.1: Analytical conditions for LA ICP-MS.

energy output	40% of 4.5 mJ
laser fluence	6.42 J/cm^2
frequency	8 Hz
carrier gas flow rates	He inline 0.6 Lmin^{-1} He outline 0.4 Lmin^{-1}
gas through torch	Ar plasma 1.05 mLmin^{-1}
isotopes analyzed	^{7}Li, ^{29}Si, ^{42}Ca, ^{45}Sc, ^{49}Ti, ^{51}V, ^{53}Cr, ^{55}Mn, ^{57}Fe, ^{59}Co, ^{60}Ni, ^{65}Cu, ^{66}Zn, ^{77}Se, ^{85}Rb, ^{88}Sr, ^{89}Y, ^{90}Zr, ^{93}Nb, ^{95}Mo, ^{118}Sn, ^{137}Ba, ^{139}La, ^{140}Ce, ^{141}Pr, ^{146}Nd, ^{147}Sm, ^{151}Eu, ^{157}Gd, ^{159}Tb, ^{163}Dy, ^{165}Ho, ^{167}Er, ^{169}Tm, ^{173}Yb, ^{175}Lu, ^{177}Hf, ^{181}Ta, ^{182}W, ^{208}Pb, ^{232}Th and ^{238}U
isotope dwell times	^{27}Al, ^{29}Si and ^{42}Ca: 5 ms; all other: 8.5 ms
settle time	2.06 ms (calculated)

Appendix 4 Supplementary Material for Chapter 4

Table A4.1. Complete EPMA data set

		wt% oxide															
Tur	Sample	SiO2	TiO2	Al2O3	FeO	MnO	ZnO	MgO	CaO	Na2O	K2O	Cl	BaO	F	SrO	V2O3	Total
Tur1	85 1grcore	34.10	0.07	36.81	10.67	0.08	0.09	1.36	0.82	1.33	0.06	0.00	0.00	0.10	0.00		85.45
Tur1	85 2grcore	33.07	0.41	38.02	9.60	0.09	0.09	1.68	1.06	1.41	0.03	0.00	0.00	0.08	0.02	-	85.52
Tur1	85 2grcore2	33.75	0.62	36.18	10.54	0.09	0.11	1.76	0.93	1.31	0.05	0.01	0.00	0.13	0.01	-	85.43
Tur1	85 2grcore3	34.76	0.49	34.89	8.37	0.06	0.09	3.93	0.82	1.58	0.05	0.00	0.00	0.21	0.00	-	85.15
Tur1	85 2grcore4	35.10	0.35	34.98	7.30	0.05	0.08	4.71	0.86	1.68	0.06	0.00	0.01	0.23	0.00	-	85.29
Tur1	85 2grcore5	35.17	0.55	34.83	8.09	0.04	0.06	4.28	0.83	1.60	0.05	0.01	0.01	0.14	0.00	-	85.60
Tur1	85 2grcore6	34.91	1.30	35.10	8.41	0.07	0.05	3.51	1.00	1.38	0.05	0.00	0.02	0.26	0.01	-	85.95
Tur1	85 2grcore7	34.03	0.60	36.11	10.63	0.08	0.03	1.76	0.92	1.33	0.05	0.00	0.02	0.09	0.01	-	85.60
Tur2	109 1 drav 1	35.39	1.39	31.85	4.76	0.03	0.00	7.74	1.16	1.99	0.08	0.01	0.00	0.26	0.00	-	84.54
Tur2	109 1 drav 2	35.48	1.35	31.67	4.82	0.03	0.00	7.83	1.28	1.93	0.07	0.00	0.03	0.32	0.05	-	84.73
Tur2	109 1 drav 3	35.42	1.33	31.80	4.73	0.02	0.00	7.63	1.09	1.99	0.08	0.00	0.00	0.17	0.00	-	84.18
Tur2	109 1 drav 4	35.71	1.28	31.27	4.81	0.02	0.04	7.75	1.28	1.91	0.07	0.00	0.06	0.23	0.00	-	84.35
Tur2	109 2 drav 1	35.38	1.45	31.68	4.77	0.01	0.01	7.66	0.99	2.02	0.07	0.00	0.06	0.17	0.00	-	84.21
Tur2	109 2 drav 2	35.23	1.31	31.58	4.80	0.04	0.00	7.65	1.10	2.06	0.05	0.00	0.00	0.34	0.00	-	84.02
Tur2	109 2 drav 3	35.47	1.25	31.99	4.75	0.02	0.00	7.56	0.96	2.11	0.07	0.00	0.02	0.23	0.03	-	84.35
Tur2	109 2 drav 4	35.28	1.42	31.76	4.77	0.03	0.00	7.64	1.00	2.00	0.07	0.00	0.00	0.12	0.00	-	84.04
Tur2	109 3 drav 1	35.09	1.31	32.15	5.40	0.05	0.00	7.09	0.88	2.09	0.07	0.01	0.04	0.33	0.01	-	84.37
Tur2	109 3 drav 2	35.43	1.08	32.17	5.45	0.03	0.03	6.87	0.86	1.93	0.06	0.00	0.00	0.26	0.00	-	84.06
Tur2	109 3 drav 3	35.10	1.59	31.85	5.27	0.04	0.00	7.35	1.05	2.03	0.07	0.00	0.04	0.20	0.00	-	84.49
Tur2	109 3 drav 4	35.03	1.46	31.92	5.15	0.03	0.00	7.29	0.90	1.87	0.05	0.01	0.00	0.20	0.01	-	83.82
Tur2	201 1 drav-1 1	35.21	1.03	32.12	3.53	0.00	0.00	8.28	1.23	1.72	0.08	0.01	0.00	0.36	0.00	-	83.43
Tur2	201 1 drav-1 2	34.99	1.30	31.88	3.56	0.02	0.02	8.44	1.61	1.53	0.08	0.01	0.03	0.45	0.00	-	83.72
Tur2	201 1 drav-1 3	35.38	1.03	32.27	3.58	0.01	0.03	8.34	1.33	1.75	0.07	0.01	0.00	0.42	0.00	-	84.04
Tur2	201 1 drav-1 4	35.83	0.89	31.95	3.56	0.01	0.00	8.29	0.90	1.85	0.05	0.01	0.02	0.43	0.02	-	83.62
Tur2	201 1 drav-2 1	34.86	1.26	31.95	3.62	0.00	0.00	8.36	1.58	1.62	0.08	0.00	0.02	0.48	0.00	-	83.62
Tur2	201 1 drav-2 2	35.03	1.28	32.14	3.77	0.01	0.02	8.24	1.54	1.64	0.07	0.00	0.00	0.40	0.00	-	83.97
Tur2	201 1 drav-2 3	34.88	1.27	32.12	3.74	0.02	0.00	8.42	1.55	1.72	0.08	0.00	0.10	0.37	0.03	-	84.12
Tur2	201 1 drav-2 4	34.98	1.11	32.58	3.40	0.03	0.03	8.35	1.39	1.74	0.07	0.00	0.02	0.53	0.00	-	84.00
Tur2	201 1 drav-3 1	34.99	1.13	32.14	3.41	0.00	0.00	8.27	1.42	1.72	0.08	0.00	0.03	0.45	0.02	-	83.48
Tur2	201 1 drav-3 2	35.08	1.17	31.71	3.58	0.00	0.01	8.36	1.49	1.70	0.07	0.00	0.02	0.39	0.00	-	83.40
Tur2	201 1 drav-3 3	35.86	0.91	31.57	3.60	0.01	0.00	8.36	0.92	1.91	0.04	0.00	0.04	0.36	0.00	-	83.43
Tur2	201 1 drav-3 4	35.52	1.10	31.63	3.69	0.00	0.05	8.28	1.25	1.75	0.06	0.00	0.02	0.45	0.00	-	83.59
Tur2	201 1 drav-4 1	34.95	1.23	31.60	3.66	0.01	0.00	8.42	1.64	1.60	0.07	0.00	0.00	0.41	0.00	-	83.41
Tur2	201 1 drav-4 2	34.85	1.31	31.62	3.54	0.00	0.03	8.47	1.60	1.60	0.07	0.00	0.00	0.39	0.00	-	83.31
Tur2	201 1 drav-4 3	34.99	1.20	31.98	3.39	0.02	0.01	8.42	1.51	1.59	0.08	0.01	0.00	0.43	0.01	-	83.44
Tur2	201 1 drav-4 4	35.06	1.11	31.82	3.39	0.00	0.00	8.29	1.28	1.81	0.07	0.00	0.00	0.42	0.00	-	83.07
Tur2	201 3 drav-1 1	35.24	1.28	31.76	3.66	0.01	0.00	8.21	1.61	1.57	0.08	0.00	0.01	0.56	0.01	-	83.76
Tur2	201 3 drav-1 2	35.19	1.31	31.56	3.48	0.03	0.00	8.37	1.59	1.57	0.08	0.00	0.00	0.41	0.00	-	83.42
Tur2	201 3 drav-1 3	35.19	1.23	32.03	3.17	0.03	0.03	8.35	1.60	1.60	0.08	0.00	0.03	0.38	0.01	-	83.57
Tur2	201 3 drav-1 4	35.31	1.31	32.18	3.29	0.00	0.02	8.43	1.62	1.69	0.09	0.00	0.05	0.41	0.03	-	84.25
Tur2	201 3 drav-2 1	35.12	1.34	31.80	3.68	0.02	0.04	8.36	1.69	1.61	0.08	0.00	0.03	0.49	0.04	-	84.09
Tur2	201 3 drav-2 2	35.08	1.30	31.92	3.74	0.01	0.00	8.31	1.67	1.55	0.08	0.00	0.00	0.61	0.01	-	84.02
Tur2	201 3 drav-2 3	35.33	1.15	32.26	3.38	0.02	0.01	8.30	1.50	1.66	0.08	0.01	0.00	0.48	0.00	-	83.96
Tur2	201 3 drav-2 4	34.85	1.18	32.23	3.50	0.00	0.00	8.28	1.53	1.65	0.09	0.00	0.00	0.57	0.04	-	83.67
Tur2	201 3 drav-3 1	35.42	1.14	32.42	3.55	0.00	0.02	8.28	1.53	1.66	0.08	0.00	0.03	0.50	0.00	-	84.43
Tur2	201 3 drav-3 2	35.04	1.16	32.72	3.66	0.01	0.00	8.09	1.48	1.63	0.07	0.00	0.01	0.45	0.00	-	84.14
Tur2	201 3 drav-3 3	34.84	1.13	32.49	3.81	0.01	0.00	8.12	1.52	1.69	0.07	0.00	0.02	0.48	0.02	-	84.00
Tur2	201 3 drav-4 1	35.24	1.15	32.10	3.63	0.01	0.01	8.22	1.48	1.67	0.07	0.00	0.00	0.53	0.04	-	83.92
Tur2	201 3 drav-4 3	35.11	1.29	31.89	3.65	0.00	0.00	8.35	1.67	1.63	0.08	0.00	0.01	0.45	0.00	-	83.94
Tur2	201 3 drav-4 4	35.26	1.25	31.94	3.80	0.00	0.03	8.21	1.58	1.63	0.07	0.00	0.02	0.50	0.00	-	84.09

Tur2	111 1 dravite-2	34.94	1.25	32.21	5.13	0.01	0.00	7.12	1.31	1.72	0.08	0.00	0.02	0.26	0.01	-	83.94
Tur2	111 1 dravite-2	34.69	1.11	32.35	5.14	0.00	0.07	7.14	1.23	1.69	0.08	0.00	0.00	0.44	0.03	-	83.79
Tur2	111 1 dravite-2	34.84	1.14	32.34	5.14	0.03	0.04	7.08	1.23	1.74	0.07	0.00	0.01	0.41	0.00	-	83.89
Tur2	111 1 dravite-2	34.84	1.07	32.31	5.16	0.00	0.00	7.05	1.29	1.71	0.08	0.00	0.01	0.47	0.00	-	83.81
Tur2	111 1 dravite-1	34.67	1.21	32.42	5.23	0.02	0.05	7.11	1.42	1.68	0.07	0.00	0.03	0.52	0.01	-	84.20
Tur2	111 1 dravite-1	34.63	1.31	32.16	5.30	0.03	0.01	7.06	1.38	1.66	0.09	0.00	0.04	0.45	0.00	-	83.93
Tur2	111 1 dravite-1	34.57	1.20	32.29	5.21	0.02	0.00	7.09	1.28	1.63	0.07	0.01	0.02	0.51	0.02	-	83.69
Tur2	111 1 dravite-1	34.80	1.29	31.99	5.30	0.02	0.00	6.94	1.36	1.72	0.09	0.01	0.00	0.34	0.00	-	83.71
Tur2	99 1 dravite-1	35.59	1.25	31.88	4.47	0.01	0.00	7.64	1.32	1.84	0.07	0.00	0.03	0.68	0.03	-	84.52
Tur2	99 1 dravite-1 2	35.28	1.38	31.88	4.59	0.01	0.04	7.74	1.47	1.73	0.09	0.00	0.00	0.60	0.01	-	84.57
Tur2	99 1 dravite-1 3	35.22	1.35	31.87	4.98	0.02	0.00	7.67	1.43	1.64	0.08	0.00	0.02	0.49	0.04	-	84.60
Tur2	99 1 dravite-1 4	35.94	1.14	32.05	4.76	0.00	0.00	7.60	1.14	1.76	0.07	0.00	0.01	0.49	0.00	-	84.75
Tur2	99 1 dravite-1 5	35.59	1.31	31.47	4.59	0.05	0.00	7.75	1.45	1.71	0.06	0.00	0.01	0.61	0.00	-	84.35
Tur2	99 1 dravite-2	35.21	1.36	31.94	4.92	0.00	0.00	7.73	1.45	1.69	0.09	0.00	0.03	0.37	0.00	-	84.61
Tur2	99 1 dravite-2 2	35.69	1.16	31.63	4.88	0.05	0.04	7.69	1.18	1.87	0.04	0.00	0.05	0.52	0.02	-	84.59
Tur2	99 1 dravite-2 3	35.98	1.17	31.84	4.89	0.03	0.01	7.78	1.23	1.79	0.07	0.00	0.01	0.45	0.02	-	85.08
Tur2	99 3 dravite-1	35.45	1.31	31.98	4.92	0.00	0.00	7.59	1.41	1.63	0.07	0.00	0.01	0.63	0.00	-	84.75
Tur2	99 3 dravite-1 2	35.48	1.31	31.99	4.96	0.01	0.00	7.53	1.43	1.62	0.08	0.00	0.00	0.41	0.08	-	84.72
Tur2	99 3 dravite-1 3	36.62	0.93	31.41	4.52	0.00	0.00	7.77	0.76	2.02	0.04	0.00	0.00	0.54	0.00	-	84.39
Tur2	99 3 dravite-1 4	35.35	1.42	31.69	4.79	0.00	0.00	7.55	1.47	1.73	0.09	0.00	0.03	0.52	0.00	-	84.41
Tur2	99 3 dravite-1 5	35.51	1.38	31.36	4.71	0.02	0.06	7.66	1.47	1.68	0.08	0.00	0.00	0.55	0.08	-	84.33
Tur2	99 3 dravite-2	35.73	1.06	32.29	4.67	0.00	0.00	7.45	1.11	1.76	0.06	0.00	0.01	0.65	0.00	-	84.51
Tur2	99 3 dravite-2 2	35.29	1.38	32.02	4.88	0.02	0.02	7.54	1.47	1.71	0.07	0.00	0.00	0.45	0.03	-	84.68
Tur2	99 3 dravite-2 3	35.33	1.37	31.72	4.94	0.00	0.02	7.56	1.46	1.68	0.08	0.00	0.00	0.53	0.10	-	84.56
Tur2	99 3 dravite-2 4	35.46	1.33	31.74	5.01	0.01	0.00	7.50	1.47	1.68	0.08	0.00	0.00	0.51	0.00	-	84.58
Tur2	85 2brrim	36.09	0.77	33.57	5.58	0.05	0.04	6.56	0.83	1.84	0.06	0.00	0.00	0.45	0.00	-	85.66
Tur2	85 2brrim2	36.25	0.81	33.54	5.21	0.02	0.03	6.97	0.90	1.80	0.04	0.00	0.00	0.31	0.00	-	85.73
Tur2	85 2brrim3	36.08	0.98	33.16	5.14	0.04	0.02	7.03	0.91	1.80	0.05	0.00	0.00	0.42	0.00	-	85.45
Tur2	85 2brrim4	36.09	0.95	33.29	5.25	0.03	0.07	6.95	0.95	1.82	0.05	0.00	0.00	0.41	0.00	-	85.69
Tur2	85 2brrim5	36.04	0.97	33.08	5.33	0.01	0.06	6.91	0.95	1.80	0.07	0.00	0.00	0.41	0.02	-	85.47
Tur2	85 2brrim6	35.93	0.91	33.20	5.37	0.04	0.03	6.88	0.95	1.81	0.06	0.00	0.00	0.38	0.00	-	85.39
Tur2	85 2brrim7	35.65	0.89	34.01	5.33	0.03	0.03	6.70	0.94	1.87	0.05	0.00	0.00	0.39	0.02	-	85.73
Tur2	85 1brownrim	36.19	0.88	32.96	5.25	0.01	0.06	6.96	0.92	1.81	0.05	0.00	0.00	0.50	0.02	-	85.39
Tur2	85 1brblrim	35.45	0.24	35.41	5.16	0.00	0.01	6.34	0.89	1.89	0.05	0.00	0.00	0.36	0.00	-	85.66
Tur3	146 3 Mgf 1	33.30	0.00	36.33	0.99	0.03	-	7.11	0.17	0.45	0.00	0.01	0.02	0.02	0.01	-	78.41
Tur3	146 3 Mgf 2	34.48	0.01	34.08	1.26	0.01	-	7.01	0.13	0.60	0.01	0.01	0.01	0.03	0.02	-	77.65
Tur3	146 3 Mgf 3	36.34	0.00	34.34	1.73	0.00	-	7.44	0.07	0.92	0.04	0.01	0.00	0.07	0.00	-	80.92
Tur3	146 3 Mgf 4	36.01	0.00	34.65	1.80	0.00	-	7.48	0.08	0.94	0.03	0.00	0.05	0.05	0.00	-	81.06
Tur3	69 1 Mgf 1	36.17	0.02	35.14	0.14	0.01	-	8.60	0.10	0.65	0.05	0.03	0.02	0.12	0.00	-	81.00
Tur3	69 1 Mgf 2	35.87	0.00	35.78	0.11	0.01	-	8.59	0.09	0.55	0.02	0.01	0.00	0.06	0.02	-	81.11
Tur3	69 1 Mgf 3	36.46	0.00	35.43	0.15	0.01	-	8.71	0.12	0.69	0.02	0.02	0.00	0.10	0.00	-	81.65
Tur3	69 1 Mgf 4	35.95	0.00	35.61	0.11	0.02	-	8.60	0.09	0.59	0.03	0.02	0.00	0.05	0.00	-	81.05
Tur3	69 2 Mgf 1	36.03	0.00	35.40	0.15	0.00	-	8.61	0.11	0.60	0.05	0.03	0.00	0.06	0.01	-	81.02
Tur3	69 2 Mgf 4	35.81	0.01	35.03	0.20	0.00	-	8.63	0.12	0.61	0.04	0.02	0.03	0.09	0.02	-	80.55
Tur3	69 2 Mgf 5	36.05	0.01	34.76	0.17	0.00	-	8.91	0.08	0.56	0.01	0.02	0.00	0.04	0.06	-	80.70
Tur3	69 2 Mgf 6	36.59	0.02	34.89	0.14	0.00	-	8.96	0.07	0.62	0.05	0.05	0.00	0.00	0.00	-	81.37
Tur3	69-1-tur1	36.97	0.01	35.45	0.11	0.00	-	8.73	0.05	0.63	0.06	0.04	0.00	0.08	0.02	-	82.10
Tur3	69-1-tur2	37.35	0.00	35.19	0.10	0.00	-	8.77	0.10	0.66	0.06	0.04	0.01	0.10	0.00	-	82.33
Tur3	69-1-tur3	37.28	0.02	35.37	0.12	0.01	-	8.65	0.12	0.69	0.06	0.04	0.00	0.12	0.00	-	82.42
Tur3	69-1-tur4	37.29	0.01	35.80	0.12	0.00	-	8.70	0.11	0.73	0.02	0.02	0.00	0.13	0.00	-	82.88
Tur3	69-1-tur5	37.11	0.02	35.11	0.16	0.01	-	8.76	0.09	0.71	0.03	0.03	0.00	0.16	0.00	-	82.11
Tur3	69-1-tur6	37.37	0.00	35.27	0.12	0.00	-	8.80	0.10	0.68	0.03	0.03	0.00	0.10	0.02	-	82.47
Tur3	69-4-tur1	36.45	0.00	35.77	0.13	0.00	-	8.44	0.12	0.63	0.02	0.03	0.01	0.01	0.00	-	81.60
Tur3	69-4-tur2	37.45	0.01	35.39	0.19	0.00	-	8.44	0.14	0.74	0.01	0.04	0.00	0.08	0.00	-	82.45
Tur3	69-4-tur3	36.84	0.02	35.73	0.11	0.01	-	8.64	0.12	0.65	0.01	0.02	0.03	0.08	0.00	-	82.19
Tur3	69-4-tur4	37.07	0.01	35.68	0.17	0.01	-	8.56	0.16	0.71	0.02	0.03	0.00	0.06	0.01	-	82.49
Tur3	69-4-tur5	35.70	0.00	36.53	0.08	0.01	-	8.47	0.09	0.52	0.02	0.02	0.00	0.13	0.00	-	81.51

Tur3	69-4-tur6	36.89	0.02	35.60	0.13	0.00	-	8.51	0.18	0.68	0.02	0.03	0.00	0.14	0.00	-	82.13
Tur3	69-4-tur7	35.92	0.01	36.62	0.08	0.00	-	8.44	0.11	0.59	0.01	0.01	0.02	0.05	0.00	-	81.85
Tur3	86-1-tur	37.00	0.03	35.46	0.16	0.02	-	8.46	0.13	0.73	0.01	0.02	0.00	0.07	0.00	-	82.04
Tur3	86-1-tur2	37.33	0.01	35.46	0.12	0.00	-	8.60	0.11	0.71	0.01	0.01	0.00	0.02	0.00	-	82.36
Tur3	86-1-tur3	37.48	0.00	35.22	0.13	0.00	-	8.61	0.10	0.83	0.08	0.01	0.00	0.11	0.00	-	82.52
Tur3	86-1-tur4	37.26	0.03	35.54	0.15	0.01	-	8.39	0.12	0.80	0.00	0.01	0.00	0.06	0.00	-	82.33
Tur3	86-1-tur5	37.47	0.01	35.49	0.20	0.01	-	8.40	0.11	0.86	0.03	0.01	0.00	0.03	0.00	-	82.60
Tur3	86-1-tur6	37.71	0.03	35.40	0.13	0.00	-	8.65	0.10	0.90	0.02	0.01	0.02	0.02	0.00	-	82.98
Tur3	86-1-tur7	37.50	0.02	35.71	0.11	0.00	-	8.56	0.12	0.72	0.01	0.01	0.00	0.05	0.00	-	82.80
Tur3	86-2-tur1	37.20	0.01	35.35	0.14	0.00	-	8.51	0.12	0.80	0.02	0.02	0.00	0.13	0.00	-	82.24
Tur3	86-2-tur2	37.91	0.00	35.18	0.11	0.00	-	8.67	0.10	0.86	0.02	0.01	0.00	0.00	0.00	-	82.87
Tur3	86-2-tur3	37.71	0.03	35.21	0.12	0.01	-	8.57	0.12	0.80	0.01	0.02	0.00	0.11	0.02	-	82.69
Tur3	86-2-tur4	37.53	0.01	35.41	0.15	0.01	-	8.44	0.13	0.76	0.01	0.02	0.03	0.06	0.01	-	82.53
Tur3	86-2-tur5	37.48	0.01	35.62	0.14	0.01	-	8.41	0.10	0.69	0.01	0.02	0.00	0.01	0.00	-	82.52
Tur3	86-2-tur6	38.09	0.01	35.10	0.14	0.02	-	8.76	0.10	0.83	0.03	0.01	0.03	0.01	0.00	-	83.13
Tur3	86-4-tur1	37.81	0.00	35.98	0.08	0.01	-	8.54	0.03	0.63	0.00	0.00	0.00	0.02	0.02	-	83.12
Tur3	86-4-tur2	36.21	0.01	36.38	0.08	0.00	-	8.31	0.08	0.41	0.01	0.00	0.00	0.01	0.00	-	81.51
Tur3	86-4-tur3	37.52	0.00	35.51	0.06	0.00	-	8.47	0.02	0.35	0.02	0.00	0.00	0.03	0.01	-	81.96
Tur3	86-4-tur5	37.54	0.00	34.39	0.09	0.00	-	8.75	0.02	0.80	0.00	0.01	0.00	0.01	0.05	-	81.67
Tur3	86-4-tur4	38.11	0.01	34.63	0.20	0.00	-	8.95	0.03	0.61	0.01	0.00	0.01	0.05	0.02	-	82.60
Tur3	86-4-tur6	37.99	0.01	35.58	0.12	0.01	-	8.87	0.03	0.63	0.01	0.00	0.01	0.00	0.00	-	83.25
Tur3	86-4-tur7	37.39	0.00	35.69	0.07	0.00	-	8.61	0.03	0.57	0.00	0.00	0.00	0.00	0.00	-	82.37
Tur3	70_1_tur1	36.16	0.01	35.45	0.10	0.00	-	8.35	0.10	0.64	0.03	0.01	0.00	0.06	0.02	-	80.91
Tur3	70_1_tur2	35.28	0.01	35.62	0.07	0.00	-	8.24	0.09	0.51	0.03	0.02	0.00	0.02	0.01	-	79.89
Tur3	70_1_tur3	37.23	0.03	34.99	0.15	0.02	-	8.48	0.12	0.71	0.00	0.02	0.00	0.12	0.06	-	81.88
Tur3	70_1_tur4	37.00	0.00	35.35	0.11	0.00	-	8.44	0.13	0.67	0.03	0.01	0.02	0.01	0.00	-	81.77
Tur3	70_1_tur5	36.92	0.01	35.34	0.10	0.02	-	8.42	0.12	0.67	0.03	0.01	0.01	0.06	0.00	-	81.68
Tur3	70_2_tur1	35.64	0.00	36.75	0.08	0.00	-	8.24	0.11	0.48	0.03	0.01	0.00	0.06	0.00	-	81.37
Tur3	70_2_tur2	36.95	0.01	36.21	0.11	0.00	-	8.44	0.13	0.57	0.02	0.01	0.02	0.00	0.00	-	82.47
Tur3	70_2_tur3	37.25	0.03	35.81	0.08	0.00	-	8.35	0.12	0.65	0.01	0.01	0.04	0.17	0.00	-	82.44
Tur3	70_2_tur4	36.45	0.01	36.40	0.08	0.01	-	8.49	0.13	0.53	0.02	0.01	0.01	0.06	0.00	-	82.17
Tur3	70_2_tur5	37.87	0.02	35.57	0.13	0.00	-	8.49	0.08	0.74	0.23	0.01	0.00	0.00	0.03	-	83.15
Tur3	70_3_tur1	37.09	0.01	36.05	0.14	0.00	-	8.37	0.13	0.66	0.01	0.02	0.03	0.02	0.07	-	82.59
Tur3	70_3_tur2	37.50	0.02	35.35	0.10	0.00	-	8.52	0.12	0.69	0.03	0.02	0.00	0.09	0.02	-	82.41
Tur3	70_3_tur3	37.30	0.00	35.22	0.09	0.01	-	8.64	0.07	0.65	0.03	0.02	0.00	0.05	0.01	-	82.07
Tur3	70_3_tur4	37.00	0.02	35.57	0.07	0.00	-	8.62	0.11	0.60	0.05	0.02	0.01	0.05	0.00	-	82.10
Tur3	70_3_tur5	36.13	0.01	36.49	0.07	0.00	-	8.41	0.11	0.53	0.06	0.03	0.02	0.11	0.01	-	81.93
Tur3	70_3_tur6	35.86	0.03	36.61	0.12	0.00	-	8.28	0.13	0.56	0.02	0.02	0.00	0.03	0.00	-	81.64
Tur3	122 1 Mgf 1	33.99	0.02	32.45	2.36	0.00	-	6.93	0.04	0.92	0.02	0.02	0.00	0.30	0.00	-	76.92
Tur3	122 1 Mgf 2	34.70	0.00	34.56	1.87	0.00	-	7.01	0.05	0.74	0.00	0.01	0.00	0.08	0.09	-	79.07
Tur3	122 1 Mgf 4	34.43	0.00	32.86	2.06	0.01	-	6.93	0.06	0.83	0.01	0.02	0.02	0.17	0.00	-	77.33
Tur3	201 4 Mgf-1 2	37.13	0.00	34.80	0.16	0.01	-	8.56	0.02	0.57	0.00	0.00	0.00	0.00	0.00	-	81.26
Tur3	201 4 Mgf-1 3	37.49	0.00	34.42	0.23	0.00	-	8.55	0.01	0.67	0.01	0.01	0.01	0.00	0.04	-	81.45
Tur3	201 4 Mgf-1 4	37.25	0.00	34.64	0.21	0.00	-	8.49	0.03	0.56	0.01	0.00	0.00	0.01	0.01	-	81.21
Tur3	201 4 Mgf-1 5	37.47	0.00	34.87	0.21	0.00	-	8.44	0.01	0.61	0.00	0.00	0.01	0.11	0.00	-	81.69
Tur3	201 4 Mgf-2 1	37.74	0.02	34.93	0.25	0.00	-	8.58	0.00	0.66	0.02	0.00	0.00	0.00	0.00	-	82.20
Tur3	201 4 Mgf-2 2	37.56	0.00	35.31	0.17	0.01	-	8.41	0.01	0.62	0.03	0.00	0.05	0.12	0.00	-	82.23
Tur3	201 5 Mgf-2 1	37.47	0.02	32.53	0.24	0.01	-	8.90	0.03	0.72	0.02	0.00	0.01	0.07	0.02	-	80.01
Tur3	32-1-1tur1	33.15	0.00	38.39	0.67	0.00	-	7.42	0.26	0.43	0.00	0.00	0.00	0.01	0.00	-	80.33
Tur3	32-1-1tur2	33.20	0.00	38.48	0.70	0.00	-	7.48	0.22	0.44	0.00	0.00	0.00	0.04	0.00	-	80.55
Tur3	32-1-1tur3	33.23	0.00	37.87	0.64	0.00	-	7.65	0.22	0.42	0.00	0.01	0.00	0.00	0.00	-	80.06
Tur3	32-1-1tur4	32.55	0.00	38.11	0.70	0.00	-	7.30	0.26	0.44	0.00	0.01	0.00	0.14	0.00	-	79.45
Tur3	32-1-1tur5	32.73	0.01	38.23	0.76	0.00	-	7.28	0.28	0.46	0.00	0.02	0.01	0.02	0.01	-	79.79
Tur3	32-3-tur1	35.10	0.00	37.59	0.86	0.01	-	7.47	0.16	0.63	0.01	0.01	0.01	0.13	0.05	-	81.96
Tur3	32-3-tur2	35.26	0.00	37.16	0.98	0.00	-	7.59	0.17	0.61	0.02	0.01	0.01	0.01	0.00	-	81.81
Tur3	32-3-tur3	33.59	0.00	37.84	0.87	0.00	-	7.31	0.25	0.51	0.02	0.01	0.02	0.07	0.00	-	80.46
Tur3	32-3-tur4	33.18	0.01	37.83	0.78	0.00	-	7.26	0.25	0.49	0.00	0.01	0.02	0.09	0.05	-	79.94
Tur3	32-3-tur5	32.85	0.01	38.18	0.68	0.00	-	7.31	0.25	0.49	0.00	0.01	0.00	0.07	0.00	-	79.83
Tur3	32-3-tur6	34.46	0.01	37.44	0.97	0.00	-	7.39	0.22	0.56	0.01	0.02	0.00	0.14	0.00	-	81.17

Tur3	29-6-tur1	35.54	0.02	37.00	1.27	0.00	-	7.89	0.11	0.57	0.00	0.01	0.02	0.01	0.00	-	82.43
Tur3	29-6-tur2	35.79	0.02	36.37	1.17	0.00	-	7.96	0.08	0.55	0.01	0.01	0.01	0.09	0.04	-	82.07
Tur3	29-6-tur3	36.50	0.01	36.21	1.30	0.01	-	7.99	0.08	0.65	0.01	0.01	0.01	0.07	0.00	-	82.83
Tur3	29-6-tur4	35.94	0.00	37.82	1.11	0.00	-	7.69	0.09	0.44	0.00	0.00	0.00	0.05	0.10	-	83.22
Tur3	99 2 mgf2	36.55	0.01	34.44	1.63	0.00	0.01	7.27	0.08	0.78	0.05	0.01	0.00	0.09	0.00	-	80.88
Tur3	99 2 mgf3	35.28	0.00	31.61	1.40	0.01	0.00	7.01	0.05	0.61	0.00	0.01	0.00	0.36	0.00	-	76.06
Tur3	423 1a	35.82	0.00	37.60	0.05	0.01	0.01	8.27	0.10	0.43	0.00	0.00	0.00	0.00	0.00	0.23	82.52
Tur3	423 1b	36.72	0.00	37.64	0.08	0.00	0.00	8.64	0.10	0.47	0.02	0.00	0.00	0.00	0.00	0.20	83.88
Tur3	423 1c	36.47	0.00	37.57	0.09	0.00	0.01	7.74	0.13	0.44	0.11	0.00	0.00	0.01	0.00	0.25	82.81
Tur3	423 1e	38.69	0.01	34.95	0.17	0.00	0.00	8.68	0.06	0.53	0.03	0.00	0.00	0.00	0.00	0.23	83.33
Tur3	423-m2	38.58	0.01	35.95	0.48	0.00	0.02	8.89	0.09	0.49	0.05	0.01	0.00	0.01	0.02	-	84.59
Tur3	423-m3	37.95	0.01	35.27	0.12	0.02	0.00	9.31	0.04	0.58	0.00	0.00	0.00	0.01	0.02	-	83.34
Tur3	423-m4	37.28	0.02	35.21	0.29	0.00	0.00	9.15	0.06	0.53	0.02	0.01	0.00	0.00	0.00	-	82.57
Tur3	423-m5	38.07	0.01	35.49	0.27	0.00	0.00	8.06	0.11	0.52	0.07	0.00	0.00	0.00	0.01	-	82.61
Tur3	423-m6	38.11	0.02	36.31	0.07	0.00	0.00	9.08	0.05	0.53	0.02	0.00	0.00	0.07	0.01	-	84.25
Tur3	425 1c	35.41	0.02	39.39	0.58	0.01	0.00	6.53	0.20	0.33	0.06	0.01	0.01	0.04	0.00	0.23	82.80
Tur3	425 1d	38.24	0.00	36.42	0.27	0.01	0.00	8.12	0.13	0.54	0.03	0.01	0.00	0.00	0.00	0.27	84.04
Tur3	425-m1	38.12	0.01	36.09	0.84	0.00	0.00	5.18	0.28	0.33	0.30	0.01	0.01	0.08	0.02	-	81.21
Tur3	425-m3	35.43	0.01	37.63	0.15	0.01	0.02	8.07	0.15	0.42	0.02	0.02	0.00	0.04	0.03	-	81.95
Tur3	425-m4	37.72	0.00	38.04	0.16	0.02	0.00	8.40	0.10	0.48	0.06	0.00	0.01	0.02	0.00	-	84.98
Tur3	425-m5	35.91	0.00	37.67	0.32	0.00	0.00	7.40	0.17	0.42	0.04	0.01	0.00	0.00	0.02	-	81.95
Tur3	425-m6	36.53	0.00	36.87	0.70	0.02	0.00	7.35	0.21	0.40	0.25	0.01	0.00	0.00	0.00	-	82.33
Tur3	425-m7	37.71	0.01	33.88	1.77	0.01	0.07	6.79	0.23	0.38	0.11	0.03	0.00	0.12	0.00	-	81.05
Tur3	110-m1	39.08	0.01	36.21	1.16	0.00	0.06	8.52	0.02	0.52	0.02	0.00	0.00	0.05	0.00	-	85.62
Tur3	110-m2	38.80	0.00	36.13	1.11	0.00	0.01	8.64	0.03	0.48	0.01	0.00	0.00	0.00	0.00	-	85.20
Tur3	110-m3	39.20	0.01	36.48	1.01	0.01	0.03	8.52	0.02	0.44	0.02	0.01	0.00	0.07	0.00	-	85.77
Tur3	110-m4	39.04	0.00	35.46	0.98	0.00	0.00	8.78	0.03	0.78	0.01	0.00	0.00	0.27	0.04	-	85.27
Tur3	110-m5	38.46	0.00	36.09	1.12	0.00	0.00	8.51	0.03	0.49	0.01	0.00	0.00	0.08	0.02	-	84.79
Tur3	110-m6	38.89	0.00	36.70	0.73	0.02	0.00	8.65	0.02	0.40	0.00	0.00	0.00	0.06	0.00	-	85.45
Tur3	110-m7	38.50	0.01	35.80	2.24	0.01	0.00	7.94	0.04	0.50	0.00	0.01	0.00	0.18	0.05	-	85.19
Tur3	110-m8	38.45	0.01	35.87	2.25	0.00	0.01	8.05	0.04	0.50	0.01	0.00	0.01	0.14	0.00	-	85.29
Tur3	110-m9	38.48	0.00	36.17	2.41	0.03	0.00	7.66	0.02	0.48	0.01	0.00	0.00	0.20	0.03	-	85.41
Tur3	110-m10	39.33	0.00	36.76	1.12	0.02	0.00	8.22	0.00	0.33	0.01	0.00	0.00	0.05	0.00	-	85.82
Tur3	110-m11	38.38	0.00	36.69	1.11	0.00	0.00	8.30	0.05	0.48	0.01	0.00	0.00	0.25	0.00	-	85.15
Tur3	462 m3	37.13	0.01	36.90	0.19	0.02	0.00	7.89	0.14	0.78	0.16	0.01	0.00	0.21	0.00	-	83.35
Tur3	462 m4	37.59	0.00	37.40	0.16	0.02	0.00	8.01	0.11	0.71	0.06	0.01	0.00	0.12	0.00	-	84.14
Tur3	462 m5	37.12	0.01	36.40	0.17	0.00	0.00	7.96	0.14	0.77	0.08	0.01	0.01	0.14	0.04	-	82.80
Tur3	462 m7	35.59	0.01	37.42	0.13	0.01	0.02	8.01	0.15	0.63	0.04	0.01	0.00	0.15	0.01	-	82.10
Tur3	462 m9	37.04	0.00	34.92	0.24	0.00	0.00	8.06	0.14	0.86	0.11	0.01	0.00	0.09	0.00	-	81.44
Tur3	462 m10	36.19	0.01	36.49	0.15	0.01	0.00	8.06	0.12	0.69	0.07	0.01	0.00	0.15	0.00	-	81.89
Tur3	462 m12	37.68	0.01	36.81	0.16	0.00	0.02	8.32	0.13	0.86	0.06	0.01	0.00	0.12	0.00	-	84.13
Tur3	462 m13	37.17	0.01	36.57	0.15	0.00	0.00	8.17	0.12	0.89	0.02	0.01	0.00	0.11	0.00	-	83.17
Tur3	462 m14	37.13	0.02	35.79	0.21	0.00	0.00	8.30	0.10	0.98	0.06	0.01	0.00	0.09	0.00	-	82.65
Tur3	436 m1	37.60	0.02	36.18	0.67	0.01	0.00	9.11	0.08	0.63	0.21	0.02	0.00	0.06	0.01	-	84.57
Tur3	436 m2	37.97	0.03	36.68	0.60	0.01	0.00	8.48	0.07	0.67	0.08	0.01	0.00	0.09	0.00	-	84.64
Tur3	436 m3	37.54	0.00	36.92	0.60	0.00	0.00	8.26	0.09	0.74	0.05	0.03	0.01	0.02	0.00	-	84.24
Tur3	436 m4	37.30	0.01	37.04	0.31	0.00	0.00	8.01	0.12	0.65	0.01	0.04	0.00	0.08	0.00	-	83.55
Tur3	436 m5	37.89	0.01	37.00	0.44	0.00	0.00	8.13	0.12	0.77	0.02	0.10	0.00	0.10	0.02	-	84.52
Tur3	436 m6	38.00	0.01	36.86	0.50	0.02	0.00	8.32	0.09	0.66	0.03	0.04	0.00	0.10	0.00	-	84.58
Tur3	436 m7	38.02	0.01	36.96	0.29	0.00	0.00	8.05	0.10	0.64	0.02	0.03	0.00	0.07	0.07	-	84.23
Tur3	436 m8	37.84	0.03	36.61	0.45	0.00	0.04	8.28	0.11	0.71	0.02	0.04	0.03	0.04	0.00	-	84.17
Tur3	436 m9	37.41	0.03	36.90	0.29	0.02	0.04	8.17	0.13	0.66	0.01	0.05	0.02	0.15	0.02	-	83.82
Tur3	436 m10	37.33	0.01	37.20	0.27	0.00	0.05	8.10	0.12	0.61	0.02	0.04	0.01	0.00	0.02	-	83.76

Tur3	440 m2	37.63	0.01	37.25	0.35	0.04	0.00	8.01	0.10	0.57	0.01	0.02	0.00	0.10	0.03	-	84.05
Tur3	440 m3	37.48	0.00	37.05	0.36	0.00	0.01	7.79	0.10	0.63	0.02	0.01	0.00	0.04	0.00	-	83.47
Tur3	440 m4	37.34	0.01	36.97	0.38	0.00	0.00	7.74	0.09	0.69	0.02	0.01	0.00	0.00	0.00	-	83.25
Tur3	440 m5	37.20	0.01	37.71	0.26	0.00	0.00	7.98	0.13	0.52	0.01	0.02	0.00	0.11	0.03	-	83.94
Tur3	440 m6	37.18	0.01	36.11	0.27	0.02	0.00	7.84	0.10	0.54	0.00	0.01	0.00	0.15	0.00	-	82.17
Tur3	440 m9	37.12	0.01	35.13	0.46	0.02	0.00	7.54	0.12	0.57	0.00	0.02	0.00	0.09	0.00	-	81.02

(-) = not analysed

Appendix 5 Supplementary Material for Chapter 5

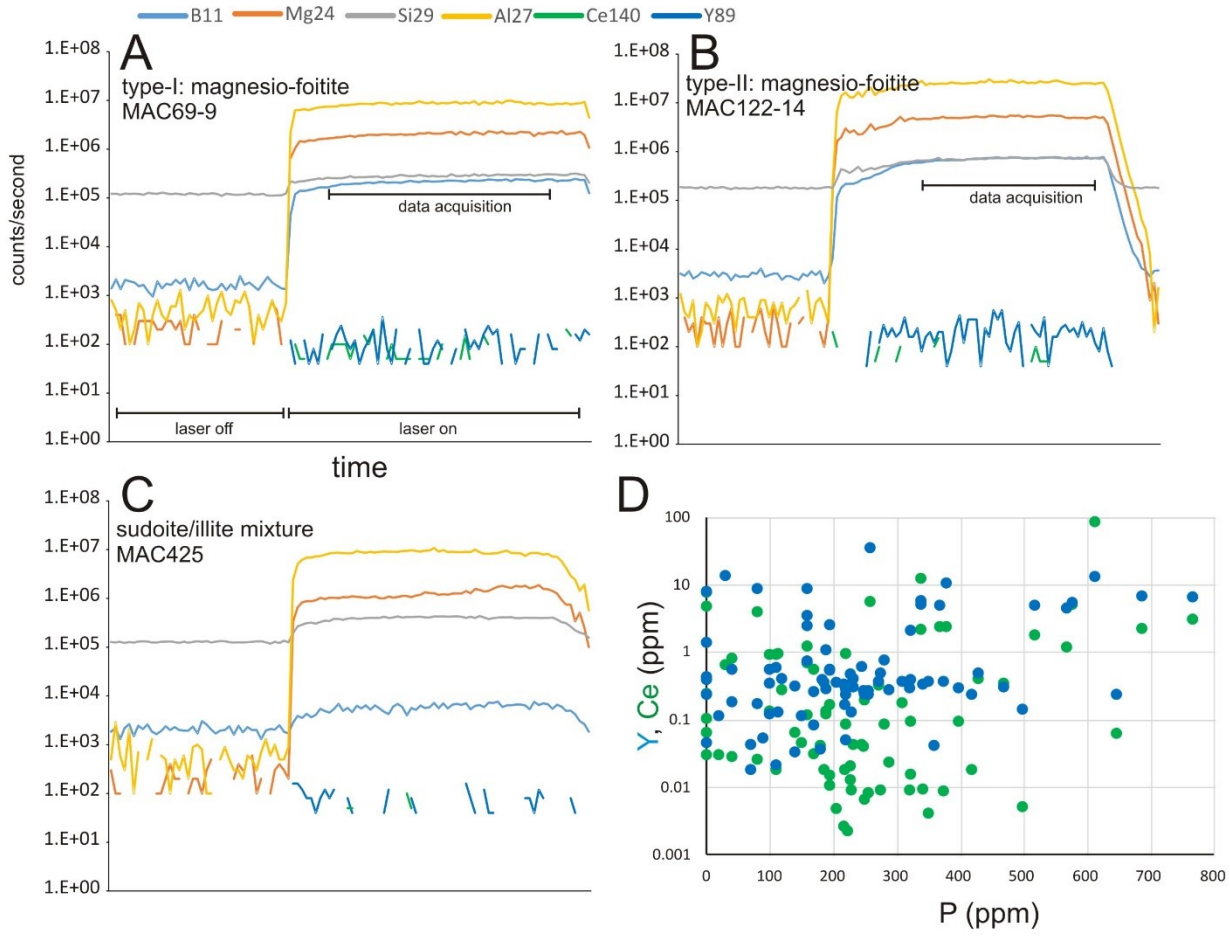

Figure A5.1: Time vs counts per second plots of LA-ICPMS results for **A)** *type-I* magnesio-foitite in MAC69, **B)** type-II magnesio-foitite in MAC122 and **C)** sudoite/illite mixture in MAC425. Plot **(D)** of P vs. Ce (green) and Y (blue) indicates no correlation between P and REE; therefore, phosphate inclusions or intergrain mineral did not contribute REE to the data.

Table A5.1: Running conditions of LA-ICP-MS system used for Mgf analysis

Laser	
Model	COMPexPro 102 F 193 nm excimer laser
Laser energy used	60 mJ
BDU Demag positior	35x
Laser fluence	~6 J/cm^2
Repetition rate	3 Hz
Spot diameter	26 - 46 microns
Ablation time (seconds)	30s background, 40s mineral ablation
Standards used	NIST610 (primary concentration standard) NIST612 (secondary concentration standard) BCR-2G (QC standard)
ICP-MS	
Model	Agilent 7700
RF power	1550 W
Sampling depth (Torch position)	5.5 mm
Carrier gas (Ar)	0.93 L/min
U/Th	~104%
ThO/Th	<0.2%
22/44 (Doubly charged ion ratio)	<0.3%
Tuning protocol	Tuned for full suite of elements (7, 89, 207 monitored during tuning)
Gas flow rate (ablation cell)	He (300 ml/min), N2 (2 ml/min) 2nd pump used (increases sensitivity)
Data acquisition parameters	
Protocol	Time resolved analysis
Sampling time	0.6202 seconds
Dwell time per isotope (sec)	^{7}Li(0.02), ^{45}Sc(0.025), ^{51}V(0.025), ^{52}Cr(0.025), ^{89}Y(0.025), ^{139}La(0.02), ^{140}Ce(0.02), ^{141}Pr(0.02), ^{146}Nd(0.02), ^{147}Sm(0.02), ^{151}Eu(0.02), ^{157}Gd(0.02), ^{159}Tb(0.02), ^{163}Dy(0.02), ^{165}Ho(0.02), ^{166}Er(0.02), ^{169}Tm(0.02), ^{172}Yb(0.02), ^{175}Lu(0.02), ^{182}W(0.025)

Table A5.2: LAICPMS results for magnesio-foitite (ppm)

Type	O	Measurement	Y_N/Ce_N	ΣREE*	Eu/Eu*	Y	La	Ce	Pr	Nd	Sm	Eu	Gd	Tb	Dy	Ho	Er	Tm	Yb	Lu	Li	Sc	V	Cr	W
LOD						0.06	0.02	0.02	0.02	0.2	0.2	0.07	0.2	0.03	0.06	0.03	0.11	0.01	0.06	0.03	4	0.4	0.4	1.4	0.05
II	vnlt	MAC146-1	>1	0.379		0.436	<0.02	<0.02	<0.02	<0.2	<0.2	<0.07	<0.2	0.052	0.156	<0.03	<0.11	<0.01	<0.06	<0.03	nd	28.7	104	9	0.078
II	vnlt	MAC146-2	5.92	0.505		0.67	<0.02	0.046	<0.02	<0.2	<0.2	<0.07	<0.2	0.05	0.24	<0.03	<0.11	<0.01	<0.06	<0.03	nd	26.9	94.1	8	0.094
II	vnlt	MAC146-3	6.68	0.519		0.526	<0.02	0.032	<0.02	<0.2	<0.2	<0.07	<0.2	0.051	0.29	<0.03	<0.11	<0.01	<0.06	<0.03	nd	24.73	76.6	8.9	0.254
II	vnlt	MAC146-4	9.40	0.444		0.74	<0.02	0.032	<0.02	<0.2	<0.2	<0.07	<0.2	0.051	0.28	<0.03	<0.11	<0.01	<0.06	<0.03	nd	25.6	91.4	20.4	0.205
II	vnlt	MAC146-5	>1	0.142		0.429	<0.02	<0.02	<0.02	<0.2	<0.2	<0.07	<0.2	<0.03	0.093	<0.03	<0.11	<0.01	<0.06	<0.03	nd	27.6	110	7.8	0.16
II	vnlt	MAC146-6	25.15	0.233		0.427	<0.02	0.007	<0.02	<0.2	<0.2	<0.07	<0.2	<0.03	0.159	<0.03	<0.11	<0.01	<0.06	<0.03	nd	28.66	105.9	7.9	0.117
II	vnlt	MAC146-7	6.78	0.362		0.467	<0.02	0.028	<0.02	<0.2	<0.2	<0.07	<0.2	0.041	0.094	<0.03	<0.11	<0.01	0.107	<0.03	nd	27.15	106.7	13.8	0.009
II	vnlt	MAC146-8	12.01	0.447		0.65	<0.02	0.022	<0.02	<0.2	<0.2	<0.07	<0.2	0.04	0.24	<0.03	<0.11	<0.01	<0.06	<0.03	nd	23.37	90.8	14.3	0.158
II	vnlt	MAC146-9	11.43	0.797		0.619	<0.02	0.022	<0.02	<0.2	<0.2	<0.07	<0.2	0.084	0.25	<0.03	<0.11	<0.01	<0.06	<0.03	nd	24.13	82.6	10.6	0.008
II	vnlt	MAC146-10	6.66	0.503		0.82	<0.02	0.05	<0.02	<0.2	<0.2	<0.07	<0.2	0.042	0.3	<0.03	<0.11	<0.01	<0.06	<0.03	nd	25.44	90.6	19.3	0.095
II	vnlt	MAC146-11	8.53	1.229		1.05	<0.02	0.05	<0.02	<0.2	<0.2	<0.07	<0.2	0.073	0.5	<0.03	<0.11	<0.01	<0.06	<0.03	nd	23.23	79.3	13.9	0.098
II	vnlt	MAC146-12	13.41	0.553		0.528	<0.02	0.016	<0.02	<0.2	<0.2	<0.07	<0.2	0.085	0.3	<0.03	<0.11	<0.01	<0.06	<0.03	nd	22.97	77.1	9.2	0.068
II	vnlt	MAC146-13	>1	0.357		0.384	<0.02	<0.02	<0.02	<0.2	<0.2	<0.07	<0.2	0.037	0.173	<0.03	<0.11	<0.01	<0.06	<0.03	nd	27.96	112	11.6	0.094
II	vnlt	MAC146-14	15.61	0.475		0.73	<0.02	0.019	<0.02	<0.2	<0.2	<0.07	<0.2	0.064	0.25	<0.03	<0.11	<0.01	<0.06	<0.03	nd	25.56	92.1	21	0.111
II	vnlt	MAC146-15	7.31	0.374		0.54	<0.02	0.03	<0.02	<0.2	<0.2	<0.07	<0.2	<0.03	0.31	<0.03	<0.11	<0.01	<0.06	<0.03	nd	24.2	95.1	12.5	0.144
II	vnlt	MAC122-1	>1	0.075		0.382	<0.02	<0.02	<0.02	<0.2	<0.2	<0.07	<0.2	<0.03	<0.06	<0.03	<0.11	<0.01	0.075	<0.03	10.3	11.43	111.9	31.8	0.074
II	vnlt	MAC122-2	5.76	0.182		0.595	<0.02	0.042	<0.02	<0.2	<0.2	<0.07	<0.2	<0.03	0.106	<0.03	<0.11	<0.01	<0.06	<0.03	10.5	12.28	99.8	27.4	0.112
II	vnlt	MAC122-3	>1	0.101		0.466	<0.02	<0.02	<0.02	<0.2	<0.2	<0.07	<0.2	<0.03	0.101	<0.03	<0.11	<0.01	<0.06	<0.03	9.3	11.1	106.4	29.3	0.066
II	vnlt	MAC122-4	>1	0.13		0.254	<0.02	<0.02	<0.02	<0.2	<0.2	<0.07	<0.2	<0.03	0.082	<0.03	<0.11	<0.01	<0.06	<0.03	10.8	11.46	116.1	33.1	0.147
II	vnlt	MAC122-5	>1	0.165		0.287	<0.02	<0.02	<0.02	<0.2	<0.2	<0.07	<0.2	<0.03	0.109	<0.03	<0.11	<0.01	<0.06	<0.03	13.1	8.5	98.5	34.7	0.087
II	vnlt	MAC122-6	>1	0		0.327	<0.02	<0.02	<0.02	<0.2	<0.2	<0.07	<0.2	<0.03	<0.06	<0.03	<0.11	<0.01	<0.06	<0.03	11.1	10.22	103.6	33.5	0.068
II	vnlt	MAC122-7	>1	0		0.23	<0.02	<0.02	<0.02	<0.2	<0.2	<0.07	<0.2	<0.03	<0.06	<0.03	<0.11	<0.01	<0.06	<0.03	10.6	10.01	113.1	33.4	0.064
II	vnlt	MAC122-8	>1	0.07		0.265	<0.02	<0.02	<0.02	<0.2	<0.2	<0.07	<0.2	<0.03	0.07	<0.03	<0.11	<0.01	<0.06	<0.03	9.1	10.12	106.2	32.1	0.056
II	vnlt	MAC122-9	>1	0.037		0.354	<0.02	<0.02	<0.02	<0.2	<0.2	<0.07	<0.2	<0.03	<0.06	<0.03	<0.11	<0.01	<0.06	<0.03	14.3	12.7	102.4	26.7	0.15
II	vnlt	MAC122-10	>1	0		0.163	<0.02	<0.02	<0.02	<0.2	<0.2	<0.07	<0.2	<0.03	<0.06	<0.03	<0.11	<0.01	<0.06	<0.03	11.4	12.12	107.3	27.3	0.101
II	vnlt	MAC122-11	3.63	0.541		0.76	<0.02	0.085	<0.02	<0.2	<0.2	<0.07	<0.2	<0.03	0.127	0.036	<0.11	<0.01	0.126	<0.03	11.6	10.75	103.3	26.3	0.092
II	vnlt	MAC122-12	8.91	1.79		2.06	<0.02	0.094	0.037	0.268	0.23	<0.07	<0.2	0.036	0.368	0.061	0.153	0.03	0.253	<0.03	24.6	12.05	107.6	29.7	0.091
II	vnlt	MAC122-13	>1	0.184		0.36	<0.02	<0.02	<0.02	<0.2	<0.2	<0.07	<0.2	<0.03	0.184	<0.03	<0.11	<0.01	<0.06	<0.03	9.6	7.56	84.7	31.2	0.064
II	vnlt	MAC122-14	>1	0.133		0.314	<0.02	<0.02	<0.02	<0.2	<0.2	<0.07	<0.2	<0.03	0.094	<0.03	<0.11	<0.01	<0.06	<0.03	10.2	9.81	101.4	29.3	<0.05
II	vnlt	MAC122-15	6.17	1.865		2.49	<0.02	0.164	0.042	<0.2	<0.2	<0.07	<0.2	0.063	0.36	0.093	0.275	0.036	0.324	0.039	34.7	12.64	117.7	27.9	0.132
II	vnlt	MAC436-1	>1	0.251		0.542	<0.02	<0.02	<0.02	<0.2	<0.2	<0.07	<0.2	<0.03	0.128	<0.03	<0.11	<0.01	0.086	<0.03	15.8	10.59	108.1	83.8	<0.05
II	vnlt	MAC436-2	>1	0.348		0.532	<0.02	<0.02	<0.02	<0.2	<0.2	<0.07	<0.2	0.044	0.179	<0.03	<0.11	<0.01	0.068	<0.03	11.4	9.82	95.8	73.7	<0.05
II	vnlt	MAC436-3	>1	0.172		0.389	<0.02	<0.02	<0.02	<0.2	<0.2	<0.07	<0.2	<0.03	0.118	<0.03	<0.11	<0.01	<0.06	<0.03	9.4	11.86	122.6	79.8	0.087
II	vnlt	MAC436-4	>1	0		0.361	<0.02	<0.02	<0.02	<0.2	<0.2	<0.07	<0.2	<0.03	<0.06	<0.03	<0.11	<0.01	<0.06	<0.03	14.7	13.48	155.5	82.3	<0.05
II	vnlt	MAC436-5	>1	0.158		0.356	<0.02	<0.02	<0.02	<0.2	<0.2	<0.07	<0.2	0.045	0.09	<0.03	<0.11	<0.01	<0.06	<0.03	11.1	10.64	108	84.7	<0.05
II	vnlt	MAC436-6	>1	0		0.327	<0.02	<0.02	<0.02	<0.2	<0.2	<0.07	<0.2	<0.03	<0.06	<0.03	<0.11	<0.01	<0.06	<0.03	9.3	11.59	128.7	86.4	0.11
II	vnlt	MAC436-7	>1	0.035		0.323	<0.02	<0.02	<0.02	<0.2	<0.2	<0.07	<0.2	<0.03	<0.06	<0.03	<0.11	<0.01	<0.06	<0.03	14.1	12.48	155.1	85.2	<0.05
II	vnlt	MAC436-8	>1	0.291		0.48	<0.02	<0.02	<0.02	<0.2	<0.2	<0.07	<0.2	<0.03	0.215	<0.03	<0.11	<0.01	<0.06	<0.03	14.5	9.17	86.3	75.8	<0.05
II	vnlt	MAC436-10	>1	0.165		0.395	<0.02	<0.02	<0.02	<0.2	<0.2	<0.07	<0.2	<0.03	0.098	<0.03	<0.11	<0.01	<0.06	<0.03	12.9	10.85	111	86.7	<0.05
II	vnlt	MAC436-11	2.92	0.173		0.302	<0.02	0.042	<0.02	<0.2	<0.2	<0.07	<0.2	<0.03	0.073	<0.03	<0.11	<0.01	<0.06	<0.03	11.1	14.48	86.7	53.2	0.061

I	dss	MAC436-12	0.05	1.549	0.126	0.45	0.94	0.102	<0.2	<0.2	<0.07	<0.2	<0.03	<0.06	<0.03	<0.11	<0.01	<0.06	<0.03	6.3	10.6	117.4	94	<0.05
I	dss	MAC436-13	0.47	0.549	0.365	0.119	0.318	0.06	<0.2	<0.2	<0.07	<0.2	<0.03	<0.06	<0.03	<0.11	<0.01	<0.06	<0.03	8.8	15.48	88.2	54.5	<0.05
II	vnlt	MAC436-14	4.86	0.084	0.275	<0.02	0.023	<0.02	<0.2	<0.2	<0.07	<0.2	<0.03	<0.06	<0.03	<0.11	<0.01	0.061	<0.03	10	15.75	78.8	45.4	0.076
II	vnlt	MAC436-15	2.68	0.0952	0.264	<0.02	0.04	0.0022	<0.2	<0.2	<0.07	<0.2	<0.03	<0.06	<0.03	<0.11	<0.01	<0.06	<0.03	8.1	12.25	100.7	60.1	<0.05
		MAC201-1		0	<0.06	<0.02	<0.02	<0.02	<0.2	<0.2	<0.07	<0.2	<0.03	<0.06	<0.03	<0.11	<0.01	<0.06	<0.03	4	10.93	100.8	7.2	<0.05
II	dss	MAC201-2	1.06	0.031	0.081	<0.02	0.031	<0.02	<0.2	<0.2	<0.07	<0.2	<0.03	<0.06	<0.03	<0.11	<0.01	<0.06	<0.03	<4.0	26.7	90.2	1.9	<0.05
	dss	MAC201-3		0	<0.06	<0.02	<0.02	<0.02	<0.2	<0.2	<0.07	<0.2	<0.03	<0.06	<0.03	<0.11	<0.01	<0.06	<0.03	12.4	23.8	63.7	5.1	<0.05
II	dss	MAC201-4	1.53	0.03	0.113	<0.02	0.03	<0.02	<0.2	<0.2	<0.07	<0.2	<0.03	<0.06	<0.03	<0.11	<0.01	<0.06	<0.03	<4.0	12.89	70.4	bdl	<0.05
II	dss	MAC201-5	>1	0	0.127	<0.02	<0.02	<0.02	<0.2	<0.2	<0.07	<0.2	<0.03	<0.06	<0.03	<0.11	<0.01	<0.06	<0.03	9.4	14.35	61.7	9	<0.05
II	dss	MAC201-6	>1	0	0.021	<0.02	<0.02	<0.02	<0.2	<0.2	<0.07	<0.2	<0.03	<0.06	<0.03	<0.11	<0.01	<0.06	<0.03	7.1	10.64	70	5.1	<0.05
II	dss	MAC201-7	2.64	0.028	0.182	<0.02	0.028	<0.02	<0.2	<0.2	<0.07	<0.2	<0.03	<0.06	<0.03	<0.11	<0.01	<0.06	<0.03	5.3	27.5	72.7	5.2	<0.05
II	vnlt	MAC201-8	2.50	0.324	0.72	0.032	0.117	<0.02	<0.2	<0.2	<0.07	<0.2	<0.03	0.07	<0.03	<0.11	0.016	<0.06	<0.03	9	20.61	60.8	5.1	<0.05
	dss	MAC201-9		0	<0.06	<0.02	<0.02	<0.02	<0.2	<0.2	<0.07	<0.2	<0.03	<0.06	<0.03	<0.11	<0.01	<0.06	<0.03	<4.0	15.57	87.2	1.6	<0.05
	dss	MAC201-10		0	<0.06	<0.02	<0.02	<0.02	<0.2	<0.2	<0.07	<0.2	<0.03	<0.06	<0.03	<0.11	<0.01	<0.06	<0.03	<4.0	12.59	68.3	2.6	<0.05
II	dss	MAC201-11	>1	0	0.12	<0.02	<0.02	<0.02	<0.2	<0.2	<0.07	<0.2	<0.03	<0.06	<0.03	<0.11	<0.01	<0.06	<0.03	<4.0	14.41	88	0.9	<0.05
II	dss	MAC201-12	3.66	0.449	1.08	<0.02	0.12	<0.02	<0.2	<0.2	<0.07	<0.2	<0.03	0.079	<0.03	<0.11	<0.01	0.1	<0.03	33.1	39.3	82.8	6.3	<0.05
	dss	MAC201-13		0	<0.06	<0.02	<0.02	<0.02	<0.2	<0.2	<0.07	<0.2	<0.03	<0.06	<0.03	<0.11	<0.01	<0.06	<0.03	<4.0	16.64	58.8	0.7	<0.05
I	dss	MAC201-14	0.61	0.417	0.404	0.028	0.271	<0.02	<0.2	<0.2	<0.07	<0.2	<0.03	0.063	<0.03	<0.11	<0.01	<0.06	<0.03	9.8	31.9	84	8.8	<0.05
I	dss	MAC201-15	0.29	0.063	0.045	<0.02	0.063	<0.02	<0.2	<0.2	<0.07	<0.2	<0.03	<0.06	<0.03	<0.11	<0.01	<0.06	<0.03	4.7	14.12	80	3.5	<0.05
II	dss	MAC201-16	1.00	0.088	0.111	0.043	0.045	<0.02	<0.2	<0.2	<0.07	<0.2	<0.03	<0.06	<0.03	<0.11	<0.01	<0.06	<0.03	<4.0	11.88	75.7	0.5	<0.05
I	dss	MAC201-17	0.28	2.7	0.55	0.77	0.8	0.109	0.58	<0.2	<0.07	<0.2	0.037	0.16	0.04	<0.11	0.018	<0.06	<0.03	13.9	23.24	81.9	15.1	<0.05
	dss	MAC201-18		0	<0.06	<0.02	<0.02	<0.02	<0.2	<0.2	<0.07	<0.2	<0.03	<0.06	<0.03	<0.11	<0.01	<0.06	<0.03	<4.0	15.7	72	6.6	<0.05
I	dss	MAC201-19	0.84	0.219	0.359	0.045	0.174	<0.02	<0.2	<0.2	<0.07	<0.2	<0.03	<0.06	<0.03	<0.11	<0.01	<0.06	<0.03	13.4	11.03	39.1	2.7	<0.05
I	dss	MAC201-20	<1	0.041	<0.06	<0.02	0.041	<0.02	<0.2	<0.2	<0.07	<0.2	<0.03	<0.06	<0.03	<0.11	<0.01	<0.06	<0.03	<4.0	14.58	99.4	bdl	<0.05
II	dss	MAC69-1	5.15	0.03	0.38	<0.02	0.03	<0.02	<0.2	<0.2	<0.07	<0.2	<0.03	<0.06	<0.03	<0.11	<0.01	<0.06	<0.03	7.2	19.48	208.1	91.7	<0.05
II	dss	MAC69-2	1.53	0.167	0.229	<0.02	0.061	0.025	<0.2	<0.2	<0.07	<0.2	<0.03	<0.06	<0.03	<0.11	<0.01	<0.06	<0.03	18.3	17.79	219.3	85.3	<0.05
II	dss	MAC69-3	>1	0	0.142	<0.02	<0.02	<0.02	<0.2	<0.2	<0.07	<0.2	<0.03	<0.06	<0.03	<0.11	<0.01	<0.06	<0.03	16.3	18.2	244.5	103.2	<0.05
II	dss	MAC69-6	1.04	0.242	0.339	<0.02	0.132	<0.02	<0.2	<0.2	<0.07	<0.2	<0.03	0.11	<0.03	<0.11	<0.01	<0.06	<0.03	8.9	25.3	210.6	82.9	<0.05
I	dss	MAC69-7	0.92	0.101	0.229	<0.02	0.101	<0.02	<0.2	<0.2	<0.07	<0.2	<0.03	<0.06	<0.03	<0.11	<0.01	<0.06	<0.03	11.5	25.66	246.7	75.1	0.057
I	dss	MAC69-8	0.37	0.595	0.303	0.22	0.337	0.038	<0.2	<0.2	<0.07	<0.2	<0.03	<0.06	<0.03	<0.11	<0.01	<0.06	<0.03	19.2	25.7	241.7	94.9	<0.05
I	dss	MAC69-9	0.70	0.383	0.418	0.11	0.243	0.03	<0.2	<0.2	<0.07	<0.2	<0.03	<0.06	<0.03	<0.11	<0.01	<0.06	<0.03	17.4	25.7	239.7	72.7	<0.05
I	dss	MAC69-10	0.85	0.258	0.279	0.038	0.133	<0.02	<0.2	<0.2	<0.07	<0.2	<0.03	<0.06	<0.03	<0.11	<0.01	<0.06	<0.03	10.6	19.1	217.2	87.5	<0.05
II	dss	MAC69-11	1.11	0.135	0.232	0.021	0.085	0.029	<0.2	<0.2	<0.07	<0.2	<0.03	<0.06	<0.03	<0.11	<0.01	<0.06	<0.03	23.2	26.9	385.6	130.4	<0.05
II	dss	MAC69-12	1.30	0.134	0.294	<0.02	0.092	<0.02	<0.2	<0.2	<0.07	<0.2	<0.03	<0.06	<0.03	<0.11	<0.01	<0.06	<0.03	20.7	22.11	221.8	80	<0.05
II	dss	MAC69-13	1.97	0.159	0.311	<0.02	0.064	<0.02	<0.2	<0.2	<0.07	<0.2	<0.03	<0.06	<0.03	<0.11	<0.01	0.095	<0.03	5	22.9	292.9	98.3	<0.05
II	dss	MAC69-14	2.80	0.025	0.172	<0.02	0.025	<0.02	<0.2	<0.2	<0.07	<0.2	<0.03	<0.06	<0.03	<0.11	<0.01	<0.06	<0.03	<4.0	15.39	233.1	48.6	<0.05
I	dss	MAC69-15	0.49	1.051	0.48	0.105	0.398	0.029	0.2	<0.2	<0.07	<0.2	<0.03	0.083	<0.03	<0.11	<0.01	0.096	<0.03	58	20.2	338.8	104.9	0.84
I	dss	MAC69-16	0.24	1.762	0.553	0.251	0.92	0.107	0.4	<0.2	<0.07	<0.2	<0.03	<0.06	<0.03	<0.11	<0.01	<0.06	<0.03	449	21.2	1031	169.6	0.057
I	dss	MAC69-17	0.49	0.218	0.231	0.026	0.192	<0.02	<0.2	<0.2	<0.07	<0.2	<0.03	<0.06	<0.03	<0.11	<0.01	<0.06	<0.03	58.3	25.4	406.6	114.8	<0.05
I	dss	MAC69-18	0.19	0.826	0.253	0.181	0.541	0.063	<0.2	<0.2	<0.07	<0.2	<0.03	<0.06	<0.03	<0.11	<0.01	<0.06	<0.03	311	27	771	160.9	<0.05
II	dss	MAC69-19	5.28	0.018	0.234	<0.02	0.018	<0.02	<0.2	<0.2	<0.07	<0.2	<0.03	<0.06	<0.03	<0.11	<0.01	<0.06	<0.03	18.1	21.6	215.2	83.4	<0.05
I	dss	MAC69-20	0.12	1.727	0.277	0.261	0.93	0.059	0.39	<0.2	<0.07	<0.2	<0.03	<0.06	<0.03	<0.11	<0.01	<0.06	<0.03	350	19.83	865	148.1	<0.05
I	dss	MAC69-22	0.26	2.04	0.59	0.317	0.92	0.119	0.45	<0.2	<0.07	<0.2	<0.03	<0.06	<0.03	<0.11	0.011	<0.06	<0.03	332	20.54	884	153	<0.05

I	dss	MAC425-1	0.43	16.34	0.71	5.3	4.85	5.06	0.58	1.24	0.67	0.198	1.07	0.252	1.44	0.148	0.54	0.042	0.25	<0.03	620	24.3	2453	148.1	0.98
I	dss	MAC425-2	0.85	13.91	0.88	6.39	3.84	3.07	0.41	1.42	0.45	0.21	1.15	0.238	1.85	0.249	0.63	0.045	0.31	0.038	1113	22.9	2296	147.2	0.37
I	dss	MAC425-3	0.42	31.293	1.16	7.94	6.18	7.66	0.79	4.63	1.8	0.72	1.96	0.81	3.9	0.471	1.17	0.178	0.94	0.084	812	24.7	2297	126.3	6.8
II	dss	MAC425-4	1.14	11.796	0.96	4.87	2.03	1.74	0.231	1.5	0.8	0.31	1.18	0.333	2.29	0.271	0.7	0.061	0.32	0.03	770	23.8	2541	159.4	0.44
II	dss	MAC425-5	8.25	10.338	0.20	13.2	0.89	0.65	0.047	0.52	0.39	0.055	1.69	0.402	3.07	0.431	1.33	0.125	0.62	0.118	720	21.9	2786	150	0.21
II	dss	MAC425-6	1.24	11.937	1.04	6.69	3.16	2.2	0.289	1.51	0.69	0.281	0.96	0.241	1.63	0.22	0.43	0.046	0.23	0.05	877	17.8	1236	132.6	0.166
II	dss	MAC425-8	1.15	7.342	0.86	3.45	2.77	1.22	0.185	0.8	0.09	0.066	0.6	0.123	0.73	0.205	0.24	0.043	0.27	<0.03	979	22.2	1605	166.6	0.051
I	dss	MAC425-9	0.16	38.291	0.65	4.95	11.7	12.2	1.04	3.91	1.73	0.4	2.01	0.652	2.59	0.259	0.74	0.064	0.93	0.066	680	24	2443	153.5	1.62
II	dss	MAC425-10	1.55	6.574	1.88	4.42	2.01	1.16	0.12	0.66	0.025	0.084	0.73	0.138	0.9	0.19	0.38	0.038	0.139	<0.03	573	27.3	1612	155.2	0.25
I	dss	MAC425-11	1.44	3.725	>1	2.45	1.77	0.69	0.028	<0.2	<0.2	0.075	0.15	0.071	0.65	0.108	0.038	0.023	0.122	<0.03	911	24.7	1927	174.3	0.078
I	dss	MAC425-12	0.84	11.49	1.08	4.79	1.78	2.31	0.164	1.54	0.59	0.26	0.9	0.45	2.13	0.314	0.66	0.062	0.28	0.05	564	24.1	2359	158.6	3.37
II	dss	MAC425-15	1.07	11.548	1.01	5.67	2.38	2.15	0.178	1.71	0.47	0.236	1.05	0.383	2.2	0.265	0.41	0.052	0.064	<0.03	502	22.2	2289	155	0.39
II	dss	MAC425-16	2.56	45.805	0.79	34.6	5.6	5.5	0.65	3.12	2.24	0.99	6.4	1.69	11.2	1.48	3.6	0.371	2.61	0.354	766	34.1	3420	161.8	1.64
II	dss	MAC425-17	1.84	12.805	0.92	10.44	2.09	2.31	0.227	0.9	0.66	0.31	1.57	0.384	2.64	0.344	0.94	0.11	0.32	<0.03	765	21.9	2676	179.7	0.172
II	dss	MAC425-18	5.09	6.47	0.67	8.52	0.9	0.68	0.13	0.24	0.14	0.093	1.25	0.209	1.71	0.281	0.49	0.056	0.22	0.071	913	20.1	3045	198	0.66
I	dss	MAC425-19	0.89	21.347	0.96	8.53	3.96	3.89	0.421	2.33	1.34	0.54	2.13	0.72	3.64	0.459	1.1	0.091	0.68	0.046	842	26.4	2568	178.2	0.235
I	ps	MAC462-1	0.93	2.092	<1	1.97	0.29	0.86	0.076	0.24	0.14	<0.07	0.15	<0.03	0.32	0.016	<0.11	<0.01	<0.06	<0.03	nd	3.9	21.8	20.3	0.17
I	ps	MAC462-3	0.33	5.733	<1	2.11	0.67	2.6	0.18	1.04	0.62	<0.07	0.28	<0.03	0.31	0.033	<0.11	<0.01	<0.06	<0.03	nd	3.94	28.9	40.6	0.43
I	ps	MAC462-6	0.21	29.663	0.43	7.1	4.7	13.5	1.32	5.2	1.04	0.102	0.5	0.23	0.94	0.27	0.96	<0.01	0.8	0.101	nd	7.8	29.3	32.7	0.23
I	ps	MAC462-9	0.19	18.561	<1	4.5	3.24	9.4	0.63	3.36	0.32	<0.07	0.48	0.092	0.64	0.099	0.3	<0.01	<0.06	<0.03	nd	3.85	24.8	17.5	0.43
II	ps	MAC462-15	1.63	0.216	<1	0.337	0.05	0.084	<0.02	<0.2	<0.2	<0.07	0.048	<0.03	0.034	<0.03	<0.11	<0.01	<0.06	<0.03	nd	8.85	15.87	17.2	0.074
I	ps	MAC462-16	0.11	10.913	0.89	1.62	1.09	5.9	0.53	2.11	0.53	0.08	<0.2	0.085	0.41	0.038	<0.11	<0.01	<0.06	<0.03	nd	7.3	18.4	46	2.12
I	ps	MAC462-17	0.06	68.17		5.1	14.2	37.4	2.6	12.3	<0.2	<0.07	<0.2	0.27	1.4	<0.03	<0.11	<0.01	<0.06	<0.03	nd	30.9	31	1	bdl
I	ps	MAC462-18	0.70	0.302		0.316	0.08	0.184	0.021	<0.2	<0.2	<0.07	<0.2	<0.03	<0.06	<0.03	<0.11	<0.01	<0.06	<0.03	nd	9.41	16.43	6	bdl

*measurements below LOD were considered 0 ppm.

where $Eu^* = \sqrt{(Sm_N * Gd_{N)}}$

O = occurance: vnlt = veinlet, dss = disseminated aggregate, ps = infilling pore space

Table A5.3: LAICPMS results for oxy-dravite (ppm)

Measurement	LOD	99-1-1A	99-1-2A	99-3-1A	99-3-1B	201-1-A	201-3-A
ΣREE		68.7	81.2	128.8	60.3	15.2	29.4
Ce_N/Y_N		92	117	170	101	69	67
Eu/Eu*		3.08	3.21	2.68	2.75	6.54	3.20
Y	0.03	0.891	0.836	0.89	0.708	0.248	0.509
La	0	17.8	21.2	34.7	16.1	4.12	7.47
Ce	0	33.2	39.7	61.6	29.0	6.99	13.9
Pr	0	3.39	3.83	6.06	2.87	0.769	1.43
Nd	0.01	10.9	12.7	20.9	9.41	2.3	4.8
Sm	0.01	1.31	1.48	2.47	1.16	0.273	0.72
Eu	0.01	0.961	1.12	1.48	0.755	0.419	0.503
Gd	0.02	0.674	0.753	1.13	0.595	0.137	0.313
Tb	0	0.0746	0.0633	0.0762	0.0448	0.0151	0.0393
Dy	0.01	0.3	0.255	0.257	0.185	0.068	0.097
Ho	0	0.0398	0.0332	0.0393	0.0325	0.009	0.0248
Er	0.01	0.065	0.092	0.072	0.069	0.0323	0.06
Tm	0.01	<0.009	<0.009	<0.009	<0.009	<0.009	<0.009
Yb	0	0.052	<0.003	0.035	0.05	0.031	0.0131
Lu	0.03	<0.03	<0.03	<0.03	<0.03	<0.03	<0.03
Li		11.9	13.1	10.4	10.5	8.8	11.8
Sc		54.4	54.3	65.5	62.5	60.8	57.2
V		588	617	1029	827	1138	1160
Cr		293	316	478	352	333	315
W		<0.02	<0.02	<0.02	<0.02	<0.02	<0.02

Appendix 6 Supplementary Material for Chapter 6

Table A6.1: Running conditions of system for trace element acquisition

Laser	
Model	COMPexPro 102 F 193 nm excimer laser
Laser energy used	90 mJ / 50% attenuation
BDU Demag position	25x
Laser fluence	~2.9 J/cm^2
Repetition rate	3 Hz
Spot diameter	36 microns
Ablation time (seconds)	30s background, 50s mineral ablation
Standards used	NIST610 (primary concentration standard) BCR-2G (QC standard)
ICP-MS	
Model	Agilent 7700
RF power	1550 W
Sampling depth (Torch position)	5.5 mm
Carrier gas (Ar)	0.92 L/min
U/Th	~107%
ThO/Th	<0.2%
22/44 (Doubly charged ion ratio)	<0.3%
Tuning protocol	Tuned for full suite of elements (47, 93, 207 monitored during tuning)
Gas flow rate (ablation cell)	He (300 ml/min), N2 (2 ml/min) 2nd pump used (increases sensitivity)
Data acquisition parameters	
Protocol	Time resolved analysis
Sampling time	0.5352
Dwell time per isotope (sec)	^{27}Al(0.015), ^{29}Si(0.015), ^{44}Ca(0.015), ^{45}Sc(0.02), ^{47}Ti(0.01), ^{51}V(0.015), ^{52}Cr(0.015), ^{55}Mn(0.015), ^{56}Fe(0.01) ^{59}Co(0.02), ^{60}Ni(0.02), ^{63}Cu(0.02), ^{66}Zn(0.015), ^{71}Ga(0.02), ^{72}Ge(0.02), ^{78}Se(0.02), ^{89}Y(0.02), ^{90}Zr(0.01), ^{93}Nb(0.015), ^{95}Mo(0.015), ^{118}Sn(0.02), ^{121}Sb(0.015), ^{125}Te(0.015), ^{178}Hf(0.02), ^{181}Ta(0.02), ^{182}W(0.02), ^{208}Pb(0.015), ^{232}Th(0.015), ^{238}U(0.015)

Table A6.2: Running conditions of system for U-Pb geochronology

Laser	
Model	COMPexPro 102 F 193 nm excimer laser
Laser energy used	90 mJ / 50% attenuation
BDU Demag position	25x
Laser fluence	~2.9 J/cm^2
Repetition rate	3 Hz
Spot diameter	36 microns
Ablation time (seconds)	30s background, 30s mineral ablation
Standards used	NIST610 (primary concentration standard) R10 (primary rutile geochron standard) R13 (QC geochron standard)
ICP-MS	
Model	Agilent 7700
RF power	1550 W
Sampling depth (Torch position)	4 mm
Carrier gas (Ar)	0.92 L/min
U/Th	~107%
ThO/Th	<0.2%
22/44 (Doubly charged ion ratio)	<0.3%
Tuning protocol	Tuned for heavy elements (207 and 238 monitored during tuning)
Gas flow rate (ablation cell)	He (300 ml/min), N2 (2 ml/min) 2nd pump used (increases sensitivity)
Data acquisition parameters	
Protocol	Time resolved analysis
Sampling time	0.2752
Dwell time per isotope (sec)	^{47}Ti (0.01), ^{90}Zr (0.01), ^{202}Hg (0.04), ^{204}Pb (0.06), ^{206}Pb (0.04), ^{207}Pb (0.06), ^{208}Pb (0.01), ^{232}Th (0.01), ^{238}U (0.015)

Table A6.3: Trace element concentration for rutile

ample	c		r	n	e	u	n	a		r	b	o	n	b	f	a		b	h		°C *
OD	.43	.46	.91	.68	.48	.56	.16	.078	.02	.02	.02	.02	.44	.69	.06	.01	.05	.20	.00	.03	
AC84-1	0.8	0005	84.2	4.68	81	.59	.2	.084	.0480	39.4	597	.94	55	.3	7.2	05.6	195	0.198	0.1	02.8	16
AC84-2	7.9	0090	01	4.68	46	.68	4.16	.167	.278	10	353	.78	72	.22	5.8	37	231		.85	9.1	10
AC84-3	1.8	280	43	0.9	87	.81	.4	.191	.79	73	649	.84	10	.89	4.6	51.2	510	.2	.9	1.4	02
AC84-4	1.9	640	74	4.68	74	.99		0.078	.056	08.1	549	.74	74	.21	1.4	42.2	561	0.198	0.1	6.3	86
AC84-7	10	5730	349	4.68	.3	.08	.3	0.078	.02	53	411	6.4	19	.23	8.9	11.5	240	0.198	0.1	7.4	18
AC84-8	62.7	5650	268	4.68	00	.13	4.16	.74	.039	88.4	180	.55	66	.57	4.7	70.5	926	0.198	0.1	2.5	05
AC84-9	1.6	3280	94	4.68	78.8	.16	.6	.177	.036	12	417	.54	82.1	.84	9.6	39.9	383	0.198	0.1	01.7	29
AC84-10	0.6	3480	017	4.68	5.48	.59	.9	0.078	.059	01.4	442	.77	37	.86	1.9	39.9	512	0.198	0.1	0.1	27
AC99 - 1	00.5	161	51.6		140	.5	.8	.59	.113	83	890	.75	1.4	.01	2.9	81.6	42	.44	.32	1.48	42
AC99 - 2	6.1	153	37.2	4.68	259	.14	.2	.7	.049	69	362	2.3	0.2		9.2	80.8	96.9	0.198	0.1	.06	21
AC99 - 3	3.9	411	03.4	4.68	579	.11	4.16	.1	.022	18	440	.13	4.6		5.7	07	51	0.198	0.1	1.44	11
AC99 - 4	8.5	375	35	4.68	244	.12	.5	.92	.063	09.5	380	.48	5.2		0.1	89.7	69	0.198	0.1	1.24	29
AC99 - 5	1.2	787	60.2	4.68	891	.36	4.16	.66	.036	59	281	.59	4.7	.14	3.4	35.2	15.2	0.198	0.1	1.03	20
AC99 - 6	5.5	484	35	4.68	005	.22	.3	.8	.065	77	330	.35	4.2	.05	5.1	10	30.7	0.198	0.1	1.82	23
AC99 - 7	5.2	349	34.9	4.68	623	.28	.8	.28	.051	36.9	869	.67	9.7	.38	9.53	36.3	50.3	0.198	0.1	0.37	34
AC99 - 8	4.3	403	30.4	4.68	338	.37	4.16	.91	.04	93.6	855	.16	5.9	.26	9.6	82	27.2	0.198	0.1	0.75	26
AC99 - 9	2.8	310	95.7	4.68	292	.36	.4	.83	.03	11	721	.21	3.2	.18	4.7	55.6	69	0.198	0.1	0.56	10
AC99 - 10	9.8	390	38.9	4.68	400	.64	.9	.23	.099	28	700	.59	5.8	.27	6.2	28.7	78	0.198	0.1	1.32	13
AC79-1	8.2	265	365	4.68	034	.55	.6	.76	.029	27.8	250	2	14.2	.24	6.3	328	211	0.198	0.1	0.2	13
AC79-2	6.6	646	362	4.68	748	.23	.8	.5	.019	66	520	.63	87.7	.08	9.8	60	65	0.198	0.1	3.8	39

AC79-3	3.7	459	262	4.68	762	.05		.01	.112	93	700	2.3	29.2	.34	2.2	51	269	0.198	0.1	8.7	06
AC79-4	7.1	412	62	4.68	777	.32	1	.01	0.02	21	881	8.4	93.1	.86	8.75	43	32	.34	.1	1.5	62
AC79-5	9.8	765	265	4.68	610	.99	.3	.43	.009	22	230	.51	82.7	.48	0.7	93.3	16	0.198	0.1	7.6	48
AC79-6	3.9	445	253	4.68	666	.9	.3	.18	.3	96.9	570	2.9	18.3	.6	1.9	48.8	251	0.198	0.1	5.6	07
AC152-1	21.4	208	37.5	4.68	332	.64	.3	.57	.047	30	685	.85	99.3	.03	8.9	05.6	022	0.198	0.1	0.4	49
AC152-2	04.4	269	53	4.68	435	.43	.6	.46	.038	42	901	.76	14.9	.39	5.4	14.4	046	0.198	.23	5.8	68
AC152-3	8.3	327	80	4.68	39	.7	.9	.45	.325	46	088	.9	17.8	.92	0.2	74.1	81	.29	.485	5.7	17
AC152-4	1.5	592	68.6	4.68	327	0.93	.4	.94	.79	02.9	353	.56	33.6	.34	2.2	37	29	.12	.94	6.9	28
AC152-5	04.9	125	330	4.68	100	.59	.5	.46	.045	18	593	.78	17	.11	9	92.1	87	0.198	0.1	7.6	47
AC152-6	13.3	308	601	4.68	56	.75	.7	.29	.016	16	803	.36	46.6	.57	4.6	50.8	59	0.198	0.1	9.2	62
AC152-7	11.8	250	592	4.68	20	.5	.9	.27	.146	18	800	.2	48.9	.36	3	52.7	64	0.198	0.1	0.4	62
AC152-8	8.5	910	081	4.68	63	.2	.3	.6		82	840	.6	58	.31	6.3	50	051	0.198	.09	7.4	04
AC152-9	28	331	797	4.68	38	.27	.2	.6	.035	17	096	1.85	13.6	.29	8.3	08.5	18	0.198	0.1	9	30
AC152-10	74.6	873	079	4.68	59	.11	4.16	.55	.21	19	497	2.9	36.9	.22	7.9	65.3	021	0.198	0.1	2.1	47
AC152-11	00.1	810	046	4.68	42	.99	4.16	.32	.05	45	441	2.3	24.8	.55	9.9	59.4	011	0.198	0.1	8.7	51
AC152-12	37.5	479	477	4.68	43.2	.48	4.16	.27	.038	83	630	.8	27.8	.99	0.2	67.3	68	0.198	0.1	2.2	24
AC127-1	5.9	460	080	4.68	36.4	.72	4.16	.21	.019	49	493	.4	82.8	.09	3.3	9.1	07.4	0.198	0.1	3.7	18
AC127-2	9.4	930	404	4.68	97	.56	4.16	.178	.048	96.1	880	.6	02.6	.07	5.7	01.2	92.5	0.198	0.1	3.9	27
AC127-3	3.5	939	361	4.68	95	.23	.8	.058	.037	63	751	0.18	76.9	.03	5.7	51.6	96.9	0.198	0.1	8.7	20
AC127-4	14	047	275	4.68	54	.88		.19	6.16	33	219	1	79.1	.66	0.6	36.7	05.8	.64	3.4	26.2	49

AC127-5	16.6	883	263	4.68	58	.84	.2	.25	.06	85	010	4.4	69.4	.67	6	96.5	15.3	0.198	0.1	4.3	24
AC127-6	3.1	361	218	4.68	60	.03	4.16	.35	.029	55.9	495	.23	83.7	.08	3.1	26.2	28.7	0.198	0.1	4.4	19
AC127-7	3.4	418	172	4.68	08	.94	4.16	.36	.038	90.7	893	4.5	89.6	.36	1.9	20.8	97.5	0.198	0.1	4.7	06
AC127-8	8.3	623	164	4.68	92	.83	4.16	.2	.027	47	689	.12	75.7	.09	2.9	09.2	09.6	0.198	0.1	1.9	17
AC127-9	16.9	600	211	4.68	10	.99	4.16	.78	.029	07	935	0.2	80.5	.39	2.7	29.9	85.6	0.198	0.1	5.4	60
AC127-10	7.7	413	057	4.68	94	.54	4.16	.07	.035	61	283	.7	73.4	.01	3.2	9.5	49.9	0.198	0.1	2.1	20
AC203-1	89.8	599	27.4	4.68	923	.03	4.16	.49	.047	056	540	0	60.3	.06	5.7	18.9	624	0.198	0.1	2.11	80
AC203-2	98.4	653	32	4.68	148	.87	4.16	.25	.041	063	918	2.4	86.3	.59	3.9	009	778	0.198	0.1	2.13	81
AC203-3	89.9	395	96	4.68	821	.96	.5	.16	.048	106	892	0.8	00.9	.64	7.9	51.1	853	0.198	0.1	7.77	86
AC203-4	052	828	21.9	4.68	336	.81	4.16	.29	.023	26	530	2	18	.79	0.8	30.8	879	0.198	0.1	4.15	63
AC203-5	000	656	09	4.68	165	.78	4.16	.06	.068	86	340	3.1	96.3	.7	1.2	73.9	796	0.198	0.1	3.12	71
AC203-6	39	836	30.5	4.68	884	.67	4.16	.66	.06	68	280	0.32	95.1	.48	1.2	29.4	542	0.198	0.1	2.3	69
AC203-7	71	484	10.7	4.68	910	.09	4.16	.44	.048	81	860	2.7	03.5	.48	0.3	21.3	574	0.198	0.1	3.23	70
AC203-8	12.8	558	18.8	4.68	181	.08	4.16	.76	.059	83	802	4.2	55	.17	0.1	020.1	581	0.198	0.1	1.76	71
AC203-10	10.7	575	74.3	4.68	639	.76	4.16	.41	.56	89	813	1.7	28	.25	1.3	47.3	679	0.198	.33	4.78	71
AC444-1	21.2	300	779	4.68	74	.56	4.16	.095	.017	020	678	0.7	23.2		1	74.5	53	0.198	0.1	8.18	75
AC444-2	7.4	088	371	4.68	68	.75	4.16	0.078	.019	33	339	.04	67.9	.54	7.2	87.1	01	0.198	0.1	3.4	33
AC444-3	03.7	920	778	4.68	79	.97	4.16	0.078	.017	97	842	.25	45.9	.63	6.4	79.1	64	0.198	0.1	3.7	27
AC444-4	13	090	805	4.68	33.6		4.16	0.078	.008	57	460	.03	45.5	.36	6.4	46.1	54	0.198	0.1	7.7	37

AC444-5	4.2	330	49	4.68	92	.86	4.16	0.078	.079	83	750	.04	45.8	.53	1.5	72.1	67	0.198	0.1	3.77	04
AC444-6	5.1	0000	305	4.68	1.8	.68	.2	0.078	.032	57	489		47.6	.01	4.9	53.4	54	0.198	0.1	8.4	19
AC444-7	9.7	020	615	4.68	66.8	.3	.3	.48	.257	53	333	.04	64.7	.17	0.5	27.9	99	0.198	.35	3.1	97
AC444-8	5.8	500	088	4.68	53	.05	4.16	0.078	.032	61	668	.28	42.4	.81	1.7	37.2	04.1	0.198	0.1	4.6	20
AC444-10	8.7	180	49	.7	05	.91	4.16	0.078	.024	04	230	.97	35.6	.16	9.4	11	61.6	0.198	0.1	9.9	45
AC441-1	2.4	712	184	4.68	321	.78	4.16	.77	.015	94	620	.79	51.3	.36	4.8	97.6	03	0.198	0.1	7.03	58
AC441-2	7.8	487	028	4.68	333	.62	4.16	.8	.036	92	732	.72	68.1	.54	7.2	86	21.1	0.198	0.1	8.73	58
AC441-3	7.7	282	124	4.68	704	.61	.3	.12	.021	03	971	.23	40	.67	7.1	23.4	51.4	0.198	0.1	5.72	60
AC441-4	6.1	862	425	4.68	012	.83		.142	.029	69	001	.02	75.1	.5	0	3.6	66	0.198	0.1	7.1	39
AC441-5	13.7	319	656	4.68	834	.22	.5	.38	.029	92	800	.39	76		9.8	43	26	0.198	0.1	4.57	26
AC441-6	17.7	835	352	4.68	572	.15	4.16	.84	.016	31	0910	.51	43.5		7.3	128	73.6	0.198	0.1	5.89	49
AC441-7	8.8	680	302	4.68	475	0.562	.9	.38	.029	44	980	.43	62.6	.12	3.9	26	90	0.198	0.1	7.7	51
AC441-8	7	209	477	4.68	120	.65	4.16	.5	.03	25	793	.89	75.7	.09	7.9	91.8	76.7	0.198	0.1	4.96	32
AC441-9	06.7	636	011	4.68	140	.92	4.16	.68	.029	79	410	.41	52.5	.3	8	40	75	0.198	0.1	7.28	56
AC441-10	3.4	433	022	4.68	069	.64	4.16	.59	.021	30	887	.01	71	.47	0.9	53.5	54.6	0.198	0.1	6.1	33
AC201-1	9.2	088	03.1	4.68	240	.12	.3	.295	.021	75	582	.53	04.3		5.3	16	751	0.198	0.1	7.09	40
AC201-2	8.7	104	15	4.68	289	.09	.8	.316	.062	17	686	.49	07.4		3.7	48.8	795	0.198	0.1	2.57	30
AC201-3	6.2	140	23.9	4.68	004	.78	.5	.169	.214	92	818	.22	07.3		5.4	98.8	769	0.198	.87	0.16	43
AC201-4	9.1	179	40.8	4.68	349	.69	.8	.3	.03	90	729	.1	7.3		4.5	79.5	912	0.198	0.1	7.66	43

AC201-5	8.4	210	32.8	4.68	478	.39	.5	.306	.043	22	624	.68	8.1	.26	7	88	865	0.198	0.1	7.8	62
AC201-6	02.8	032	73.7	4.68	295	.16	.3	.39	.069	95	464	.31	3	.77	8.6	37.9	739	0.198	0.1	2.47	59
AC201-7	11	575	63.2	4.68	772	.25	.1	.33	.019	053	016	.92	6.4	.68	8.6	20.5	995	0.198	0.1	7.82	79
AC201-8	10	502	68.4	4.68	787	.46	.6	.77	.039	036	843	.6	9.9	.57	6.1	17.4	055	0.198	0.1	9.5	77
AC201-9	06.7	882	43.7	4.68	369	.35	.7	.5	.022	65.1	355		11.6	.57	3.3	70.1	584	0.198	0.1	7.51	00
AC201-10	06.3	749	37.7	4.68	603	.99	.1	.49	.36	027	452	.6	7.3	.6	2.6	50.2	110	0.198	.75	7.5	76
AC201-11	04.2	746	24.4	4.68	646	.91	.3	.77	.029	035	484	.9	3.2		3.9	46.1	322	0.198	0.1	5.51	77
AC201-12	03.3	732	53	4.68	045	.39	.3	.136	.081	16	283	.02	07.8		2.8	43.8	544	0.198	.38	0.98	47
AC201-13	02.3	772	16.6	4.68	630	.75	.3	.51	.016	53	128	0.64	7.1		7.4	87.7	599	0.198	.313	5.16	67
AC201-14	8.4	814	07.3	4.68	236	.62	.5	.46	.066	58.2	711	0.7	2.4		6.1	09.3	502	0.198	0.1	7.78	37
AC98-1	47.5	1430	765	4.68	608	.5	4.16	.34	.06	67.2	3240	.57	10.4	.16	3	643	787	0.198	0.1	7.37	00
AC98-3	18.3	0220	81	4.68	827	.17	.7	.3	.075	24	4660	8.6	77.9	.09	3.6	447	564	0.198	0.1	7.45	48
AC98-6	60.4	990	468	4.68	600	.25	4.16	.01	.036	71	4860	2.4	03.4	.29	9	050	520	0.198	0.1	9.3	77
AC86-1	7	317	31	4.68	20	.51	.9	.241	.376	38.4	189	.49	01.2	.47	6.8	87.5	62	.34		6.9	15
AC86-2	1.8	280	03	4.68	92	.2	.2	.083	.037	79	119	.07	03.6	.27	7.3	88	29	0.198	0.1	8.4	23
AC86-4	0.1	258	13	4.68	80	.1	.7	.14	.83	15	188	.7	98.9	.27	8.9	0.1	16	0.198	.8	0.1	60
AC86-5	1.7	0374	782	4.68	12	.65	.6	.01	.33	49	836	5.1	02.1	.57	7.4	50.3	78	0.198	.96	0.2	36
AC86-6	3.6	519	54	4.68	95	.51	4.16	.39	.303	18	378	.18	28.6	.47	4.6	58.1	45	0.198	.49	2.1	11
AC86-7	8.1	260	270	4.68	29	.64	4.16	.37	.38	70	034	3.4	13	.48	7	27.8	50	.29	.9	9.6	22
AC86-8	7.6	018	303	4.68	90	.76	4.16	.33	.89	56	323		95.1	.29	3.8	9	085	.68	.3	5.1	19
AC86-9	5.8	974	151	4.68	37	.29	4.16	.059	.052	85.9	310	3	20.5	.95	0.9	7.5	76	0.198	0.1	2.2	81
AC86-10	3	567	33	4.68	82	.09	.9	.201	.288	37	756	.81	93	.92	8.9	41.9	26	.44	.84	0	15
AC70-1	02.6	142	825	4.68	82	.74	4.16	.25	.9	73	133	0.3	85.3	.98	5.6	93.5	19	0.198	.65	6	55

AC70-2	7.3	655	162	4.68	10	.12	.3	.073	.02	64	267	.2	07.2	.64	3.3	22.6	40	0.198	0.1	0.57	00
AC70-3	03.3	684	468	.1	118	.19	.1	.67	.12	74	808	7.5	76.3	.47	9.9	39.5	44	.36	3.7	7	77
AC70-4	1.8	110	361	4.68	520	1	0.7	.09	.49	80	565	.14	97.5	.92	7.2	48.4	18	.25	5.1	9.2	24
AC70-5	9.8	320	091	.2	072	.8	.7	.49	.79	22	650	.05	67.8	.56	8.5	32.4	99	.4	.02	8.5	31
AC70-6	4.4	776	472	4.68	19	.98	.1	.137	.52	25	910	.86	92.3	.48	6.7	19.1	84.5	0.198		7.9	13
AC436-2	40	840	642	4.68	34	.14	4.16	.5	.5	88	592	.75	25	.8	6.8	17.5	511	.24	.23	5.8	42
AC436-3	8.9	871	078	4.68	38	.2	4.16	.27	.035	60	540	.33	26.5	.38	9.7	21.9	449	0.198	0.1	8.3	38
AC436-4	1.7	320	013	4.68	11	.14	4.16	.45	.048	30	590	.56	06.9	.92	0.9	32.2	589	0.198	0.1	5	92
AC436-5	8.2	960	32	4.68	69	.77	4.16	0.078	.038	94	651	.37	80.2	.02	7.78	40.9	312	0.198	0.1	4.9	43
AC436-6	1.2	398	013	4.68	74	.17	4.16	.203	.089	42	410	.46	11.4	.34	8.3	28.3	298	0.198	0.1	6.76	35
AC436-7	8.4	600	04	4.68	6.9	.5	4.16	.141	.035	47	974		38	.93	7.7	09.1	176	0.198	0.1	1.9	36
AC436-8	4.7	560	188	4.68	65	.12	.5	.089	.023	06	120	.86	28.7	.7	1.8	43	524	0.198	0.1	0.83	45
AC436-9	7.8	963	121	4.68	98	.66		0.078	.015	82	981	.11	73.6	.61	9.1	6.3	17	0.198	0.1	0.9	04
AC436-10	6.4	750	057	4.68	98	.02	4.16	.085	.0057	12	826	.16	10	.73	6.1	55.2	400	0.198	0.1	9.1	29
AC436-11	00.7	300	344	4.68	42	.2	.1	.57	.029	30	680	.11	49.8	.65	0.3	41	729	0.198	0.1	6.6	33
AC420-1	0.9	682	340	.8	99		.2	.48	.7	26	166	.4	44.4	.75	3.7	25.3	71	.73	5.6	0.5	13
AC420-2	3	040	497	4.68	21	.95	4.16	.8	.45	62	03	.2	02.2	.81	6.3	8.5	6	.48	4.6	5.3	43
AC420-3	8.9	591	77	4.68	096	.83	.6	.5	.49	41.9	341	.85	09.6	.21	4.7	01.5	24.7	.67	.28	3.8	68
AC420-4	13	097	580	4.68	79	.07	4.16	.45	.032	012	704	4	82.5	.6	9.6	76.8	426	0.198	0.1	2.7	74
AC420-5	13.2	267	530	4.68	90	.99	4.16	.091	.02	79	150	6	95.3	.83	2	89.6	368	0.198	0.1	1.1	56
AC420-6	00.4	663	423	4.68	61	.79	4.16	.082	.023	95.9	657	.6	42.7	.8	7.4	10.8	231	0.198	0.1	9.5	44

AC420-7	9.7	516	258	4.68	89	.17	4.16	.75	.086	55	856	.28	50.4	.04	5.2	29.6	224	0.198	.31	0.86	98
AC420-8	10.6	870	447	4.68	85		.6	.093	.034	85	704	0.6	21.4	.2	6.9	68.9	218	0.198	0.1	5.7	42
AC420-9	10.6	148	552	4.68	16	.86	4.16	0.078	.042	16	014	0.2	26.8	.03	1.4	29.6	218	.46	0.1	9.48	62
AC420-10	8.4	685	554	4.68	092	.8	4.16	.35	.035	90	205	3.2	18.7	.85	4.3	36.5	253	0.198	0.1	0.7	58

*calculated using geothermometer by Zack et al. (2004), uncertainty of ± 50 °C; Ni, Co, Ge, Se, Sb are below detection limits.

Appendix Table A6.4: Trace element concentrations in anatase.

ample	a	c		r	n	e	u	n	a		r	b	o	n	f	a		b	h	
AC98-2	151	2.6	16.9	59	4.68	562	.89	.7	.22	.112	70	36	.1	.39	.81	8.7	3.8	.82	.61	15
AC406-2	97	7.4	9.6	08.7	.8	650	.85	.4	.75	.64	37	968	.6	.89	7.3	0.5	5.5	0.4	9.1	80

AC406-3	90	6.8	4.7	99	4.68	360	.87	.2	.59	.83	68	391	.9	.81	6.3	57	6	8.4	2	63
AC406-4	151	9.2	9.7	47	.5	430	.23	4.16	.21	.24	86	212	.52	.66	3.1	3.9	5.4	0.4	8.6	05
AC406-7	80	9.8	3	04.5	.7	030	.91	.3	.47	.48	58	021	.8	.68	6.9	0.5	0	1.6	6.6	81
AC406-10	40	0.8	2.1	99	.2	410	.85	.5	.5	.88	64	377	.04	.48	.11	94	8.3	5.1	8.6	16
AC426-1	80	1.1	14.7	97	1.4	063	.98	.7	.53	.11	558	812	.34	33	35	67	15	.98	8.7	5.7
AC426-2	27	.87	0.8	89	.7	597		4.16	0.078	.580	858	775	0.2	07	17	60	69	.17	5.4	.17
AC426-4	151	1.6	6.6	67.3	4.68	373	0.562	4.16	0.078	.512	477	000	.081	4.8	53	77	68	.6	7.8	.15
AC426-6	151	4.79	3.3	47.8	4.68	073	.09	4.16	0.078	.04	888	920	0.2	6.9	35	45	37	.088	.36	.58
AC426-7	151	3.2	5.1	48.8	4.68	338	.66	.9	0.078	.42	119	855	0.2	6.8	56	57	60	.96	1.2	.04
AC426-8	760	.85	3.5	94	4.2	743	.49	4.16	0.078	.08	390	845	0.2	9.3	59	39	342	.5	2.5	.52
AC426-10	390	5.71	4.8	66.5	.1	178	0.562	4.16	.027	.45	947	921	.02	2.0	23	60	02	.83	7.5	1.0
AC430-3	151	7.8	9.5	2.2	4.68	850	.44	4.16	.19	.05	62	937	.27	.81	7	02	0.9	.77	.2	9.3
AC436-1	151	.29	2.9		4.68	05	.58	4.16	.72	.111	1.4	156	0.2	.55	.76	5.2	1.9	.21	.38	.49

Ni, Co, Ge, Se, Sb are below detection limits.

Appendix Table A6.5: U-Pb data for rutile and anatase determined by LAICPMS

Sample	^{04}Pb	^{32}Th	^{38}U	b^{207}/U^{235}	±2σ	b^{206}/U^{238}	±2σ	Pb^{207}/U^{235} Age	±2σ	Pb^{206}/U^{238} Age	±2σ
AC420 - 1M	0.2	4.6	2.7	.96	.23	.184	.019	091	5	090	8
AC420 - 7M	0.9	.91	4.41	.24	.25	.3043	.01	676	8	711	9
AC420 - 10M	0.7	.93	1.88	.3	.27	.2973	.0093	702	9	677	6
AC420 - 4M	1.1		2.32	.37	.25	.3026	.0093	709	8	704	7
AC420 - 18M	3		6.63	.45	.26	.3091	.0094	716	8	736	6
AC420 - 19M	0.8		9.7	.48	.27	.3015	.0099	722	1	701	9
AC420 - 3M	1.4		1.06	.51	.27	.3024	.0097	726	9	705	9
AC420 - 5M	0.2		8.96	.53	.27	.3122	.01	741	0	750	1
AC420 - 9M	.6	.89	2.28	.6	.28	.31	.0096	747	1	740	7
AC420 - 8M	0.4		9.12	.63	.3	.3132	.011	742	5	754	4
AC420 - 6M	0.5	.8	5.61	.65	.28	.3168	.01	754	0	780	3
AC420 - 11M	.8	.11	1.29	.65	.28	.3132	.01	760	3	755	1
AC127 - 12M	0.2	.082	6.55	.41	.26	.3002	.0094	710	9	694	6
AC127 - 16M	.8	.0097	3	.41	.26	.3097	.0097	718	8	738	8
AC127 - 30M	1	.0014	1.3	.41	.25	.3018	.0095	711	8	699	7
AC127 - 7M	.1		3.7	.47	.26	.309	.0096	719	9	735	7
AC127 - 19M	2.4		2.3	.47	.27	.3082	.01	720	9	731	1
AC127 - 23M	1		9.6	.52	.26	.3087	.0092	732	9	736	7
AC127 - 8M	.4		6	.56	.26	.3091	.0096	744	7	736	8
AC127 - 28M	.2		5.11	.56	.27	.3103	.0093	736	9	741	6
AC127 - 27M	.1		2.66	.57	.25	.3063	.0094	746	7	722	7
AC127 - 22M	.4		0	.58	.27	.3136	.0095	739	0	758	7
AC127 - 5M	0.4	.491	2.39	.6	.27	.3032	.0092	748	7	709	7
AC127 - 14M	.3		9.5	.6	.28	.3151	.011	750	9	765	3
AC127 - 26M	0.2		6.5	.61	.27	.3132	.0097	761	7	756	7

M AC127 - 13	.6	.054	5.2	.62	.26	.3206	.0098	760	8	792	8
M AC127 - 29	1		2.1	.65	.27	.3148	.011	764	2	762	2
M AC127 - 3	.2		5.3	.66	.26	.3101	.0095	757	9	743	8
M AC127 - 20	.6		6.15	.66	.26	.3192	.01	758	6	784	0
M AC127 - 1	1		5.86	.68	.29	.316	.01	757	3	769	0
M AC127 - 15	.7		1.3	.7	.27	.3168	.01	763	0	773	0
M AC127 - 10	.7		1.3	.71	.26	.3169	.01	767	9	773	9
M AC127 - 6	.2	.085	7.9	.72	.27	.3124	.0093	776	7	758	6
M AC127 - 11	1.2	.29	5.7	.72	.27	.3197	.0097	772	6	788	8
M AC127 - 2	.2	.46	3.8	.78	.29	.3137	.011	774	1	761	3
M AC127 - 25	.6	.176	9.4	.82	.29	.3168	.011	787	0	772	2
M AC127 - 9	.1	.42	1	.87	.27	.3196	.01	798	7	786	9
M AC127 - 18	.7	.051	2.7	.21	.33	.3449	.012	842	4	908	9
M AC127 - 17	.1	.175	4	.22	.29	.3268	.01	857	1	828	0
M AC127 - 4	.7	.54	6.04	.94	.36	.3391	.011	961	4	881	3
M AC99 - 3	.2	.26	3.86	.77	.32	.2552	.011	584	3	462	9
M AC99 - 11	0.8		.46	.2	.39	.284	.013	658	8	612	6
M AC99 - 20	.6		1.47	.29	.39	.2988	.012	690	7	682	0
M AC99 - 13	1.6	.0118	3.44	.35	.36	.2939	.012	703	0	663	2
M AC99 - 24	.1		1.3	.35	.37	.315	.014	689	2	761	0
M AC99 - 19	0.1		5.71	.38	.31	.3025	.012	699	0	701	8
M AC99 - 8	.5		4.76	.41	.34	.3056	.012	715	4	716	0
M AC99 - 15	.2		1.89	.43	.34	.313	.014	705	3	751	9
M AC99 - 18	0.6		2.79	.46	.41	.312	.014	727	5	756	6
M AC99 - 27	.6		5.32	.46	.32	.3	.012	709	0	693	9
M AC99 - 22	0.3		1.06	.47	.33	.3167	.013	721	2	776	2
M AC99 - 29	.8		7	.49	.31	.2975	.011	736	9	676	7
M AC99 - 6	0.8		4.46	.51	.35	.3091	.013	735	6	745	4
M AC99 - 9	.7		2.84	.52	.36	.303	.013	731	6	707	3
M AC99 - 10	.1		1.71	.52	.35	.3029	.013	764	0	708	3

M AC99 - 12	0.7		1.67	.53	.38	.2914	.012	749	0	645	9
M AC99 - 16	.3	.302	3.65	.53	.39	.3082	.013	728	9	734	1
M AC99 - 14	2	.8	1.35	.58	.39	.302	.013	738	7	699	6
M AC99 - 2	1.5		.18	.59	.41	.309	.015	757	6	736	3
M AC99 - 21	1.4		2.99	.6	.35	.302	.014	739	5	698	7
M AC99 - 17	.2		2.35	.61	.38	.314	.013	749	9	763	3
M AC99 - 1	0.4		4.02	.7	.34	.3152	.013	776	2	762	3
M AC99 - 25			1.55	.7	.37	.2996	.012	751	1	692	6
M AC99 - 28	.2		5.23	.7	.33	.3052	.012	771	8	719	9
M AC99 - 23	0.4		0.89	.72	.37	.3172	.012	769	6	773	8
M AC99 - 5	1.8	.019	0.58	.93	.37	.315	.014	805	4	762	9
M AC99 - 7	.2	.79	5.68	.2	.37	.325	.012	842	3	811	9
M AC99 - 4		.97	5.05	.41	.41	.3	.013	885	3	687	3
M AC436 - 3		.0016	2.28	.29	.28	.3008	.01	687	2	698	8
M AC436 - 10			2.92	.5	.28	.3103	.011	735	3	745	5
M AC436 - 9	.3		9.62	.53	.27	.3147	.0099	732	1	762	9
M AC436 - 8	1.4	.67	7.81	.55	.29	.3127	.011	732	3	756	3
M AC436 - 1	2.8		6.72	.63	.28	.3147	.01	760	7	762	1
M AC436 - 7	1.6	.0063	0.9	.63	.28	.308	.0097	753	9	730	8
M AC436 - 5	1.5		1.26	.69	.28	.3086	.01	761	9	735	1
M AC436 - 2	.1		8	.71	.33	.3187	.012	764	9	780	0
M AC436 - 6	2.6		2.9	.73	.29	.3193	.011	778	2	784	6
M AC436 - 4	0.3		3.23	.82	.31	.3207	.011	785	4	795	5
M AC201 - 10	10	4.5	1.9	.37	.28	.218	.012	507	6	264	6
M AC201 - 15			3.08	.21	.31	.311	.012	669	3	745	3
M AC201 - 24	17		4.25	.26	.31	.305	.012	679	2	717	9
M AC201 - 19	5		5.11	.29	.29	.302	.012	687	9	706	2
M AC201 - 30			6.98	.39	.32	.308	.012	702	9	728	9
M AC201 - 29			2.98	.40	.32	.307	.012	714	0	723	0
M AC201 - 1	5	.239	3.88	.42	.32	.306	.012	718	8	720	1

MAC201-20	14		3.65	.45	.32	.303	.013	716	1	706	3
MAC201-17	32		9.61	.48	.32	.312	.013	719	0	747	2
MAC201-3	21		4.02	.49	.31	.309	.012	730	0	734	0
MAC201-5	19	.331	9.8	.51	.32	.306	.012	720	8	717	8
MAC201-4	11		7.1	.52	.31	.312	.013	740	5	751	0
MAC201-2	15	.17	9.49	.53	.35	.309	.014	723	6	733	9
MAC201-9	25	.07	8.04	.53	.31	.311	.012	733	9	743	0
MAC201-18	12		3.16	.53	.31	.306	.012	734	9	720	9
MAC201-21	8	.37	7	.53	.33	.301	.013	728	2	698	1
MAC201-43	15		1.82	.54	.35	.311	.013	739	4	743	3
MAC201-27	5		2.5	.54	.33	.307	.012	736	3	728	9
MAC201-8	16	.4	2.88	.55	.32	.319	.013	734	7	781	4
MAC201-40	8		6.14	.56	.32	.309	.012	738	6	734	9
MAC201-22	3		6.95	.56	.32	.309	.013	742	0	737	1
MAC201-45		.28	4.42	.57	.32	.309	.013	754	9	733	3
MAC201-14		.0132	3.73	.58	.33	.310	.012	748	7	741	0
MAC201-31	15	.81	4.14	.58	.32	.307	.012	749	7	731	3
MAC201-34	2		1.62	.59	.32	.319	.013	748	3	784	3
MAC201-28	9		8.69	.61	.32	.315	.013	751	8	765	3
MAC201-23	14		5.61	.62	.34	.311	.013	742	1	745	5
MAC201-38	1		7.71	.62	.35	.306	.014	753	6	718	8
MAC201-7	4	.8	7.8	.63	.55	.310	.014	758	1	742	9
MAC201-35	1		0.94	.64	.35	.322	.014	748	2	803	8
MAC201-39	1	.037	3.51	.68	.32	.323	.013	769	8	804	3
MAC201-41	21		3.59	.68	.34	.315	.014	768	9	772	1

MAC201 - 42	13	4.43	3.23	.69	.33	.310	.013	767	9	738	2
MAC201 - 26	20		6.49	.70	.36	.318	.014	768	2	784	8
MAC201 - 36	4		5.02	.71	.33	.317	.013	766	9	772	4
MAC201 - 16	15		1.3	.72	.33	.315	.012	767	1	766	9
MAC201 - 32		.255	9.06	.74	.32	.318	.012	771	8	781	1
MAC201 - 37			5.45	.75	.39	.318	.015	773	0	774	1
MAC201 - 13			8.13	.77	.35	.333	.014	778	9	848	8
MAC201 - 33	4	.157	7.24	.80	.38	.316	.013	769	7	767	4
MAC201 - 25	19		6.28	.81	.35	.314	.013	774	0	758	3
MAC201 - 11	19	.019	6.79	.83	.34	.330	.013	794	0	838	4
MAC201 - 6	2	.52	9.7	.89	.35	.317	.012	792	0	777	8
MAC201 - 12			0.16	.12	.37	.327	.014	838	0	820	0
MAC79 - 4	17	.994	2.3	.27	.17	.154	.007	206	0	23	9
MAC79 - 15	4	.68	0.6	.62	.22	.165	.010	286	2	87	6
MAC79 - 1	2	4600	90000	.40	.35	.171	.013	468	1	017	5
MAC79 - 12	8	6.54	65	.54	.32	.146	.009	535	1	75	3
MAC79 - 18		.179	4.9	.56	.30	.234	.014	524	8	353	2
MAC79 - 20	9		4.87	.38	.31	.304	.012	710	6	708	0
MAC79 - 13		.0011	5.71	.39	.33	.313	.012	718	1	753	1
MAC79 - 21	9		6.6	.49	.30	.308	.012	726	5	731	9
MAC79 - 17	7		3.38	.51	.32	.307	.013	727	7	723	3
MAC79 - 6		.049	1.6	.53	.31	.313	.012	742	9	754	7
MAC79 - 5	6	.0014	2.13	.53	.33	.311	.012	734	2	745	0
MAC79 - 3	6	.176	9.8	.54	.31	.311	.012	736	7	744	0
MAC79 - 14			9.83	.56	.33	.307	.013	735	3	721	3
MAC79 - 8		.036	6.13	.60	.36	.324	.014	740	4	814	8
MAC79 - 7			0.03	.63	.35	.315	.014	751	4	779	7
MAC79 - 11			4.54	.84	.34	.332	.014	780	9	854	6
MAC79 - 2	10		0.3	.96	.33	.326	.013	815	7	815	2

M AC79 - 19	8	.86	3.1	.53	.94	.318	.019	935	00	778	4
M AC70 - 12	1	.147	.53	.89	.19	.062	.006	50	10	85	6
M AC70 - 7		1.12	1	.71	.28	.253	.012	576	8	451	9
M AC70 - 6	2	.8	9.19	.40	.32	.305	.012	719	8	713	2
M AC70 - 14	24		4.81	.41	.35	.301	.013	707	5	692	4
M AC70 - 21	8	.088	3.29	.51	.32	.304	.012	728	9	714	0
M AC70 - 18		.753	1.44	.54	.32	.310	.013	737	2	745	5
M AC70 - 20		.55	4.74	.55	.33	.310	.012	731	1	738	0
M AC70 - 3		.49	0.9	.57	.34	.311	.013	748	6	744	4
M AC70 - 9		2.34	1.16	.61	.31	.312	.013	751	7	752	2
M AC70 - 17	3	.627	7.97	.67	.34	.314	.013	753	0	762	2
M AC70 - 24	10	.324	0.62	.67	.39	.317	.017	772	5	774	1
M AC70 - 26	27	.82	1.83	.68	.33	.313	.012	775	7	755	1
M AC70 - 15	12	5.3	5.48	.75	.33	.332	.014	765	0	846	4
M AC70 - 2	19	.5	3.74	.80	.35	.330	.013	793	0	838	4
M AC70 - 22		.18	3.95	.82	.35	.322	.013	779	0	796	4
M AC70 - 5	13	1.65	1.76	.90	.34	.309	.012	806	1	737	8
M AC70 - 11	6	.72	6.73	.94	.36	.335	.014	803	0	858	6
M AC70 - 10	5	2.5	3.1	.52	.41	.385	.016	037	9	098	9
M AC70 - 28	3	.41	3.61	.66	.52	.404	.016	181	2	185	3
M AC444 - 13	22	.95	30.5	.09	.12	.083	.008	22	4	10	8
M AC444 - 2	2	.26	7.4	.57	.24	.251	.011	532	3	443	5
M AC444 - 1	5		4.57	.36	.29	.304	.012	696	5	709	8
M AC444 - 10	5		5.58	.51	.28	.310	.012	726	0	740	9
M AC444 - 15	13		6.34	.56	.29	.315	.012	733	3	763	8
M AC444 - 14	15	.0078	3.49	.57	.30	.322	.012	740	6	796	9
M AC444 - 30	2		9.15	.58	.29	.307	.011	740	3	727	5
M AC444 - 9	8		8.16	.62	.29	.319	.012	753	1	781	8
M AC444 - 21	9	.03	4.7	.62	.31	.312	.014	756	5	757	0
M AC444 - 12	10		7.11	.62	.33	.312	.012	749	6	747	1

MAC444 - 3	9	.084	7.56	.67	.30	.308	.011	755	3	730	6
MAC444 - 16	19	.049	5.69	.72	.29	.308	.012	763	2	731	7
MAC444 - 8	2	.176	8.83	.77	.31	.318	.012	781	0	780	8
MAC444 - 17			2.72	.78	.30	.316	.012	778	4	766	0
MAC444 - 29	4		8.98	.80	.30	.318	.012	790	2	779	6
MAC444 - 22	5	.074	1.55	.81	.30	.314	.012	789	1	758	0
MAC444 - 23	1	.236	8.88	.81	.31	.305	.011	779	6	715	3
MAC444 - 20	8		4.5	.84	.34	.321	.013	792	9	795	3
MAC444 - 24			0.91	.84	.28	.308	.011	787	9	730	4
MAC444 - 28	5		7	.85	.30	.311	.012	798	2	753	0
MAC444 - 19	3		6.58	.86	.50	.313	.015	805	1	760	0
MAC444 - 5			1.37	.88	.29	.336	.013	794	0	875	1
MAC444 - 27			0.12	.88	.31	.326	.012	792	4	815	8
MAC444 - 26			6.55	.88	.29	.306	.012	795	0	720	7
MAC444 - 6	5		4.99	.89	.30	.323	.012	804	2	811	1
MAC444 - 18	10		6.25	.90	.31	.329	.013	802	4	832	1
MAC444 - 25	5		0.4	.90	.31	.320	.013	792	3	788	3
MAC426 - 9		7.3	3.79	.32	.31	.248	.012	471	3	423	3
MAC426 - 10	20	.35	.27	.55	.50	.280	.019	580	20	610	7
MAC426 - 6	57	6.5	6	.57	.27	.274	.013	527	0	555	3
MAC426 - 2		.25	.03	.74	.45	.278	.015	563	00	572	8
MAC426 - 8		.75	.09	.75	.72	.284	.023	340	10	610	20
MAC426 - 7	17	6.7	.36	.89	.49	.274	.017	620	2	550	7
MAC426 - 1		.15	.64	.00	.91	.224	.026	440	80	280	30
MAC426 - 5	6	.41	.649	.61	.86	.272	.027	770	40	560	40
MAC203 - 13	12	.393	8.11	.35	.29	.307	.012	703	6	722	7

MAC203 - 14			9.24	.36	.28	.301	.012	715	7	696	8
MAC203 - 26	8	.0016	6.42	.45	.30	.310	.012	719	3	737	8
MAC203 - 29	16		8.75	.49	.31	.298	.011	719	8	680	6
MAC203 - 5	11		1.06	.51	.37	.321	.014	757	8	791	0
MAC203 - 19	11		9.3	.56	.30	.313	.012	746	6	761	8
MAC203 - 20	17		7.41	.57	.31	.307	.012	755	8	727	6
MAC203 - 28	14		0.83	.60	.30	.309	.011	745	5	733	6
MAC203 - 16		.176	3.76	.61	.30	.315	.012	750	5	762	8
MAC203 - 1	13		3.01	.62	.30	.325	.012	757	5	814	0
MAC203 - 17	9		4.11	.63	.31	.306	.012	773	6	720	8
MAC203 - 6	7		4.17	.65	.33	.317	.013	750	0	773	3
MAC203 - 12	3	.017	8.56	.66	.32	.312	.012	763	8	752	7
MAC203 - 11	13	.49	5.85	.67	.32	.316	.012	768	6	767	0
MAC203 - 2	9		4.66	.69	.32	.329	.013	769	6	832	3
MAC203 - 7	11.2		5.32	.70	.33	.329	.013	758	7	832	4
MAC203 - 4	25		6.26	.70	.36	.308	.013	743	5	726	5
MAC203 - 9	8	.095	8.3	.74	.32	.318	.012	768	7	776	9
MAC203 - 3	15		4.81	.75	.30	.317	.012	785	0	774	9
MAC203 - 10	1		8.65	.76	.30	.318	.013	772	3	782	3
MAC203 - 24	9	.5	1.1	.77	.33	.318	.013	773	7	776	4
MAC203 - 8	2		7.53	.80	.31	.316	.012	785	4	774	8
MAC203 - 18	1		8.82	.81	.31	.315	.012	784	5	761	1
MAC203 - 21	11		5.5	.83	.33	.320	.013	781	9	787	3
MAC203 - 30		.0163	5.92	.84	.36	.314	.013	784	2	763	2
MAC203 - 22	10	.087	9.78	.91	.35	.320	.013	807	7	788	2
MAC203 - 25	9		5.44	.91	.33	.322	.013	790	8	797	3

MAC203 - 23	8	.268	9.63	.96	.33	.329	.013	812	5	829	2
MAC203 - 27	4		8.88	.08	.34	.331	.013	833	5	840	2
MAC152 - 6	3		7.8	.52	.27	.309	.011	734	9	738	4
MAC152 - 12	15		4.3	.56	.29	.312	.012	739	4	749	7
MAC152 - 3		.072	0.5	.58	.28	.310	.011	741	0	741	3
MAC152 - 7	2	.71	3.06	.59	.28	.313	.011	744	0	752	5
MAC152 - 14		.19	9.44	.62	.27	.312	.011	750	0	751	7
MAC152 - 8	4	.226	1.99	.62	.28	.308	.011	747	0	728	4
MAC152 - 4			0.3	.70	.28	.314	.011	767	9	759	4
MAC152 - 2			7	.72	.28	.308	.011	772	9	731	3
MAC152 - 13	10		8.82	.73	.28	.328	.011	775	1	829	5
MAC152 - 9			0.4	.73	.28	.307	.011	772	3	722	4
MAC152 - 11	6	.652	3.91	.75	.29	.322	.012	781	2	798	8
MAC152 - 5		.41	3.95	.76	.31	.318	.012	778	3	776	7
MAC152 - 10		.0015	3.5	.76	.28	.318	.011	778	9	778	4
MAC152 - 1	7		4.7	.93	.29	.322	.012	805	0	805	7
MAC84 - 20	8	.94	.52	.44	.70	.196	.024	020	50	150	30
MAC84 - 15	3	.91	1.31	.04	.31	.269	.011	623	3	536	5
MAC84 - 4	21	.27	10.4	.37	.25	.312	.011	703	7	750	3
MAC84 - 6	15	.021	09.7	.38	.26	.315	.011	710	9	764	3
MAC84 - 9	14		10.2	.41	.26	.315	.011	712	8	765	6
MAC84 - 24	33	.44	7.7	.41	.26	.296	.010	713	1	674	2
MAC84 - 17	23	.253	4.5	.47	.26	.308	.011	720	9	730	4
MAC84 - 11	18	0.51	29.7	.47	.27	.307	.012	720	0	730	9
MAC84 - 16	27		8.6	.49	.27	.315	.012	733	1	762	5
MAC84 - 23	3		1.11	.50	.28	.303	.011	727	2	704	3
MAC84 - 8	12		07.5	.51	.27	.320	.012	735	9	795	8
MAC84 - 13	27	.073	09.5	.52	.26	.318	.011	736	7	782	4
MAC84 - 22	33	.38	4.6	.52	.27	.307	.011	728	0	723	2
MAC84 - 19	15	.206	05.5	.53	.26	.309	.011	738	8	736	4

M AC84 - 2	15		17.7	.54	.26	.313	.011	741	0	755	7
M AC84 - 5	19	.48	06.7	.54	.27	.317	.011	736	0	774	6
M AC84 - 26	33		00.8	.55	.26	.300	.011	737	8	692	4
M AC84 - 10	19		11.3	.56	.27	.319	.011	737	0	784	5
M AC84 - 14	19		08.2	.59	.28	.322	.011	750	1	799	6
M AC84 - 21	14	.424	5.01	.60	.29	.300	.011	739	3	691	5
M AC84 - 18	18	.88	03.9	.61	.27	.312	.011	752	7	749	5
M AC84 - 30	8		09.6	.62	.27	.306	.011	754	8	720	3
M AC84 - 27	22	.021	08.4	.63	.28	.304	.011	748	1	710	4
M AC84 - 29	18		08.6	.65	.28	.311	.011	766	1	746	6
M AC84 - 1	9		12.6	.75	.27	.318	.011	773	9	780	6
M AC84 - 28	22		07.5	.77	.27	.312	.011	780	0	752	5
M AC84 - 25	22		02.9	.87	.28	.315	.012	792	0	768	8

negative ^{204}Pb values indicate below detection limits.

grey shaded values used for Concordia diagrams and ages

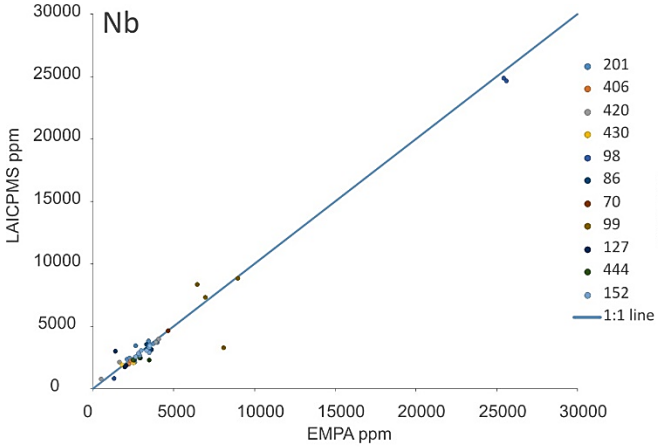
Nb
LAICPMS ppm
EMPA ppm
0
5000
10000
15000
20000
25000
30000
201
406
420
430
98
86
70
99
127
444
152
1:1 line

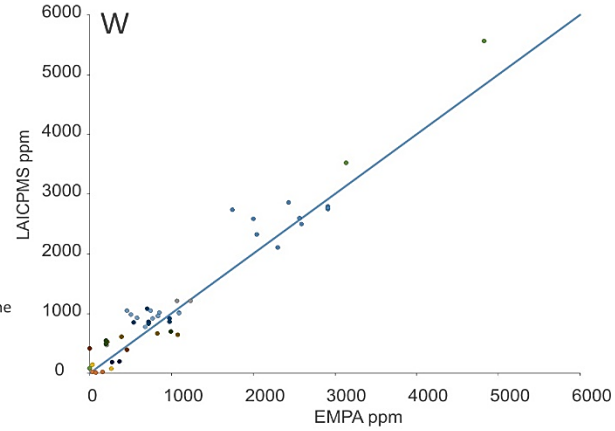
W
LAICPMS ppm
EMPA ppm
0
1000
2000
3000
4000
5000
6000

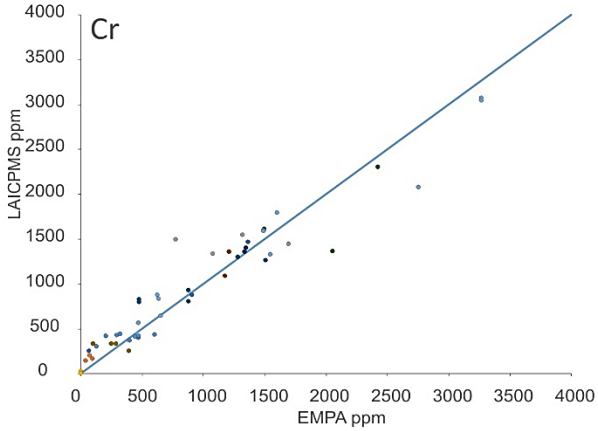
Cr
LAICPMS ppm
EMPA ppm
0
500
1000
1500
2000
2500
3000
3500
4000

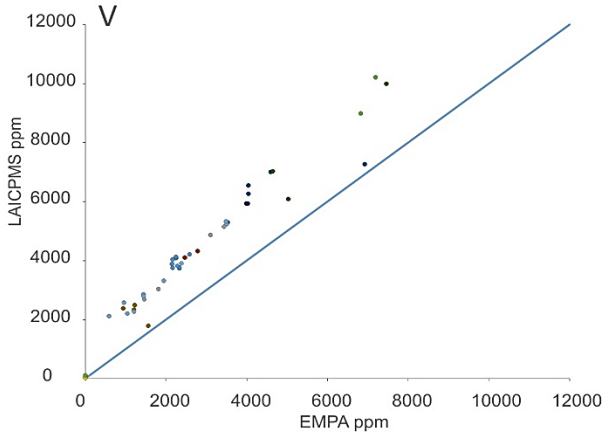
V
LAICPMS ppm
EMPA ppm
0
2000
4000
6000
8000
10000
12000

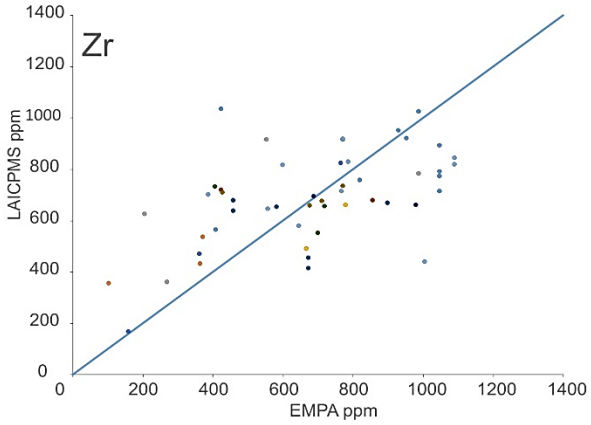
Zr
LAICPMS ppm
EMPA ppm
0
200
400
600
800
1000
1200
1400

Figure A6.1: Bi-plots of EPMA and LAICPMS data of the same grains showing agreement for Nd, W and Cr. The LAICPMS results for V is consistently higher by ~1000 ppm, whereas Zr shows a scatter.

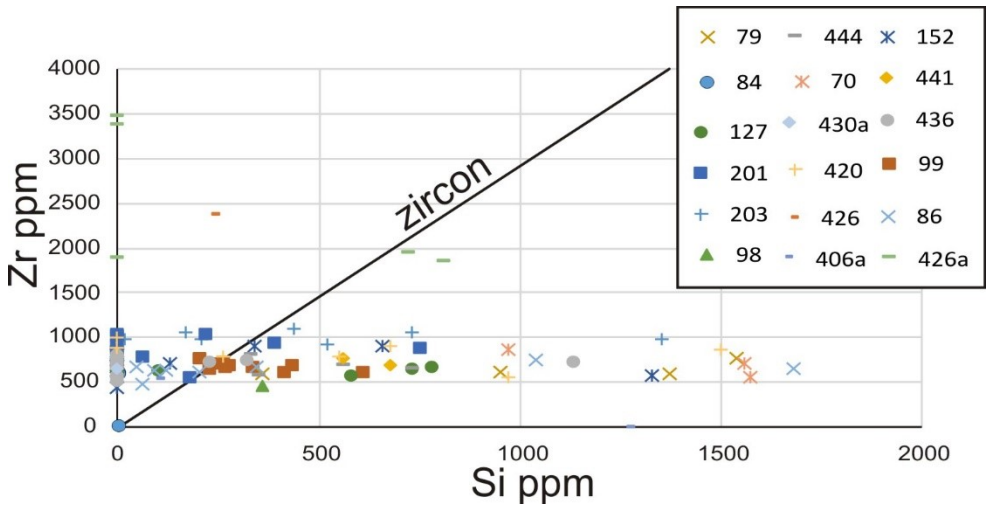

Figure A6.2: Bi-plot of Si and Zr for anatase and rutile determined by LAICPMS. The black zircon line indicates stoichiometric proportions between Si and Zr in zircon. The lack of correlation between the data and zircon line indicates that Zr was not contributed by zircon inclusions.

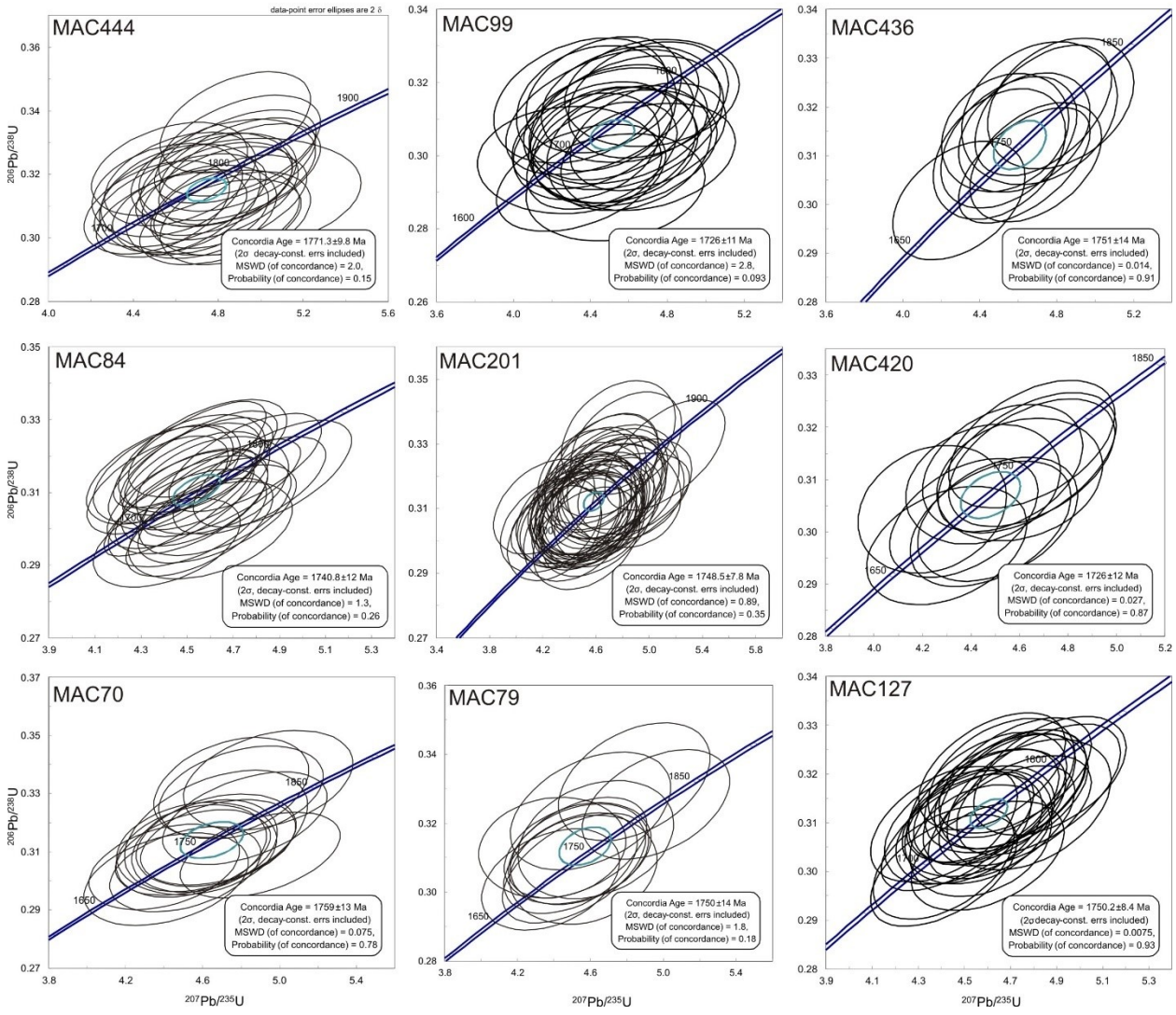

Figure A6.3: U-Pb concordia diagrams (constructed using Isoplot 4.15) based on rutile compositions.